Author:
Bailey, S. J

Title:
Cathodoluminescence of quantum well structures

Cathodoluminescence of Quantum Well Structures

Simon J. Bailey, B.Sc.

H.H. Wills Physics Laboratory,
University of Bristol.

A thesis submitted in partial fulfilment of the requirement for admission to the Degree of Doctor of Philosophy of the University of Bristol.

December 1987

Memorandum

This thesis is submitted to the University of Bristol in support of an application for admission to the degree of Doctor of Philosophy. Except where stated in the text, the work was carried out by myself between October 1984 and September 1987 under the supervision of Professor J.W. Steeds. No part of this thesis has previously been submitted to this or any other university.

S.J. Bailey

December 1987.

Abstract

Recent advances in semiconductor growth techniques allow epitaxial layers of III-V semiconductors to be grown with near monolayer precision. Such techniques have been used to fabricate a number of high performance electronic and optoelectronic devices. In particular considerable effort has been devoted to the growth of GaAs/$A\ell_xGa_{1-x}As$ structures utilizing quasi two-dimensional carrier confinement, especially quantum well structures. Extensive investigations have been performed on quantum well structures using a variety of analytical techniques but the optical and electronic properties of extended defects have not received much attention.

In this study low temperature cathodoluminescence in a transmission electron microscope was used to examine defects in undoped single and multiple GaAs/$A\ell_xGa_{1-x}As$ quantum well structures grown by molecular beam epitaxy. Stacking faults, oval defects, misfit dislocations and screw threading dislocations were studied in detail. No evidence was found for quantum well width fluctuations in the vicinity of any defect. Cathodoluminescence spectra acquired with the electron beam illuminating stacking faults, oval defects and misfit dislocations showed emission features which were ascribed to extrinsic quantum well luminescence arising from enhanced impurity concentrations around the defects. All four types of defect decreased the intensity of the dominant quantum well emission and hence would be expected to have detrimental effects on optoelectronic devices.

The results obtained from cathodoluminescence in a transmission electron microscope were compared with results obtained using a scanning electron microscope and demonstrated that cathodoluminescence is an effective technique for characterizing undoped GaAs/$A\ell_x Ga_{1-x}As$ quantum well structures, provided that low temperatures and monochromatic (as opposed to integrated) cathodoluminescence imaging are used.

Dedicated to my parents, my sister and to Louise Marshall.

Acknowledgements

I would like to thank my supervisor, Professor J.W. Steeds for his help and encouragement. I would also like to thank all members of the Bristol E.M. group, both past and present, who have contributed to this work through helpful discussions and assistance. My special thanks go to C.J. Kiely, S. Myhajlenko and A.R. Preston for their assistance with microscopy and to R. Vincent for his excellent maintenance of the EM430 and EM400. I would also like to extend my thanks to P.J. Dobson for providing samples and valuable discussions. I am grateful to Diane Cokayne for patiently typing this thesis. The financial support of the S.E.R.C. is gratefully acknowledged.

CONTENTS

CHAPTER ONE

INTRODUCTION AND BACKGROUND

1.1. Introduction

In recent years semiconductor growth techniques such as molecular beam epitaxy (MBE) and metal organic chemical vapour deposition (MOCVD) have been developed to the point where epitaxial layers of III-V semiconductors can be grown with near monolayer precision. These techniques have allowed fabrication of a wide variety of high performance optoelectronic and electronic devices utilising quasi 2-dimensional carrier confinement effects. Typical examples include high electron mobility transistors (HEMT) for high speed logic circuits (Mimura et al., 1980) and multiple quantum well (MQW) lasers (Tsang, 1981) with low threshold currents and adjustable emission wavelengths. Multilayer structures have been grown from a number of III-V semiconductors using both MBE (Joyce, 1985) and MOCVD (Ludowise, 1985) but the GaAs/$A\ell_xGa_{1-x}As$ system has been most extensively developed. Techniques such as photoluminescence (PL), cathodoluminescence (CL), secondary ion mass spectroscopy (SIMS) and transmission electron microscopy (TEM) have been used to characterise GaAs/$A\ell_xGa_{1-x}As$ multilayer structures but the optical properties of crystallographic defects in quantum well (QW) structures have not been investigated thoroughly. In the current study undoped single and multiple GaAs/$A\ell_xGa_{1-x}As$ QW structures were examined using low temperature CL in a TEM so that the optical properties of various crystallographic defects could be investigated and an assessment made of the effectiveness of CL as a method of determining defect densities.

The remainder of this chapter discusses luminescence excitation mechanisms and optical processes in semiconductors including QW structures.

1.2. Luminescence Excitation Mechanisms

Light is emitted from materials as a result of electronic transitions between quantum mechanical states and can provide information about the characteristic energy levels present. Luminescence originates with an initial excited state and terminates, after photon emission, in a lower energy state. An excitation process is required to populate the excited states. For semiconductors excitation is usually performed by bombardment with photons to give photoluminescence (PL), electrons to give cathodoluminescence (CL), or by applying a voltage to give electroluminescence (EL). PL is a well established technique which has been applied to a wide range of semiconductors. The use of tunable dye lasers as the excitation source allows the energy of the exciting photons to be varied while the luminescence intensity at a fixed photon energy is measured. This technique, photoluminescence excitation spectroscopy (PLE), is particularly useful in characterizing semiconductors and is considerably more powerful than CL for detailed analysis of electronic transitions. The major advantage of CL over PL is that the excited volume can be highly localised by the use of a small electron probe. This allows higher spatial resolutions to be obtained. Care must be taken when comparing CL and PL spectra as CL generally gives much higher excitation densities than PL.

1.2.1. Cathodoluminescence

CL can be performed either in a scanning electron microscope (SEM), or in a transmission electron microscope (TEM). In either case interaction between the electron beam and a semiconductor produces a number of useful signals such as backscattered electrons, secondary electrons and photons but only CL will be discussed here. In a semiconductor the incident high energy electrons excite electrons from the conduction band to the valence band thus creating electron-hole pairs. These electron-hole pairs can then recombine via a number of radiative and non-radiative processes (see section 1.3).

CL from bulk samples has been extensively studied (Yacobi and Holt, 1986) in the SEM and offers a number of advantages over TEM CL. The large specimen chambers of most SEM's allow efficient cooling of samples to liquid helium temperatures and provide space for efficient light collection optics. SEM CL has been reviewed most recently by Spivak et al. (1986). The major disadvantages of SEM CL are the limited spatial resolution, which can approach 1-2 μm but is generally worse, and the inability to form direct images of any defects present in the semiconductor, although dislocations have been located subsequent to SEM CL studies by chemical etching, TEM and X-ray topography.

Pennycook (1981) has expressed the spatial resolution in a CL image as

$$d = (d_p^2 + d_G^2 + L^2)^{\frac{1}{2}}$$

where d_p is the electron probe diameter, d_G is the diameter of the volume in which electron hole pairs are generated and L is

the minority carrier diffusion length. Generally d_p is small, L depends on the sample quality and d_G is determined by interactions between the electron beam and the semiconductor allowing for both elastic and inelastic scattering. Archard (1961) proposed a model where incident electrons lose their energy within a sphere of radius $R_G = R_K - Z_D$, assuming electrons penetrate to a depth Z_D without loss of energy. Kanaya and Okayama (1972) have calculated R_K using the expression

$$R_K = \frac{2.76 \times 10^{-10} AE^{1.67}}{\rho Z^{0.89}}$$

where A is the average atomic weight, z is the average atomic number, ρ is the density and E is the energy of the incident electrons. According to Archard's model z_d can be written as

$$z_D = \frac{R_K}{(1 + 0.187\ z^{0.67})}$$

which gives the radius of the generation volume in GaAs as 1.66 μm for 20 kV electrons. Therefore the maximum spatial resolution in GaAs using 20 kV electrons is 3.3 μm.

TEM CL allows direct correlations to be made between defects and features on CL spectra and images,and can provide information on the electronic properties of the defects. TEM CL must be performed on thin specimens where surface recombination effects are more important than for bulk specimens. Simultaneous TEM and CL imaging are normally performed with much higher accelerating

voltages than for SEM CL which, combined with the thinner specimen used in the former case, significantly reduces the size of the generation volume. For thin films Archard's model is no longer appropriate as it predicts a decrease in spatial resolution due to a larger generation volume. This does not agree with the experimental results of Petroff et al. (1978), who observed improved resolution of dislocations in thin $Al_xGa_{1-x}As$ layers on increasing the accelerating voltage. Wittry (1958) estimated the volume excited by an infinitely small electron probe to aid quantification of x-ray microanalysis. Brown (1981) has extended this calculation to the case of thin films to find the extent of beam spreading. Goldstein et al. (1977) used a simple model to find the broadening b of an electron beam from a small probe at the bottom of a thin foil as

$$b \cong 2 \times 10^5 \frac{Z}{E}\left[\frac{\rho}{A}\right]^{\frac{1}{2}} t^{\frac{3}{2}} \qquad (1.1)$$

where t is the sample thickness. Figure 1.1 shows b plotted against t for GaAs and an accelerating voltage of 120 kV. Note that equation 1.1 only includes elastic single scattering and neglects relativistic effects. Wittry (1984) has reviewed electron beam-specimen interactions with reference to CL and EBIC. The spatial resolution obtainable using CL from thin films is also modified by the minority carrier diffusion length. However GaAs generally has a high surface recombination velocity which reduces the effective diffusion length. Shockley (1950) has shown that in the limit of infinite surface recombination velocity the effective diffusion length reduces from L to t/π if L is

greater than t. Pennycook (1981) measured the widths of CL images of dislocations in TEM foils but observed a t/2.2 dependence rather than the theoretical t/π relationship. Although spatial resolution improves with decreasing thickness the CL intensity simultaneously decreases. For TEM foils where surface recombination is the limiting factor, the CL intensity is proportional to t^2 so that a compromise must be made between spatial resolution and an acceptable signal to noise ratio. For very thin films the effective thickness determining the CL intensity and spatial resolution may be less than the actual specimen thickness due to a dead layer at the surface, possibly due to band bending. Wittry and Kyser (1967) have postulated the existence of this layer based on the variations of CL intensity with respect to accelerating voltage (for GaAs).

For TEM QW samples (section 1.4) carrier confinement reduces the effects of high surface recombination velocity with respect to monochromatic CL images acquired at the energy of the QW luminescence so that spatial resolution should be determined primarily by the minority carrier diffusion length. For QW samples with cladding layers thick enough to give detectable luminescence then the spatial resolution obtainable using this emission should be proportional to the layer thickness (neglecting the possible presence of a dead layer near the specimen surface).

1.3. Optical Processes in Semiconductors

Radiative recombination in semiconductors can be classified into intrinsic and extrinsic transitions. Intrinsic transitions arise from the pure semiconductor while extrinsic transitions are

due to the presence of impurities.

The simplest form of intrinsic recombination is due to free carriers (band to band recombination) recombining across the semiconductor band gap. Band to band recombination is only observed in the purest semiconductors at low temperatures but at higher temperatures can contribute significantly to the total recombination spectrum. At low temperatures coulombic forces between free electrons and holes lead to the formation of Wannier excitons where the electron orbits the hole,lowering the total energy of the bound electron hole pair. If the exciton is treated in the same way as a hydrogen atom then the exciton ionizatíon energy can be written as

$$E_x = \frac{m^* e^4}{2\hbar^2 \epsilon^2 n^2}$$

where e is the chargeon the electron, ϵ is the dielectric constant, n is the principle quantum number, $\hbar$ is Planck's constant divided by 2π and m^* is the reduced mass

$$\frac{1}{m^*} = \frac{1}{m_e} + \frac{1}{m_h}$$

formed from the effective masses m_e and m_h of the electron and hole. Excitons are free to move throughout the semiconductor until they recombine or become trapped by an impurity or defect. The energy of radiative recombination from free excitons is $E_g - E_x$ where E_g is the semiconductor band gap. For the ground state (n = 1) of a free exciton in GaAs, E_x is approximately 4 meV.

The radius a_x of a free exciton in this state is given by

$$a_x = \varepsilon a_o / m^*$$

where $a_o = 5.29 \times 10^{-11}$m. For GaAs m^* is smaller than the mass of an electron so that a_x is greater than the dimensions of the unit cell. In GaAs a_x is approximately 100Å. Excitons can be destroyed by local electric fields or by thermalization for temperatures where $k_B T$ is greater than E_x.

In direct gap semiconductors, excitons can interact strongly with phonons to form a mixed state known as a polariton (Hopfield, 1958). Polariton-exciton luminescence from GaAs at low temperatures shows the free exciton peak split into a doublet (Bloss et al., 1985). Due to the small energy difference between the two peaks of the doublet (< 1 meV) this structure cannot be observed at the higher temperatures (~ 30K) used in the current work so polaritons will not be considered further.

1.3.1. Extrinsic Recombination

Extrinsic recombination in semiconductors occurs in the presence of impurities or defects. Even in the purest direct gap semiconductors extrinsic luminescence is generally stronger than intrinsic luminescence. The literature on extrinsic recombination in semiconductors is very extensive and will only be discussed briefly here. Donors, acceptors and more complex defects or impurity states give rise to energy levels within the semiconductor band gap which can be classed as shallow or deep levels. Shallow levels have energies close to either the conduction or valence band and can be described using effective mass theory and the

hydrogen atom analogy. Deeper levels have energies near the centre of the band gap and are highly localised centres so that the effective mass theory is no longer applicable. Substitutional impurity atoms sitting on either a Ga or As site in GaAs generally give rise to shallow levels if each atom only donates a single carrier to the crystal binding. As only s electrons take part in the binding, the energy of the shallow level is close to that predicted by the hydrogenic model, although some variations occur depending on the chemical nature of the impurity. The binding energy of a carrier to the impurity is given by

$$E_B = \frac{m^* e^4}{2h^2 \varepsilon^2 n^2}$$

where m^* is the effective mass of the carrier. As electrons and holes in GaAs have different effective masses the carrier binding energies are different, 34 meV and 5.2 meV for acceptors and donors respectively. Free to bound (FB) recombination involves either transitions of electrons from the conduction band to acceptor states ($e - A^o$) or of holes from the valence band to donor states ($h - D^o$). FB transition energies are given by $E = E_g - E_B + K$ where K is the kinetic energy of the free carrier. FB transitions are usually only observed in semiconductors with low impurity concentrations when interactions between impurity atoms are not important.

The binding energies of excitons can be increased by the presence of point defects such as neutral or ionised impurities. Under these conditions it is energetically favourable for the exciton to remain in the vicinity of the defect to form a bound exciton (BE).

BE emission lines in emission spectra are generally narrow, partly because no free particles are involved. In GaAs, BE transitions due to excitons bound to neutral donors, ionised donors and neutral acceptors plus a number of more complicated transitions are possible. The first three transitions are normally referred to as (D^{o} X), (D^{+}X) and (A^{o}X) respectively. Excitons bound to ionised acceptors are not energetically favoured in GaAs and are not observed (Hopfield, 1964). Bound excitons can also be described by analogy with the hydrogen atom using the effective mass theory. Dean and Herbert (1979) have reviewed BE's in semiconductors.

If both donors and acceptors are present in a semiconductor then donor-acceptor pair recombination (D^{o}-A^{o}) can occur. (D^{o}-A^{o}) recombination is due to a transition between an electron bound to a donor and a hole bound to an acceptor. The impurities are neutral in the initial state of a (D^{o}-A^{o}) transition but are ionized in the final state. The coulomb interaction between the impurities lowers the energy of the final state so that the energy of the luminescence is reduced by this amount. The energy of the emitted photon in a (D^{o}- A^{o}) transition is given by

$$E = E_g - E_A - E_D + e^2/\varepsilon r$$

where E_A and E_D are the acceptor and donor binding energies and r is the separation between the donor and acceptor. For substitutional impurities the donor and acceptor must occupy lattice sites so that r has discrete values and (D^{o}- A^{o}) luminescence at low

temperatures shows a series of discrete lines. Up to 300 lines have been observed in GaP (Gershenzon, 1966). Different emission energies have been observed depending on whether the donor and acceptor occupy similar (type I) or dissimilar (type II) lattice sites.

Energy levels in a semiconductor which cannot be described using simple effective mass theory are known as deep levels. Deep levels can give rise to both radiative and non-radiative recombination. Substitutional impurities which contribute more than one carrier to the crystal binding, transitions metals and rare earths all give rise to deep levels. The high binding energies of electrons or holes for deep levels strengthens the coupling to phonons so that luminescence from deep levels often show phonon replicas. In GaAs the longitudinal optical phonon coupling is strongest. Shallow levels do not normally exhibit strong phonon coupling. Due to the high binding energy electrons have small orbits for deep levels giving strong localization of the bound electron and hence strong phonon coupling.

Non-radiative recombination can affect the radiative efficiency of a semiconductor. Non-radiative transitions are difficult to study experimentally, although techniques such as deep level transient spectroscopy can reveal some electron and hole traps. There are a number of possible non-radiative recombination routes in most semiconductors. For example, surface or interfacial recombination, crystal defects such as dislocations, Auger transitions and deep levels.

1.4. Quantum Wells

Superlattice and quantum well structures were first proposed by Esaki and Tsu (1970). Subsequent refinement of the MBE (Joyce, 1985) and MOCVD (Ludowise, 1985) growth techniques has made it possible to grow complicated structures with abrupt changes of doping and composition. There are two main categories of super-lattice structure, modulation doped and compositionally modulated superlattices. Modulation doped superlattices have been discussed by Dohler (1983) and will not be included here. Compositional superlattices represent a class of artificial semiconductor structures in which carrier transport is restricted so that quantum size effects become significant. In a quantum well (QW) or superlattice structure electrons and holes are confined within thin layers to form quasi two-dimensional electron and hole gases. Quasi two-dimensional carrier transport is also exploited in a number of semiconductor devices which are not based on the QW, for example silicon metal oxide semiconductor field effect transistors. The quantum size effect becomes operative in a semi-conductor layer structure when the layer thickness becomes comparable to the De Broglie wavelength of an electronic particle. For a $GaAs/A\ell_xGa_{1-x}As$ QW this thickness is of the order 500 Å. Carrier confinement in a compositional superlattice is achieved by varying the band gap of the structure in the growth direction to create potential wells. A quantum well in the $GaAs/A\ell_{1-x}Ga_xAs$ system is illustrated in Figure 1.2. In this structure both electrons and holes are confined to the GaAs layer in a type I QW. Figure 1.3 illustrates a type II QW in the GaSb/InAs system where both the conduction band and valence bands in the QW (InAs) have lower energies than the valence band of the barrier (GaSb). As QW's in

the GaAs/$A\ell_x Ga_{1-x}As$ system have received the most attention in the literature and were the only QW structures examined in the current work the following discussion will be restricted to this system.

The simplest way to calculate the energy levels of electrons and holes in a QW is to consider the QW as an infinite strength one-dimensional potential well in both the conduction and valence bands (Dingle, 1975) and solve the Schröedinger equation;

$$-\frac{h^2}{2m^*}\left(\frac{d^2\psi}{dz^2}\right) = E\psi$$

where m^* is the effective mass of the electron or hole, ψ is the wavefunction and E is the energy of the level. The solution to this equation is

$$E_n = \frac{h^2}{2m^*}\left(\frac{n\pi}{L_z}\right)^2$$

where L_z is the width of the QW due to a series of discrete bound states within the QW. This approach can readily be extended to a three dimensional situation. The energy eigenvalues are then

$$E_n = \frac{h^2}{2m^*}\left(\frac{n\pi}{L_z}\right)^2 + \frac{h^2}{2m^*}(k^2_x + k^2_y)$$

where k_x and k_y are the momentum wave vectors in the x and y directions. Each confined particle state E_n has a continuum of values for k_x and k_y giving rise to a subband. For GaAs the valence band

has three branches at $\underline{k} = 0$. The two upper bands are termed the heavy hole and light hole bands and have approximately the same energy but different effective masses. Casey and Panish (1978). In a QW the light hole and heavy hole states are separated so that for each quantum number n there are two energy subbands corresponding to the light and heavy holes, the heavy hole having a lower value of E_n. A physically more realistic calculation of QW energy states represents the QW as potential wells of finite depth (Dingle et al., 1974) but can only be performed if the valence and conduction band discontinuities (ΔE_v and ΔE_v) are known. When Dingle et al. (1974) first detected quantization in optical absorption measurements on GaAs/$A\ell_x Ga_{1-x}As$ MQW structures they used values for E_v and E_c of $0.12\Delta E_g$ and $0.88\Delta E_g$ where ΔE_g is the difference in band gaps between the $A\ell_x Ga_{1-x}As$ and GaAs layers. Band offsets in a GaAs/$A\ell_x Ga_{1-x}$ interface have since been the subject of vigorous debate, although in recent years general agreement has been reached for a value of approximately $\frac{3}{2}$ for the ratio $\Delta E_c/\Delta E_v$. However the GaAs/$A\ell_x Ga_{1-x}As$ interface is the only system for which a consensus has been achieved. Band offsets and their measurement have recently been reviewed by Heinrich and Langer (1986).

For finite depth potential wells the time independent Schrödinger equation must be solved both within the wells and within the barriers. Solutions for the energy levels are the transcendental equations (Kolbas and Holonyak, 1984).

$$\alpha \tan\left(\frac{\alpha L_z}{2}\right) = \beta \quad \text{(symmetric states)}$$

and

$$\alpha \cot\left(\frac{\alpha L_z}{2}\right) = -\beta \quad \text{(antisymmetric states)}$$

where $\alpha = (2mE/h^2)^{\frac{1}{2}}$ and $\beta = [2m(\Delta E_b - E)/h^2]^{\frac{1}{2}}$. ΔE_b is the appropriate band offset. Solutions to these equations can be obtained numerically. For MQW structures calculations of energy levels become considerably more complicated although a Kronig-Penney model (Kittel, 1976) can be used for structures with ten or more QW's. Even for SQW structures accurate calculations of energy levels are considerably more complex than the simple models discussed here but in general are based on the work of Bastard (1982).

1.5. Optical Processes in Quantum Wells

From the previous discussion the major effect of quantum confinement on the luminescence of GaAs QW's as compared with bulk GaAs would be expected to be a shift to higher energy of the intrinsic luminescence. Radiative transitions in QW's are theoretically possible from any of the electron states to any of the heavy or light hole states. For example from the n^{th} electron state to the m^{th} light hole state. However the most probable transitions are for $n = m$ because the electron and hole wavefunctions for $n \neq m$ are nearly orthogonal. The lowest energy transition in a QW is the $n = 1$ electron to $m = 1$ heavy hole transition. Therefore PL or CL spectra from an undoped GaAs structure (in the absence of excitonic effects) should have this recombination route as the dominant radiative process at low temperatures. For higher temperatures and depending on both the position of the Fermi level and the width of the QW, electron to light hole transitions might also be observed.

In addition to the energy shift due to quantum size effects luminescence from QW's shows a number of differences as compared to luminescence from bulk semiconductors. Low temperature PL of high quality, undoped bulk GaAs is usually dominated by extrinsic features (Kunzel and Ploog, 1981) such as (e - A^{o}) recombination plus emission close to the exciton edge due to BE and (h - D^{o}) transitions. Weak emission due to free exciton (polariton) transitions has also been detected. Absorption, exciton and emission measurements on GaAs QW's of equivalent quality all show that intrinsic free exciton recombination is the dominant radiative process (Weisbuch et al., 1981). Even at room temperature Dawson et al. (1983) have shown that PL from 55Å GaAs QW's is dominated by free exciton recombination, thermal population of light hole states allowing detection of both light and heavy hole excitons. The n = 1 electron to heavy hole and light hole excitonic transitions are normally denoted n = 1 X(e - hh) and n =1X(e - 1h) respectively. The assignments of emission features to light and heavy hole transitions have been confirmed by linear and circular optical polarization experiments. Intrinsic excitonic recombination dominates QW luminescence due to carrier confinement favouring exciton formation and increasing the excitonic recombination rate. Bimberg et al. (1984) have shown that n = 1 X(e - hh) recombination increases by an order of magnitude when the QW width is decreased from infinity to 52Å , implying that unless the average spatial separation of impurities is comparable with the free exciton diameter, free exciton recombination will occur before the exciton

can be captured by a neutral impurity. For a 50Å QW this would require an impurity concentration of order $2 \times 10^{17} cm^{-3}$ (Balkan et al., 1986).

In addition to the n = 1 excitonic emission other transitions have been observed such as n = 2 (e - 1h) and n = 2 (e - 1h) transitions using PLE. Forbidden transitions such as $(e_1 - hh_3)$ and $(e_2 - \ell h_1)$ have also been observed (Duggan et al., 1985). The subscripts denote the initial quantum numbers (n) of the electrons and holes. Normally only the 1s state of the n = 1 X(e - hh) exciton can be detected by PL although observation of the 2s state has been reported (Moore et al., 1986).

In the previous section simple methods of calculating the energy levels of QW's were discussed but ignored the excitonic nature of the dominant emission processes. Full calculations of transition energies use the envelope function approximation (Bastard, 1982) including the effect of non-parabolicity of the conduction band and correcting for the exciton binding energy. In a truly 2-dimensional system the exciton binding energy is four times greater than for a bulk exciton. Considerable theoretical effort has been devoted to establishing reliable exciton binding energies in QW's (Greene et al., 1984). In a perfect QW structure all the interfaces would be atomically flat. In a real $GaAs/A\ell_x Ga_{1-x}As$ QW, interfaces can deviate from ideality in a number of ways. The interface may be graded in composition so that the square well calculations are not valid. The agreement between calculated and experimental transition energies suggests that this effect is not significant. A more important effect is that,although the

the interfaces are abrupt,they are not smooth so that the well width varies in monolayer steps. If the spatial separation of the steps is less than the exciton diameter (~ 150Å), the exciton samples an average well width that broadens the free exciton PL peak. Weisbuch et al. (1981a) observed such a broadening of the free exciton peak when comparing PL spectra from 50Å QW's with PL spectra from 220Å QW's. More recently Bimberg et al. (1987) analysed the line shape of the free exciton emission from QW's to show that the step density for an $Al_xGa_{1-x}As$/GaAs interface (in order of growth) is higher than for a GaAs/$Al_xGa_{1-x}As$ interface. For step separations much smaller than the exciton diameter, the interface roughness becomes less significant and can lead to sharpening of free exciton PL. Step densities in GaAs/$Al_xGa_{1-x}As$ layers have been decreased by the use of growth interrupts during MBE growth, immediately prior to interface formation, allowing smoothing of the growth surface to occur. The majority of the smoothing (for a QW) has been shown to occur at the GaAs/$Al_xGa_{1-x}As$ interface (Tanaka et al., 1986). In some cases this smoothing is sufficient to increase the step density to values significantly greater than the exciton diameter. Depending on the exciton position it then experiences a different QW width. PL spectra from such structures show split peaks, each peak corresponding to a different well width (Sakaki et al., 1985). Free exciton peak energies measured by PL are often several meV lower than the values obtained by PLE or absorption measurements (Bastard et al., 1984). This effect, the Stokes shift has also been linked to interface steps (Delalande et al., 1985) but may also be due to impurity effects.

The Stokes shift is frequently used as a measure of QW quality. Good quality samples show only a very small Stokes shift. A simplistic explanation of the Stokes shift is that excitons have a tendency to become localised in the wider parts of a QW such that the excitonic emission is shifted to slightly longer wavelengths in a PL spectrum. Exciton creation (as detected by PLE or optical absorption) will occur without this spatial preference and will represent a different average over the interface. Exciton trapping at interface steps can also give rise to bound exciton characteristics in PL spectra.

1.5.1. Extrinsic Luminescence from Quantum Wells

Early studies of QW luminescence concentrated on the intrinsic, excitonic character of the luminescence. Extrinsic QW luminescence was first reported by Miller et al. (1982) for both Be doped and nominally undoped SQW samples. In both cases the emission was attributed to (e - A^{o}) recombination and was considerably weaker and broader than the dominant n = 1 X(e - hh) emission. Shallow impurities in QW structures have recently been reviewed by Delalande (1987). Extrinsic transitions in QW have not been extensively studied. Most authors have reported results for (e - A^{o}) recombination although emission from excitons bound to acceptors (Miller et al., 1983) and donor to heavy hole transitions (Lambert et al., 1983) have also been reported.

Calculations of extrinsic QW transition energies were first performed by Bastard (1981) for a hydrogenic impurity in a quantum well with infinite barriers. Although this model does not represent a completely realistic physical situation it illustrates two

important points. Firstly, that the binding energy of an impurity at the centre of a QW is higher than for an impurity at the edge of a QW. Secondly, that (for either position) the binding energy of the impurity increases monotonically by a factor of 4 as the well width decreases from infinity to zero. Greene and Bajaj (1985) used a more sophisticated calculation for donors in a finite depth potential well. For this case the impurity binding energy does not increase monotonically as the well width decreases but reaches a maximum for a well width of 20 - 50Å . Jarosik et al. (1985) obtained good agreement between results obtained from Si doped QW's using far infrared magnetospectroscopy and the calculations of Greene and Bajaj (1985).

Shallow acceptors in QW's have higher binding energies than donors and are easier to study using PL but calculations of acceptor binding energies are more complicated than for donors, partly because of the degeneracy of the GaAs valence band at $\underline{k} = 0$. Masselink et al. (1985) performed a simplified calculation of acceptor binding energies and obtained good agreement with the PL results of Miller et al. (1983), obtained for nominally undoped (residual carbon being the acceptor) and Be doped QW structures. The behaviour of acceptor binding energies with well width and impurity position are qualitatively similar to donor binding energies.

1.6. The Scope of this Investigation

Although considerable research has been performed on QW's in the GaAs/$Al_xGa_{1-x}As$ system relatively little work has been performed on the optical and electronic properties of crystal

defects in these structures. In the current study TEM CL was used to assess the optical properties of a number of different defects in undoped SQW and MQW GaAs/$A\ell_xGa_{1-x}As$ structures.

Chapter Two describes the experimental techniques used, the structures examined and the specimen preparation. Also included is a brief description of the most common artefacts generated by the CL system used in the current work. In Chapters Three, Four and Five, CL and TEM results from stacking faults, oval defects and dislocations in the QW structures are presented. Chapter Six describes a simple theoretical treatment of CL intensity around isolated dislocations in QW structures and compares the theoretical calculations with experimental results. Chapter Seven briefly presents results obtained using SEM CL on bulk QW samples and discusses the possibility of using SEM CL to identify defects. Conclusions and suggestions for further work are presented in Chapter Eight.

Unless otherwise stated, all the CL results presented in this thesis were acquired at a temperature of approximately 35K, using accelerating voltages of 20 kV and 120 kV (for SEM and TEM specimens respectively.

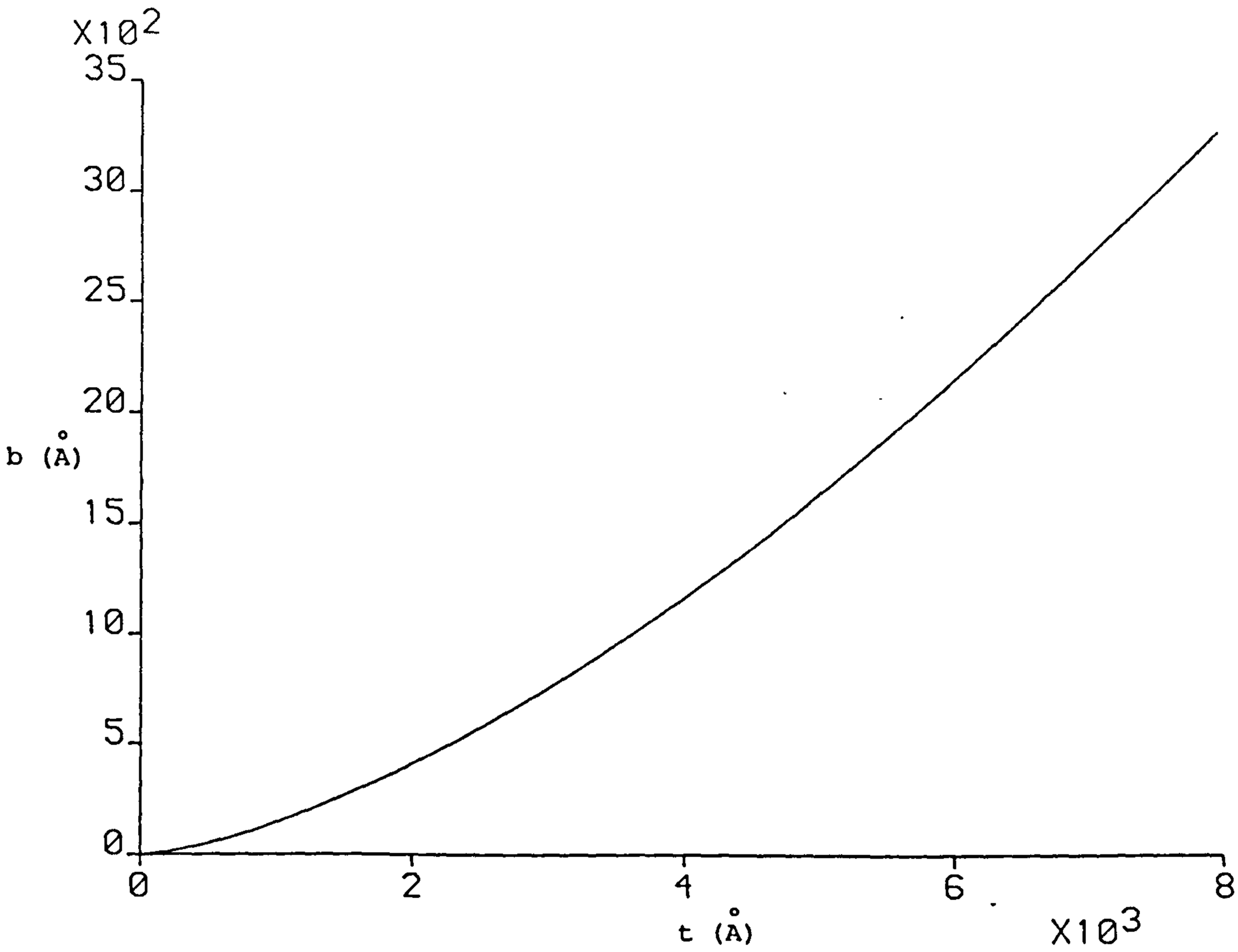

1.1 Graph of beam broadening (b) against thickness (t) for GaAs bombarded by 120 kV electrons.

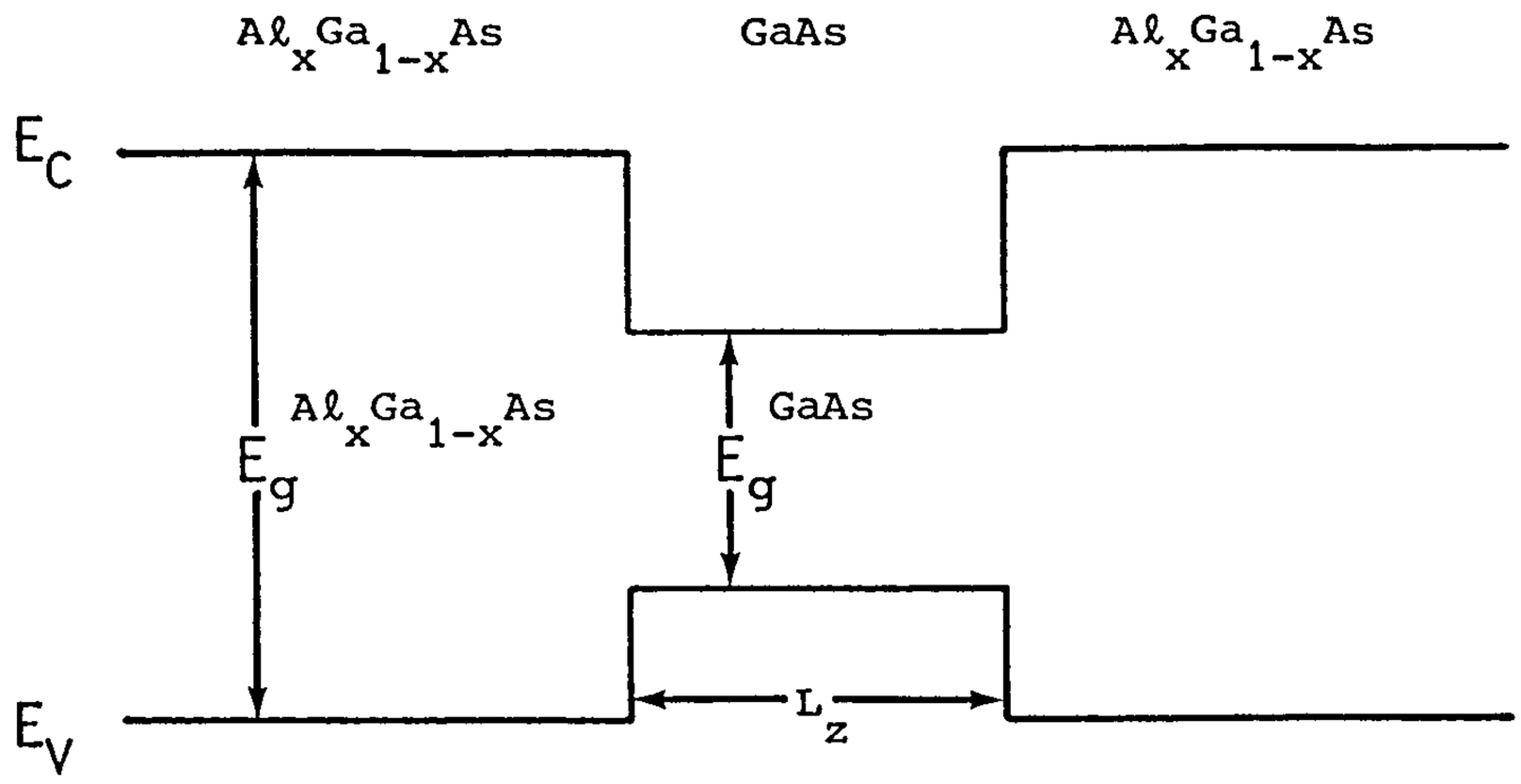

1.2 A type I ($Al_xGa_{1-x}As$/GaAs) quantum well structure.

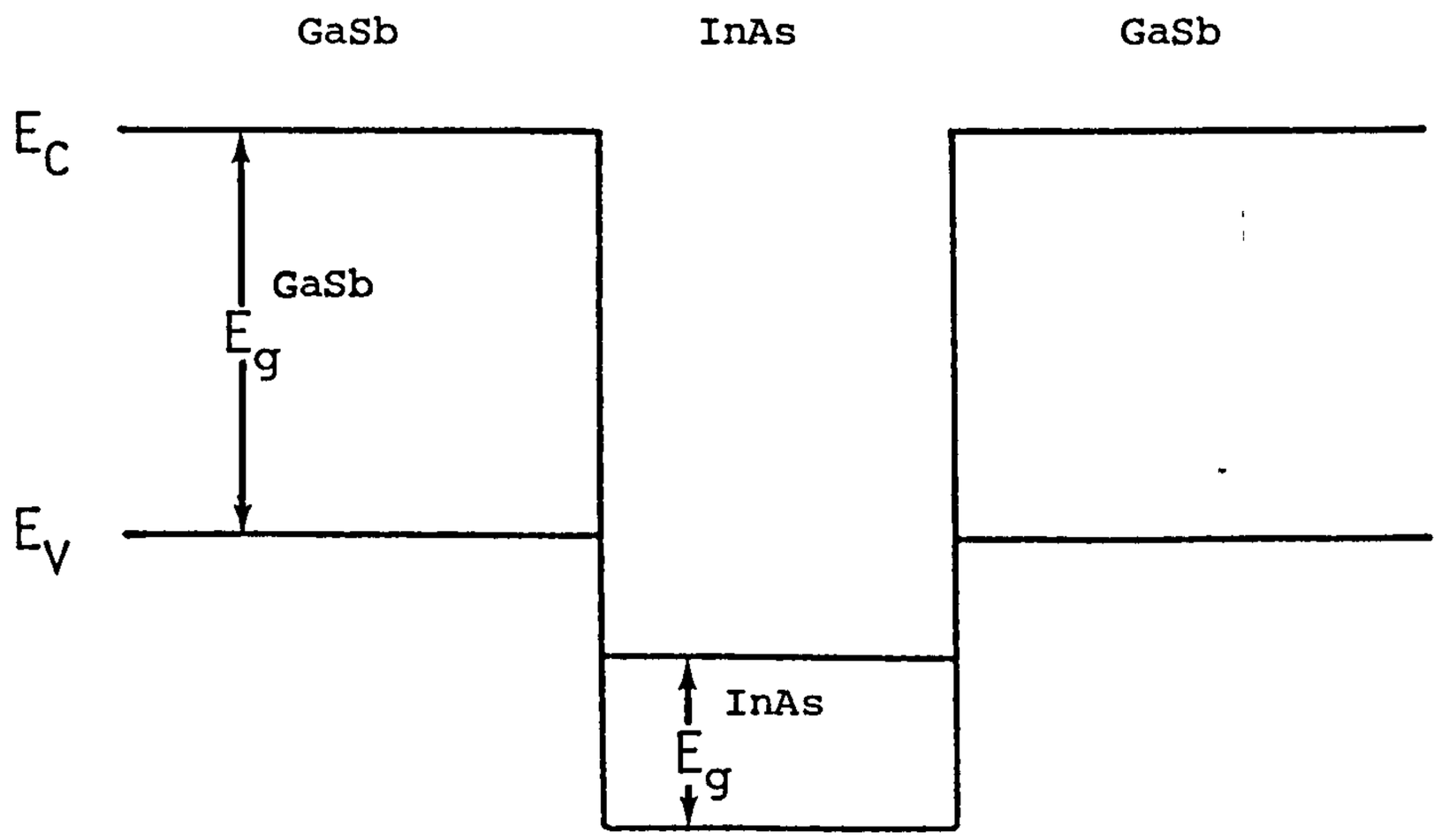

1.3 A type II (GaSb/InAs) quantum well structure.

CHAPTER TWO

EXPERIMENTAL TECHNIQUES AND SAMPLE PREPARATION

2.1. Introduction

In this Chapter an outline is given of the main experimental techniques and equipment used in this study. The QW samples investigated are briefly described. Also included is a detailed account of the techniques used to prepare specimens suitable for examination in a transmission electron microscope. Finally, the CL system used in this study is described and some of the artefacts it can generate are briefly discussed.

2.2. Electron Microscopes

In this study, two transmission electron microscopes were used, a Philips EM430 and a Philips EM400. Each of these machines uses an ion getter pump to obtain a high vacuum in the region of the specimen. This is necessary to minimise hydrocarbon contamination of samples, particularly when a small convergent probe is used. Low temperature CL was found to be particularly sensitive to contamination effects especially if the microscope vacuum was substandard for any reason.

2.2.1. The EM430 and Radiation Damage

The EM430 is a medium voltage transmission electron microscope operating in the range 50-300 kV and capable of producing a 20Å highly convergent probe. In addition the Bristol EM430 is equipped with a Link AN 10000 energy dispersive X-ray (EDX) analysis system and a Gatan model 607 electron energy loss (EELS)

spectrometer. In this study, the EM430 was used primarily to characterize crystal defects using bright field and dark field imaging, although some EDX and EELS work was performed. For the relatively thick TEM specimens produced by the chemical etching technique outlined in section 2.4.1. the additional penetration of 300 kV electrons greatly facilitated defect characterization. Descriptions of TEM imaging techniques can be found in many text-books on electron microscopy. For example, Hirsch et al. (1965), Thomas and Goringe (1979), or Loretto and Smallman (1975).

The EM430 could only be used for defect characterization after all CL work had been completed due to radiation damage. This occurred in two ways, firstly electron damage and secondly, ion damage. At electron energies greater than approximately 150 kV, luminescence from GaAs/$A\ell_x Ga_{1-x}As$ QW structures is rapidly quenched after relatively short exposures to the electron beam. This effect was seldom observed in this study due to the far more serious problem of ion damage. This was caused by negative ions, created in the electron gun area, being accelerated down the microscope column and striking the TEM specimen. Unlike electron damage, which only occurred on regions of the sample illuminated by the electron beam,ion damage occurred over all areas of the sample that were in direct 'line of sight' of the electron gun-ions are obviously much heavier than electrons and are not appreciably deflected by the electron microscope lenses. In practice the microscope condenser aperture limits the size of the ion damaged area on the specimen. For example, using a 200 μm diameter condenser aperture a 200 μm diameter area of the specimen is ion

damaged. Ion damage occurs at voltages far lower than electron damage due to the more efficient transfer of energy to atoms in the specimen. Ion damage was not usually observed in the EM400 except during one six week period when the usual tungsten filament was replaced with a Denka LaB_6 filament. LaB_6 filaments produced by other manufacturers did not give ion damage. Figure 2.1 shows an integrated CL image of a QW sample ion damaged in the EM400. The dark, oval region, slightly left of centre at the top of the image, took less than ten minutes to form at 120 kV. The dark regions on the left and right of the image were formed when using a larger condenser aperture. When the LaB_6 filament was replaced with a new tungsten filament, no ion damage could be detected.

In early 1987 Philips modified the EM430 so that the electron beam was deflected, allowing the condensor aperture to be displaced (without significant degradation of the microscope performance) such that there was no longer a direct 'line of sight' path between the electron gun and the TEM specimen. This modification went a long way towards eliminating the ion damage problem.

2.3. QW Samples

All the samples examined in this study were grown by MBE on (001) semi-insulating GaAs substrates at either the Philips Research Laboratories, Redhill, Surrey, or at the Coordinated Science Laboratory, University of Illinois, U.S.A.

Most work described in this study was performed on four QW samples designated KLB116, KLB121, G43 and @ 1965. All of these were grown at the Philips Research Laboratories except @ 1965, which was grown at the Coordinated Science Laboratory.

The structures of these four samples are illustrated schematically in Figure 2.2. Note that samples KLB116 and KLB121 were SQW structures, while G43 and @ 1965 were MQW structures.

2.4. Sample Preparation

In this study the effects of crystallographic defects on the luminescence of GaAs/$A\ell_x Ga_{1-x}As$ SQW and MQW structures were examined, the principal experimental techniques used being TEM and (S) TEM CL. These methods require the preparation of thin electron transparent specimens. Most of the QW samples showed defect densities in the range $10^3 - 10^4$ cm^{-2}, so that samples with large electron transparent areas were required to increase the number of defects that could be examined. Obviously, cross-sectioned samples would have been unsuitable due to the low probability of finding a defect within the small electron transparent area. Some ion-thinned plan view samples were prepared but this technique was abandoned for two reasons. Firstly, insufficient electron transparent area was obtained. Secondly, room temperature ion thinning damaged specimens such that the CL intensity observed in subsequent experiments was reduced by several orders of magnitude. Ion thinning at liquid nitrogen temperatures produced less damage but the only ion thinner available for this purpose was unsuitable due to excessive vibration of the rotating specimen mount. To overcome the above problems a specimen preparation technique was developed which used chemical etchants to produce specimens with large electron transparent regions.

2.4.1. Chemical Specimen Preparation

A cross-section through a typical QW sample is shown in

Figure 2.3. To prepare plan-view TEM specimens the substrate and part of the epilayer must be removed without producing significant mechanical damage to the epilayers. This was done using the following procedure. The as-grown material was cleaved along {110} planes into 2 mm by 2 mm pieces and degreased using Analar 1-1-1 trichloroethane, acetone and methanol (in an ultrasonic bath). The sample was then mounted (epilayer down) on the cleaned specimen stage of a Gatan model 656 precision dimple grinder. After grinding the centre of the specimen to a thickness of approximately 50 μm using 1 μm diamond paste, the specimen was removed from the specimen stage and cleaned by rinsing in the solvents mentioned above. Specimens dimpled in this way had a rough uneven surface. While the dimpler could have been used with a polishing wheel to produce a better surface this was not normally done as the process took at least an hour, during which time the dimpler required frequent supervision. Instead specimens were mounted (epilayer down) on glass slides using 'black' wax to hold the sample in place and protect the epilayer surface from chemical etchants. Care was taken to prevent wax flowing under the sample as optical transparency provides a useful estimate of sample thickness for GaAs samples that are less than 1 μm thick. Samples were then immersed in an etchant containing H_2SO_4, H_2O_2 and deionized water in the ratio 3:1:1 (Iida and Ito, 1971). This etchant removes GaAs at the rate of 0.4 μm per minute and produces a highly polished surface. Fresh etchant must be used for each sample as the H_2O_2 decomposes during the course of a few hours. Analar grade chemicals must be used to ensure reproducible results. After

etching samples to a thickness of 15 μm (at the centre) they were removed from the etchant, rinsed and dried. To remove the remainder of the substrate from the centre of the sample a mixture of NH_4OH and H_2O_2 in the ratio 1:19 (Adachi and Oe, 1983) was used. This etchant attacks GaAs more rapidly than $Al_xGa_{1-x}As$. For example, $Al_{0.3}Ga_{0.7}As$ is removed approximately 100 times more slowly than GaAs (GaAs being removed at the rate of 2.5 μm per minute at room temperature.) This property was used to effectively stop the etching process at the first $Al_xGa_{1-x}As$ layer encountered. Samples were removed from this etchant, rinsed and dried only when the substrate had been removed from a circular region approximately 1 mm in diameter. For sample G43 no further etching was required as samples were 0.4 μm thick at this stage. The other QW samples, however, were roughly 1 μm thick at this stage and so required further etching. First they were rinsed in dilute HCl to remove any Al_2O_3 formed. Further etching was accomplished by returning the sample to the H_2SO_4 etchant described earlier. This etchant is not significantly affected by the aluminium composition of an $Al_xGa_{1-x}As$ layer but attacks thin (less than 1 μm) GaAs films approximately 5 times more rapidly than thicker material. Sample thickness was normally judged from the optical transparency and colour of the thin film. For example, a back lit GaAs film appeared dark red when 1 μm thick but was bright yellow when 0.1 μm thick.

After rinsing in deionized water and drying, samples were removed from the black mounting wax by immersing them in 1-1-1 trichloroethane overnight. Failure to leave the sample in the solvent for a sufficient length of time sometimes left a minute

quantity of wax holding the thin area of the sample to the glass slide. Attempting to move a sample held in this way left the electron transparent area stuck to the slide and separated from the remainder of the sample. Several additional rinses in fresh analar 1-1-1 trichloroethane were needed to remove all traces of black wax, followed by a rinsing in acetone. Prior to removing the glass slide (with the sample on it) from the acetone, the sample was turned over using a cocktail stick such that the epi-layers were no longer in contact with the slide. Without this precaution the electron transparent area frequently adhered to the slide on removal of the sample and slide from the solvent. Tweezers could not be used on thinned samples without damaging or destroying the electron transparent area. After removing the sample and slide from the solvent and allowing to dry, a small spot of silver dag was placed on a copper grid and the grid touched to the sample. This proved sufficient to stick the sample to the grid and ensured that the sample was only attached to the grid by one corner. This prevents the difference in thermal expansion co-efficients between the sample and the grid from cracking the sample on cooling for CL work. Finally, the grid plus sample were mounted (with silver dag) in a brass cup suitable for use in either a liquid helium cooled specimen holder or a normal tilt-rotate holder.

Samples prepared as outlined above were typically 0.2 to 0.4 μm thick over an approximately circular area with a diameter of about 1 mm.

A simplified schematic diagram of the specimen preparation process is shown in Figure 2.4.

2.4.2. Advantages of Chemical Etching

The main advantage of the chemical specimen preparation technique used in this study was the relatively large electron transparent area produced, allowing defects to be located even in the highest quality samples with low defect densities. However, the technique has a number of drawbacks, the most important of which is the extreme fragility of the thin area. Great care was needed whenever specimens were handled. Some samples proved particularly delicate due to the presence of microscopic pinholes in the thin area which readily nucleated cracks. Specimens of @ 1965 were especially prone to this effect and as a result frequently broke when cooled for CL work.

There was one other problem with the chemical etching technique. Samples could not be prepared with thicknesses less than 0.1 μm. The reason for this was simply that specimens thinner than this were almost impossible to handle and invariably broke either during preparation or when being cooled in the microscope for CL work.

2.4.3.Use of a Precision Ion Milling System

For EELS work thinner samples were required. These were prepared from normal chemically prepared specimens in a Gatan model 645 Precision Ion Milling System (PIMS). Figure 2.5 shows a schematic diagram of the PIMS. Samples were inserted via an airlock allowing direct insertion of standard Philips specimen holders so that specimens could be transferred quickly from an electron microscope to the PIMS. The PIMS has an ion gun situated at the top of the column into which argon is fed via a needle valve.

The argon is ionized by an irridium coated tungsten filament and the ions accelerated to a preselected voltage in the range 1 - 10 kV. The resultant ion beam is divergent and so is condensed, to increase the ion current, by an electrostatic lens near the top of the column. Below the condensor lens are a set of electrostatic X-Y deflection plates. Voltages applied across these plates raster the ion beam over an area of the sample selected by the operator. Focusing of the ion beam onto the sample is achieved by an objective lens below the deflection plates. Secondary ions or electrons are accelerated onto a phosphor screen and a photo-multiplier used to convert the resultant light into an electrical signal. This signal is used to form an image of the sample on a video monitor.

The minimum ion probe size obtainable with the PIMS is 2 μm. By frequently transferring a sample from the PIMS to an electron microscope for higher resolution examination it proved possible to thin a desired area with considerable accuracy, although this procedure was very time consuming. As for conventional ion-thinning, use of the PIMS strongly degraded CL intensity, far more than could be accounted for by the change in sample thickness.

2.5. Experimental CL System

All the CL work described in this study was performed on a TEM-CL system constructed on the EM 400 by Roberts (1981), and later modified by Myhajlenko (1983), Aplin (1983) and Day (1987). The optical arrangement for this system is shown in Figure 2.6. Light generated in the sample by the electron beam is collected

at one focus of a retractable ellipsoidal mirror. A small hole in the mirror allows the electron beam to strike the sample. Light collected by the mirror is deflected by a further planar mirror and passes out of the microscope through a quartz window and into a Bentham M300 monochromator. This monochromator was modified by Aplin (1983) to allow light to be deflected to one of four detectors. At the same time the quartz waveguide initially used by Roberts to transmit light from the microscope to the monochromator was replaced by the quartz lens and window arrangement shown in Figure 2.6. This reduced the total thickness of quartz in the optical path, reducing the absorption losses incurred at 1.0 and 0.89 eV due to OH^- present in the quartz. The four detectors available for light detection are an S20 (Hamamatsu) photomultiplier, an RCA 31034A photomultiplier with extended S20 response using a GaAs photocathode, a liquid nitrogen cooled North Coast EO 817 germanium photodiode (implemented by Myhajlenko, 1983) and a parallel detection system using a CCD (implemented by Day, 1987).

In addition to the CL system, the EM400 was also equipped with an EDX detector controlled by a Link systems 860 II minicomputer. Further analytical facilities, including a scanning unit (interfaced to the Link 860) with a secondary electron and transmitted electron detector, allowed the microscope to operate in both TEM and STEM modes.

CL data can be acquired in number of different modes. The Hamamatsu photomultiplier detected light at the entrance to the monochromator (before the diffraction grating), and so operated

as an integrated CL detector, signals being displayed on the scanning unit video screen. The RCA photomultiplier and Ge photodiode were both interfaced to the Link 860 computer and could be used in one of three different modes. Firstly, the computer could be used to control the monochromator and acquire CL spectra. Secondly, 1000 channel monochromatic linescans could be acquired using a signal generator to control the electron beam scanning and pixel dwell time for the computer. Thirdly, the computer can be used to control the electron beam rastering so that monochromatic images can be acquired. These images are 128 by 128 pixels square, each pixel containing 0 to 255 counts.

Data collected using the Link 860 computer can be transferred to a VAX 11/750 computer. Image manipulation on the VAX computer was performed using the SEMPER V image processing software and displayed on a RAMTEK Marquis high resolution video terminal. The RCA photomultiplier was operated over the energy range 1.4 to 4.0 eV in a photon pulse counting mode to produce pulses for the Link computer. However, the Ge photodiode produces a voltage signal, which is interfaced to the Link computer via a voltage-frequency converter. This detector is sensitive over the energy range 0.7 to 1.4 eV. Due to the low sensitivity of the Ge photodiode as compared to a photomultiplier, long acquisition times (up to an hour) are required with this detector. To avoid voltage drift problems this detector is used in an a.c. mode, the electron beam being deflected on and off the specimen at approximately 400 Hz. A Brookdale 5205 lock-in amplifier is used as a phase sensitive detector to produce a d.c. voltage, which is then processed in the

usual fashion. The CCD parallel detection system is also interfaced to the Link computer for data acquisition. This detector is sensitive over the approximate range 1.4 to 2.0 eV but can only be used to acquire spectra over 0.1 to 0.2 eV of this range at any one time due to the limited energy dispersion of the Bentham monochromator. Monochromatic CL images could not be obtained with this detector. Instead, linescan 'images' could be acquired the horizontal direction on the image corresponding to the electron beam position and the vertical direction corresponding to the photon energy.

2.6. Artefacts in CL Spectra and Images

In the previous section the EM 400 CL system was described. Further details can be found in Roberts (1983). The current section gives details of some of the artefacts this system can generate causing incorrect interpretation of results. Great care is sometimes needed to distinguish genuine effects from artefacts.

2.6.1. Artefacts of Data Processing

All the CL results presented in this study were transferred from the Link 860 computer to the VAX 11/750 computer before plotting or printing the data. All the CL spectra plotted in this study have been rescaled so that the maximum signal in any spectrum has an intensity of unity. This means that the intensities of features cannot be directly compared where appropriate indications of relative intensities have been included. Similarly, all monochromatic images have been rescaled to give an intensity range

between 0 (black) and 255 (white). Comparison of the intensity of CL images is further complicated as images are normally acquired such that the maximum intensity of the raw data is 255 to give the best signal to noise ratio. This is normally done by varying any one of three parameters; pixel dwell time, electron beam intensity or the width of the monochromator entrance slits.

A further artefact in monochromatic CL images is due only indirectly to the data processing. Although images are displayed as square images the raster scanned by the electron beam is not square but is normally a parallelogram. Careful adjustment produces a rectangular raster but this is difficult unless a feature known to be rectangular is being examined. Obviously, images obtained using a rectangular raster are distorted when displayed as a square image.

2.6.2. Spurious Signal Modulations

Spurious signal modulations can arise in a number of ways. Obviously acquiring a spectrum while scanning the electron beam will superpose modulations on CL spectra if the dwell time per spectrum channel is less than the time required for the electron beam to scan a complete a frame. Of course this assumes that the CL intensity varies significantly across the region being scanned. In general CL spectra should never be acquired while the electron beam is being scanned. In addition to the modulation mentioned above, sharp features in a CL spectrum can be blurred due to averaging over the scanned region.

Modulations on CL spectra can also be generated by vibration

of the sample. The specimen stage used for low temperature CL is cooled by a continuous flow of liquid helium drawn through the cold stage by a simple diaphragm pump. Vibrations from the pump can be transmitted to the specimen stage via the tubing connecting the stage to the pump and also by the oscillatory nature of the vacuum produced by a diaphragm pump. This vibration is normally only significant at high magnifications. However, slower and stronger oscillations in the helium flow rate can occur if ice crystals are inadvertently allowed to form within the helium transfer system. This effect in turn can produce oscillations of up to 0.5 μm in the position of the TEM specimen. Obviously, such an oscillation is a severe impediment to obtaining useful CL spectra and images.

Irregular fluctuations in CL intensity are not normally observed. However, if the tungsten microscope filament is approaching the end of its useful life the intensity of the electron beam can vary substantially. This effect can give spurious peaks and distortions on CL spectra or streaks on monochromatic images. A similar effect can be observed if the sample is a poor electrical conductor so that it becomes charged.

2.6.3. Spurious Signals

For the artefacts described so far the specimen was the only source of light considered. However, there are several other sources of light within the microscope. The EM 400 CL was designed around an ellipsoidal mirror with a small focus (≈ 50 μm across) in order to collect light efficiently from the specimen but also

to reject as much stray light as possible. Even so, scattering within the microscope allows some stray light into the optical system.

There are two main sources of stray light within the microscope. Firstly, light generated by the microscope can be reflected from the specimen into the light collection optics. This can be detected in a number of ways such as reducing the size of, or misaligning the condensor aperture - at the expense of either electron beam intensity or minimum probe size respectively. Secondly, backscattered electrons can strike luminescent materials within the specimen chamber. For example, oxides on the microscope pole pieces or the mirror surfaces. Contributions from these sources are negligible except when the signal from the specimen is very weak.

2.6.4. Contamination

Contamination of the specimen due to carbon deposited on the specimen surface can severely distort both CL spectra and images. Figures 2.7 and 2.8 illustrate this effect for monochromatic images. Figure 2.7 shows two monochromatic images of a misfit dislocation in a specimen of G43, acquired at two different energies. In Figure 2.7a) a bright circular region due to contamination can clearly be seen. However, in Figure 2.7b) the background CL intensity is much lower so the circular region cannot be seen. Instead, the part of the dislocation inside the contaminated area appears bright, giving the false impression that part of the dislocation does not emit light at

this energy. Figure 2.8 shows another example where, at one photon energy, the contaminated area appears dark, while at the second photon energy, the same area appears bright.

To avoid contamination effects in CL data, exposure of the specimen to the electron beam must be minimized and the electron beam intensity must be kept as low as possible. Valuable information can be obtained if CL spectra are acquired for different specimen temperatures, or with a range of electron beam intensities. Such experiments require prolonged exposure to the electron beam such that contamination produces irreversible changes in CL spectra, and frequently makes the data useless.

Although no systematic study of contamination was performed in the current work the following observations were made. As stated above, contamination increases with the intensity of the electron beam and the length of time that the specimen is exposed to the electron beam. Operating the microscope with a substandard vacuum also increased the rate of contamination. The effects of contamination on CL data varied with no apparent pattern between specimens of different materials and even between different specimens of the same material. For example, for a given luminescence feature observed in a particular material, contamination could increase or decrease the CL intensity or even shift the emission energy slightly. The reasons for this behaviour are not known.

Although the effects on luminescence of exposure to an electron beam have been attributed to contamination, it is possible that they might be due to some other effect such as sub-threshold

electron radiation damage.

2.6.5. Interference Effects

For specimens with optically smooth surfaces, optical interference can occur due to multiple internal reflections. Trommer (1981) gave the CL intensity, $I(\lambda)$ emitted by a sample at a wavelength λ as:

$$I(\lambda) = I_o(\lambda) \int_0^{2\pi} \left[\sum_{k=0}^{\infty} r^{2k} \, \mathrm{Sin}\left(\frac{4\pi d k n \mathrm{Cos}\theta_i}{\lambda} + t \right) \right]^2 dt \qquad (2.1)$$

where $I_o(\lambda)$ is the envelope function of the luminescence spectrum, r is the reflection coefficient for the sample - vacuum interface, d is the sample thickness, n is the refractive index of the sample, and θ_i is the internal reflection angle with respect to the surface normal. The integral in t accounts for time averaging. Note that absorption is not included. This equation shows that interference effects can be manifested, either spatially on a CL image due to changes in specimen thickness, or on a CL spectrum as the observed photon energy is varied. Figure 2.9 shows a monochromatic image of a TEM specimen prepared from sample @ 1965. The interference fringes are due to the specimen thickness increasing towards the upper right of the image. The region without fringes at the lower left of the image is of approximately constant thickness. Spectral interference effects are only normally seen when strong broad CL emission occurs over a relatively wide energy range, typically greater than 0.2 eV.

In this study great care was taken to ensure that interference

effects were not misinterpreted as genuine CL features. Using equation 2.1 it was shown that for the normal specimen thicknesses used (typically less than 0.5 μm) interference produces only a gentle gradient over the energy range of a typical spectrum. As an additional precaution specimens of different thicknesses, for each of the materials examined in this study, were investigated using CL. No significant interference effects were found on any CL spectrum.

Figure 2.9 also illustrates another artefact of the CL system. The small focal area of the CL mirror gives variations in the CL collection efficiency across low magnification images. This can be clearly seen in Figure 2.9. Adjusting the distance between the specimens and the CL mirror produces more uniform images. However, this is not always feasible because of the loss of collection efficiency that this creates.

2.6.6. Absorption Effects

Warwick and Booker (1983) observed 'ghost' peaks in CL spectra from bulk InP due to absorption effects, which they explained with the following hypothesis. Light can emerge from a specimen either directly or after internal reflection. Figure 2.10 illustrates this. Only the ray labelled A emerges directly from the specimen but this constitutes only a few percent of the total light generated (Gooch, 1973). The reflected rays (labelled B and C) must pass through the specimen before escaping from the specimen. For InP the higher energy light is absorbed more rapidly than the lower energy light, so that a low energy peak

appeared on CL spectra. To eliminate this effect Warwick and Booker placed a circular aperture disk on their specimens so that most of the internally reflected light could not escape from the specimen. Except for very pure InP, a 100 μm diameter aperture successfully eliminated the ghost peak.

In the current work ghost peaks were not observed for any of the materials examined. CL spectra acquired from both TEM specimens and bulk material were compared and found to contain identical spectral features showing that absorption effects can be neglected. As a further check CL spectra acquired with the CL mirror correctly aligned were compared with CL spectra acquired with the CL mirror misaligned (for both bulk and TEM specimens). This procedure effectively changes the area of light collection from approximately 50 μm across to 200 μm across. Again, no changes in CL spectra were observed.

There are two main reasons for the lack of ghost peaks in CL spectra from the QW samples examined in this study. As compared to an SEM CL system the EM 400 CL system has a smaller focal area that will not collect light following paths such as those labelled B and C in Figure 2.10. Secondly, CL spectra from QW materials showed much narrower luminescence peaks than observed for InP by Warwick and Booker.

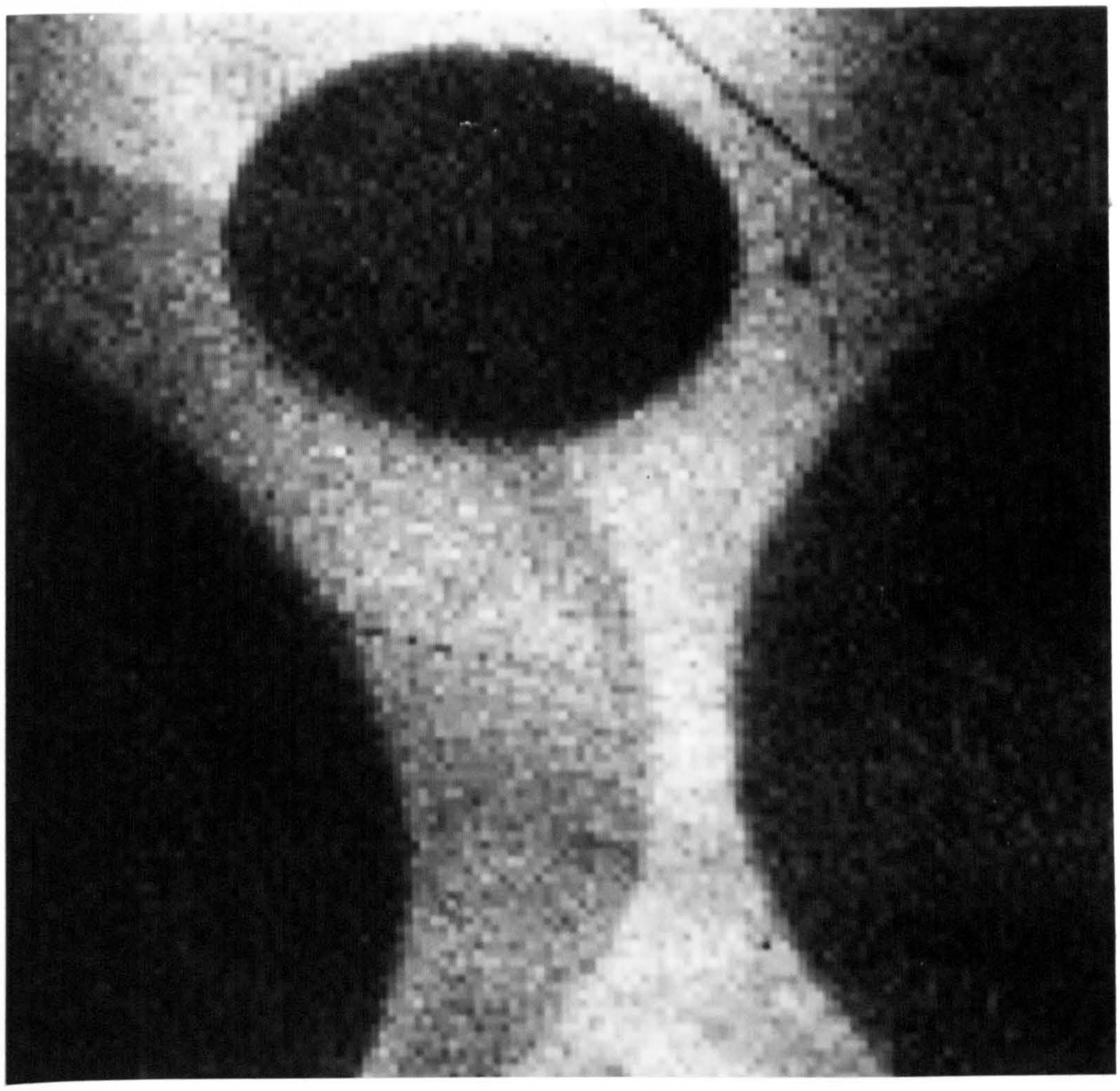

2.1 Integrated CL image of a QW structure showing regions of reduced CL intensity due to ion damage.

KLB116

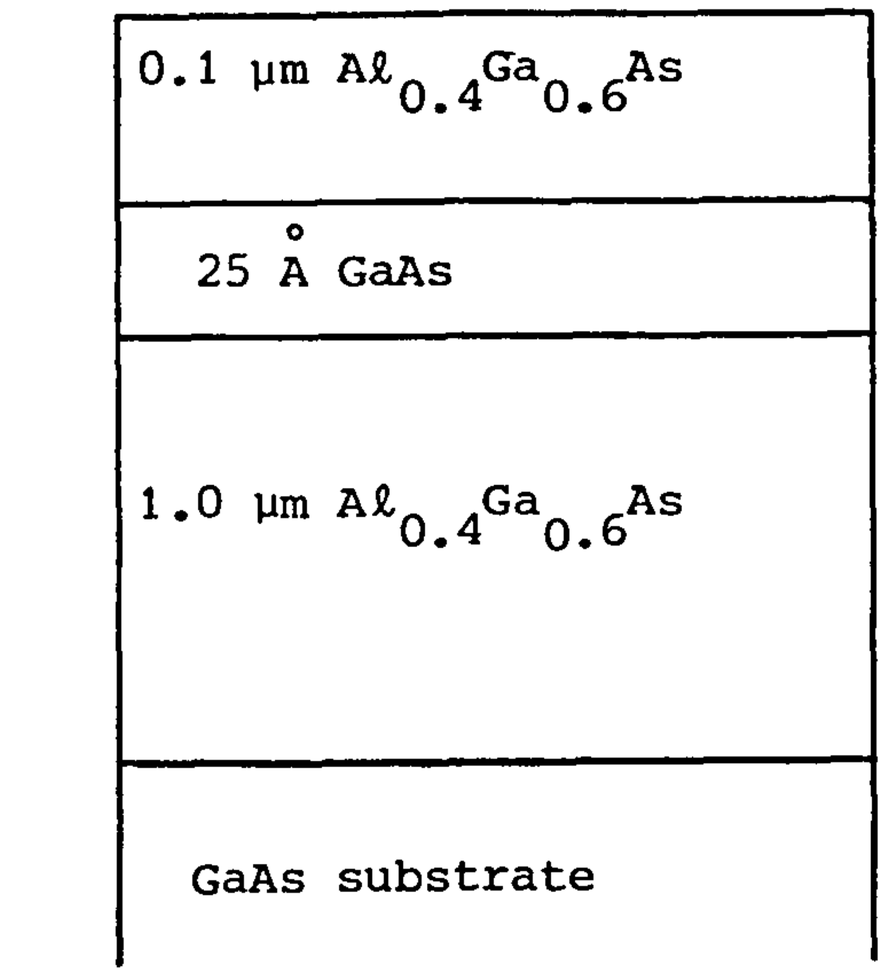

KLB121

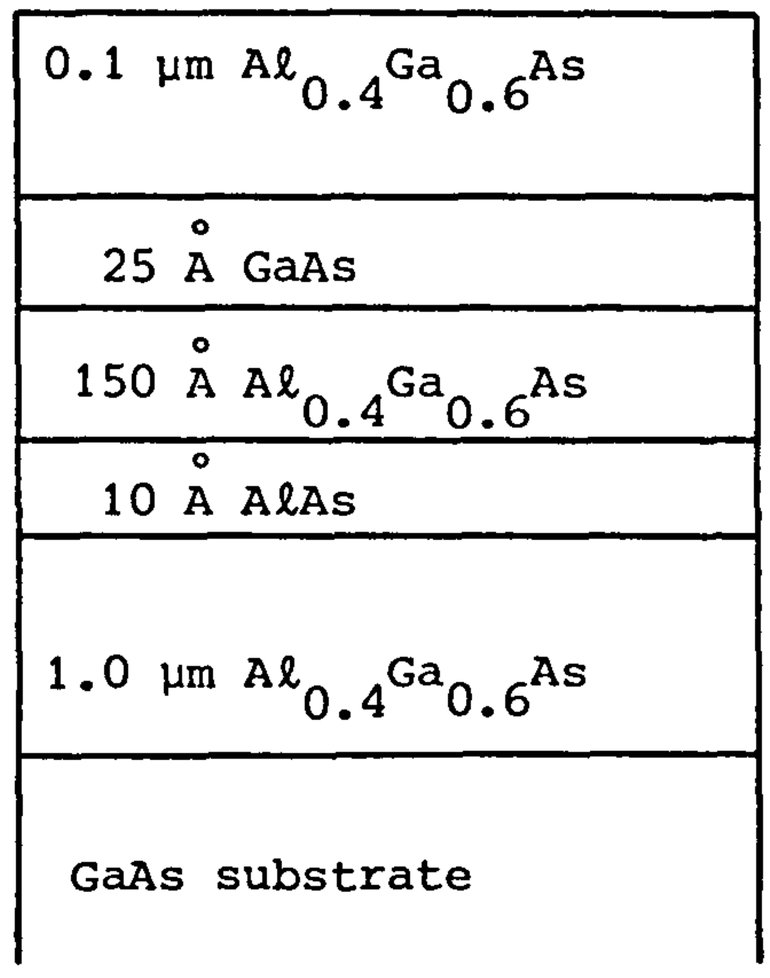

G43

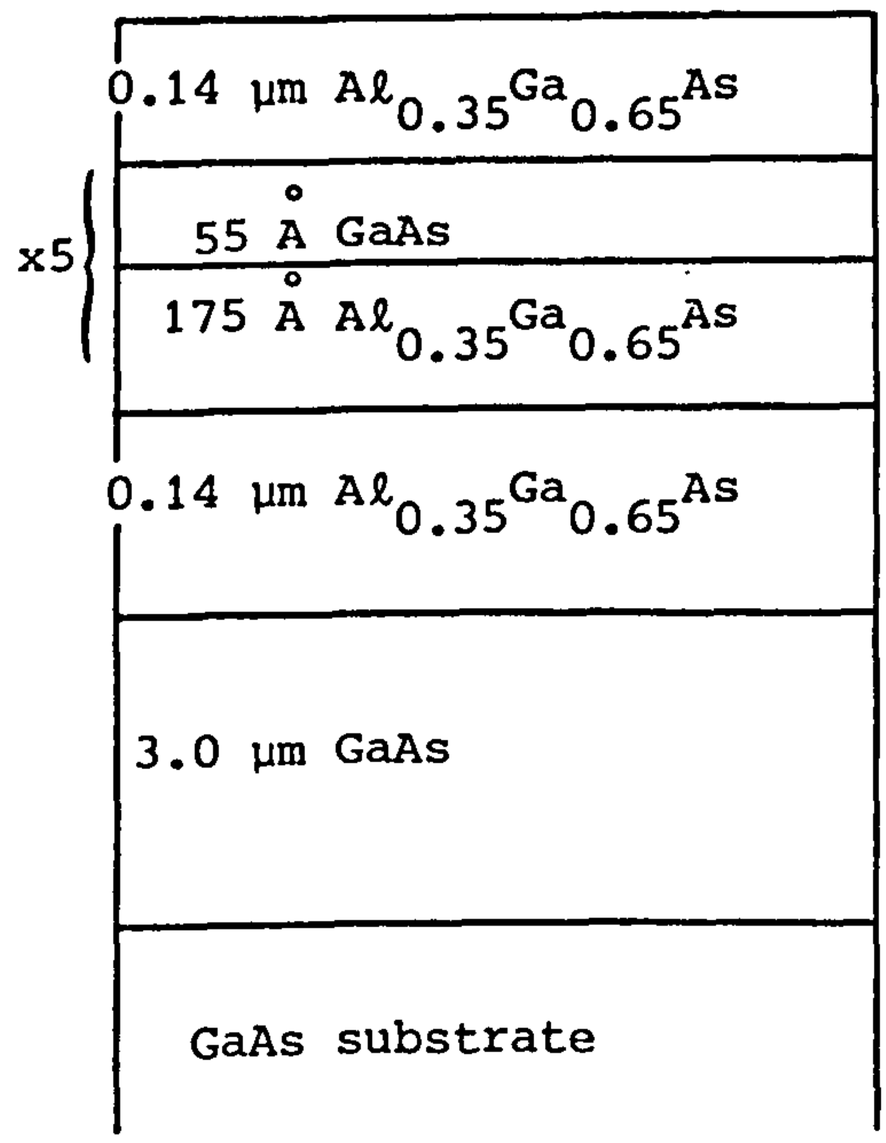

@1965

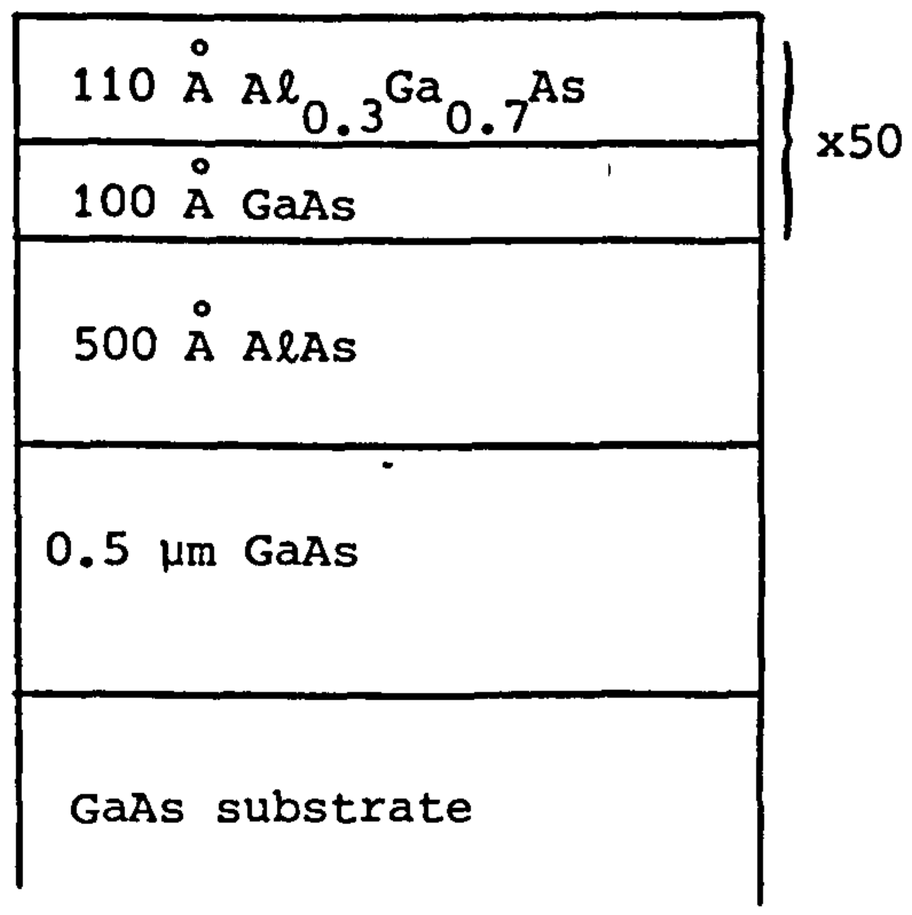

2.2 Schematic diagrams of the four (nominally undoped) QW structures investigated in this study.

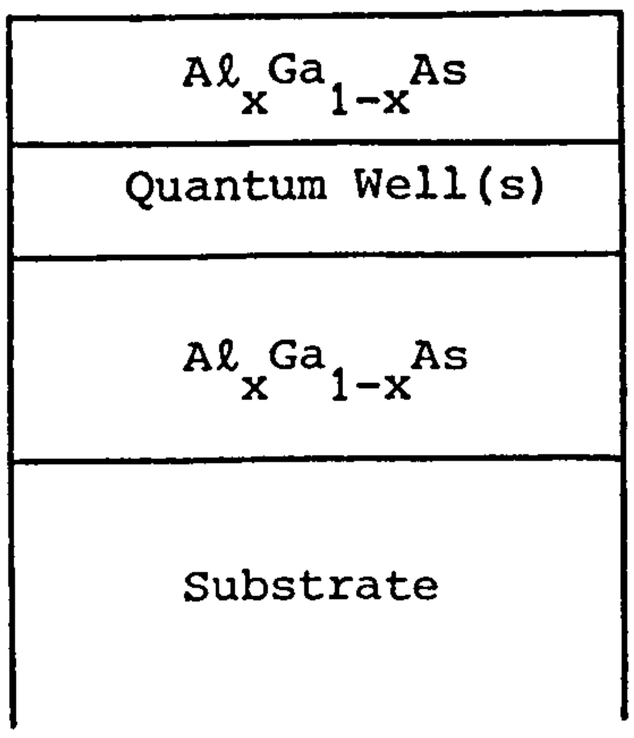

2.3 Schematic diagram of a typical QW structure.

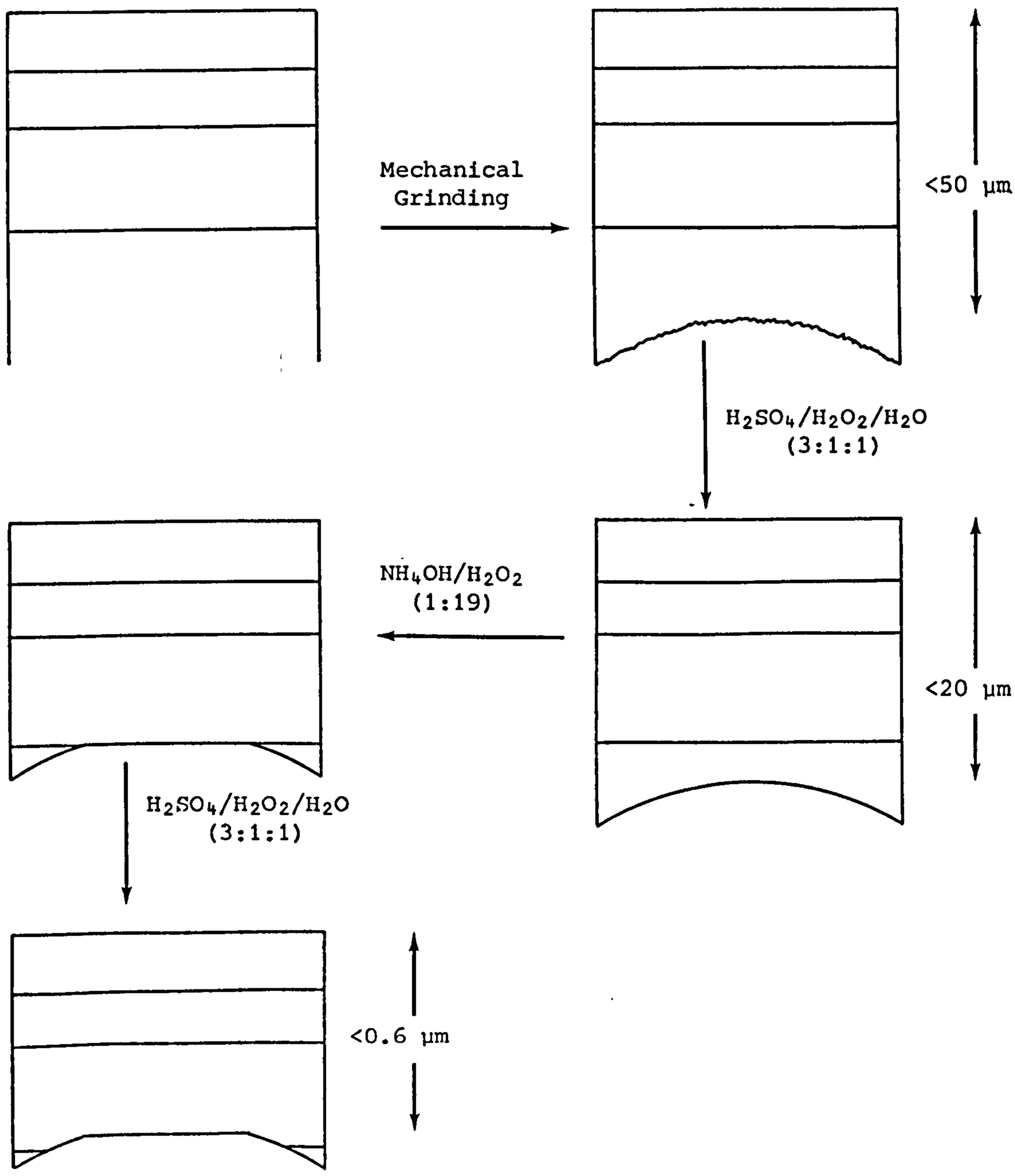

2.4 Simplified diagram of TEM specimen preparation.

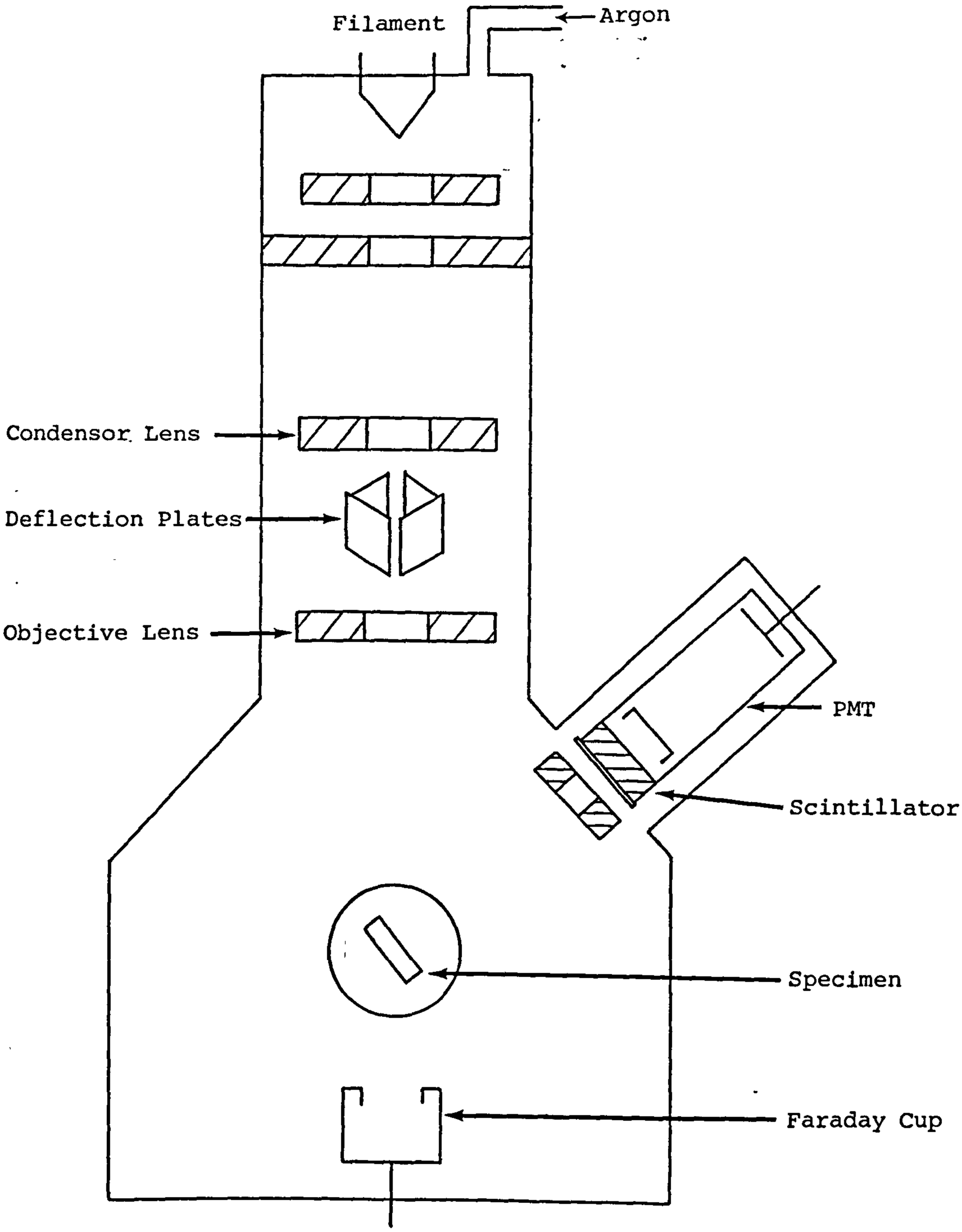

2.5 Schematic diagram of the PIMS

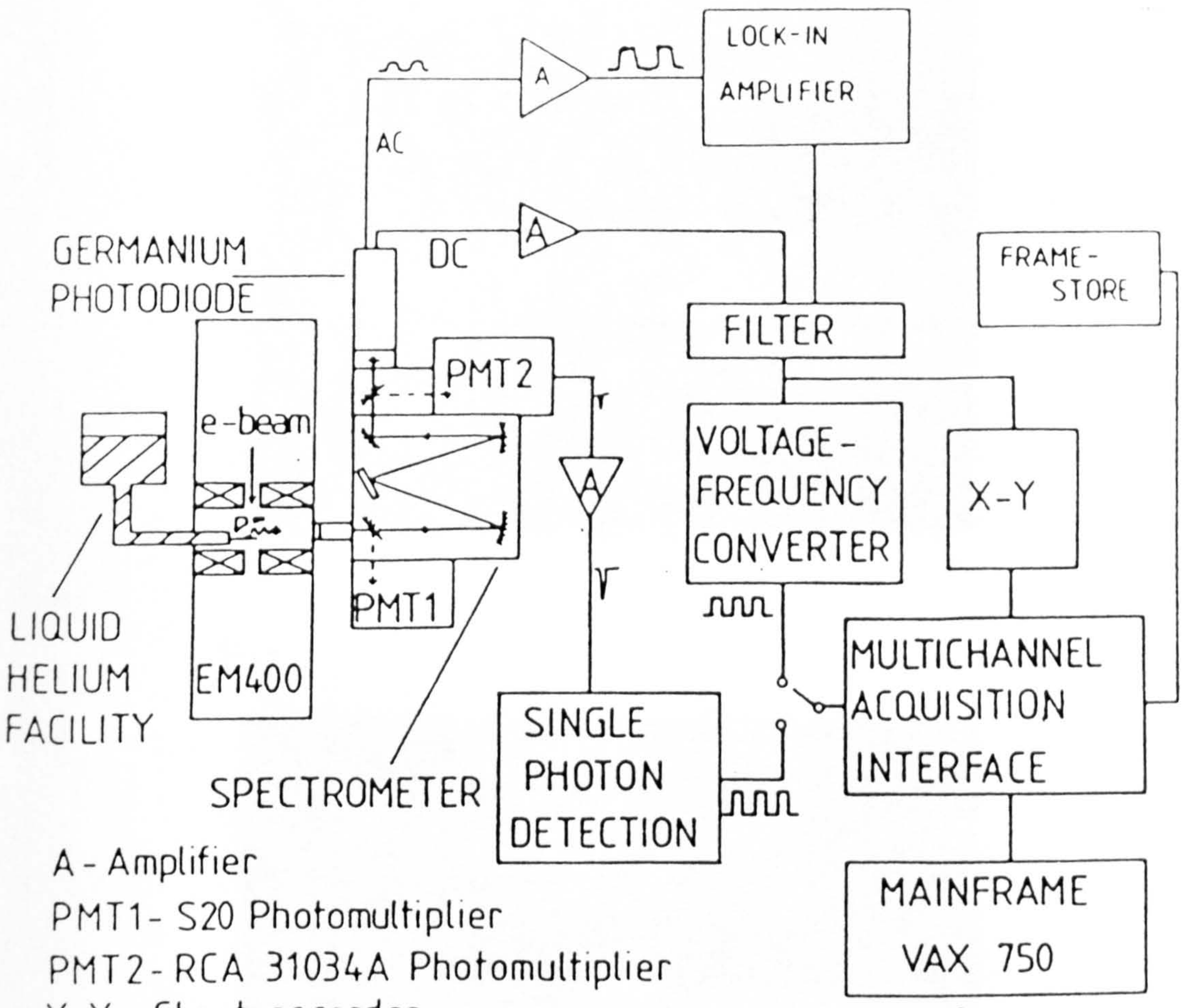

2.6 Schematic diagram of detectors and signal processing facilities. (Courtesy of S. Myhajlenko).

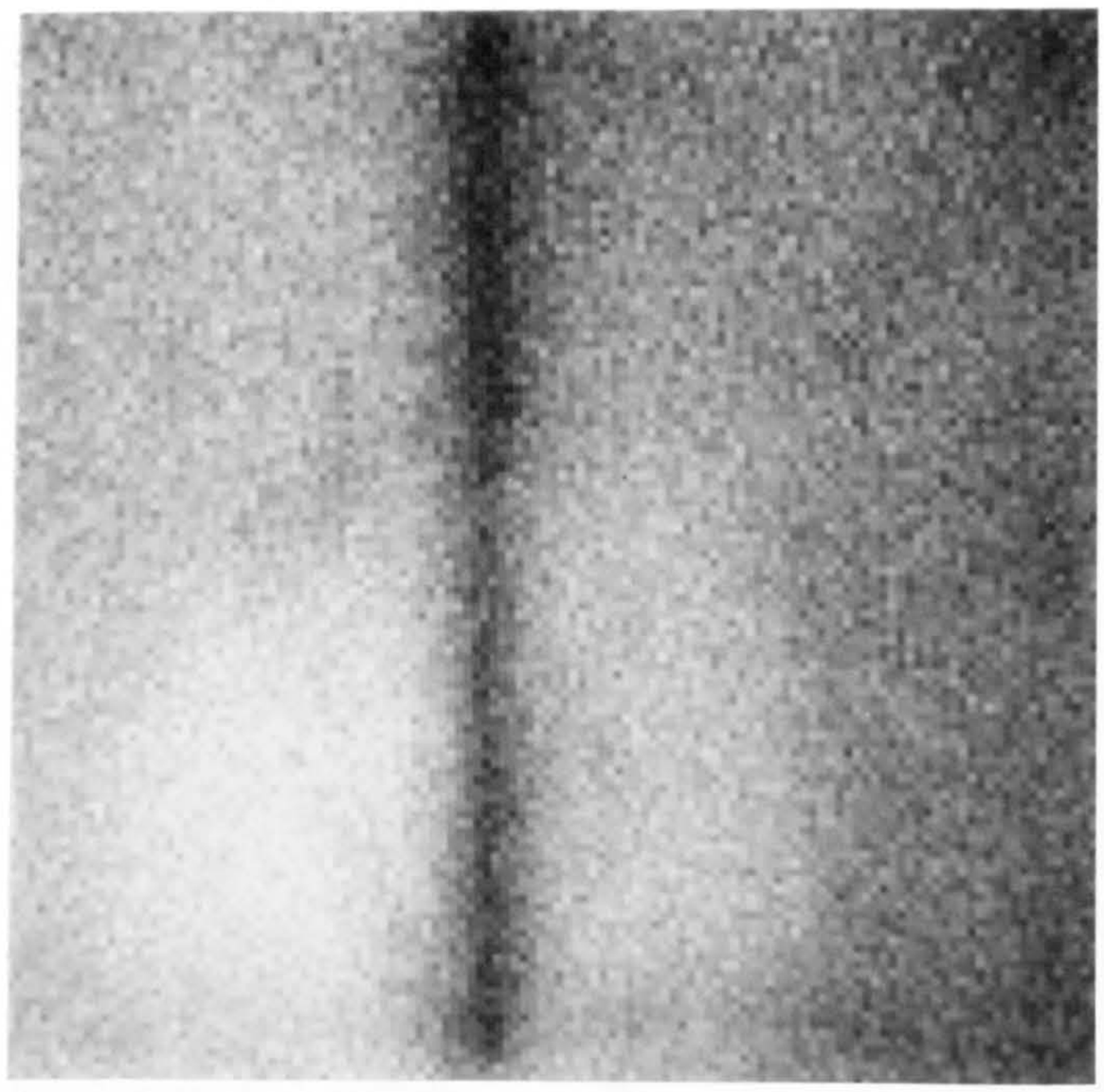

a)

10 µm

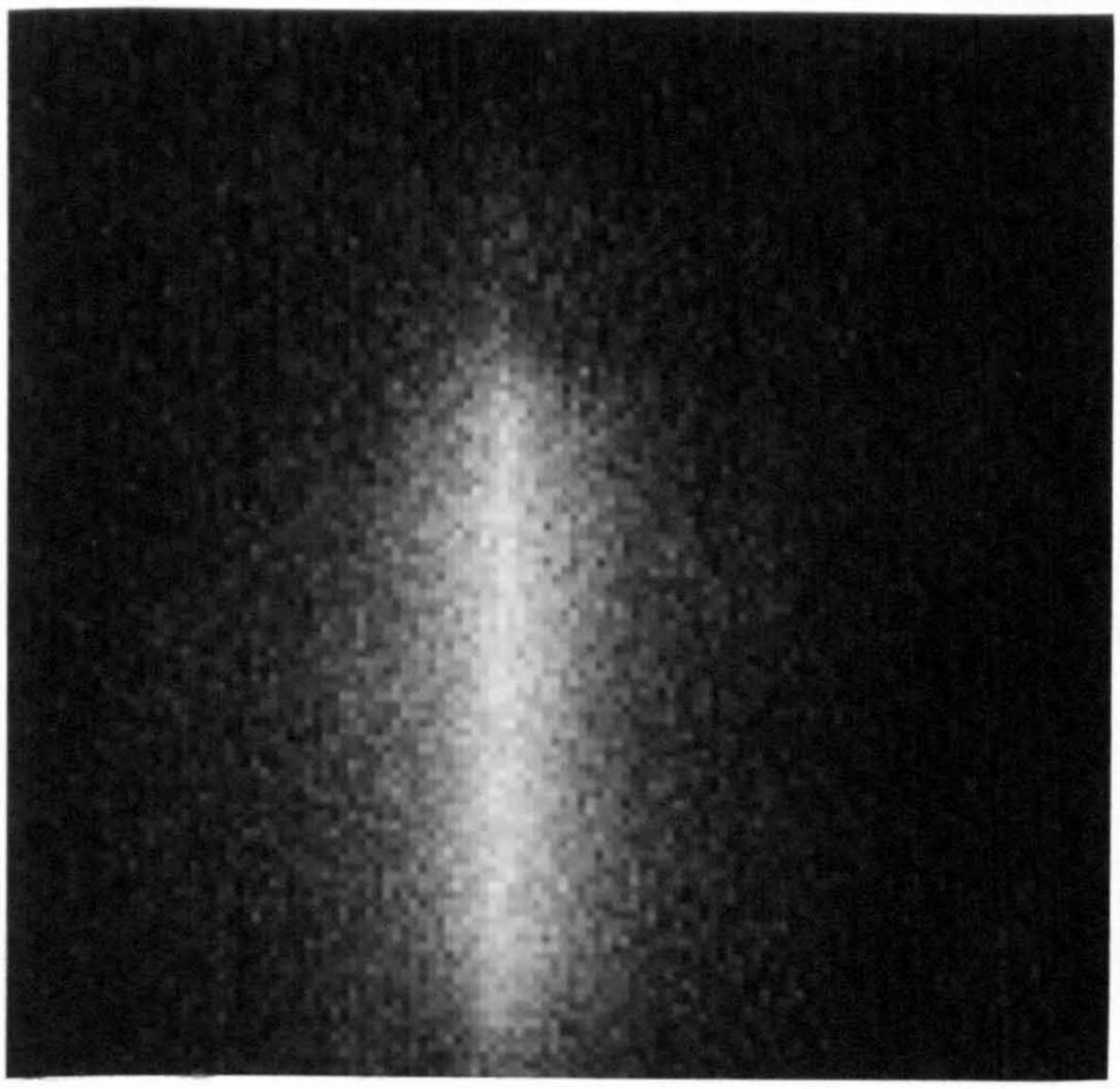

b)

2.7 Monochromatic CL images (acquired at different photon energies) from the same region. A circle of enhanced CL intensity due to contamination can be seen in a) but is harder to discern in b) where the background intensity is lower.

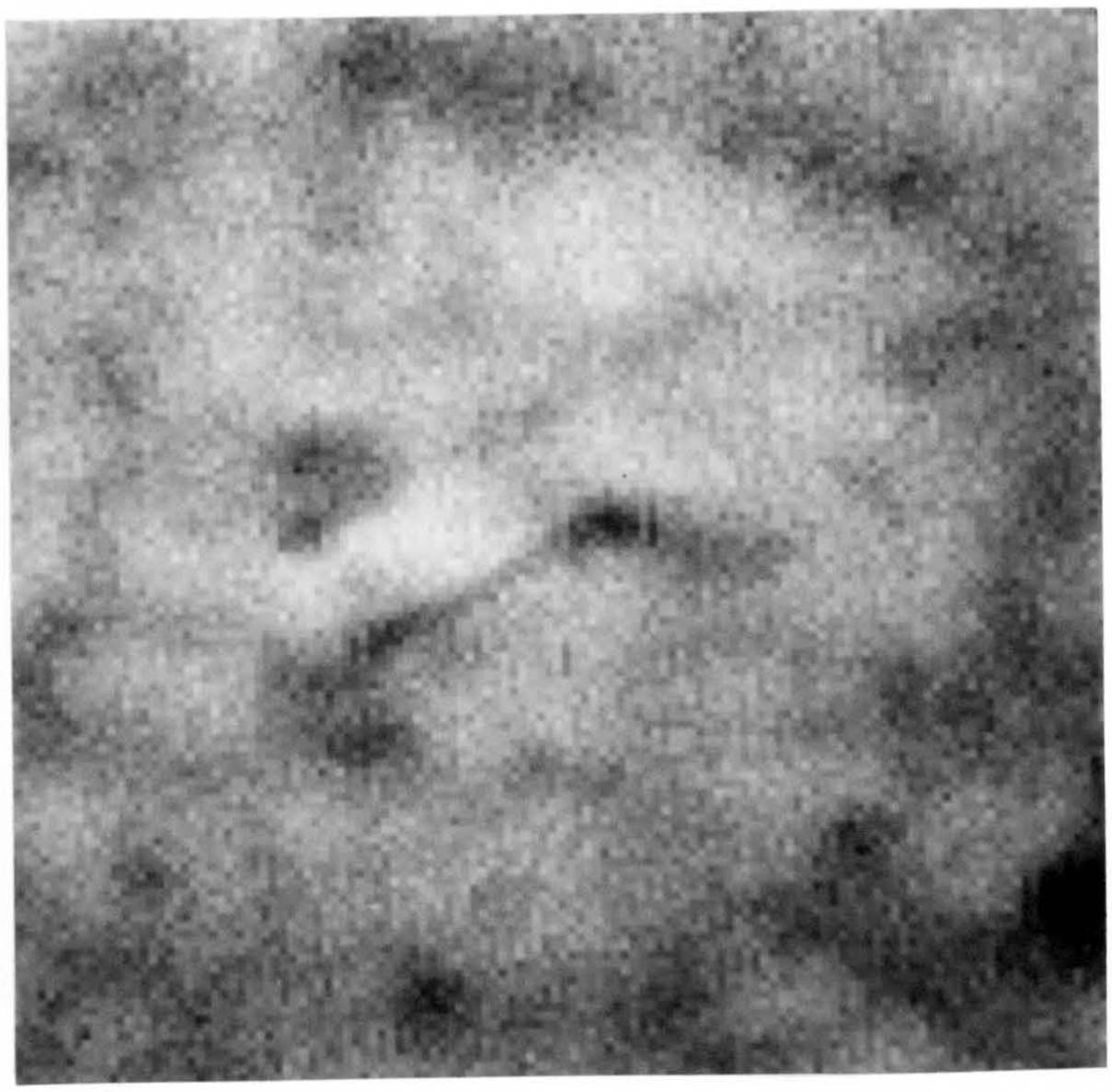

a)

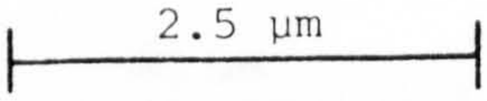

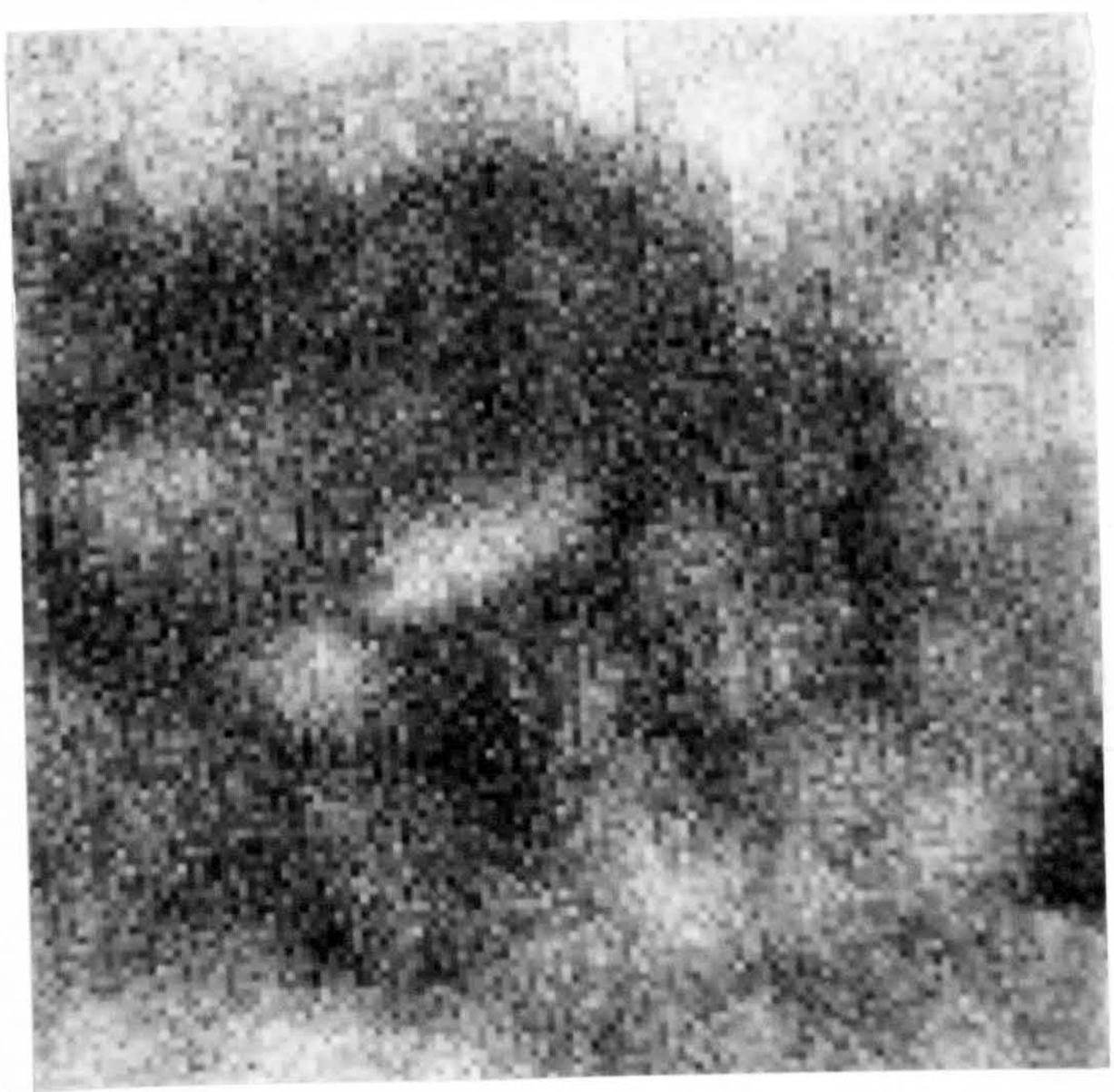

b)

2.8 Monochromatic CL images (acquired at different photon energies) from the same region. In a) a circular region of contamination shows bright CL contrast whereas in b) the CL contrast is dark.

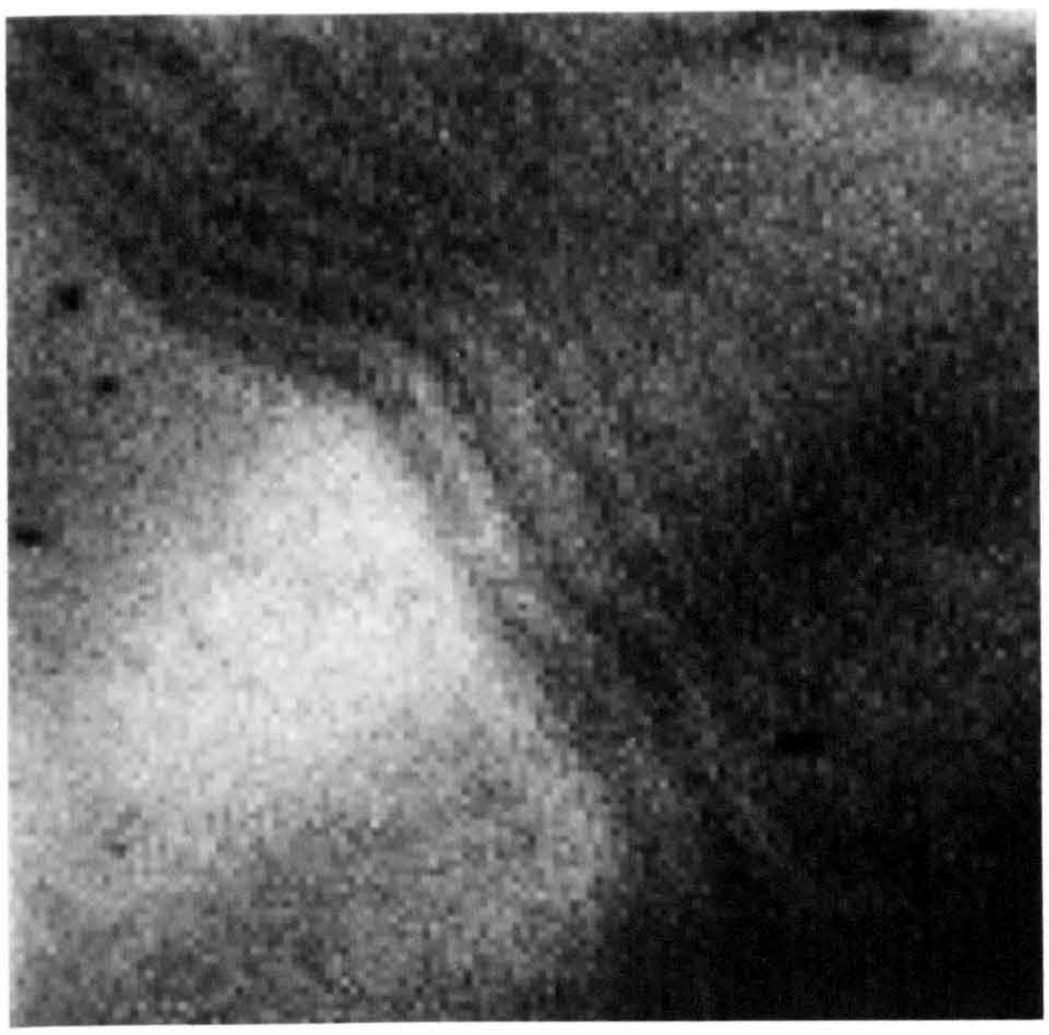

2.9 Integrated CL image showing interference fringes due to changes in specimen thickness.

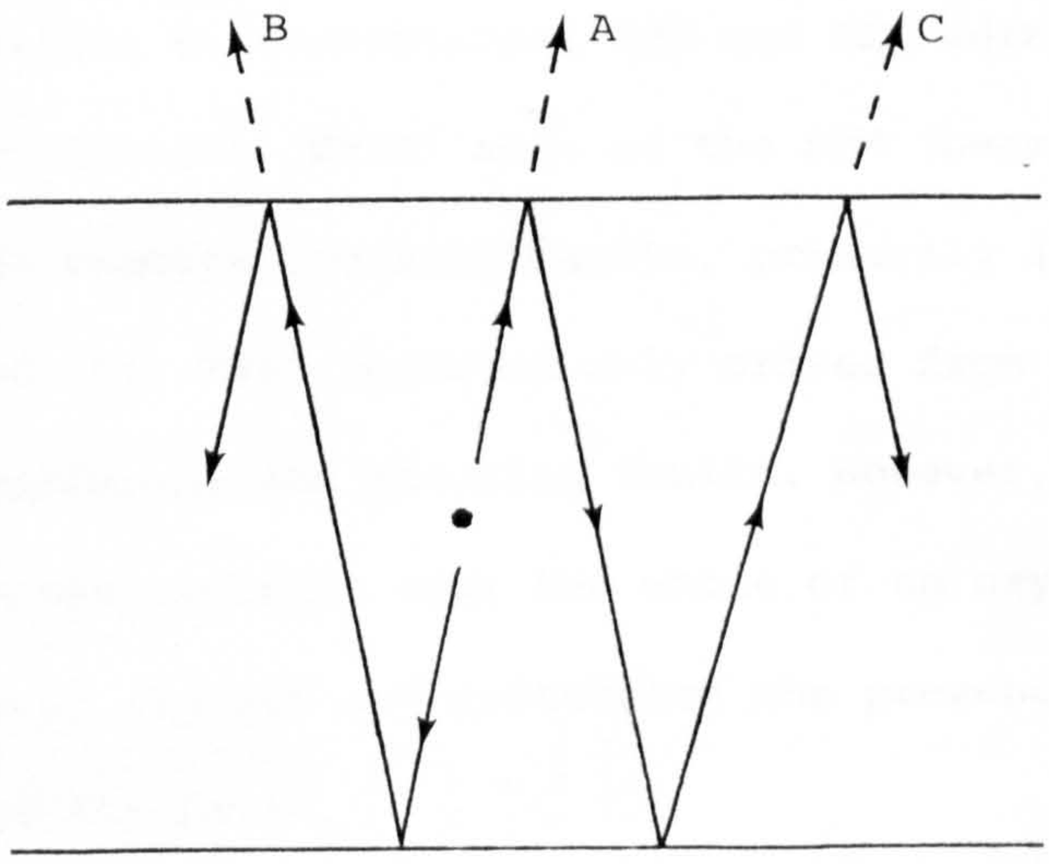

2.10 Ray paths for light escaping from the top surface of a semiconductor specimen.

CHAPTER THREE

STACKING FAULTS

Stacking faults in semiconductors have been extensively studied, most authors concentrating on silicon (for example, Ravi, 1976). In GaAs and $Al_xGa_{1-x}As$ epitaxial layers, stacking faults have not in general been studied in their own right but have been included in the loose category of oval defects (Kakibayashi,1984). The reason for this is simply that the majority of studies of defects in epitaxial layers have used SEM and Nomarski optical microscopy as the principal analytical techniques. In the current work, oval defects and stacking faults were readily distinguished using both TEM and CL and so they are considered separately. It should be noted that oval defects were occasionally found to have stacking faults associated with them. Such were relatively rare and were not studied.

In addition to conventional TEM and SEM work, the electron beam induced current (EBIC) mode of the SEM (Leamy, 1982) has been used to examine stacking faults, primarily in silicon. Most authors find that EBIC contrast only arises from the partial dislocations bordering the stacking faults. However, Varker and Ravi (1974) observed contrast over the whole of an oxygen induced stacking fault (in Si) and postulated the presence of an impurity cloud around the fault.

CL has rarely been used to investigate stacking faults. Shiller and Boulou (1975) could not distinguish stacking faults in GaAs, although reduced CL intensity was observed at the partia; dislocations. In InP, Attollini et al. (1986) studied pyramidal

stacking faults using both EBIC and integrated CL imaging. One pair of opposing stacking faults showed dark EBIC contrast, indicating that enhanced carrier recombination only occurred on this pair of faults. The same stacking faults appeared bright in CL images suggesting firstly, that the enhanced recombination occurred via a radiative transition, and secondly that impurities segregate preferentially on either {111}A or {111}B planes (section 3.1).

In this Chapter, TEM and TEM CL results from stacking faults in several different quantum well structures will be presented. Results from the lower quality SQW structures (KLB116 and KLB121) are used to investigate the origin of the stacking faults and the nature of the associated luminescence. Results from a higher quality MQW sample are then interpreted in the light of this information. It should be emphasized that all the CL results included in this Chapter were examined for possible artefacts as outlined in section 2.5. However, no such artefacts were found.

Diffraction patterns were taken from all the stacking faults observed in this study. The lack of extra diffraction spots at any of these defects showed that the defects were stacking faults rather than twins (which can sometimes give similar contrast in TEM micrographs).

3.1. Crystallography of Stacking Faults

GaAs crystallizes in the sphalerite (Zincblende) structure. This structure can be regarded as two interpenetrating fcc lattices with Ga atoms occupying sites on one sublattice and As atoms occupying sites on the other sublattice. The two sublattices are

displaced by ¼ of a body diagonal (Figure 3.1). As nearest neighbour atoms are different in the sphalerite structure there is no centre of inversion symmetry between adjacent atoms. As a result GaAs is polar so that the (111) and $(\bar{1}\bar{1}\bar{1})$ planes are not equivalent. This is illustrated in Figure 3.2. A (111) surface can terminate on either plane PQ or plane RS. If the surface terminates on RS three bonds per atom must be broken as compared to only one broken bond per atom for a plane terminating on PQ. Therefore a (111) surface will always end on Ga atoms while a $(\bar{1}\bar{1}\bar{1})$ plane will end on As atoms. By convention, the Ga rich face is referred to as {111}Ga or {111}A and the As rich face is designated $\{\bar{1}\bar{1}\bar{1}\}$As or $\{\bar{1}\bar{1}\bar{1}\}$B.

3.1.1. Stacking Faults

The atoms on each sublattice of the sphalerite structure can be represented by Greek and Roman letters respectively. The structure can then be expressed in terms of the stacking of close packed layers on {111} planes as

.... aαbβcγaαbβcγ ....

There are now two different types of stacking fault. Intrinsic faults are equivalent to removal of a double layer of atoms (arrowed)

.... aαbβcγaαbβaαbβcγaαbβ ....
↑

Extrinsic faults are equivalent to insertion of a double layer of atoms (arrowed).

.... aαbβcγaαbβaαcγaαbβcγaα ....
↑

3.1.2. Stacking Faults in Epitaxial Layers

Mendelson (1961) has discussed the crystallography of stacking

fault polyhedra in epitaxial Si layers grown on substrates of various orientations. Stacking faults nucleating on (001) substrates form pyramidal structures (Figure 3.3). In GaAs adjacent faults on the pyramid occur on planes of opposite polarity either on {111}Ga or $\{\bar{1}\bar{1}\bar{1}\}$As. Booker (1964) has also determined that adjacent planes are of opposite character, such that intrinsic and extrinsic faults oppose each other. The partial dislocations formed where two stacking faults meet are termed stair rod dislocations with $\frac{a}{6}$ <110> Burgers vectors. The {111}Ga and $\{\bar{1}\bar{1}\bar{1}\}$As planes intersect the (001) surface parallel to orthogonal <110> directions, the {111}Ga planes intersecting the surface along $[1\bar{1}0]$ and the $\{\bar{1}\bar{1}\bar{1}\}$As planes intersecting the surface parallel to [110].

Booker (1964) has observed that one side of a pyramidal stacking fault can 'fold back' towards the opposing face (Figure 3.5). Note that the fault which changes plane bends through an obtuse angle and changes character from intrinsic to extrinsic or vice versa. Kotani (1977) has suggested that for GaAs/$A\ell_xGa_{1-x}$As layers, folding back occurs due to lattice stresses generated either by lattice mismatch or by misgrowth.

The final type of stacking fault observed in (001) GaAs/$A\ell_xGa_{1-x}$As epilayers is the single, isolated fault generated by slip on {111} planes. The partial dislocations at the edges of the fault are Shockley partials with $\frac{a}{6}$ <211> Burgers vectors (Read, 1953). These faults have a typical width of less than 1 μm (Kotani et al., 1977) which greatly exceeds the equilibrium value of approximately 50Å observed for dissociation of $\frac{a}{2}$ <110> dislocations into Shockley partials. This implies a reduction in the stacking fault energy, possibly due to impurities.

3.1.3. Nucleation of Stacking Faults

The mechanisms of stacking fault nucleation have been reviewed by Stowell (1974) and by Ravi and Varker (1974). Several alternative mechanisms have been proposed, including hydrocarbon substrate contamination, substrate damage, small oxide islands on the substrate or extended dislocations in the substrate. Bafleur and Munoz-Yague (1983) examined MBE GaAs epilayers, concluding that stacking faults nucleated at the substrate interface but were not generated by extended substrate dislocations. Wang et al. (1986) also studied stacking faults in GaAs, suggesting that either residual oxide left on the substrate before growth or carbon contamination of the substrate generated the faults. Chai et al. (1985) found evidence linking residual sulphur (originating with the sulphuric acid based etch used in substrate preparation) with stacking faults. Using secondary ion mass spectroscopy, sulphur was detected at the substrate interface of GaAs wafers containing a high density of stacking faults.

3.2. Stacking Faults in KLB116

3.2.1. TEM Results

Preliminary TEM samples of KLB116 were prepared by chemically removing the substrate, leaving the 1.1 μm thick epilayer completely intact. This is barely thin enough to obtain useful TEM bright field images in the EM 400 at 120 kV. The advantage of this is that the whole of the stacking fault can be examined. TEM examination revealed a high density ($10^5 cm^{-2}$) of stacking faults, most of which were highly complicated structures such as the one shown in Figure 3.6. Pyramidal stacking faults were not usually observed in this

sample. A typical TEM specimen of KLB116 contained upwards of 1000 stacking faults of which only one or two were simple isolated faults such as the one shown in Figure 3.6. All the stacking faults examined in this sample originated at the same surface. Knowledge of the orientation of TEM foils in the electron microscope was used to deduce that all the stacking faults nucleated in the vicinity of the substrate interface. Many stacking faults showed contrast at the nucleation point suggesting that the faults are generated by substrate contamination.

In order to determine the intrinsic or extrinsic character of stacking faults thinner TEM specimens were required. These were prepared by removing the substrate and part of the first $Al_xGa_{1-x}As$ layer with chemical etchants. Specimens prepared in this fashion were typically between 0.3 and 0.4 μm thick. Stacking faults in these specimens were characterised using the method of Gevers et al. (1963) as described in Thomas and Goringe (1979). In this method the nature of a stacking fault is determined by comparing the colour of stacking fault fringes in bright field and dark field TEM images, taken using the same diffracting vector, $\underline{g}$. It should be noted that modern electron microscopes tilt the electron beam to obtain dark field images. This procedure reverses $\underline{g}$ between bright and dark field so that care must be taken when applying Gevers method.

Simple stacking faults in KLB116 were determined to be of two different types, folded back faults or single faults. Each type was found to occur with the long edge parallel to either [110] or $[1\bar{1}0]$. Folded back faults occurred with the intrinsic fault or the

extrinsic fault furthest from the substrate.

3.2.2. CL Results

CL was initially performed on the 1.1 μm thick TEM specimens. This had the advantage that both the $Al_xGa_{1-x}As$ and the QW luminescence could be investigated. Figure 3.8 shows a CL spectra from unfaulted crystal. The two main peaks are the $Al_xGa_{1-x}As$ BE emission at 2.018 eV and the QW emission at 1.675 eV. The nature of the QW luminescence will be discussed in more detail in section 3.2.3. The weak structures at 1.993 eV and 1.927 eV are ascribed to $Al_xGa_{1-x}As$ FB transitions. Figure 3.9 shows a CL spectra from a complicated stacking fault such as the one shown in Figure 3.6. The QW luminescence in particular is complex and varied considerably between stacking faults and would be difficult to interpret. For this reason, results will only be presented for simple faults. For simplicity, CL spectra will be split into three separate regions as marked A, B and C on Figure 3.8. The luminescence from stacking faults will be discussed separately for each region. Region A is the $Al_xGa_{1-x}As$ emission, region B is the QW luminescence and region C is the intermediate region.

Consider region A first. Figure 3.10 shows two CL spectra acquired within this energy range, one from a stacking fault and one from an adjacent region of unfaulted crystal. The $Al_xGa_{1-x}As$ BE emission is reduced in intensity at the stacking fault and shifts slightly towards lower energy. This indicates firstly a reduction in crystal quality and secondly that the slight red shift may possibly be due to an increased impurity concentration at the stacking fault. The strong

FB emission at approximately 1.987 eV could also be interpreted in terms of an enhanced impurity concentration at the stacking fault. It is possible that acquiring CL spectra over a range of different temperatures and electron beam intensities might have yielded sufficient information to prove that impurities are present (in the $Al_xGa_{1-x}As$ layers) near stacking faults and possibly allowing the impurities to be identified. However, examination of a number of different stacking faults showed that the FB emission occurred at a different energy for each fault. Considerable variations in intensity between different faults were also observed. Therefore it seems likely that if impurities are present then both the nature and the concentration of the impurities vary from defect to defect. The magnitude of the BE red shift also varied substantially over the range 0 to 20 meV. As a result temperature and excitation intensity experiments would have needed to be performed on each stacking fault in turn. This was not considered to be feasible, partly due to the contamination problems inherent in this type of measurement (section 2.5).

Although the presence of impurities could not be proved, monochromatic CL imaging was used to investigate the spatial distribution of the $Al_xGa_{1-x}As$ luminescence features. It was found that the FB emission was strongest and the BE weakest when the electron beam was illuminating the nucleation point of the stacking fault, consistent with the likelihood that the impurity concentration is highest in this region. However, no impurities could be detected by EDX analysis. One TEM specimen was ion thinned using the PIMS so that EELS could be performed on the portion of the first $Al_xGa_{1-x}As$ cladding layer closest to the substrate. The only

impurities detected were carbon due to contamination and argon implanted by the ion thinning process.

Now considering region B of Figure 3.8, the QW luminescence. This region was only investigated for a few of the very simplest stacking faults. Figure 3.11 compares a spectrum from a typical simple stacking fault with a spectrum from adjacent unfaulted crystal. At the stacking fault a strong extra emission peak appears at lower energy than the normal QW emission. In contrast to the $Al_xGa_{1-x}As$ luminescence which varied considerably between different stacking faults, this extra emission consistently appeared 40-45 meV below the normal QW peak. Monochromatic CL imaging showed this peak arising from the region of crystal where the stacking fault passed through the QW,near the top surface of the sample.

In region C of Figure 3.8, the intermediate energy range, interesting results were obtained. Figure 3.12 compares CL spectra at and adjacent to a stacking fault. A number of peaks can be seen emanating from the stacking fault. It should be stressed that these features are much weaker than either the $Al_xGa_{1-x}As$ or QW emission. From monochromatic images it was found that these luminescence features arise from the region where the partial dislocations bordering the stacking fault intersect the QW. This is surprising given that all these peaks occur at energies higher than the QW luminescence. Although several different stacking faults were examined in energy range C, they all gave radically different results with the emission from the two different partials on the same stacking fault also giving completely different spectra.

Having examined 1.1 μm TEM specimens, similar CL experiments

were performed on thinner specimens. BF and DF TEM micrographs of a typical stacking fault are shown in Figure 3.13. Applying Gevers rule, this defect is a simple intrinsic stacking fault. Figures 3.14a) and b) show the $Al_xGa_{1-x}As$ and QW luminescence from this stacking fault as compared to control spectra acquired from adjacent unfaulted crystal. These spectra are qualitatively similar to those obtained from thicker specimens. Thus the emission features seen at stacking faults are not likely to be generated by absorption or interference effects and are almost certainly genuine. The change in QW emission energy between Figure 3.14b) and Figure 3.8 is ascribed to a change in QW thickness between the two pieces of material used to prepare the two TEM specimens. Calculations as described in section 3.2.3 showed that a change in well width of three monolayers would account for this change in QW emission energy. Monochromatic CL images acquired from the stacking fault of Figure 3.13 are shown in Figures 3.15a) to d), corresponding to the energies of the $Al_xGa_{1-x}As$ BE, $Al_xGa_{1-x}As$ FB, normal QW and stacking fault QW emissions respectively. The most obvious feature of the $Al_xGa_{1-x}As$ BE image is the mottled intensity variations. This effect was only observed on chemically thinned samples not on bulk material. The origin of this effect is unclear but may be due to variations in surface recombination velocity due to the chemical etchants used to prepare TEM specimens. A second feature of the $Al_xGa_{1-x}As$ BE image is the dark region roughly corresponding to the intersection of the stacking fault with the QW. In the $Al_xGa_{1-x}As$ FB image a single bright spot can be seen, corresponding to the region of crystal directly over the nucleation point of the stacking fault

(the nucleation point itself has been chemically removed in this sample). Adjacent to this is a faint bright band corresponding to the intersection of the stacking fault with the first (substrate side) $A\ell_x Ga_{1-x}As$ interface. In the QW image the stacking fault appears simply as a dark triangular region encompassing both the nucleation point and the QW intersection. In the stacking fault QW image, both the region of the nucleation point and the QW intersection appear bright although they are not well resolved as separate regions.

In order to distinguish between the two QW emissions, CL spectra were acquired from this stacking fault. It was found to be impossible to obtain reliable data on the variation of the peak intensities with temperature. Thermal expansion and contraction of the liquid helium cooled specimen stage caused the stacking fault to drift out of the electron beam during the course of the experiment. As the stacking fault luminescence originates from a localized area, inaccuracies in repositioning the specimen rendered the intensity data meaningless. Studying the variation in energy of the QW peaks over the temperature range 30-200K proved more reliable despite some small irreversible changes due to contamination. This data is plotted in Figure 3.16 for both QW peaks. However, the two peaks cannot be distinguished using this data.

3.2.3. Discussion

TEM examination of KLB116 showed that all the stacking faults observed in the epitaxial layers were nucleated at or close to the substrate interface. Careful inspection of TEM micrographs provided evidence that the faults were generated by contamination of the

substrate prior to epitaxial growth.

CL spectra acquired from stacking faults showed enhanced $Al_xGa_{1-x}As$ FB emission from the stacking fault nucleation point, with the energy and intensity of the FB transitions varying between different stacking faults. This result provides further evidence that the stacking faults are engendered by substrate contamination but also suggests that the contaminants vary from defect to defect. This suggests that, for KLB116 only, stacking faults are not nucleated by sulphurous residues (Chai et al., 1985) but possibly by hydrocarbon contamination or drying stains on the substrate.

The QW emission from stacking faults showed a consistent extra emission peak arising from both the region over the nucleation point and the vicinity of the intersection of the fault with the QW. This peak always appeared at approximately the same energy. There are two possible ways this emission could arise. Firstly, by a local change in quantum well thickness. Secondly, due to impurities incorporated in the quantum well. A simple calculation based on a particle in a finite box model (see Kolbas and Holonyak, 1984) showed that an increase in well width equivalent to 2.6 monolayers would produce emission at the required energy. A more sophisticated calculation using the envelope function approximation (G. Bastard, 1982) was kindly performed by P.J. Dobson at the Philips Research Laboratories, Surrey, a similar result being obtained. It seems highly unlikely that a stacking fault could generate this change in well width. Therefore the enhanced stacking fault emission may be due to increased levels of impurity

in the QW although there are alternative explanations such as excitons being bound to the stacking fault thus lowering the QW emission energy. The evidence for increased levels of impurities is as follows. Results from the investigation of the $Al_xGa_{1-x}As$ luminescence suggested that impurities might be present in the crystal around the nucleation points of stacking faults. Comparison of results from TEM specimens of different thicknesses suggested that impurities were diffusing through the $Al_xGa_{1-x}As$ along both the growth direction and along the stacking fault. The evidence for impurities diffusing up the stacking fault and being incorporated in growth was the observation of a faint bright band in the $Al_xGa_{1-x}As$ FB monochromatic CL image, Figure 3.16b), believed to be due to impurity trapping (in the $Al_xGa_{1-x}As$ layer) at the $Al_xGa_{1-x}As$/GaAs interface. The extra QW emission originates from the same region of crystal as the $Al_xGa_{1-x}As$ FB emission but is much stronger. As impurity trapping is known to occur at $Al_xGa_{1-x}As$/GaAs interfaces, most of the impurity incorporating in the GaAs side of the interface (Miller et al., 1982), it is believed that impurities may be incorporated in the QW at stacking faults. However, the normal and stacking fault QW luminescence showed similar behaviour when the specimen temperature was varied. Therefore if the stacking fault QW luminescence is impurity related then the normal QW luminescence must also be an impurity related emission rather than the expected n = 1 X(e - hh) emission. This conclusion was confirmed by the simple expedient of varying the intensity of the electron beam illuminating the stacking fault. Both QW emission peaks shifted to higher energy with increased excitation. This is indicative on n = 1 (e - a) recombination process (Woodbridge et al., 1984). For

the normal QW emission the acceptor is almost certainly carbon. The acceptor or acceptors giving rise to the stacking fault emission cannot be identified from the current work.

So far the anomalous CL emission observed in the region between the $Al_xGa_{1-x}As$ and the QW luminescence has not been discussed. This emission was found to be extremely variable but arose from the regions where the partial dislocations bordering stacking faults passed through the quantum well. Partial dislocations at opposite ends of the same stacking fault gave radically different emission features. With the available information the cause of this luminescence is impossible to identify. As the luminescence peaks occur at higher energies than the quantum well luminescence it seems reasonable to suppose that this emission arises from a region of the $Al_xGa_{1-x}As$ close to the QW layer. It is conjectured that impurities gettered at the QW interface are segregating on the dislocations and giving deep level luminescence in the $Al_xGa_{1-x}As$.

3.3. Stacking Faults in KLB121

The major difference between the structures KLB116 and KLB121 was that for KLB121 a nominally 10Å AlAs prelayer was grown just before the QW but separated from it by a 150Å $Al_xGa_{1-x}As$ layer. The prelayer was included to improve the quality of the QW by gettering impurities. Woodbridge et al. (1984) performed luminescence measurements on KLB121 and identified the QW emission as the n = 1 X (e - hh) transition but observed a weak low energy shoulder from an n = 1 (e - a) transition, the acceptor being assumed to be carbon.

Due to the higher quality of KLB121 and the presence of the

AlAs prelayer the work on KLB116 suggested that stacking faults would have less of an effect on the QW emission and would provide further evidence that the stacking fault luminescence is due to impurities rather than a QW width fluctuation.

3.3.1. TEM Results

TEM samples of KLB121 were prepared with thicknesses in the range 0.2 to 0.4 μm. Thicker 1 μm samples like those prepared from KLB116 were not produced. Preliminary TEM investigations showed a stacking fault density of around $10^4 cm^{-2}$. Although complicated stacking faults were predominant, the percentage of simple defects was much higher than for KLB116. From the size of the faults it was inferred that again all the stacking faults were nucleated at or close to the substrate interface.

Three different types of stacking fault were observed in KLB121. Firstly, pyramidal faults such as the one shown in Figure 3.17. The pyramid appears truncated because part of the substrate side of the first $Al_xGa_{1-x}As$ layer has been removed. Comparing the BF and DF images and using the method of Gevers et al. (1963) allowed the intrinsic or extrinsic character of the stacking faults to be determined. As expected for epitaxial GaAs/$Al_xGa_{1-x}As$ layers grown on an (001) substrate (see section 3.1.2.), opposing pairs of faults were of the same character. In Figure 3.17b) the intrinsic and extrinsic faults have been labelled I and E respectively. TEM examination of ten or more pyramids revealed that all of them formed in the same orientation. In other words, the top edges of the extrinsic faults were always parallel to the same <110> direction

while the top edges of the intrinsic faults were parallel to the orthogonal <1$\bar{1}$0> direction. A.R, Preston used the method of Tafto and Spence (1982) to distinguish between the [110] and [1$\bar{1}$0] directions (Bailey et al., 1987). Using this information the top edges of the extrinsic faults were found to be parallel to the [110] direction. Therefore the extrinsic faults lay on {$\bar{1}\bar{1}\bar{1}$}As planes while the intrinsic faults lay on {111}Ga planes.

An example of the second type of stacking fault found in KLB121 is shown in Figure 3.18. Again using Gevers',rule this example is a simple intrinsic fault. Similar extrinsic faults were also observed, the relative numbers of intrinsic and extrinsic faults being approximately equal. The orientation of these faults was found to correspond to the orientation of the full stacking faults. In other words, the intrinsic faults again formed on {111}Ga planes and the extrinsic faults formed on {111}As planes.

The final type of stacking fault found in KLB121 is shown in Figure 3.19. At first sight this appears identical to the simple intrinsic/extrinsic fault. Closer examination of the BF micrograph shows that the stacking fault fringes are not symmetric as would be expected for a simple intrinsic/extrinsic fault (Hirsh et al., 1965). Therefore this structure is a folded back pyramid. Applying Gevers' rule the uppermost fault (furthest from the substrate) is extrinsic and the lower fault is intrinsic. The faults at the edges of the structure were not determined, nor was the separation of the intrinsic/extrinsic pair. Booker (1964) showed that the fault which changes plane in a folded back defect changes character. Thus if folded back faults are formed from pyramidal faults then it is

expected that the lower fault should lie on a {111}Ga plane if it is intrinsic. Similarly, an extrinsic lower fault should lie on a $\{\bar{1}\bar{1}\bar{1}\}$As plane. This was confirmed by experiment, folded back faults occurring on both {111} planes.

Kotani et al. (1977) observed similar stacking faults in GaAs/$A\ell_xGa_{1-x}As$ layers grown by liquid phase epitaxy (LPE). In contrast to the present study where stacking faults only folded back at or near to the substrate interface, Kotani et al. also observed faults folding back at subsequent GaAs/$A\ell_xGa_{1-x}As$ interfaces. This difference in behaviour is believed to be due to differences between the MBE and LPE growth processes.

3.3.2. CL Results

The QW luminescence from stacking faults in KLB121 behaved in a qualitatively similar manner to KLB116, the additional QW peak originating from the regions where the stacking faults intersect the QW. As expected this peak was considerably weaker than for KLB116. Figure 3.20 compares a CL spectrum from a simple intrinsic stacking fault with a CL spectrum from unfaulted crystal. The n = 1 (e - a) peak from the stacking fault does not correspond in energy to the background emission. The major difference between CL results from KLB121 and KLB116 was that in KLB121 the energy of the n = 1 (e - a) stacking fault emission was not constant, the peak being between 10 and 30 meV below the n = 1 X(e - hh) emission.

During the course of investigations into the luminescence of stacking faults in KLB121 some faults were found which gave somewhat different results. Instead of the usual weak n = 1 (e - a)

peak some faults gave a very strong peak in this position with the n = 1 X(e - hh) emission peak being undetectable. Figure 3.21 shows CL spectra from and adjacent to a stacking fault exhibiting this behaviour. Figure 3.22 shows four monochromatic images acquired at the energies of the Al_xGa_{1-x}BE, Al_xGa_{1-x}As FB, QW n = 1 X(e - hh) and QW n = 1(e - a) transitions. The increased brightness at the lower left of all four images is an artefact of the CL system right collection optics (at low magnifications) occurring due to non-uniform collection efficiency across the field of view. Clearly the strong n = 1(e - a) emission observed at the stacking fault is unrelated to the fault but is due to the cellular structure visible in Figure 3.22. Using conventional TEM BF and DF imaging the cellular structure can just be distinguished (Figure 3.23), possibly due to small thickness variations occurring either during growth or resulting from the TEM specimen preparation due to different etching rates of regions with different impurity levels. After thorough examination of this specimen using TEM and CL it was found that all the stacking faults were located in the bright bands of the cellular structure, the apex of pyramidal faults being close to the centre of the bright band (Figure 3.24). Apart from two specimens which were free of this effect, the cellular structures were present in all specimens of KLB121 including bulk material. As stacking faults were only found in the bright bands of the cellular structure, work on stacking faults in KLB121 was complicated by the superimposed effects of the cellular structure and was therefore abandoned. However, the one to one correlation between faults and cell walls again points to the involvement of

impurities in the formation of stacking faults.

The anomalous emission observed from partial dislocations in KLB116 was not seen in KLB121. This was taken to be the consequence of the higher purity of the other sample.

3.3.3. Discussion

Stacking faults in KLB121 were observed by TEM to grow in preferred orientations. Discussion of this phenomenon is deferred until section 3.6.4.

CL of stacking faults in KLB121 gave reduced intensity n = 1(e - a) QW emission as compared to faults in KLB116, in agreement with the impurity model for the luminescence. Further studies of stacking faults in KLB121 were precluded by a cellular structure of higher impurity concentration containing a higher than normal density of stacking faults. As the cellular structure was observed in both the QW and $A\ell_xGa_{1-x}As$ luminescence (irrespective of sample thickness) the impurities probably originate at the substrate interface,perhaps linked to the cellular structure sometimes observed in GaAs liquid encapsulated Czochralski grown GaAs substrates (Stirland et al., 1983). Like other stacking faults, faults formed in the cell structure were nucleated at or close to the substrate interface providing further evidence that stacking fault nucleation is linked to impurities and substrate contamination.

3.4. Stacking Faults in @1965

3.4.1. TEM Results

In sample @ 1965 the stacking fault density was about $10^3 cm^{-2}$, much lower than for KLB116 or KLB121. The complicated multiple

faults seen in the latter samples were not observed in @ 1965. Only two types of stacking fault were found in this material, pyramidal faults and folded back faults, both nucleated at or near to the substrate interface.

Considering full pyramidal stacking faults first, A.R. Preston again used the method of Tafto and Spence (1982) to distinguish between the [110] and [1$\bar{1}$0] directions. Using Gevers' rule intrinsic faults were only found on {111} Ga planes. This is the same result as obtained for KLB121. Figure 3.25 shows BF and DF TEM micrographs (imaged with $\underline{g}$ = 400) of a typical pyramidal stacking fault in @ 1965. The intrinsic and extrinsic faults have been labelled I and E respectively. The contrast from the extrinsic faults behaves as expected (Hirsch et al., 1965) but unusual effects can be seen at the intrinsic faults. Specifically, the stacking fault fringes bend together near the middle of each intrinsic fault. Figure 3.26 shows a BF TEM micrograph, with $\underline{g}$ = 2$\bar{2}$0 of the same stacking fault. For this diffracting vector, the intrinsic faults are invisible. Spindle shaped regions of bright contrast can be observed over the intrinsic faults, approximately centred on the lines where the faults emerge from the growth surface side of the crystal. These bright patches correspond to a decrease in crystal thickness due to hollows on the growth surface. As the hollows appear to be on the growth surface rather than the substrate side of the specimen then they must be a genuine consequence of growth rather than a product of the specimen preparation technique.

TEM micrographs of a typical folded back stacking fault in @1965 are shown in Figure 3.27, imaged for $\underline{g}$ = 2$\bar{2}$0 in BF and DF. The uppermost fault is intrinsic and the lower fault is extrinsic

(from application of Geyers' rule). Remembering that stacking faults change character when they bend through obtuse angles, then this fault was formed when one extrinsic fault of a full pyramid folded back. Although more than ten folded back stacking faults were located they all formed via an extrinsic fault folding back.

3.4.2. CL Results

Sample @ 1965 was much higher quality than either KLB116 or KLB121 but did not have $A\ell_xGa_{1-x}As$ cladding layers around the QW's. The only $A\ell_xGa_{1-x}As$ present was in the barriers between the QW's. No luminescence could be detected from these barriers in either bulk or TEM samples. In general CL results in @ 1965 were highly consistent. However, CL experiments were performed on TEM specimens prepared from two different pieces of @ 1965, cut from different parts of the same wafer. CL spectra from the two different pieces, although uniform across the individual pieces, showed that the n = 1 X(e - hh) emission occurred at different energies for the two different pieces, suggesting that the growth rate was slightly non-uniform across the wafer. Stacking fault luminescence from the two pieces was found to be identical for folded back stacking faults but significant differences were found for pyramidal faults.

Figure 3.28 compares a CL spectrum acquired from a pyramidal stacking fault with a spectrum acquired from adjacent unfaulted crystal. The specimen used to obtain these spectra was produced from the first piece of @1965 (piece 1). In addition to the n = 1 X(e - hh) and n = 1 X (e - ℓh) luminescence at 1.541 and 1.548 eV two weak peaks can be observed approximately 9 and 14 meV

below the heavy hole peak, For unfaulted crystal a very weak shoulder can be seen at around 21 meV below the heavy hole peak. This is probably an n = 1(e - a) transition, the acceptor is most likely carbon as this is the dominant background impurity in virtually all MBE systems. The stacking fault spectra shows a broad tail at the same energy.

Figure 3.29 shows similar CL spectra for a pyramidal stacking fault in a specimen made from the second piece of 1965 (piece 2). The n = 1 X(e - hh) and n = 1 X(e - ℓh) emissions have shifted to higher energy by approximately 7 meV. Again the stacking fault shows emission features 9, 14 and 21 meV below the heavy hole transition. Unlike the pyramidal stacking fault in piece 1, the stacking fault emission in this example is dominated by the peak 14 meV below the n = 1 X(e - hh) peak. The -9 meV emission is barely discernible as an asymmetry on the -14 meV peak. The -21 meV emission is slightly stronger and better resolved than for piece 1. In order to ascertain the nature of the subsidiary peaks, the intensity of the electron beam illumination was varied when illuminating pyramidal stacking faults in both piece 1 and piece 2. Results from piece 1 were inconclusive but for piece 2 a shift to higher energy was observed for the -14 meV peak. This is indicative of n = 1 (e - a) transition (B. Lambert et al., 1982). The -9 meV and -21 meV emissions were not sufficiently well resolved to form any conclusion.

Figures 3.30 and 3.31 show monochromatic CL images obtained from the same defects used to acquire the CL spectra of Figures 3.28 and 3.29 respectively. The images a) and b) in each figure

were acquired at the energies of the n = 1 X(e - ℓh) and n = 1 X(e - hh) luminescence respectively. Images c) to e) in each figure were acquired at the energies of the -9, -14 and -21 meV peaks respectively. The orientation of the stacking faults has been marked on the light hole images, the intrinsic and extrinsic faults being denoted by I and E respectively. In both sets of images it is immediately apparent that all three impurity emissions emanated most strongly from the vicinity of the intrinsic faults to give two bright bars. In the same regions the light hole and heavy hole emissions decrease in intensity. As expected the light hole and heavy hole emissions are identical. All the images are slightly distorted because the raster used to drive the electron beam is not perfectly square. In both Figure 3.30 and Figure 3.31 the planes of the stacking fault can just be distinguished as faint dark lines. Although the two sets of images are fairly similar there are two minor differences. Firstly, the -21 meV emission is much weaker in Figure 3.30 (piece 1) than in Figure 3.31 (piece 2). Secondly, in Figure 3.30 d) the intrinsic faults do not show well resolved double bright bars, as the area of enhanced luminescence elongates towards the extrinsic faults. It should be stressed that the examples given are typical of a number of stacking fault pyramids examined in samples of both piece 1 and piece 2, very little variation being observed between different faults even when samples of different thicknesses were examined. It is also worth mentioning that pyramidal stacking faults in piece 1 and piece 2 could not be distinguished by conventional TEM BF and DF imaging.

CL spectra from folded back stacking faults were much simpler than CL spectra from the pyramids. Allowing for the shift in the light

hole and heavy hole emissions; piece 1 and piece 2 gave identical results. Figure 3.32 compares a CL spectrum from a folded back stacking fault with a spectrum from adjacent crystal. These spectra were acquired from a TEM specimen prepared from piece 1. As piece 2 behaved in an identical fashion to piece 1, piece 2 results have not been included. In Figure 3.33 the stacking fault shows a single strong impurity peak 21 meV below the heavy hole peak. For increased electron beam intensity this impurity peak shifts to slightly higher intensity and so is ascribed to an n = 1 (e - a) transition. As the energy of this peak corresponds to that of the background emission seen in unfaulted crystal then the acceptor is almost certainly carbon. Figure 3.33 shows three monochromatic images acquired from a folded back stacking fault at the energies of the light hole, heavy hole and carbon luminescence. The orientation of the stacking fault is marked on the light hole image. Like the intrinsic faults of a pyramidal defect, both the light hole and heavy luminescence decrease at the stacking fault, while the carbon impurity emission is enhanced. A faint dark line can be seen dividing the impurity luminescence. This corresponds to the position of the stacking fault planes.

The anomalous emission observed from partial dislocations bordering stacking faults in KLB116 was not seen in @ 1965.

3.4.3. Discussion

TEM observations of pyramidal stacking faults in @ 1965 were in agreement with the results of Kakibayashi et al. (1984) in that spindle shaped hollows were observed over the faults intersecting

the growth surface parallel to the [1$\bar{1}$0] direction. However, Kakibayashi et al, did not determine the intrinsic-extrinsic character of the stacking faults although they did determine that the faults were generated at the substrate-epilayer interface.

CL results from both pyramidal and folded back stacking faults in @ 1965 were far more consistent than in KLB116 or KLB121. Full pyramids showed strong impurity emission emanating from the intrinsic faults, the heavy and light hole luminescence decreasing over the same faults for two reasons. Firstly, the crystal is thinner here and secondly, the impurity transition provides a competing recombination route reducing the number of carriers recombining via the normal excitonic routes. For folded back stacking faults no thickness changes were observed so the loss of heavy and light hole luminescence must be solely due to the impurity recombination route or routes.

The two major impurity emissions observed for pyramidal stacking faults were 9 and 14 meV below the heavy hole emission. However, the two different pieces of @ 1965 examined differed in the relative strengths of these two features. For piece 2 both emissions were stronger than for piece 1, but the -14 meV emission increased the most. Although there is insufficient information to account for this behaviour it is conjectured that the -9 and -14 meV luminescence features are due to the same impurity located at the edge and the centre of the QW respectively (see Green and Bajaj, 1985). Miller et al. (1982) found that acceptors in QW's were incorporated at the edge of the well. Therefore, for piece 2, where the impurity luminescence (and hence the impurity concentration) is higher, it seems reasonable to assume that impurities are forced

into the centre of the well such that the centre well (-14 meV) emissions becomes dominant.

3.5. Other Samples

Before discussing stacking faults in general, two other samples will be mentioned.

The MQW structure G43 contained a very low density of stacking faults. In fact only one stacking fault was ever located in this material. Unfortunately, this fault could not be studied as it was examined during the period when the EM400 was producing severe ion damage in all quantum well samples (see section 2.1.1.).

D19, a sample which has not been mentioned previously, was not a QW sample but a simple $Al_{0.2}Ga_{0.8}As$ epilayer grown on an (001)GaAs substrate by MBE. Unlike the nominally undoped QW structures, this sample was Si doped to $4 \times 10^{17} cm^{-3}$. TEM examination revealed a high density ($10^{5} cm^{-2}$) of pyramidal stacking faults. Neither CL spectra nor monochromatic CL imaging could distinguish the stacking faults from the surrounding crystal. The stair-rod partial dislocations were similarly invisible to CL. TEM analysis of these stacking faults was performed by A.R. Preston, who made two observations relevant to the present study. Firstly, he determined that like KLB121 and @1965 pyramidal faults were preferentially orientated so that all the intrinsic faults were on {111} Ga planes. Secondly, that no change in crystal thickness occurred over either the extrinsic or intrinsic faults.

3.6. Discussion

3.6.1. Substrate Contamination

Stacking faults in four different GaAs/$Al_xGa_{1-x}As$ structures were examined using TEM CL. All the stacking faults nucleated in the vicinity of the substrate interface. CL spectra from TEM specimens of the SQW structures KLB116 and KLB121 suggested that impurities were incorporated in the cladding layers surrounding the quantum wells. Monochromatic CL images provided evidence that the impurities were concentrated in the regions around the stacking fault nucleation points. Therefore it seems likely that the stacking faults in the SQW structures are induced by substrate contamination. This conclusion was substantiated by TEM of 1.1 μm thick specimens of KLB116. For these specimens the stacking fault nucleation points were imaged, showing obvious signs of substrate contamination. Although EDX analysis was used on a number of stacking faults, no foreign elements could be detected. For the $Al_{0.2}Ga_{0.8}As$ epilayer it was also assumed that the stacking faults were nucleated by substrate contamination, although no attempt was made to confirm this assumption. The origin of stacking faults in @ 1965 will be discussed shortly.

CL was also used to investigate QW luminescence in the vicinity of stacking faults. Impurity luminescence of variable strength was found associated with all stacking faults. Varying the incident electron beam intensity and observing the effect on CL spectra identified the impurity luminescence as being due to n = 1 (e - a) transitions. There are two possible sources for the impurities; either residual dopants accumulate at the stacking faults or contaminants are transported from the substrate to the QW. The

former hypothesis is readily disproved in two ways. Firstly, in KLB121 and @1965 the energies of the stacking fault QW luminescence did not generally correspond to the energy of the background impurity luminescence from unfaulted crystal (there was only one exception). Secondly, if impurities have been removed from the surrounding crystal then obviously the radiative efficiency of the light hole and heavy hole luminescence will be increased. Hence, monochromatic CL images acquired at the energies of the light hole and heavy hole emissions should show regions of enhanced luminescence around stacking faults. This effect was not observed for any stacking fault examined in this study. Therefore the impurities incorporated in the QW layers must originate exclusively with the substrate contamination nucleating the faults. From this it follows that, like the SQW samples, stacking faults in @ 1965 must be nucleated by substrate contamination. Unfortunately, the nature of the contamination could not be identified. For the SQW samples the impurities varied from stacking fault to stacking fault. For @ 1965 only carbon was identified. Identification of impurities in QW's is particularly difficult because the energy of the luminescence depends on the well width and the position of the impurity within the well (Bastard, 1981) as well as the nature of the impurity. While Chai et al. (1985) identified sulphur on the substrates of GaAs epilayers containing high densities of stacking faults it is highly unlikely that a single impurity is responsible for all the stacking faults observed in the present study.

3.6.2. Impurity Incorporation in Quantum Wells

Having established that stacking faults are induced by substrate contamination it remains to show how impurities at the substrate become incorporated in the QW layers. In KLB116 impurity luminescence was observed from two separate regions. Above the nucleation point (in the growth direction) and at the intersection of the stacking fault with the QW. The region above the nucleation point will be considered first.

Two mechanisms have been proposed for impurity gettering in QW layers. Miller et al. (1982) suggested that impurities could float ahead of the growing $Al_xGa_{1-x}As$ layer and become incorporated in the GaAs QW's when the Al flux is turned off. This mechanism requires a solubility difference for the impurity between GaAs and $Al_xGa_{1-x}As$ but implies that impurities can inhibit growth by pinning growth steps on the surface. On the other hand, Petroff et al. (1984) proposed that the small misfit strain across an $Al_xGa_{1-x}As$/GaAs interface favours migration of impurities owing to the size differential between the impurity atoms and the atoms of the host lattice. During growth and subsequent cooling of the structures impurities will diffuse into or out of the QW layers. Although little evidence to support either mechanism was found in this study, the explanation of Miller et al. is favoured for the following reason. Complicated stacking faults in both KLB121 and KLB116 frequently showed growth suppression over the centre of the defect. For this to occur impurities must be present on the $Al_xGa_{1-x}As$ surface during growth. In addition, if impurities were diffusing from the stacking fault nucleation

points to the QW then the corresponding spot of QW luminescence would be expected to be of similar size to the thickness of the $Al_xGa_{1-x}As$ layer. However, this spot is considerably smaller than that. Therefore it is concluded that impurities from the substrate contamination simply float above the $Al_xGa_{1-x}As$ layer until the Al flux is shut off when they rapidly become incorporated in the QW.

For all the QW samples it is obvious that impurities are in some fashion transported up the stacking fault planes prior to incorporation in the QW. This is clearly indicated by the impurity QW luminescence. Also, the observation of a relatively large region of reduced growth over the intrinsic planes of pyramidal stacking faults implied that impurities are migrating up the stacking faults and on to the growth surface. In KLB116 CL showed that impurities are incorporated on both sides of an $Al_xGa_{1-x}As$/GaAs interface. As the impurity luminescence from the QW is much stronger than that from the $Al_xGa_{1-x}As$ it is inferred that most of the impurities are deposited on the GaAs side of the interface. Both Miller et al. (1982) and Petroff et al. (1984) also found that impurity gettering occurred primarily into the GaAs layer.

Impurity transport up the stacking fault plane is believed to be driven by the concentration gradient between the defect nucleation point and the surface. For this to take place the stacking fault must have an affinity for impurity atoms. Suzuki (1962) established that solute atoms could interact with stacking faults so that in general the energy of the solute atom at the stacking fault is different from the energy in the rest of the lattice. Therefore it will be energetically favourable for some impurities to segregate

at the stacking fault. There seems no reason that impurity atoms cannot then diffuse along the fault plane as is known to happen at oxygen induced stacking faults in silicon (Ravi and Varker, 1974). As the free energy of a surface is normally considerably higher than that of a stacking fault (Hirthe and Lothe, 1968) impurities should then be able to move onto the surface. Thus the impurity QW luminescence from the intersection of stacking faults with the QW can be explained by Suzuki segregation of impurities to the stacking faults followed by diffusion up the faults. Incorporation of the impurities into the GaAs can then occur by the mechanism proposed by Miller et al.

3.6.3. Comparison of Pyramidal and Folded Back Faults

In @ 1965 pyramidal stacking faults gave impurity luminescence predominantly from the intrinsic faults with little emission from the extrinsic faults. If the impurities segregating at the faults are purely determined by the character of the fault then folded back faults would be expected to give similar CL spectra to pyramids. However, the two types of fault gave quite different results. There are two possible reasons for this. Firstly, the intrinsic-extrinsic fault pair comprising a folded back stacking fault may be sufficiently close together that the two faults interact. In this study, no attempt was made to determine the fault separation. Secondly, that impurity segregation is influenced both by the intrinsic-extrinsic character and the polarity of the faults.

3.6.4. Preferential Orientation of Stacking Faults

In all the pyramidal stacking faults observed in this study

and also including those analysed by A.R. Preston in D19, the intrinsic faults were always formed on the {111} Ga planes while the extrinsic faults were on $\{\bar{1}\bar{1}\bar{1}\}$ As planes. Pyramidal stacking faults are induced when a small piece of crystal at the substrate interface is displaced in the growth direction (Kakibayashi et al., 1984) thus providing the shear displacement required to generate the stacking faults. This displacement is generated by substrate contamination, the nature of which (for KLB121) has been shown to vary from stacking fault to fault. As the three samples containing pyramidal stacking faults were also grown on three different MBE machines, it is highly unlikely that the magnitude of the displacement is constant. Therefore, the preferential orientation of the stacking faults must reflect a fundamental property of the GaAs structure making formation of intrinsic faults on {111} Ga planes energetically favourable as compared to their formation on $\{\bar{1}\bar{1}\bar{1}\}$ As planes. What is less clear is why for KLB121 folded back stacking faults could form by either intrinsic or extrinsic faults changing plane, whereas in @ 1965 only extrinsic faults changed plane. Kotani et al. (1977) proposed that the forces required to switch a stacking fault from one plane to another could originate with lattice mismatch between epitaxial layers or stresses generated by misgrowth. However, neither of these mechanisms can account for the discrepancy between faults in KLB121 and @ 1965. Instead, it is believed that Suzuki segregation is responsible. In KLB121 different impurities were observed at different stacking faults. Each impurity will effect the stacking fault energy by different amounts. Thus sometimes it will be favourable for the intrinsic faults to change planes while on other

occasions bending of extrinsic planes will be preferred. On the other hand, only one impurity was observed at back stacking faults in @ 1965 so that different faults behave in an identical manner.

3.6.5. General Comments

In this section, mention will be made of a few experimental observations which have not been discussed previously.

The lack of CL contrast from stacking faults in D19, the $Al_xGa_{1-x}As$ epilayer is surprising. However, this sample was highly doped ($4 \times 10^{17} cm^{-2}$) so that small changes in impurity concentration may only produce negligible changes in CL. Also impurities diffusing up the stacking faults would not be incorporated efficiently without the gettering action of a $GaAs/Al_xGa_{1-x}As$ interface, although the impurities may well be present on the surface. Due to the high surface recombination of GaAs and $Al_xGa_{1-x}As$ (Yablonovitch et al., 1987) luminescence cannot be detected from surfaces. It is also possible that the high dopant concentration may introduce dopant atoms into sites which would otherwise be occupied by impurities.

Growth suppression was only observed for pyramidal faults in @ 1965 (neglecting the complicated faults in the SQW structures). Sample @ 1965 was grown in a different laboratory to the other samples so this difference may be due to different growth conditions or substrate preparation techniques.

The anomalous CL emission observed around the intersections of partial dislocations with the QW in KLB116 was unusual in that it was only observed in this material, which was also the lowest quality. As this emission occurred at energies higher than the QW

emission then it is believed that it must stem from a region of one of the $Al_xGa_{1-x}As$ cladding layers close to the QW interfaces. The mechanism responsible for this luminescence is unknown but may be linked to impurity segregation at the partial dislocations.

There is an increasing body of evidence linking asymmetries between TEM micrographs of stacking faults imaged in $+\underline{g}$ and $-\underline{g}$ to the presence of impurities at the stacking faults (Humble and Morton, 1987). However, such asymmetries were not investigated in this study.

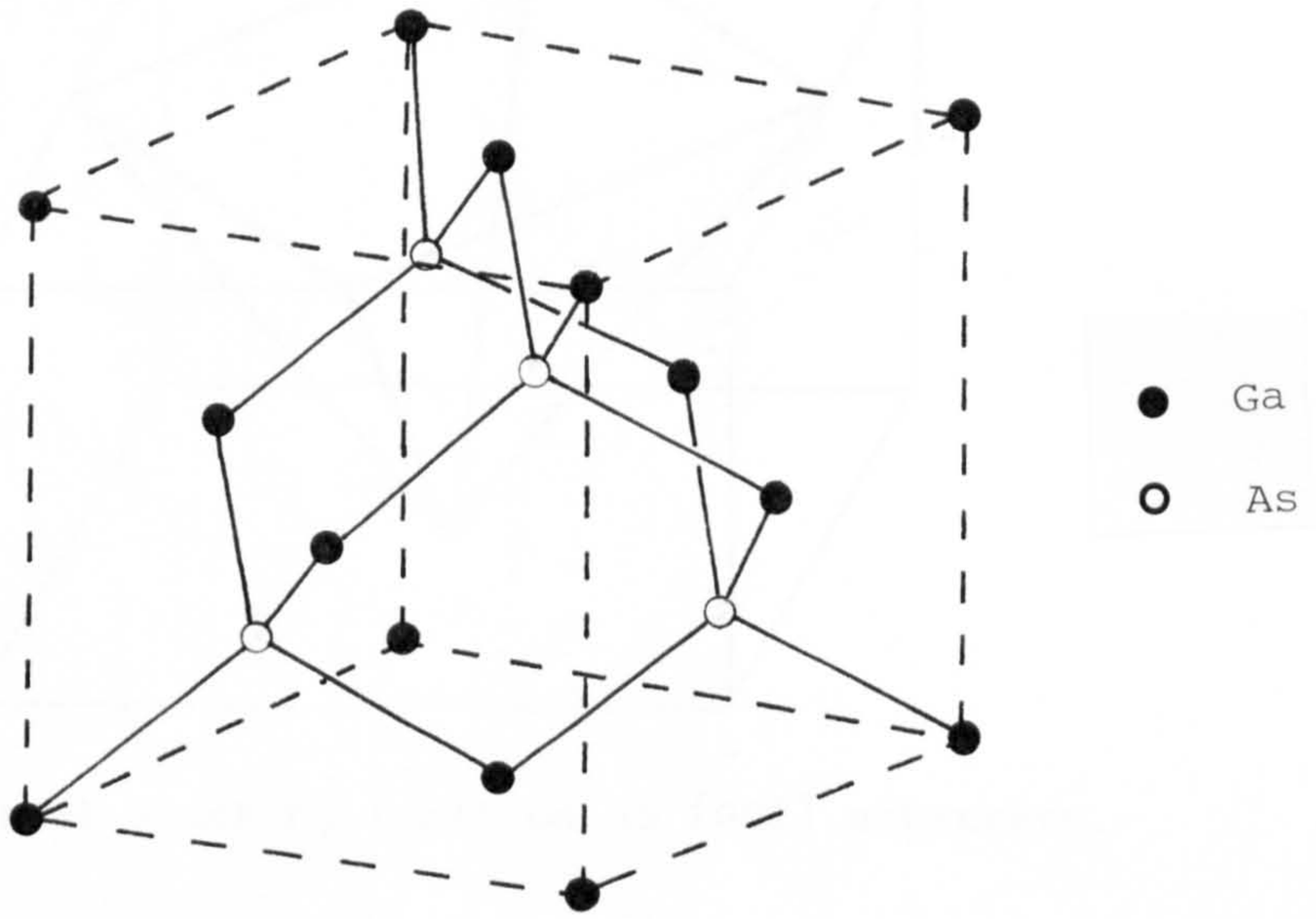

3.1 The sphalerite structure.

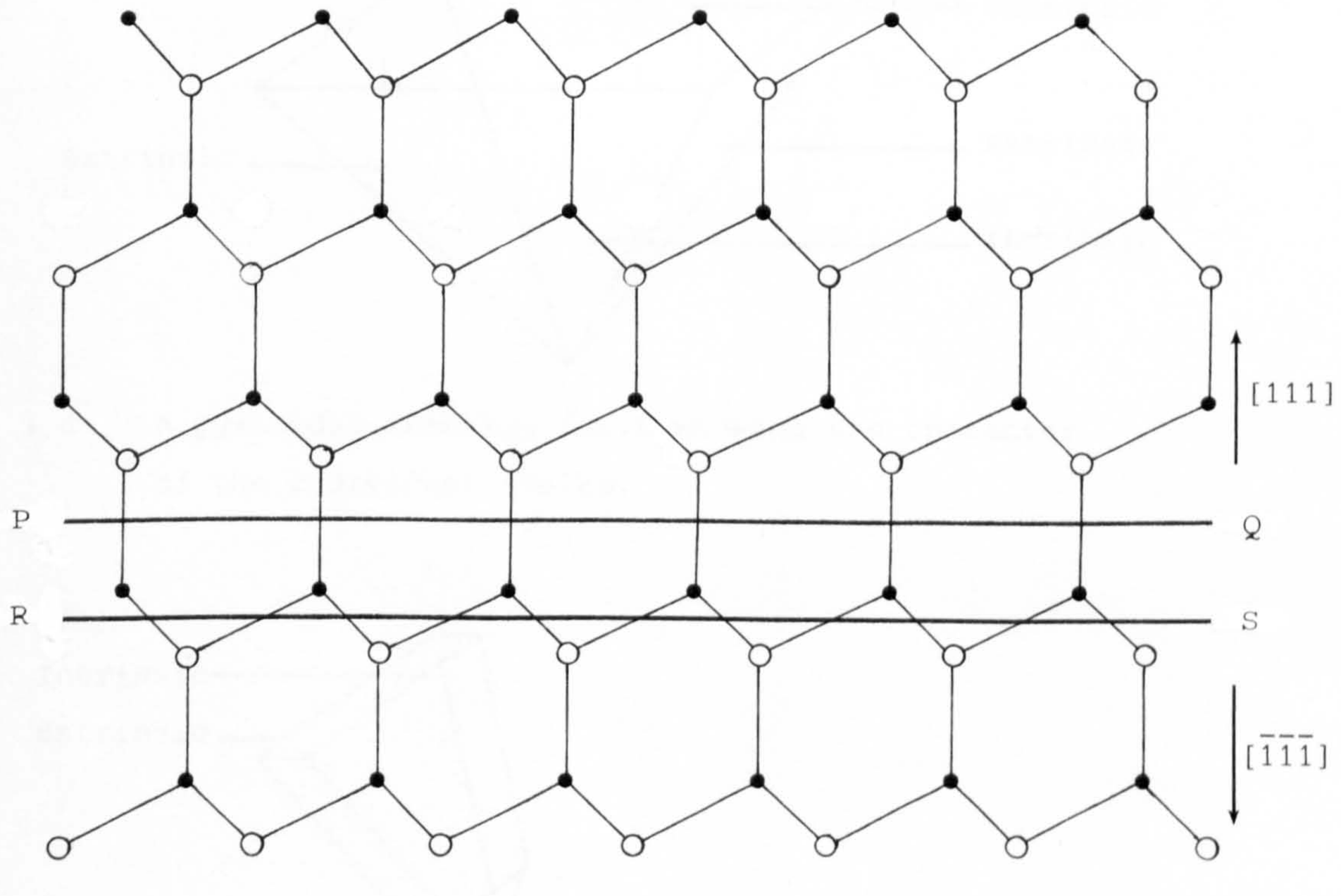

3.2 The non-equivalence of the [111] and [$\bar{1}\bar{1}\bar{1}$] directions in the sphalerite structure.

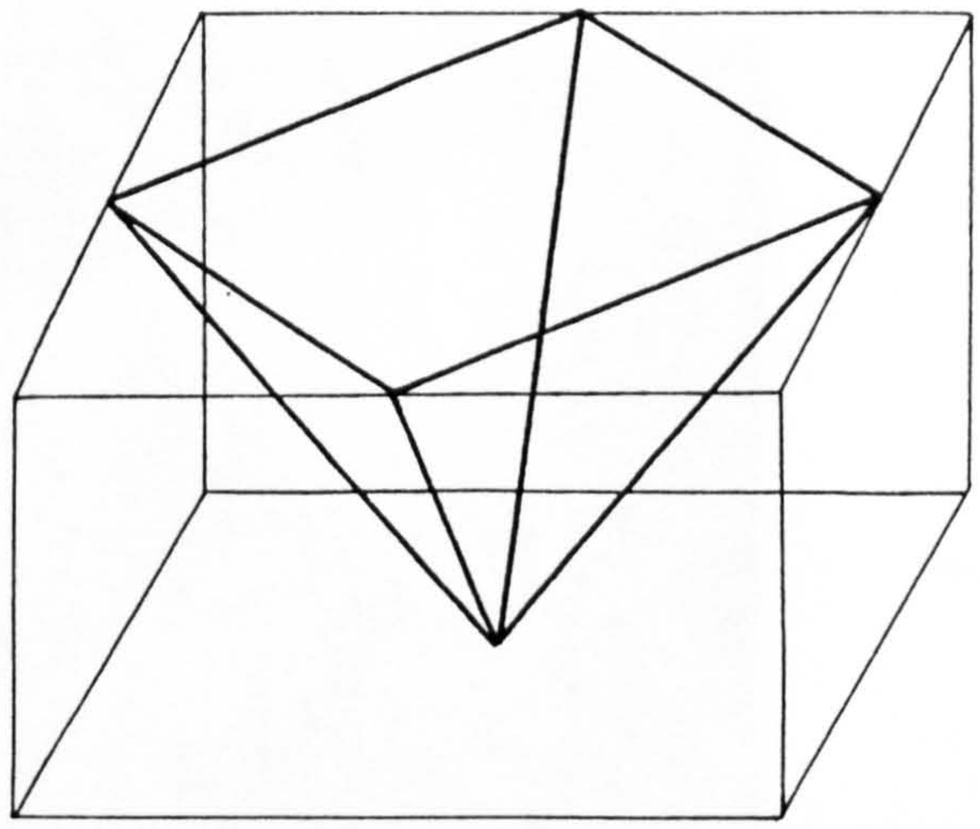

3.3 A pyramidal stacking fault on an {001} substrate.

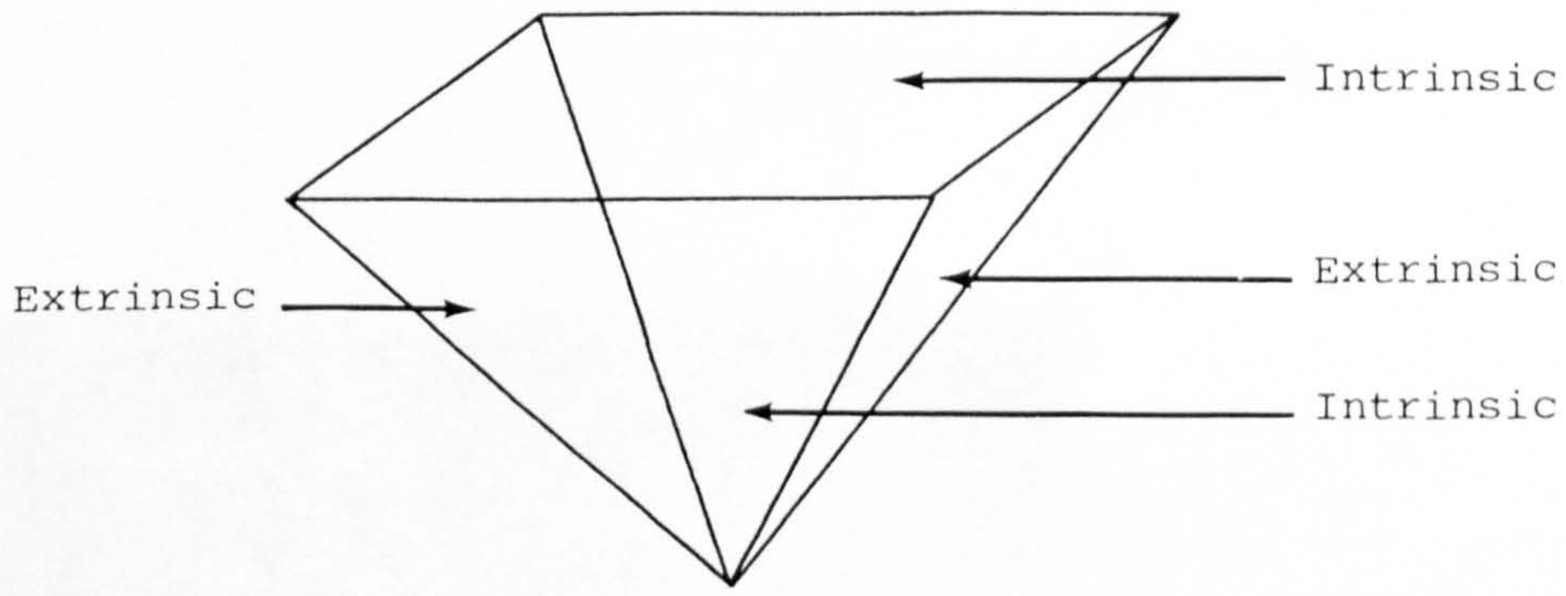

3.4 A pyramidal stacking fault showing the character of the individual faults.

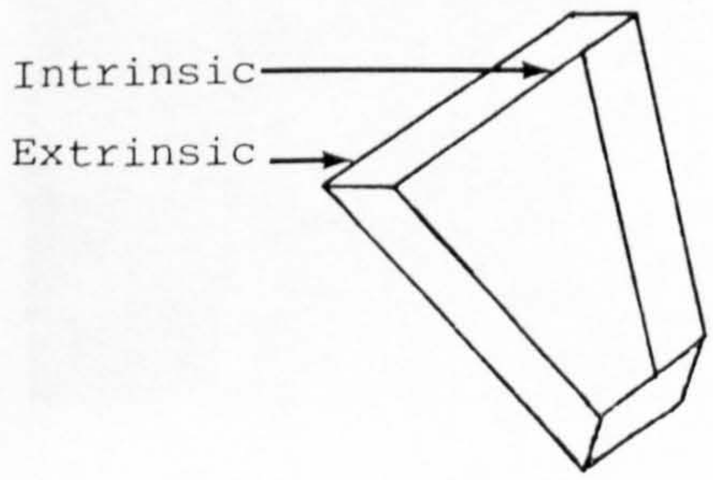

3.5 A 'folded back' stacking fault.

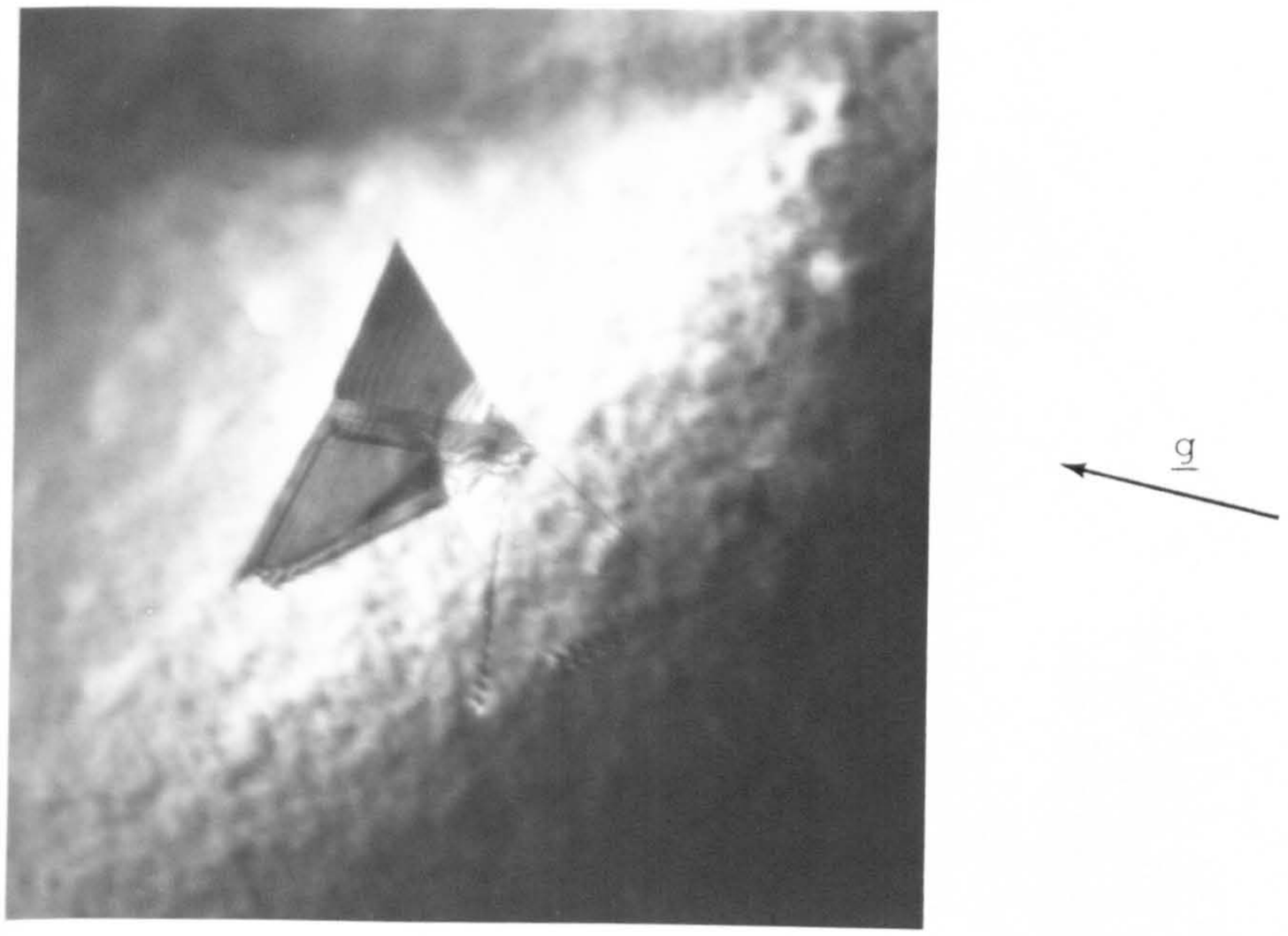

3.6 BF TEM micrograph of a typical stacking fault in KLB116 imaged for g=220.

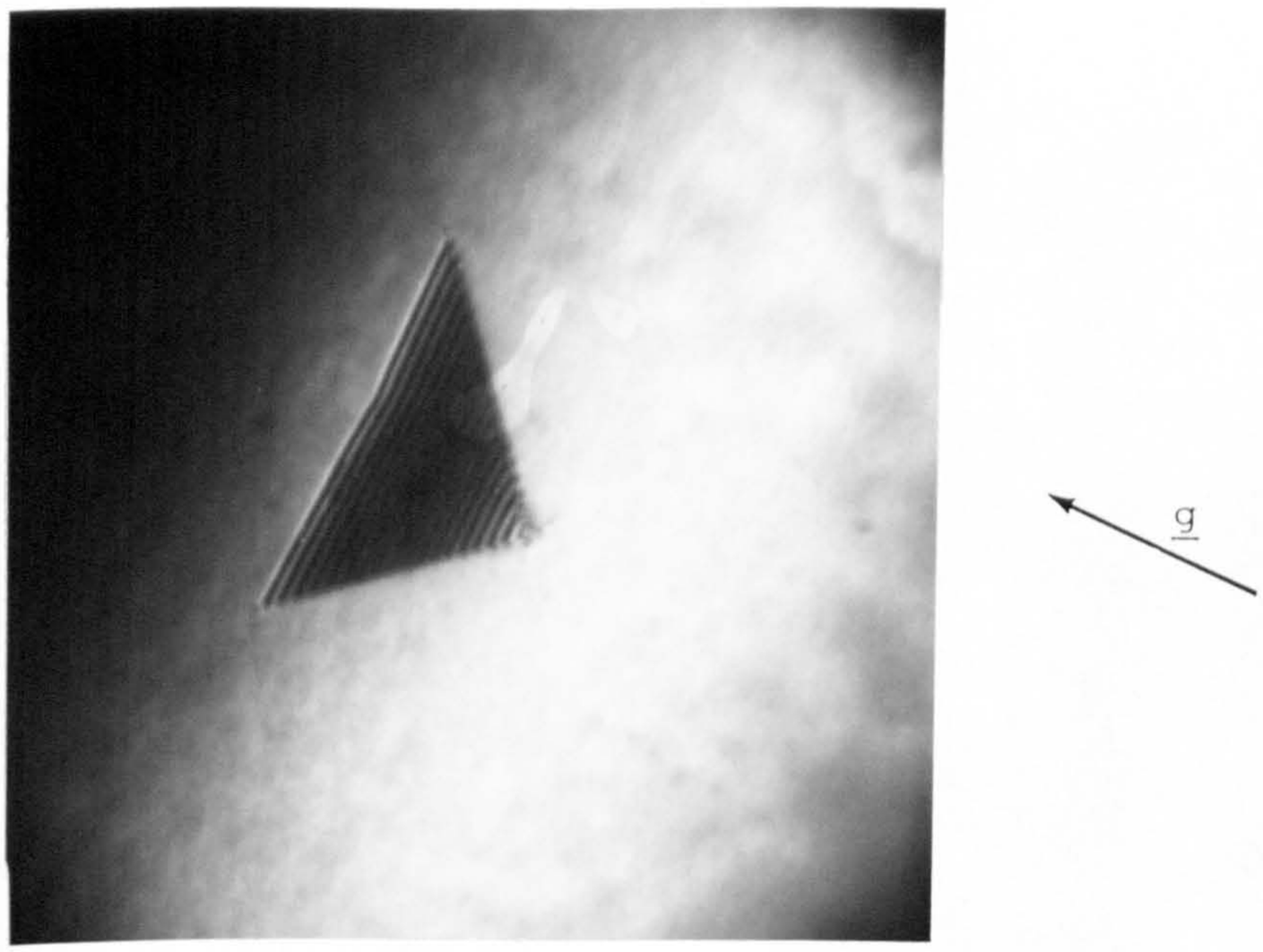

3.7 BF TEM micrograph of a simple stacking fault in KLB116 imaged for g=220.

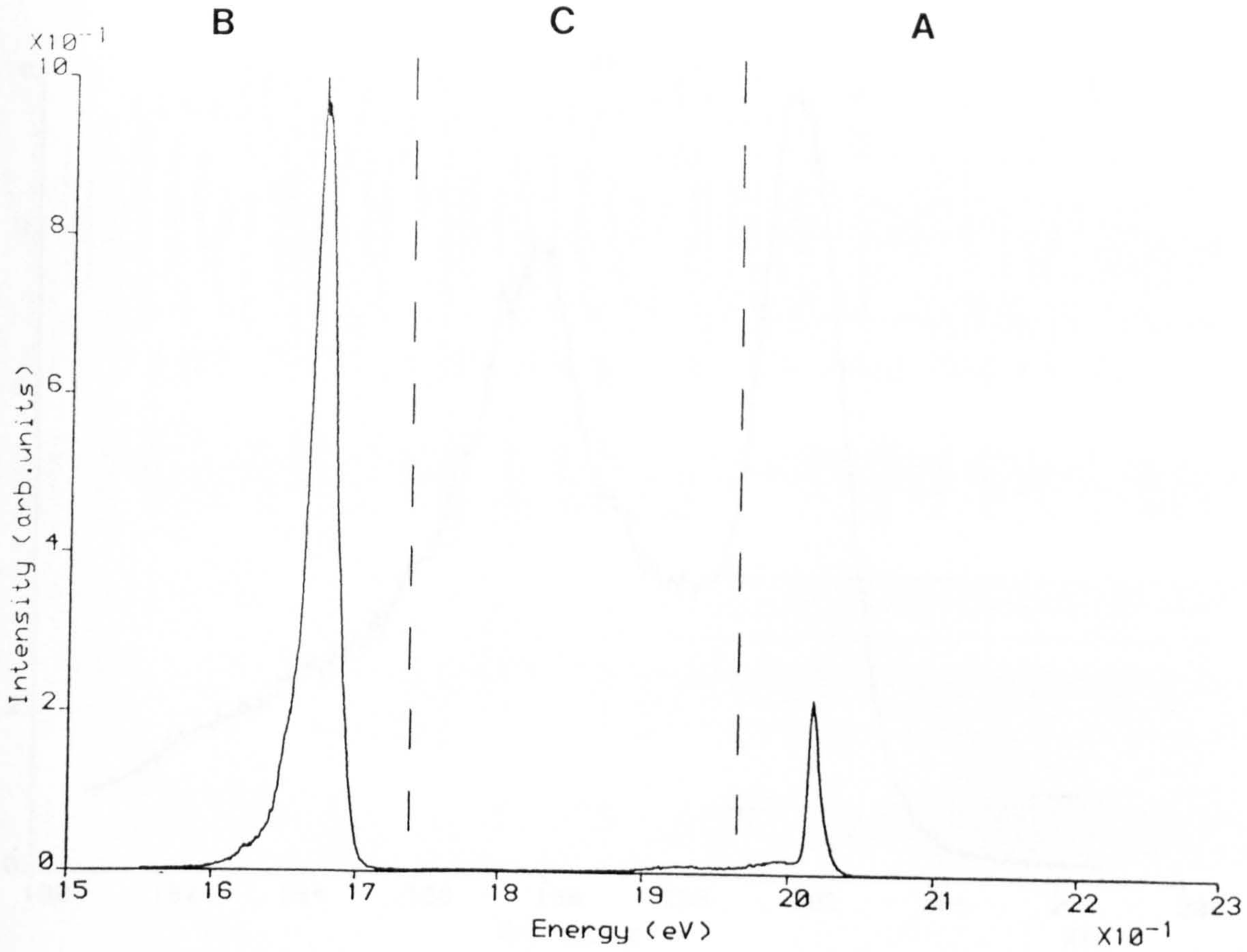

3.8 CL spectrum from unfaulted KLB116 split into three regions.

A) $Al_xGa_{1-x}As$ emission B) QW emission C) intermediate.

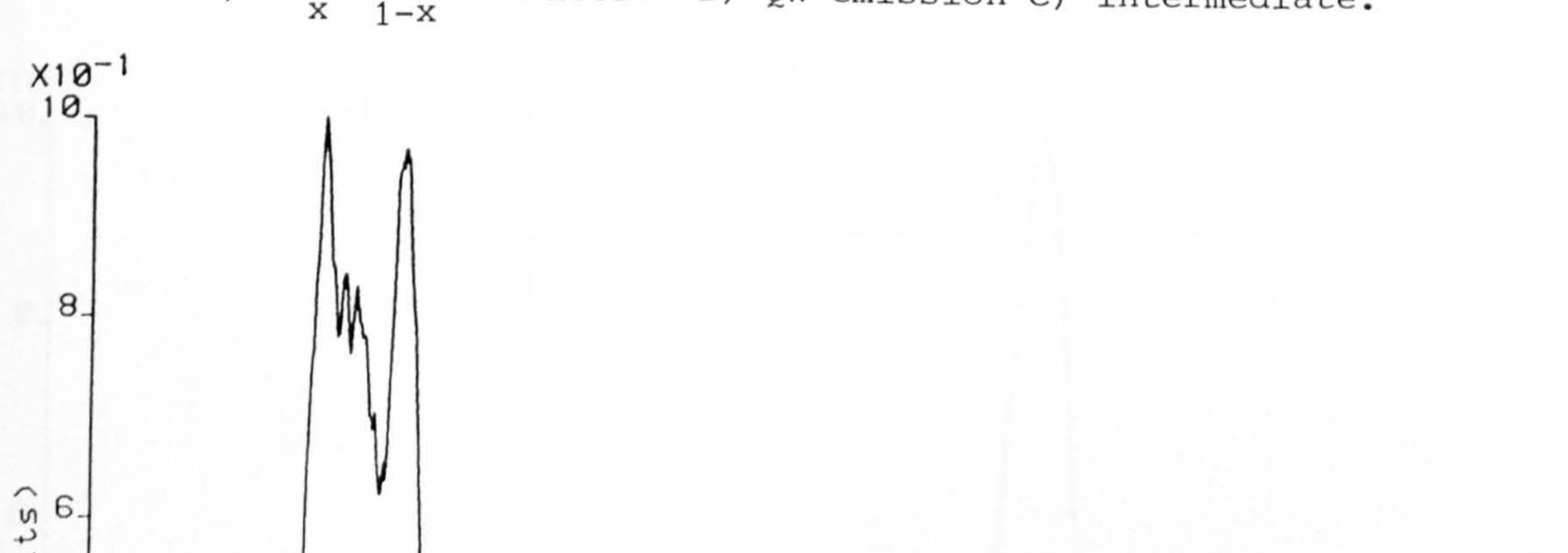

3.9 CL spectrum from a complex stacking fault in KLB116.

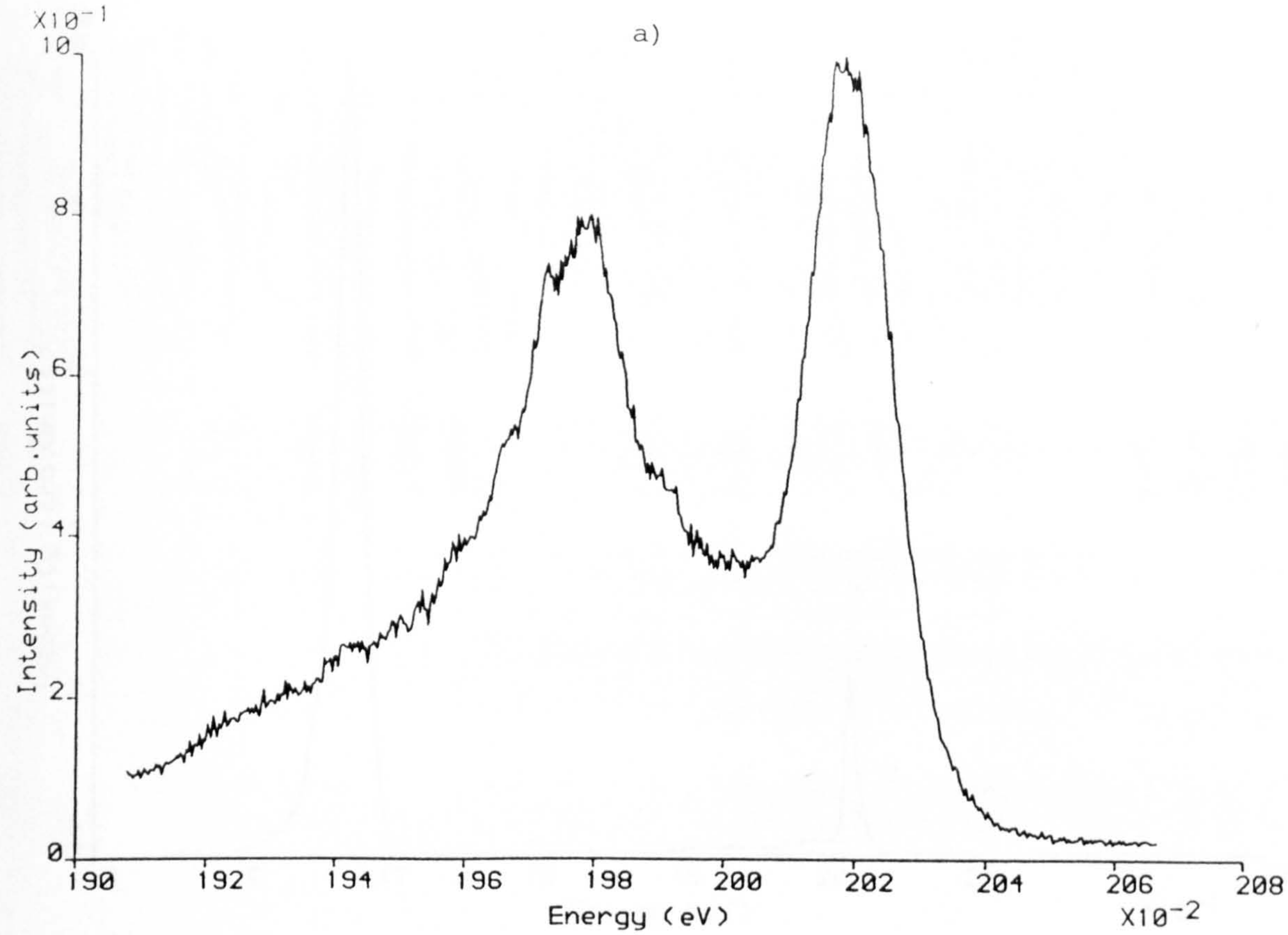

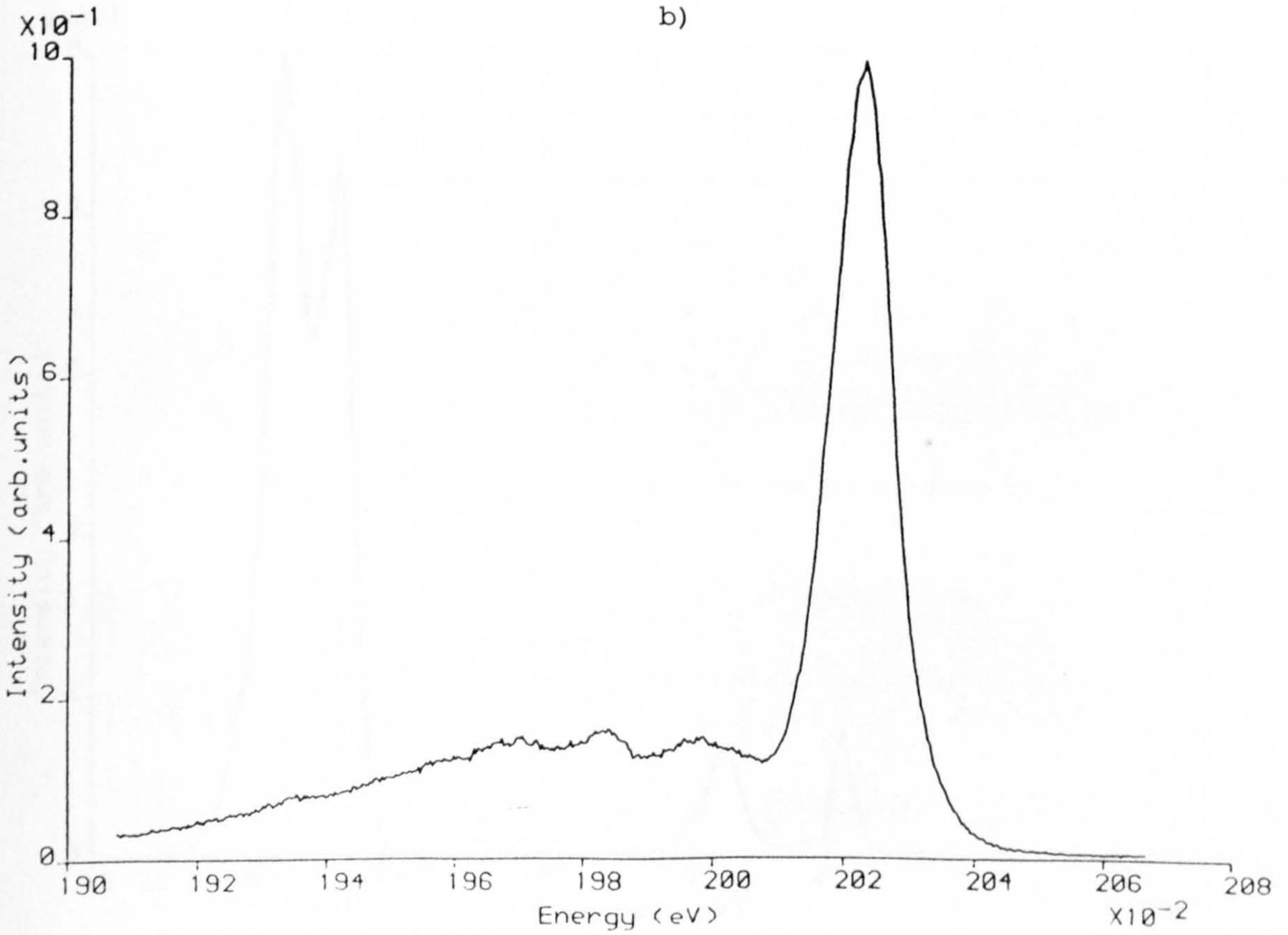

3.10 CL spectrum from a stacking fault (a) as compared to a CL spectrum from unfaulted crystal (b) in KLB116.

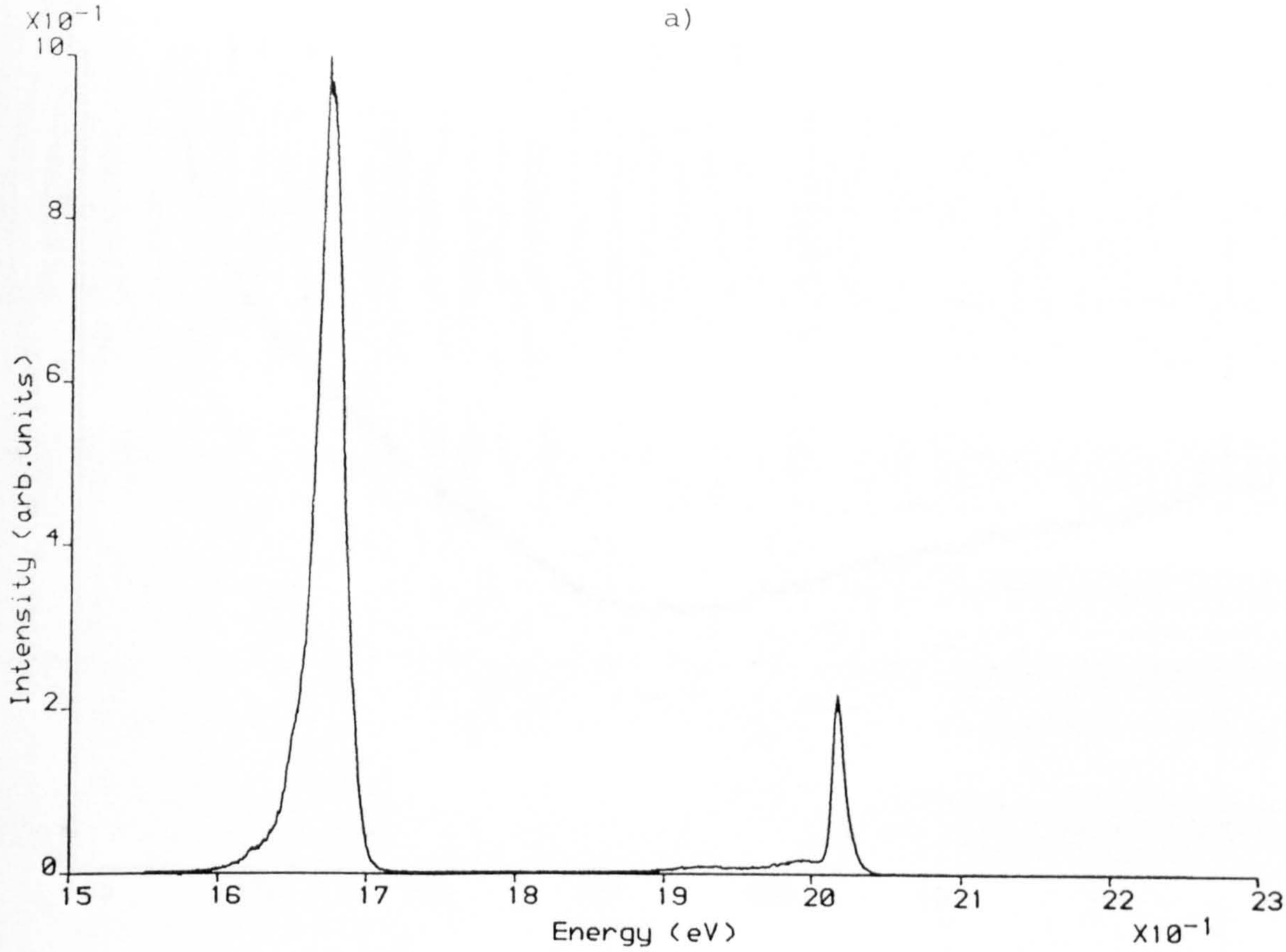

3.11 CL spectrum from unfaulted crystal (a) as compared to a CL spectrum from a simple stacking fault (b) in KLB116.

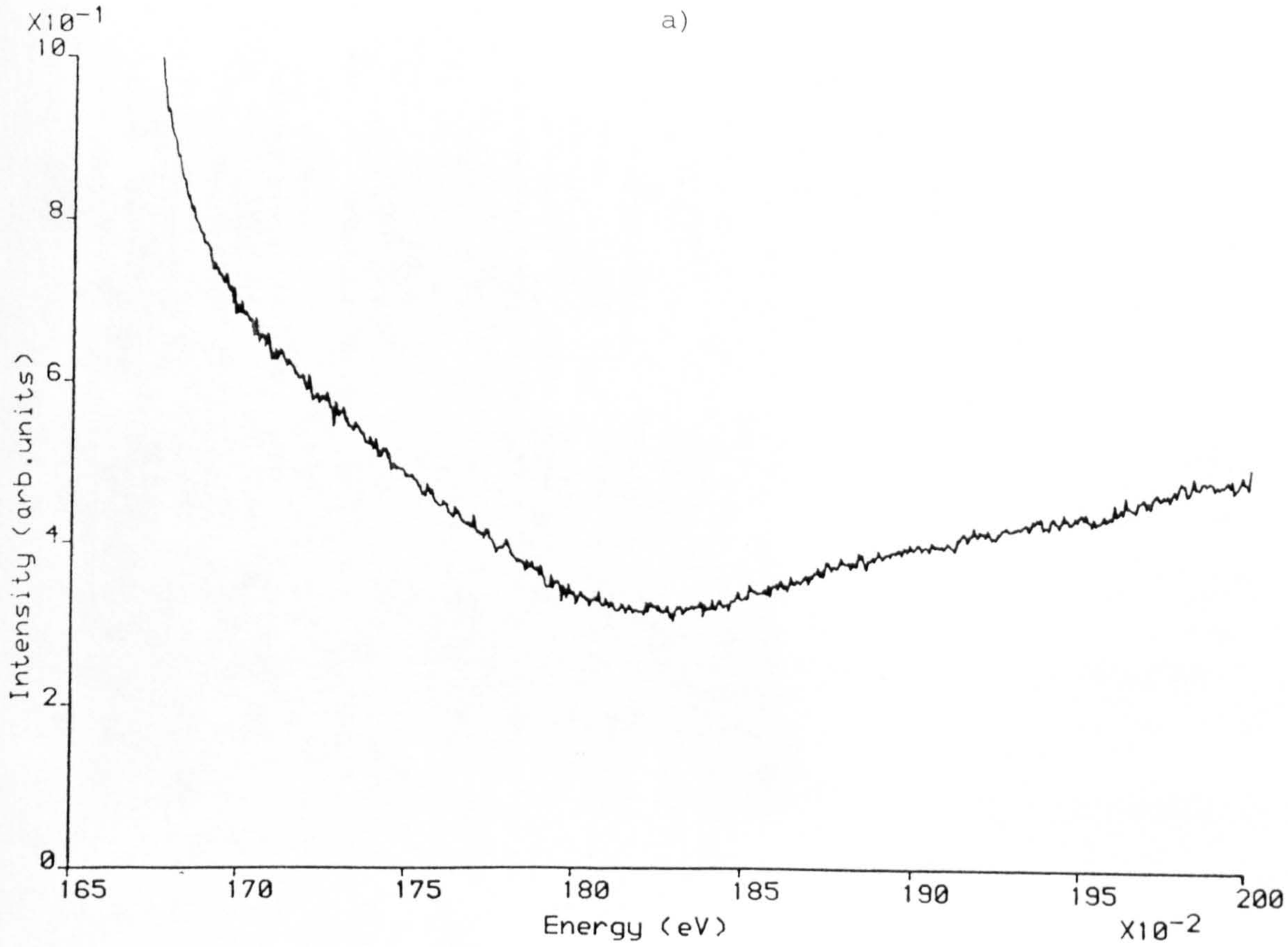

3.12 CL spectra from a region adjacent to a stacking fault (a) and from a stacking fault (b) in KLB116.

a)

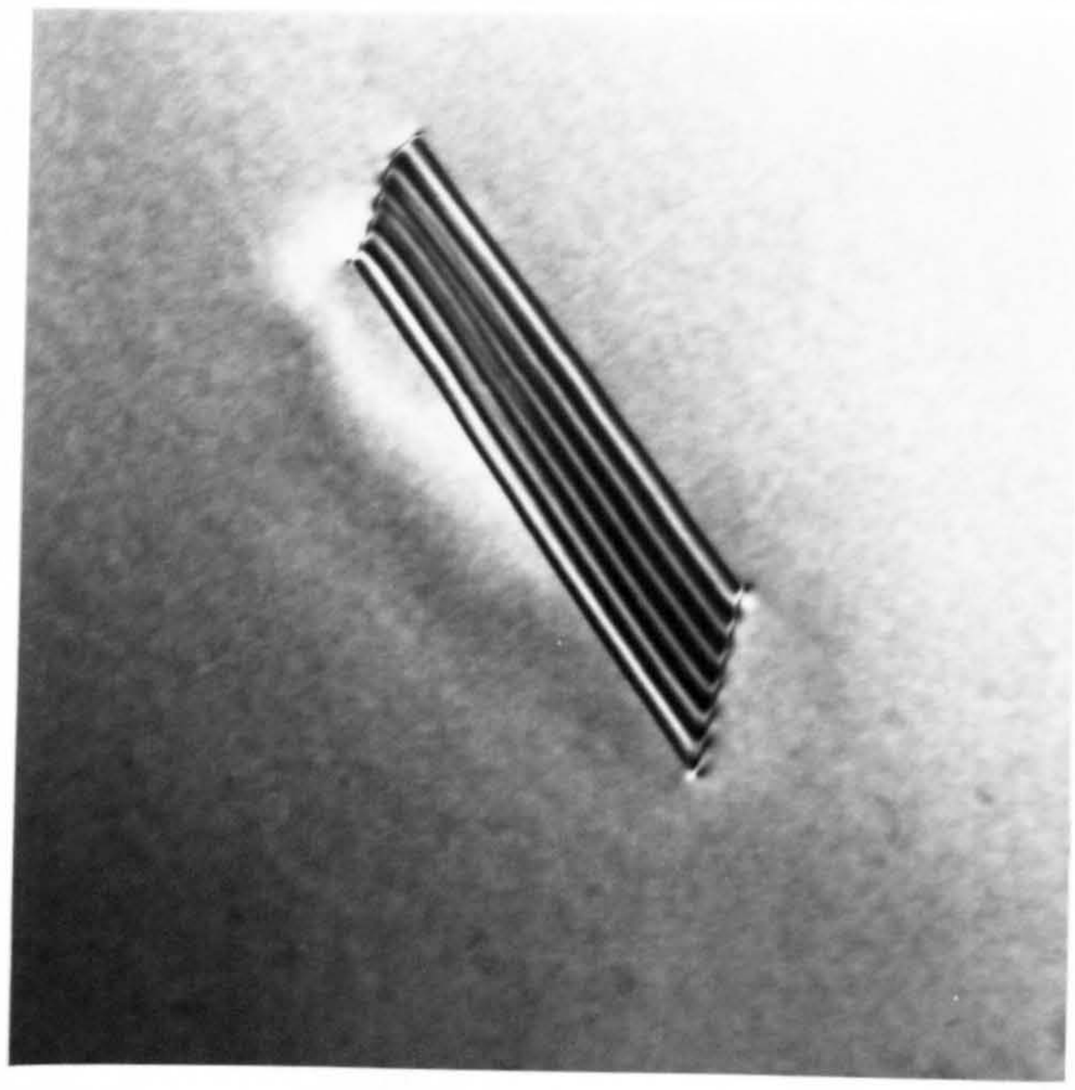

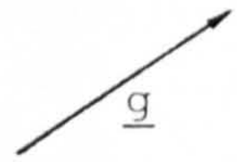

1 µm

b)

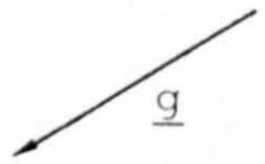

3.13 TEM micrographs of an intrinsic stacking fault in KLB116
a) BF, $\underline{g}$=220 b) DF, $\underline{g}=\bar{2}\bar{2}0$.

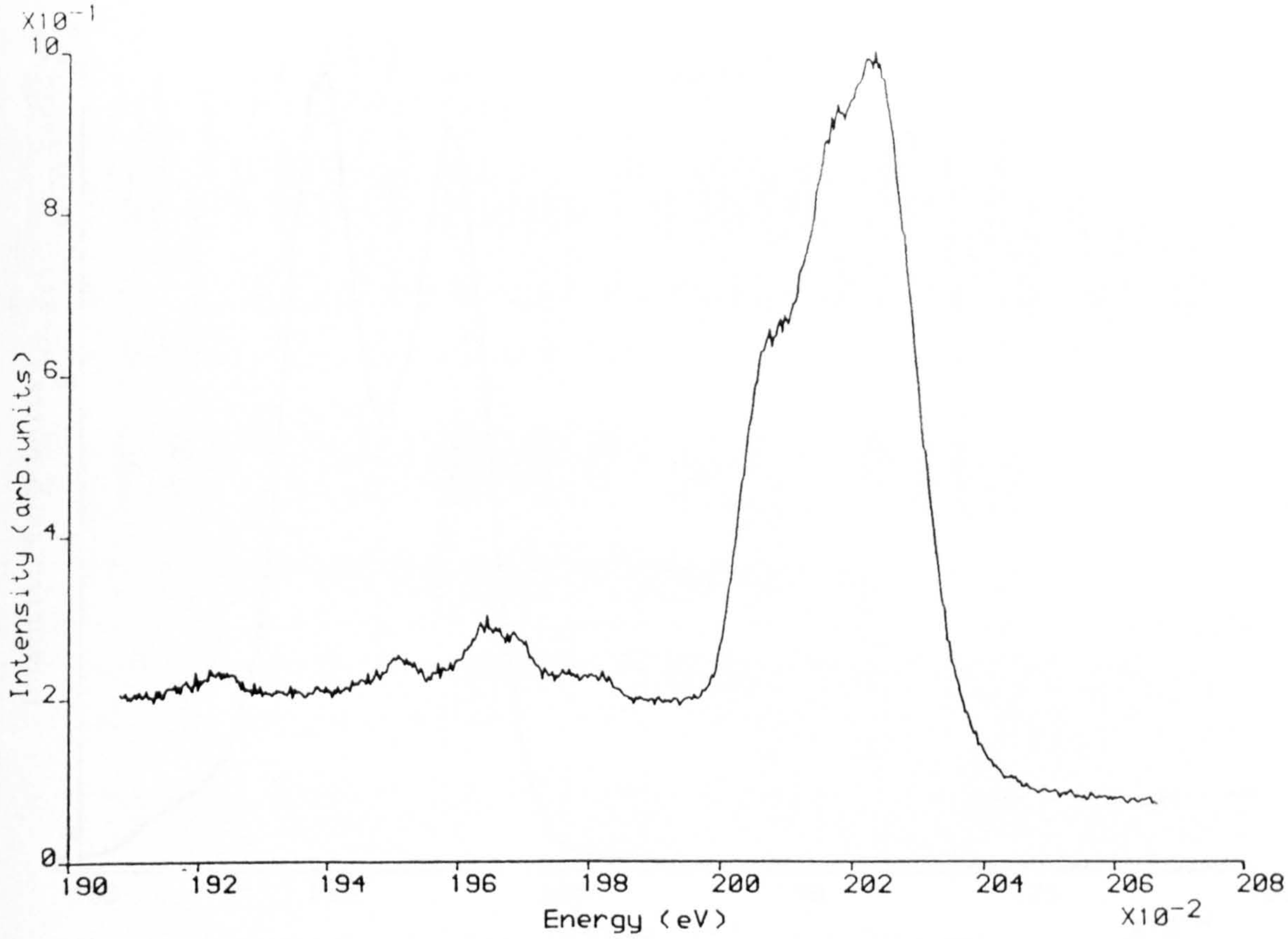

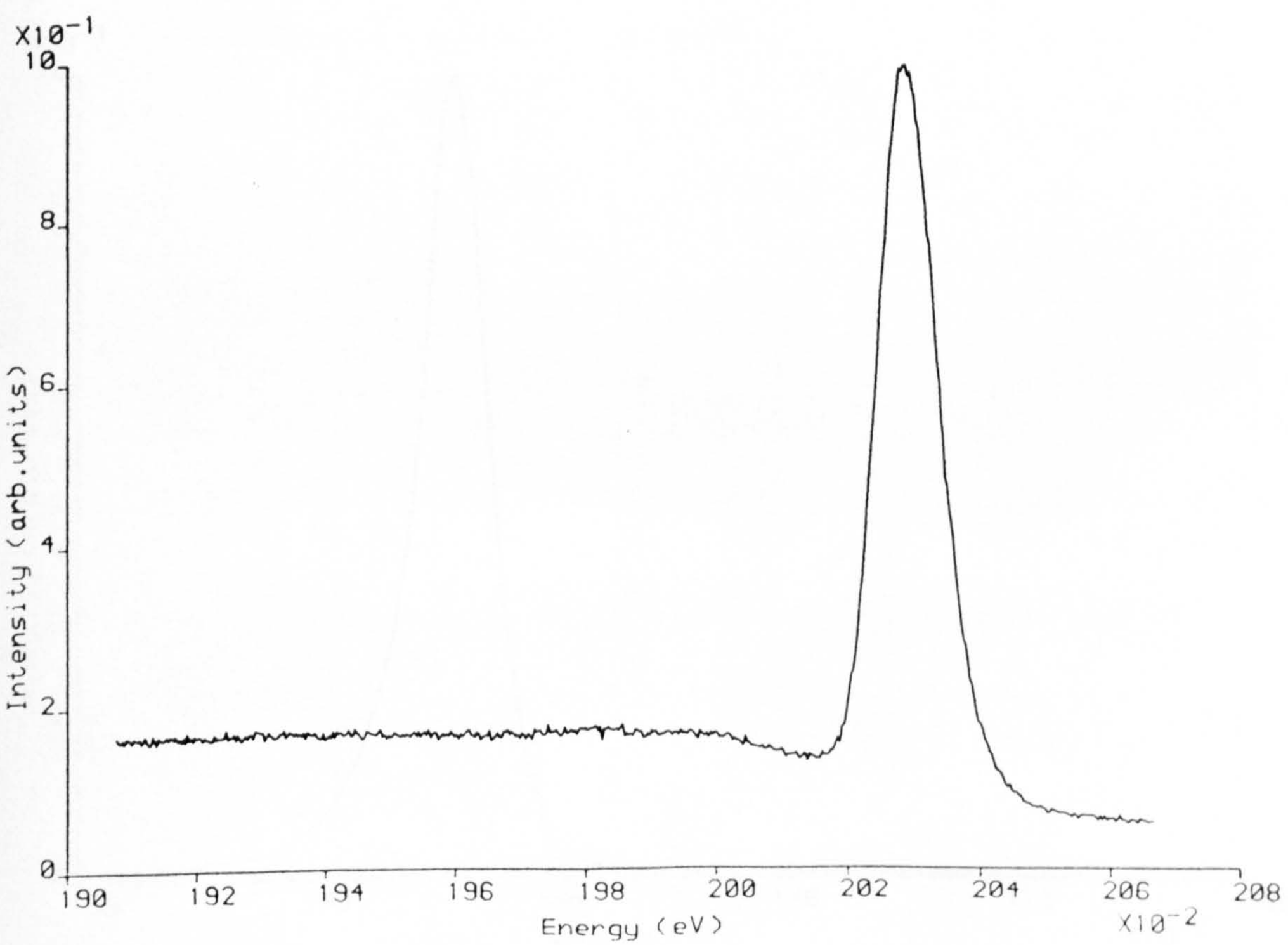

3.14 a) $Al_xGa_{1-x}As$ emission from a stacking fault (top) as compared to unfaulted crystal (bottom) in KLB116.

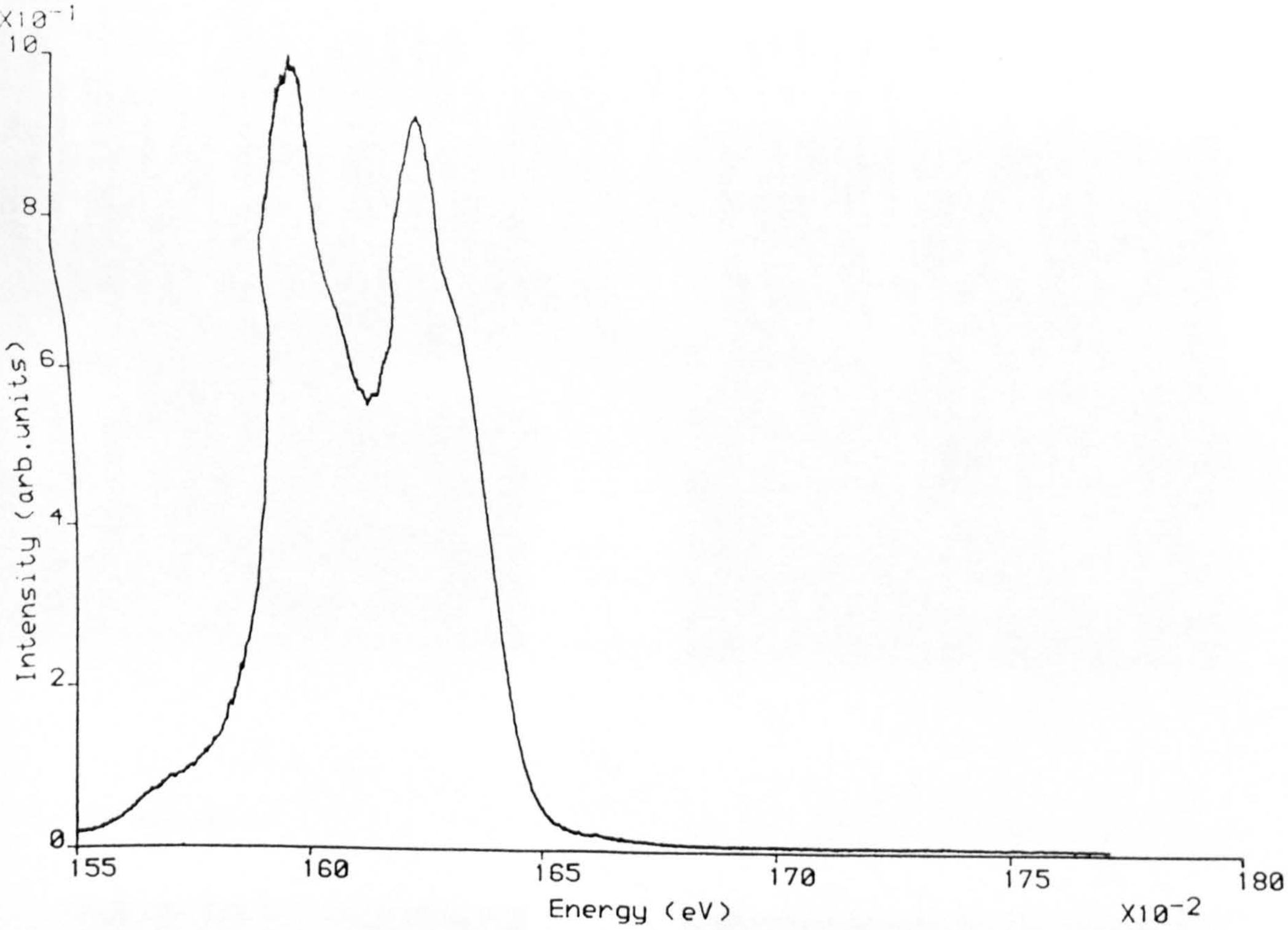

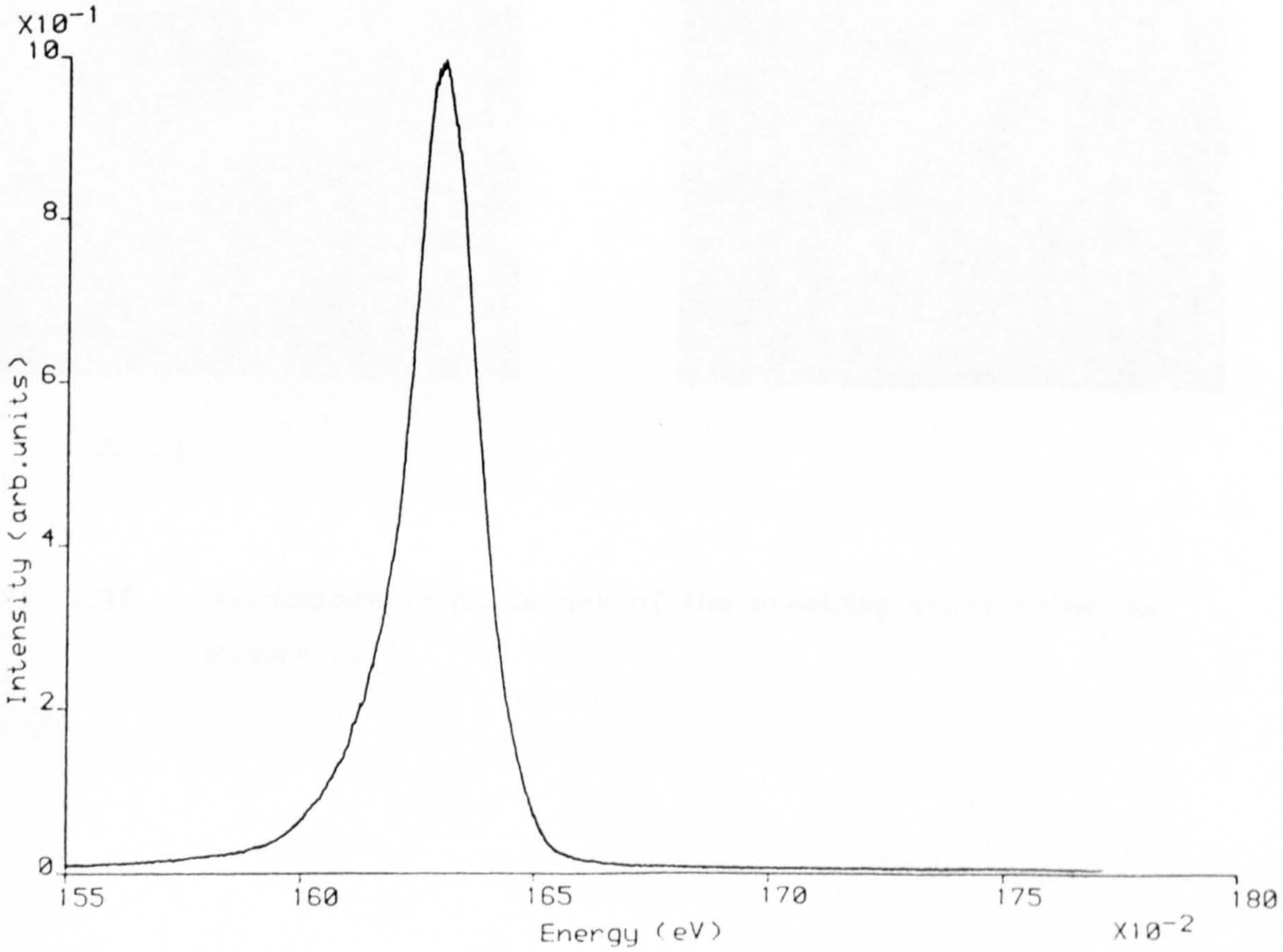

3.14 b) QW emission from a stacking fault (top) as compared to unfaulted crystal (bottom) in KLB116.

a) $A\ell_x Ga_{1-x}As$ BE emission

b) $A\ell_x Ga_{1-x}As$ FB emission

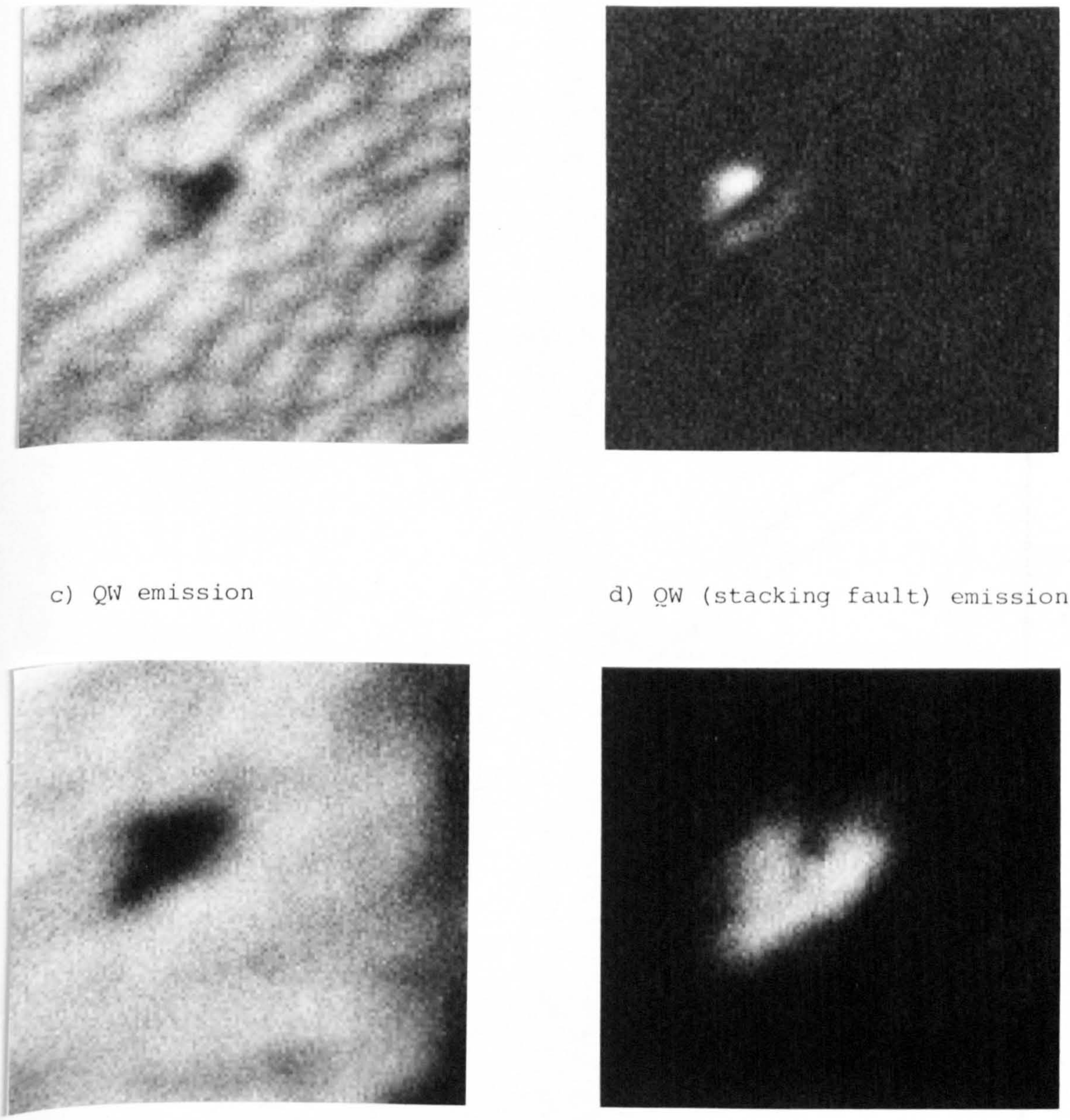

c) QW emission

d) QW (stacking fault) emission

2 μm

3.15 Monochromatic CL images of the stacking fault shown in Figure 3.13.

3.16 Graphs of emission energy against temperature for the normal QW and the stacking fault related luminescence in KLB116. To facilitate comparisons of the two graphs the emission energies have been plotted relative to arbitrary origins.

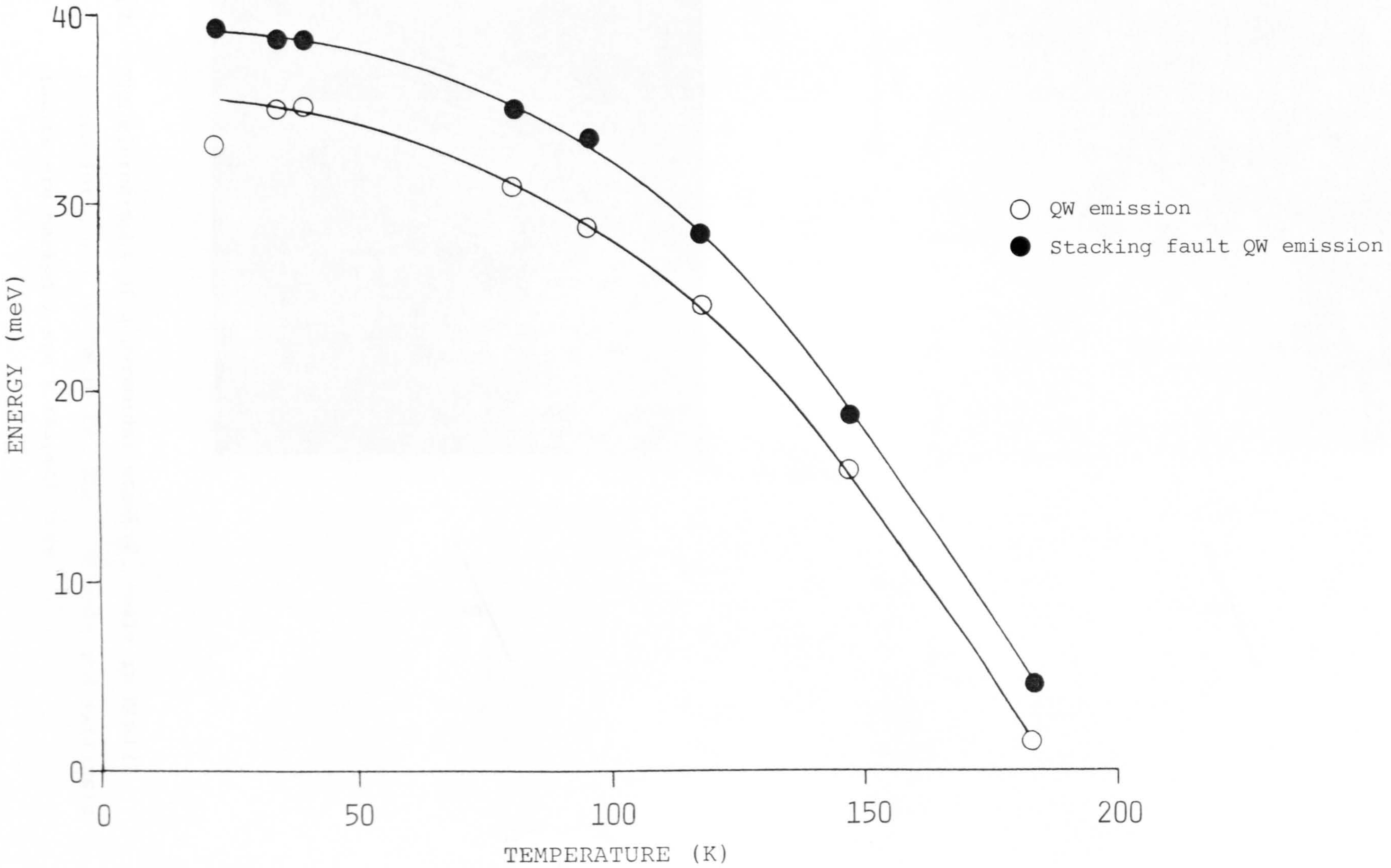

a)

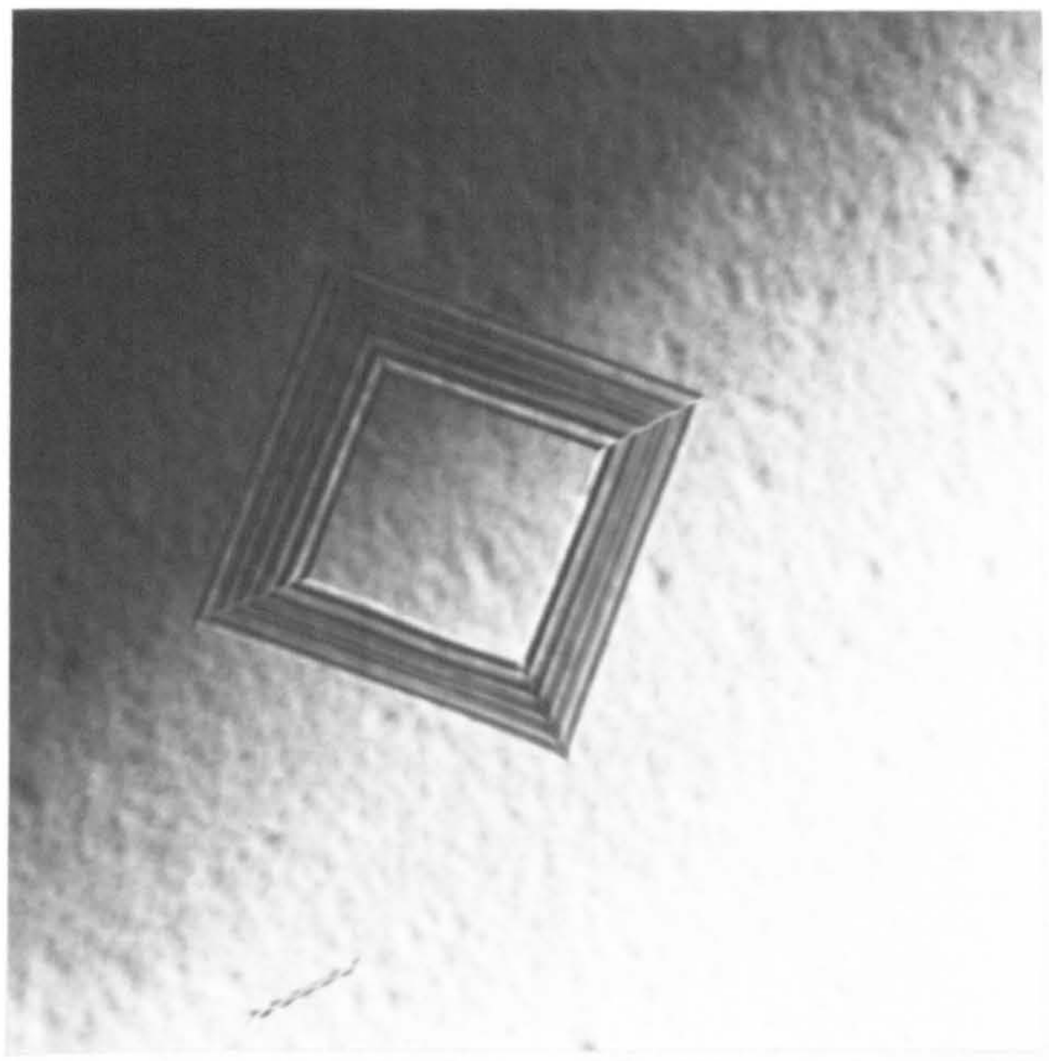

b)

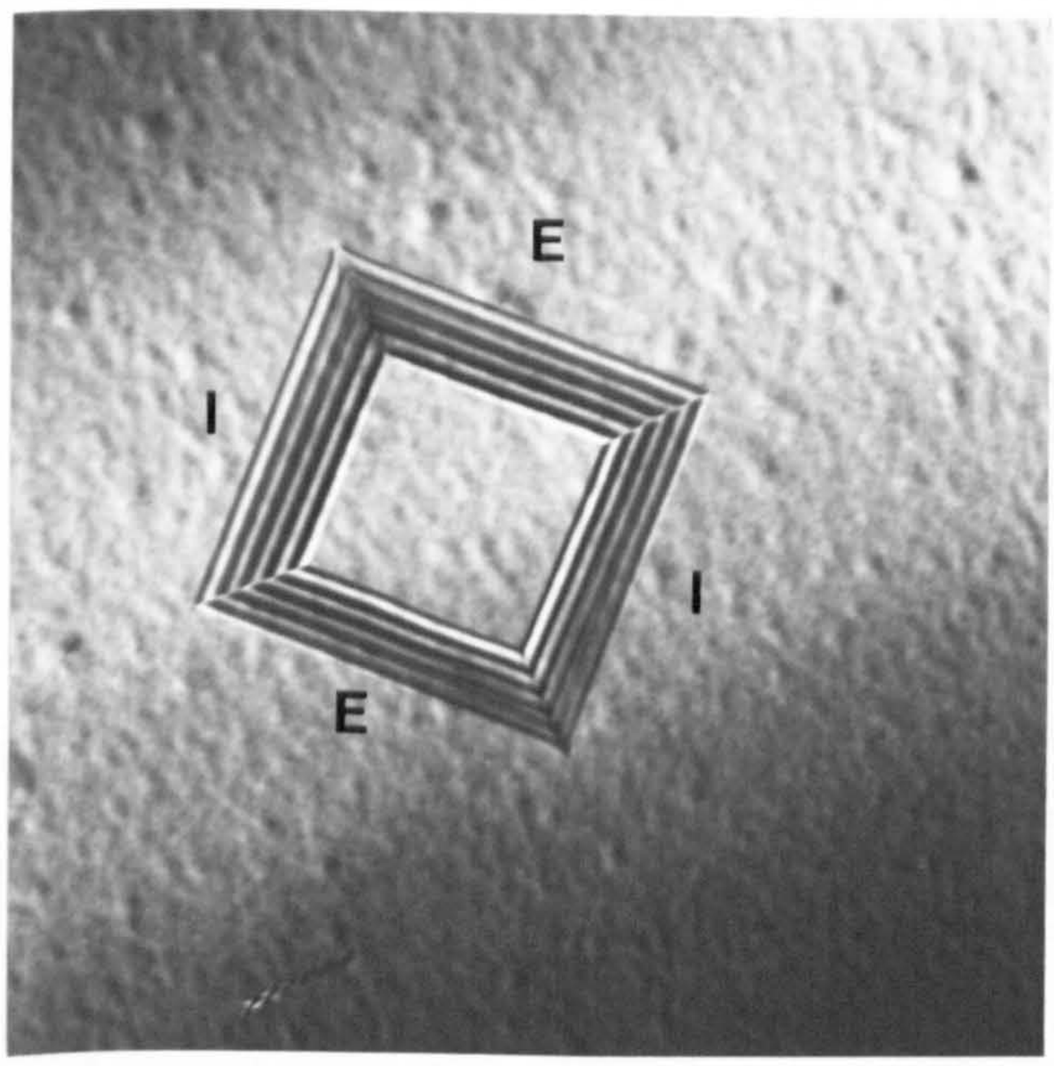

3.17 TEM micrographs of a pyramidal stacking fault in KLB121 imaged for g=400. a) BF b) DF. The intrinsic and extrinsic faults are marked I and E respectively.

a)

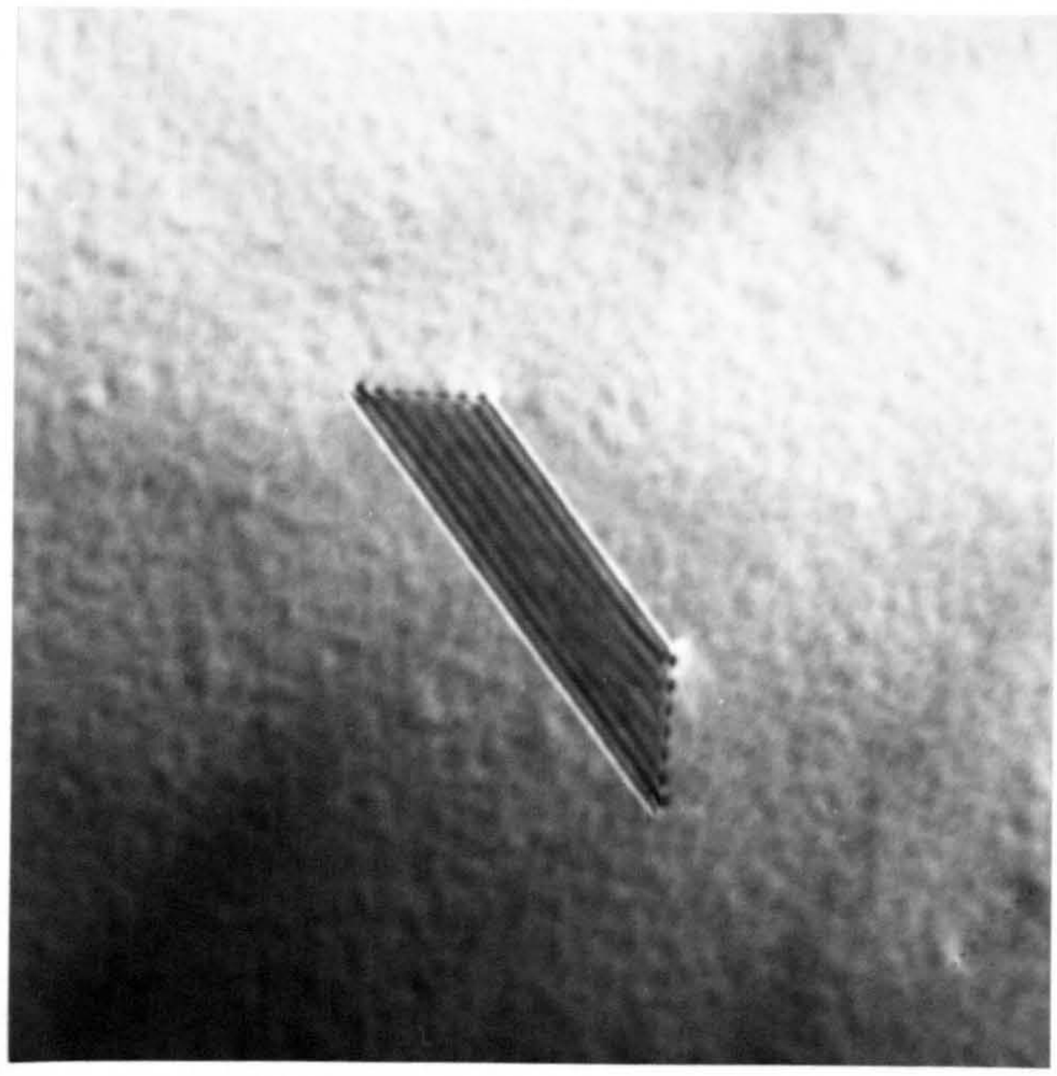

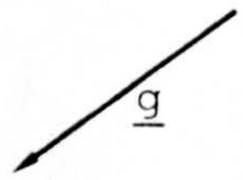

1 μm

b)

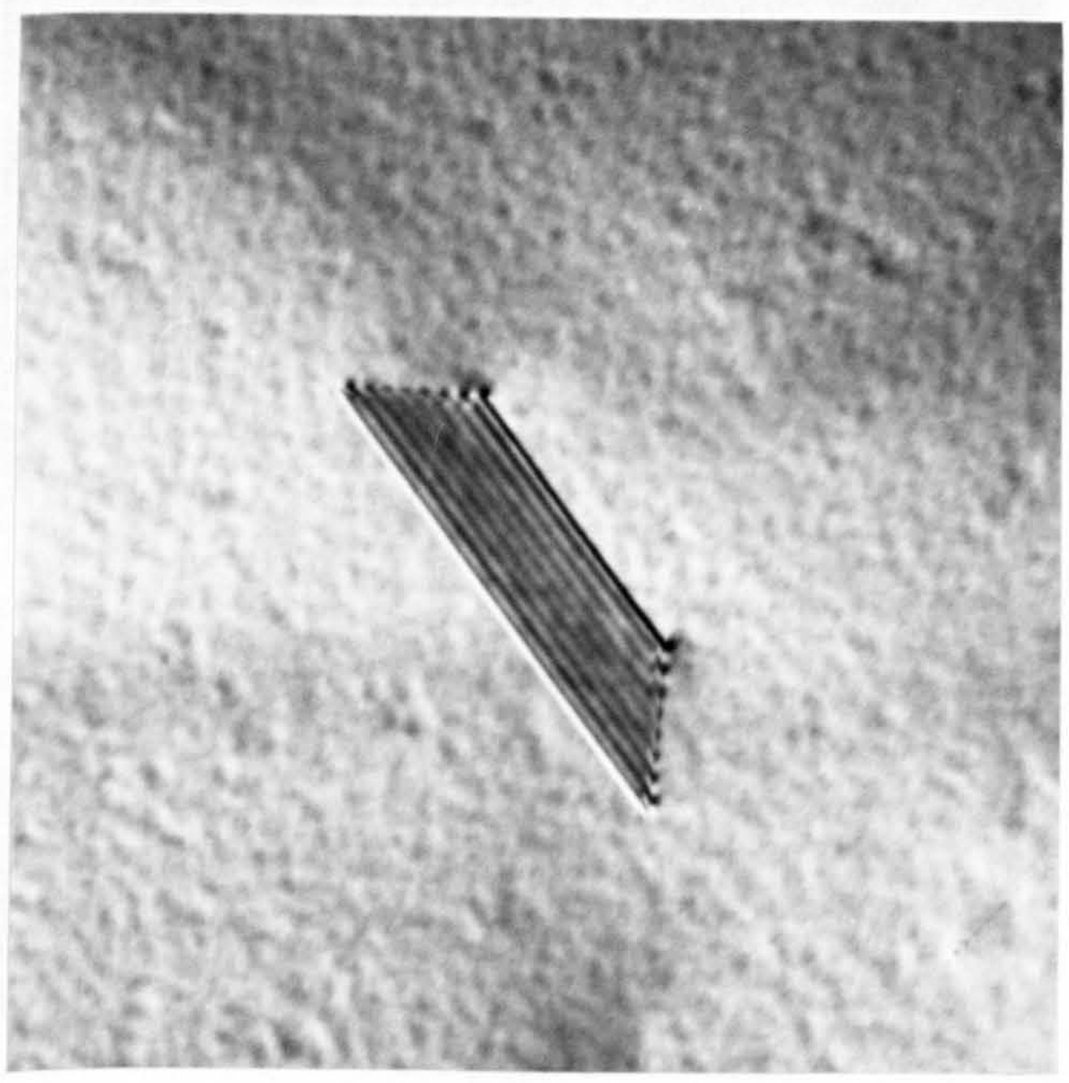

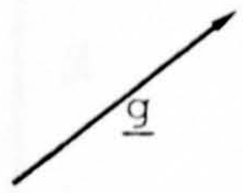

3.18 TEM micrographs of an intrinsic stacking fault in KLB121
a) BF, $\underline{g}$=220 b) DF, g=$\bar{2}\bar{2}0$.

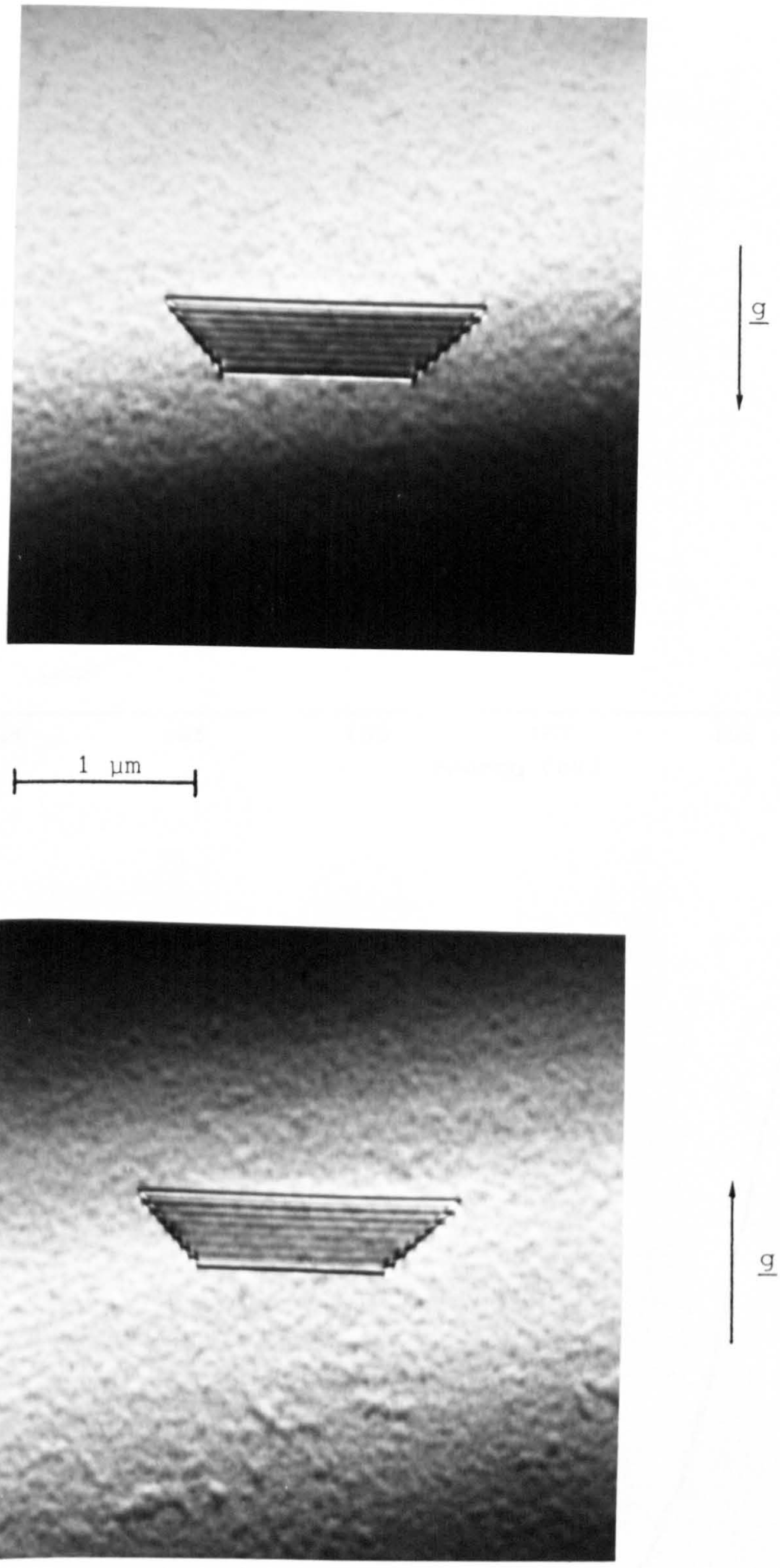

3.19 TEM micrographs of a folded back stacking fault in in KLB121. The extrinsic fault is uppermost.
a) BF, $\underline{g}$=220 b) DF, g=$\bar{2}\bar{2}0$.

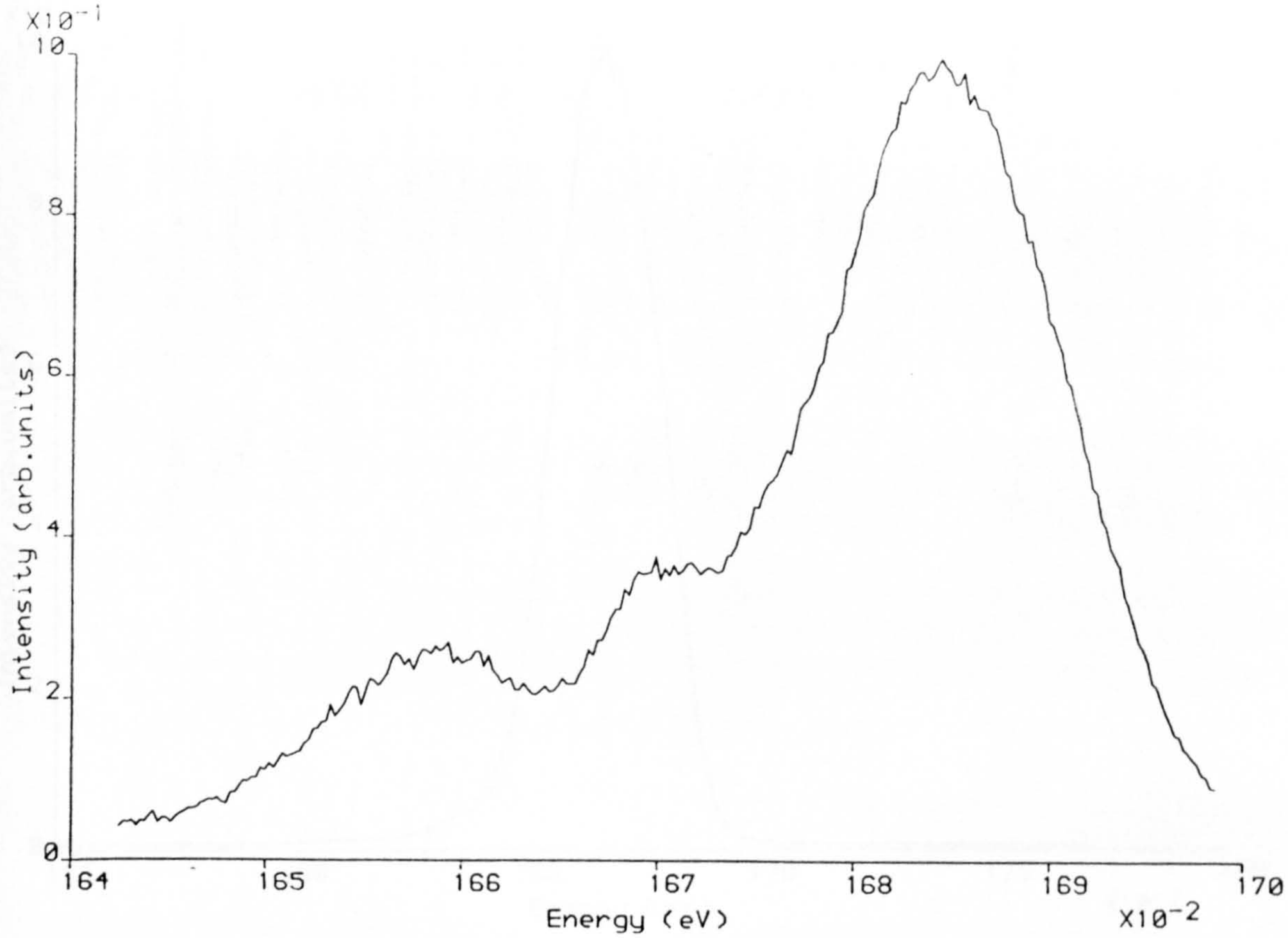

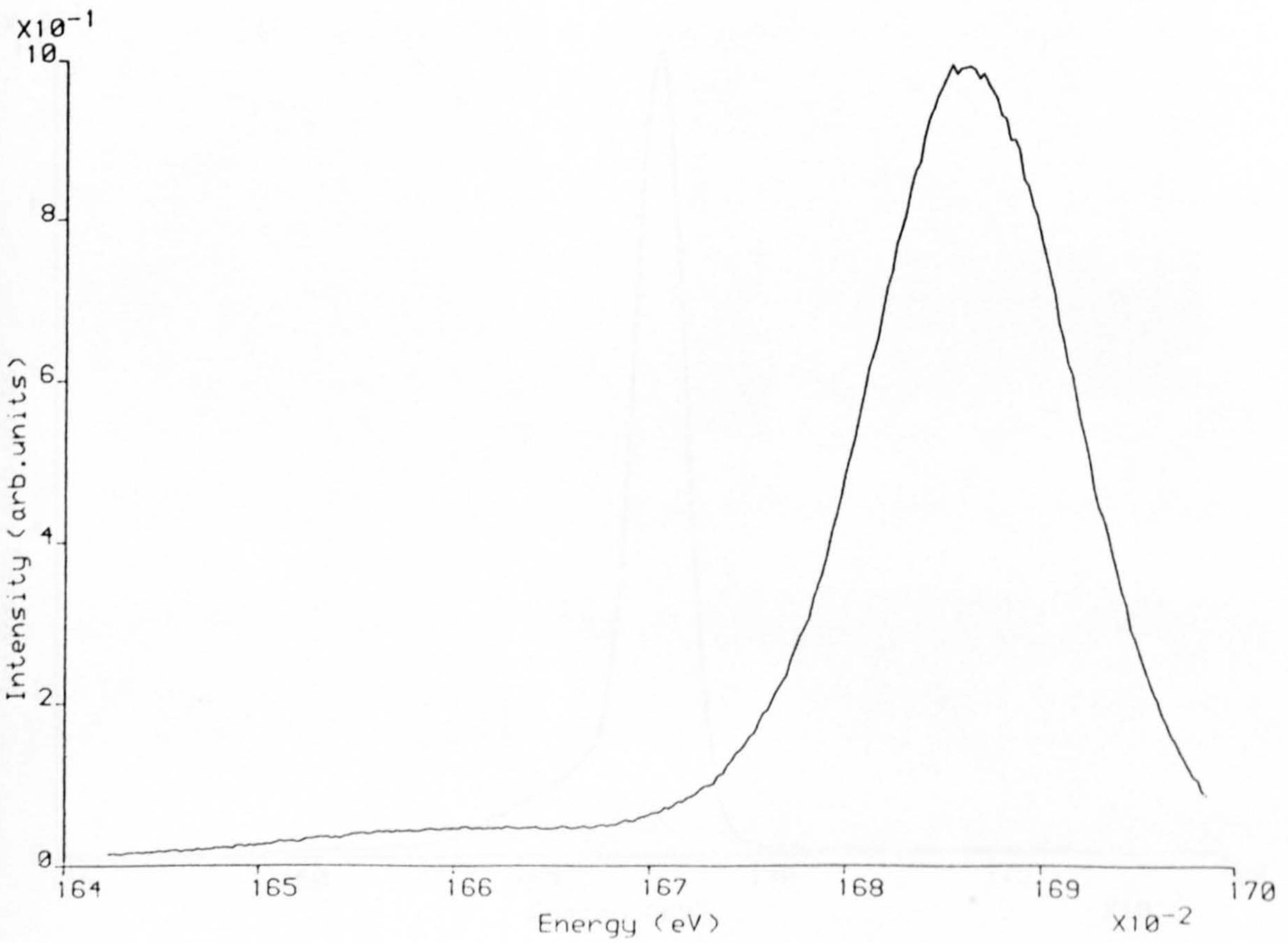

3.20 CL spectra from KLB121 showing the QW emission from a stacking fault (top) and adjacent crystal (bottom).

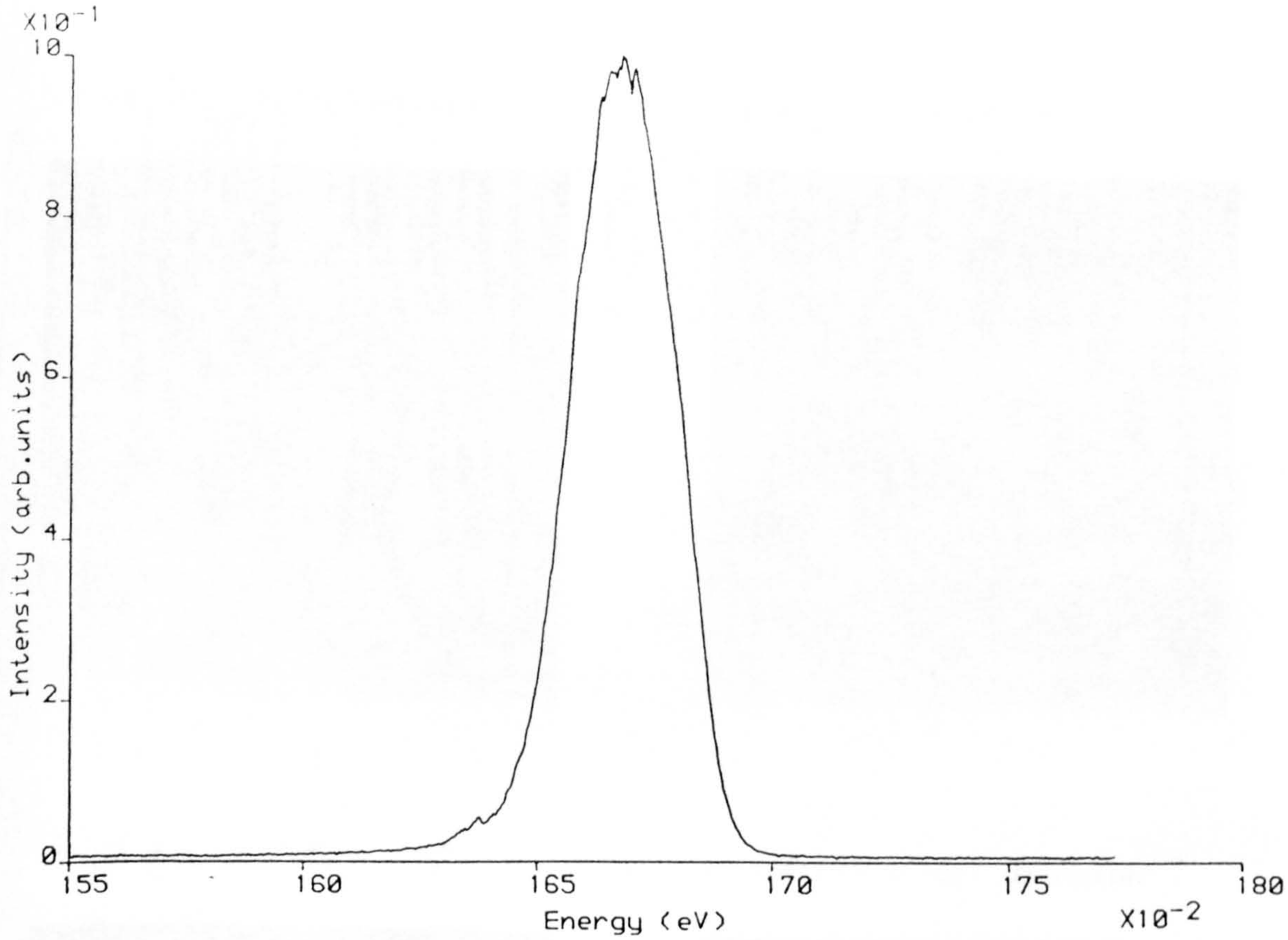

3.21 CL spectra from KLB121 showing the QW emission from a stacking fault (top) as compared to adjacent crystal (bottom).

a) $Al_xGa_{1-x}As$ BE emission

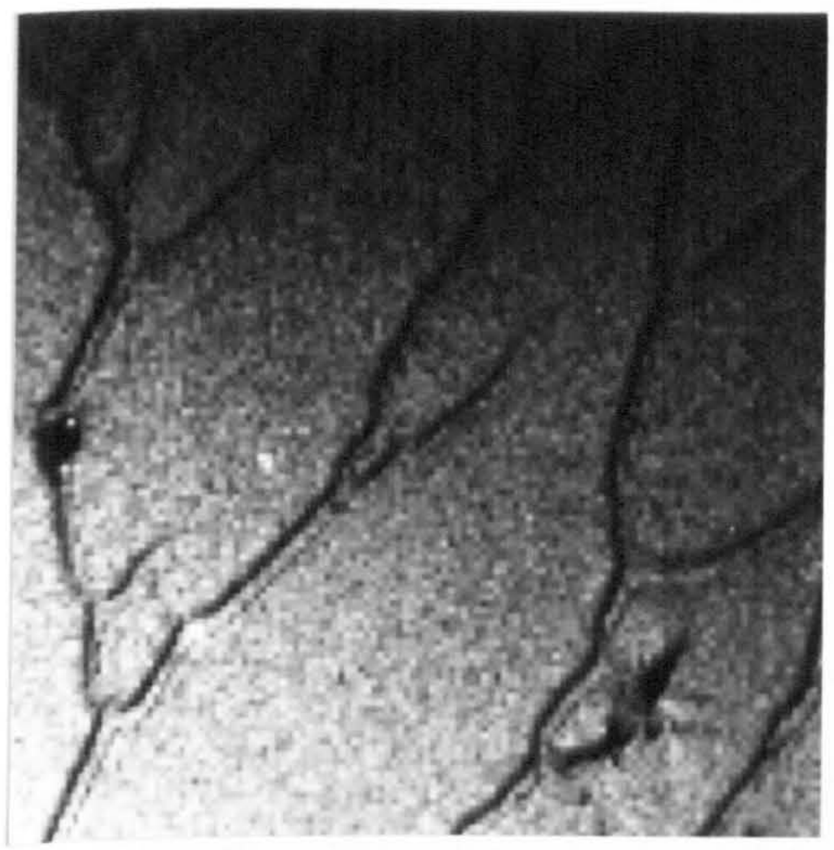

b) $Al_xGa_{1-x}As$ FE emission

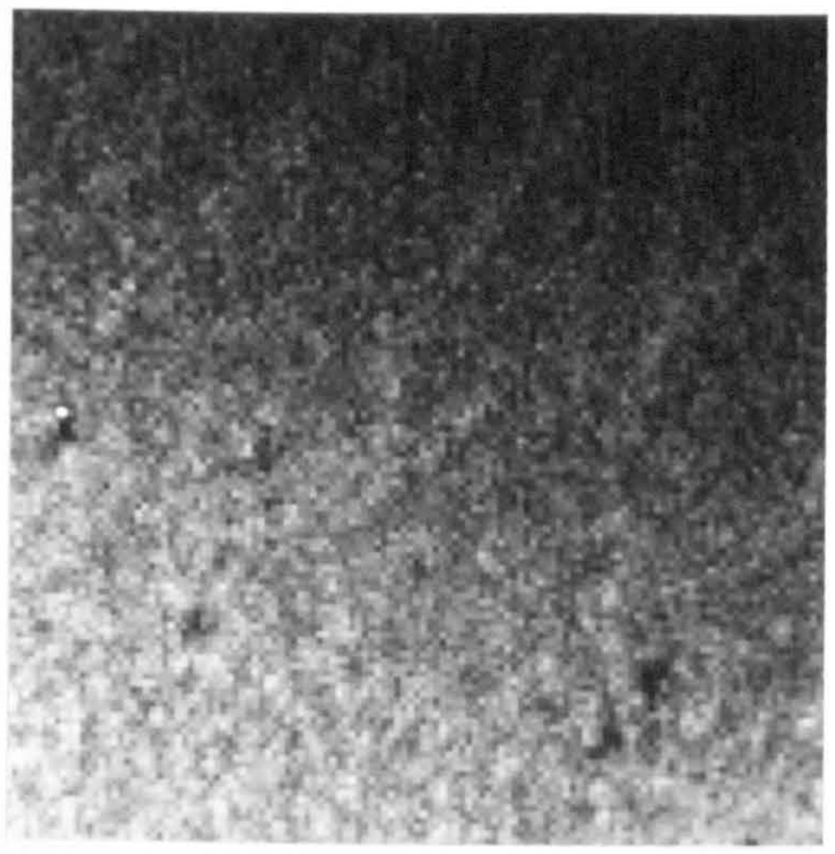

c) QW emission

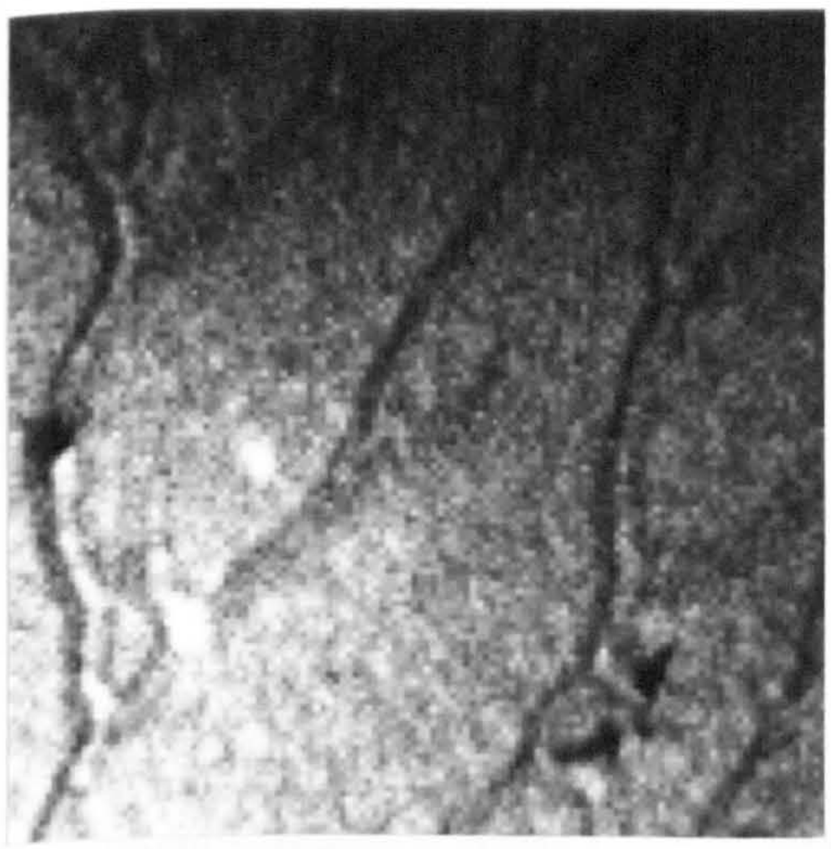

d) QW (impurity) emission

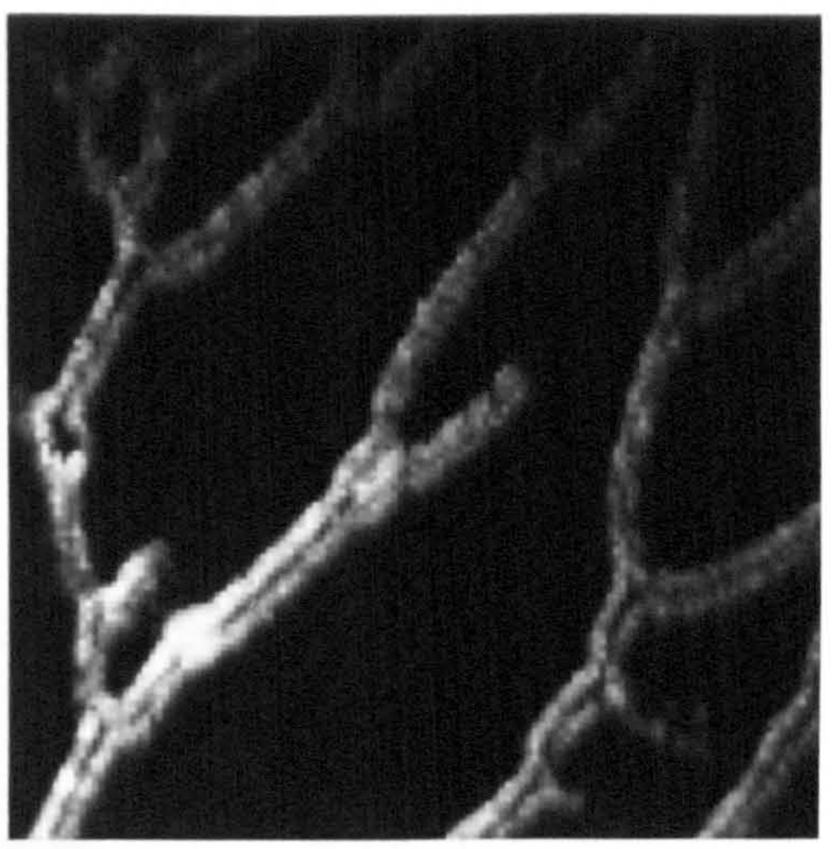

20 μm

3.22 Monochromatic CL images showing cellular structure.

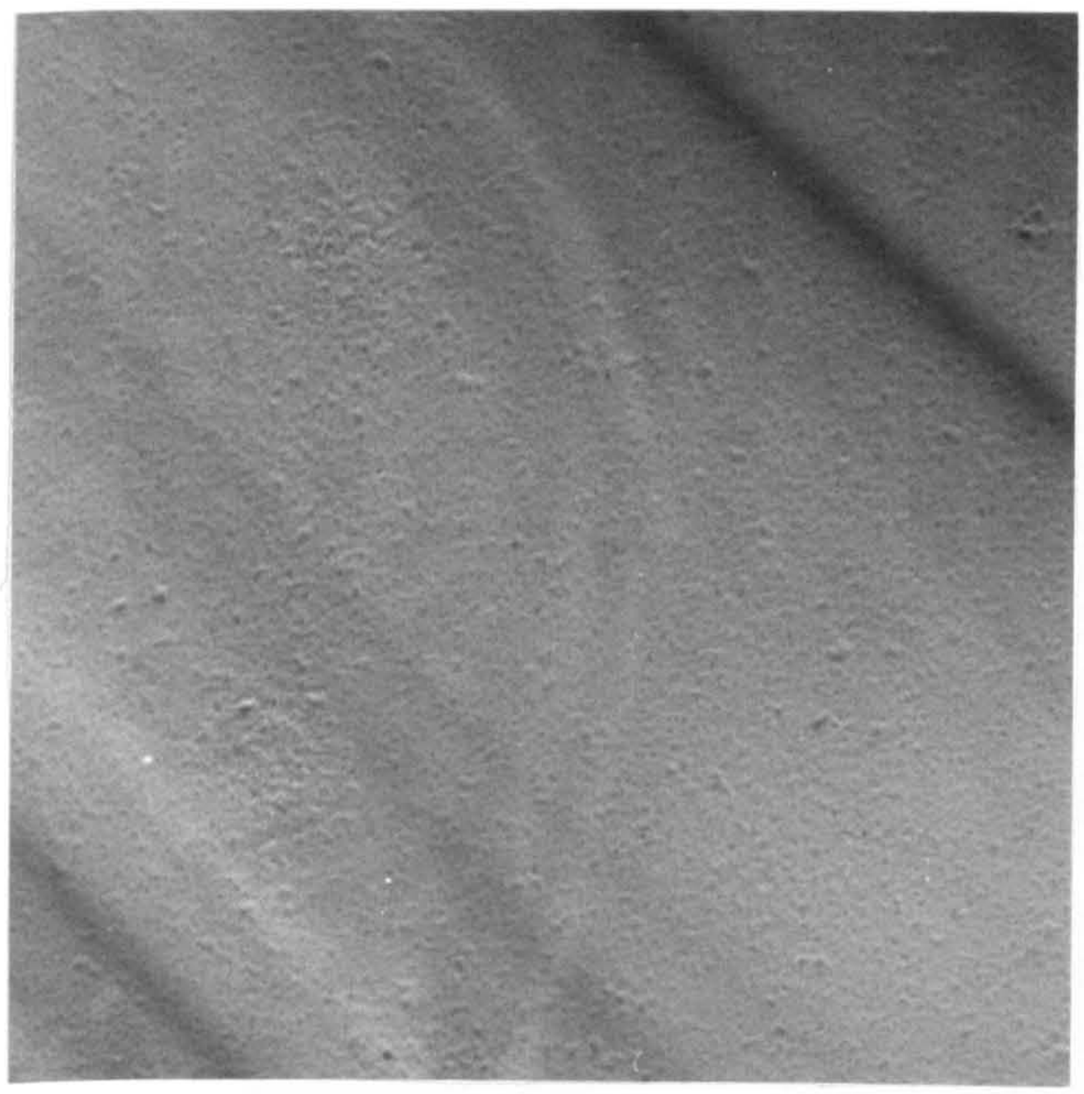

3.23 BF TEM micrograph showing faint contrast due to cellular structure.

3.24 BF TEM micrograph showing showing part of the cellular structure passing through the centre of a stacking fault.

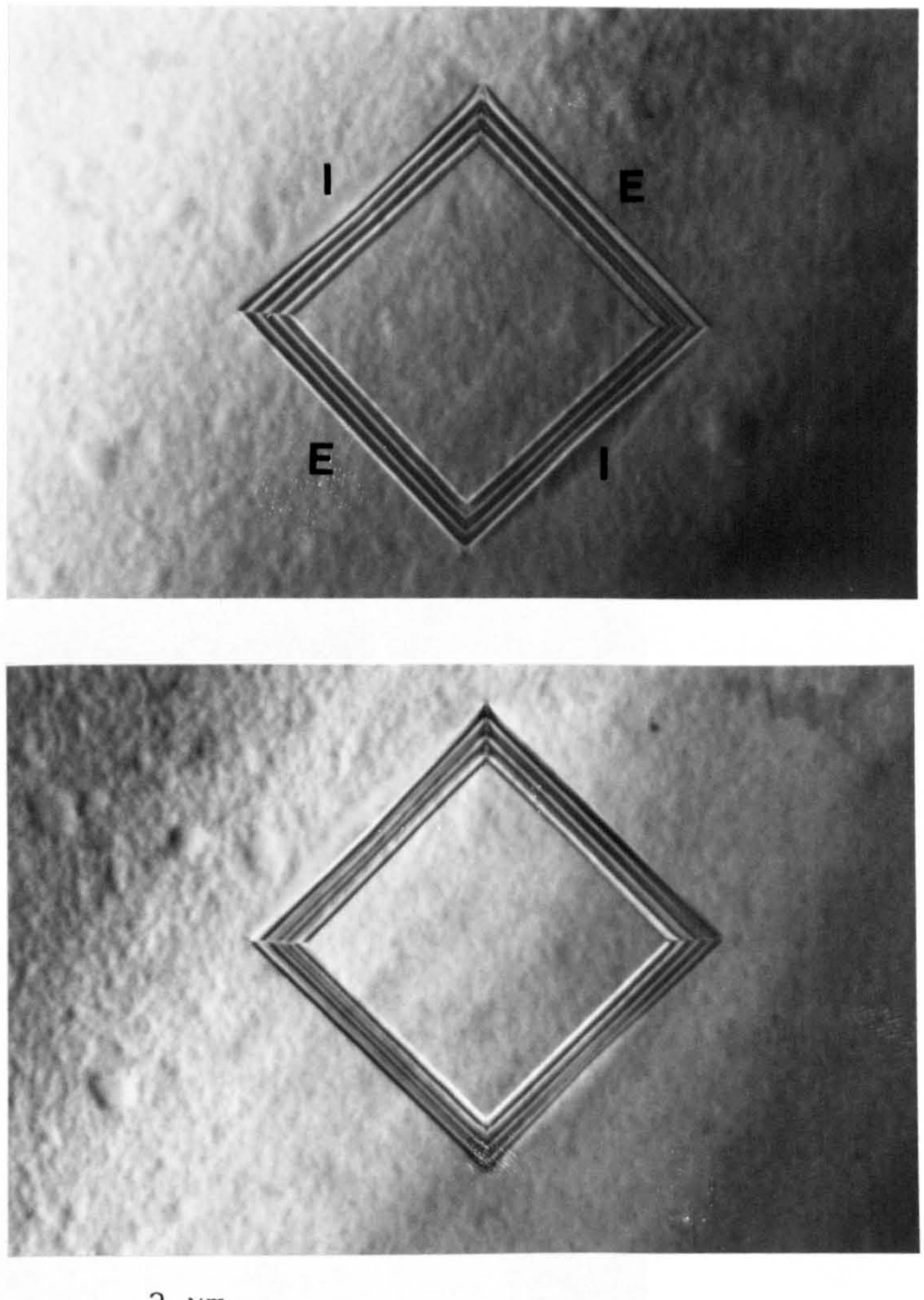

3.25 TEM micrographs of a pyramidal stacking fault in @1965. a) BF, $\underline{g}$=040 b) DF, $\underline{g}$=0$\bar{4}$0. The intrinsic and extrinsic faults are labelled I and E respectively.

3.26 BF TEM micrograph of a pyramidal stacking fault in @1965, imaged with $\underline{g}$=2$\bar{2}$0, showing weak contrast from the intrinsic faults.

a)

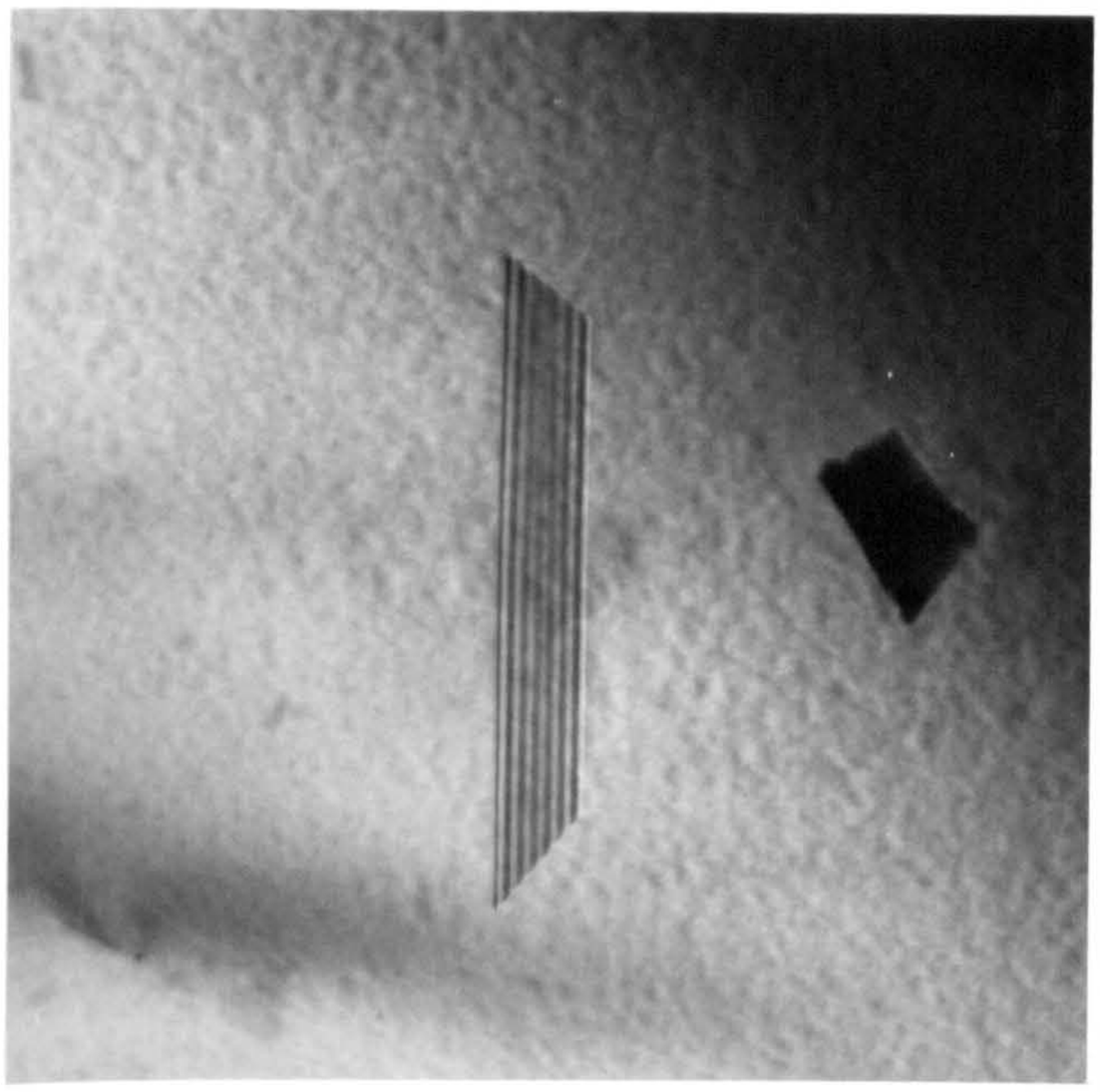

g

2 μm

b)

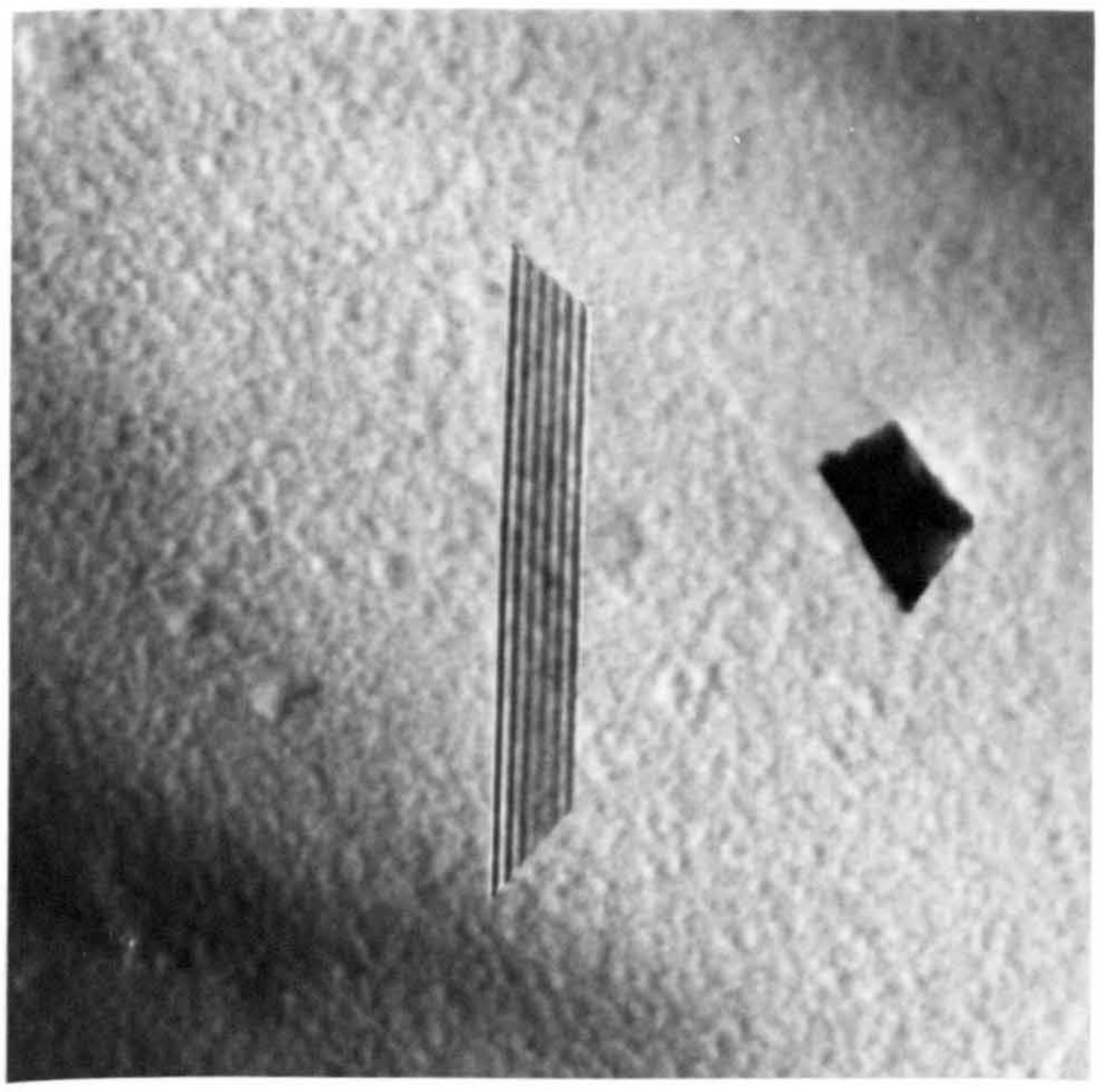

g

3.27 TEM micrographs of a folded back stacking fault in @1965. a) BF, $\underline{g}=2\bar{2}0$.

a)

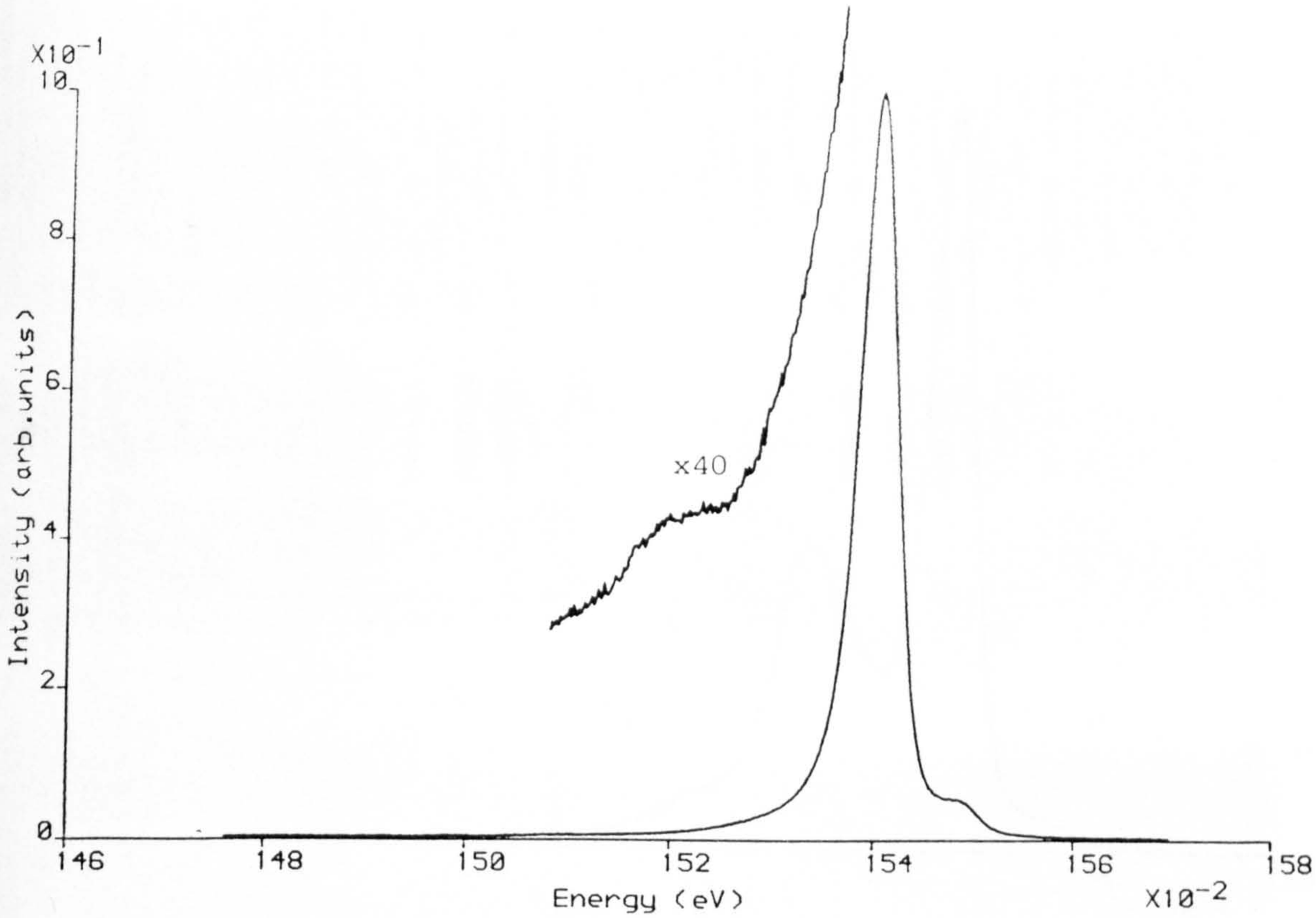

b)

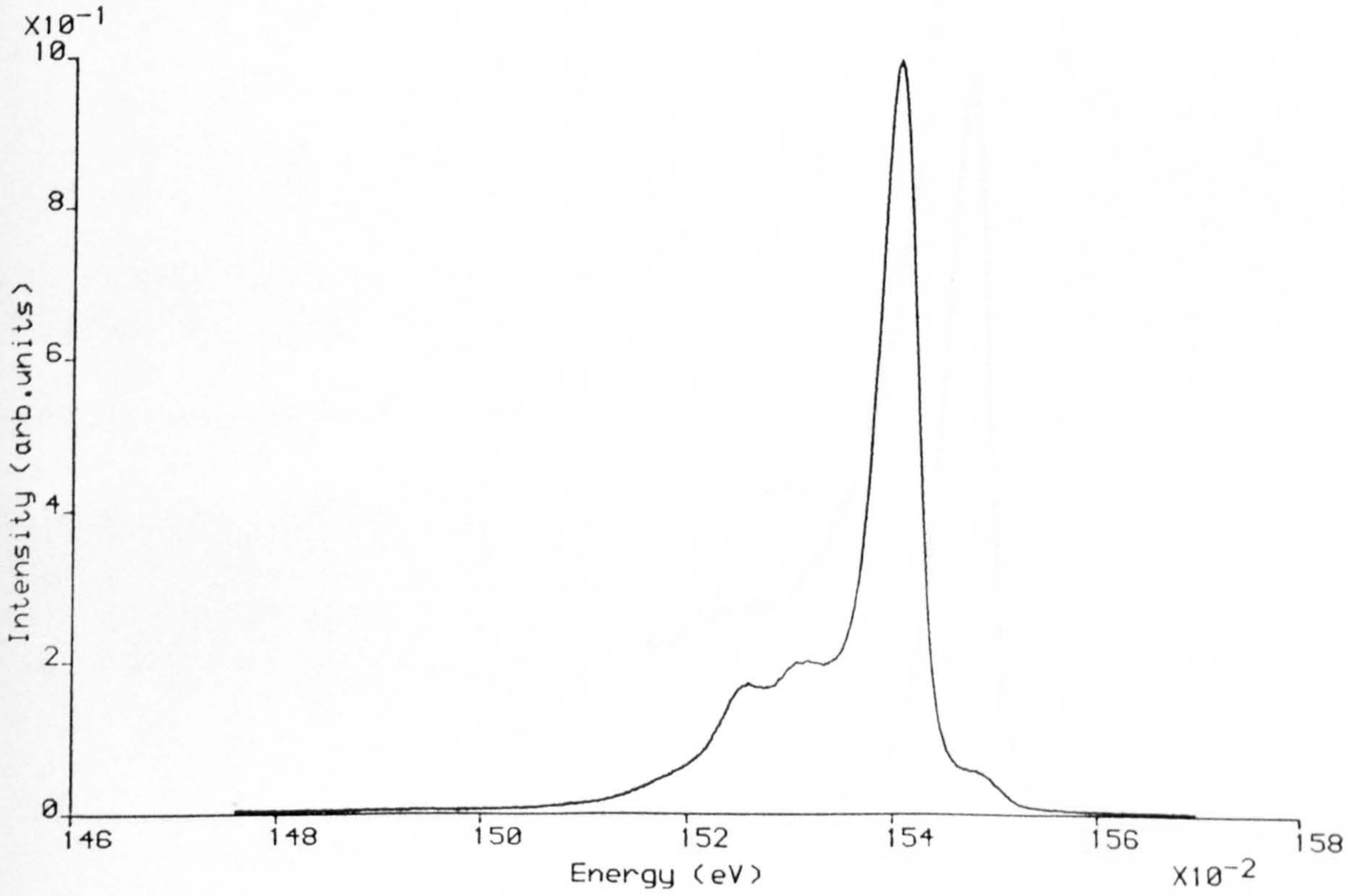

3.28 a) CL spectrum from unfaulted @1965 (piece 1) b) CL spectrum from a pyramidal stacking fault in @1965 (piece 1).

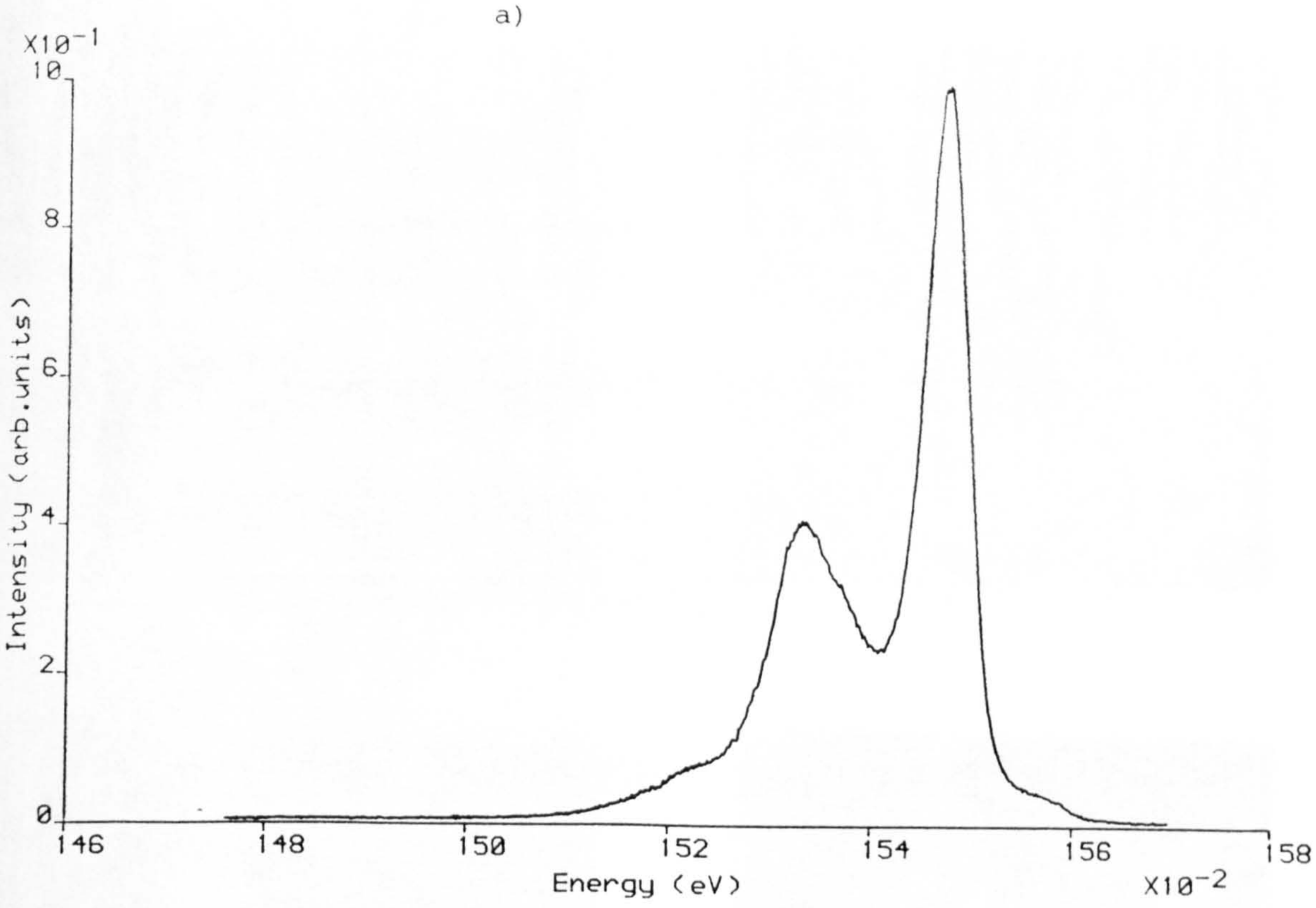

3.29 CL spectra from @1965 (piece 2). a) from a pyramidal stacking fault b) from adjacent unfaulted crystal.

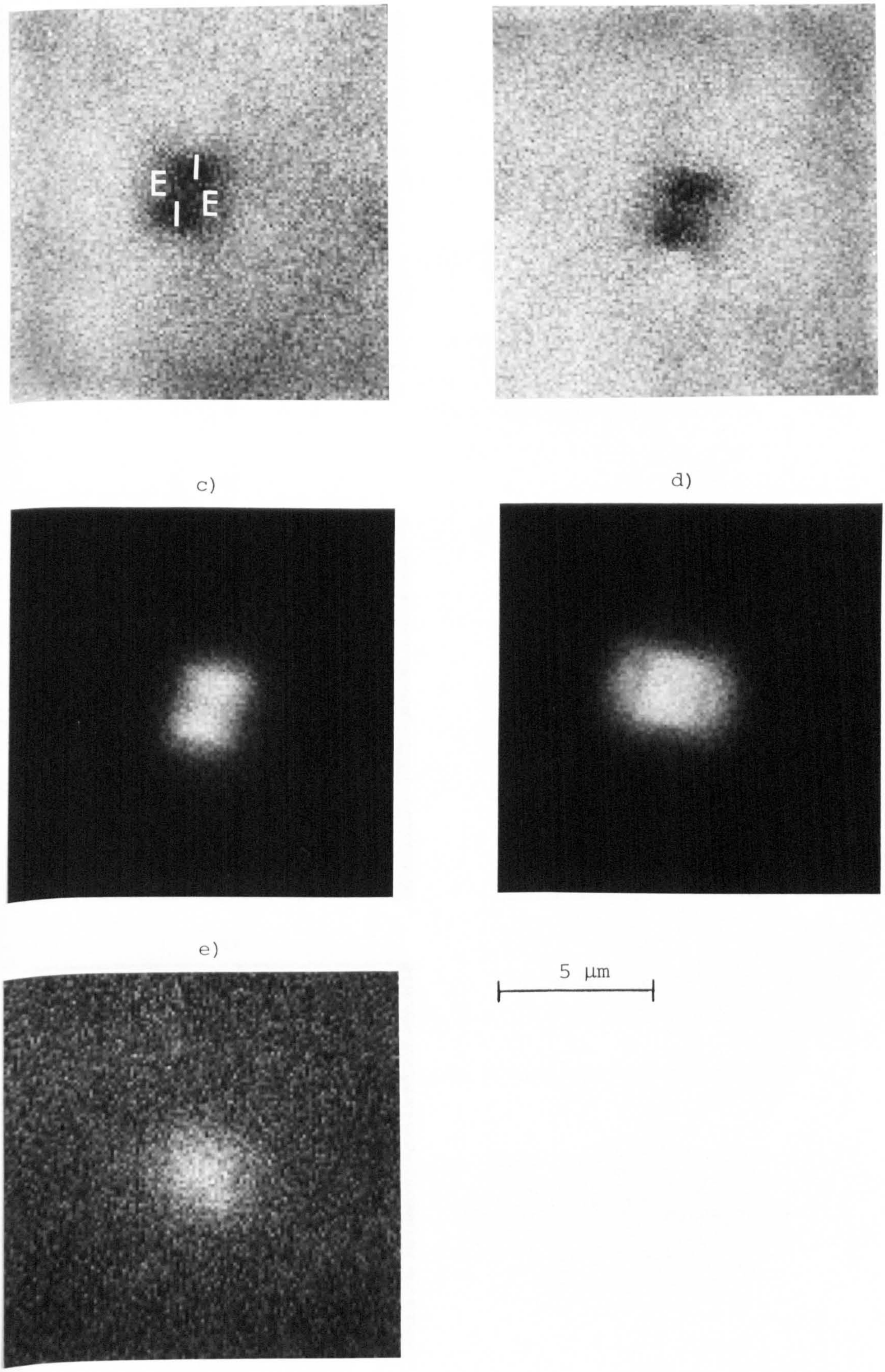

3.30 Monochromatic CL images of a pyramidal stacking fault in @1965 (piece 1). a) n=1(e-ℓh) emission b) n=1(e-hh) emission c), d) and e) 9, 14, and 21 meV below the n=1(e-hh) emission. The position of the stacking fault is marked on a).

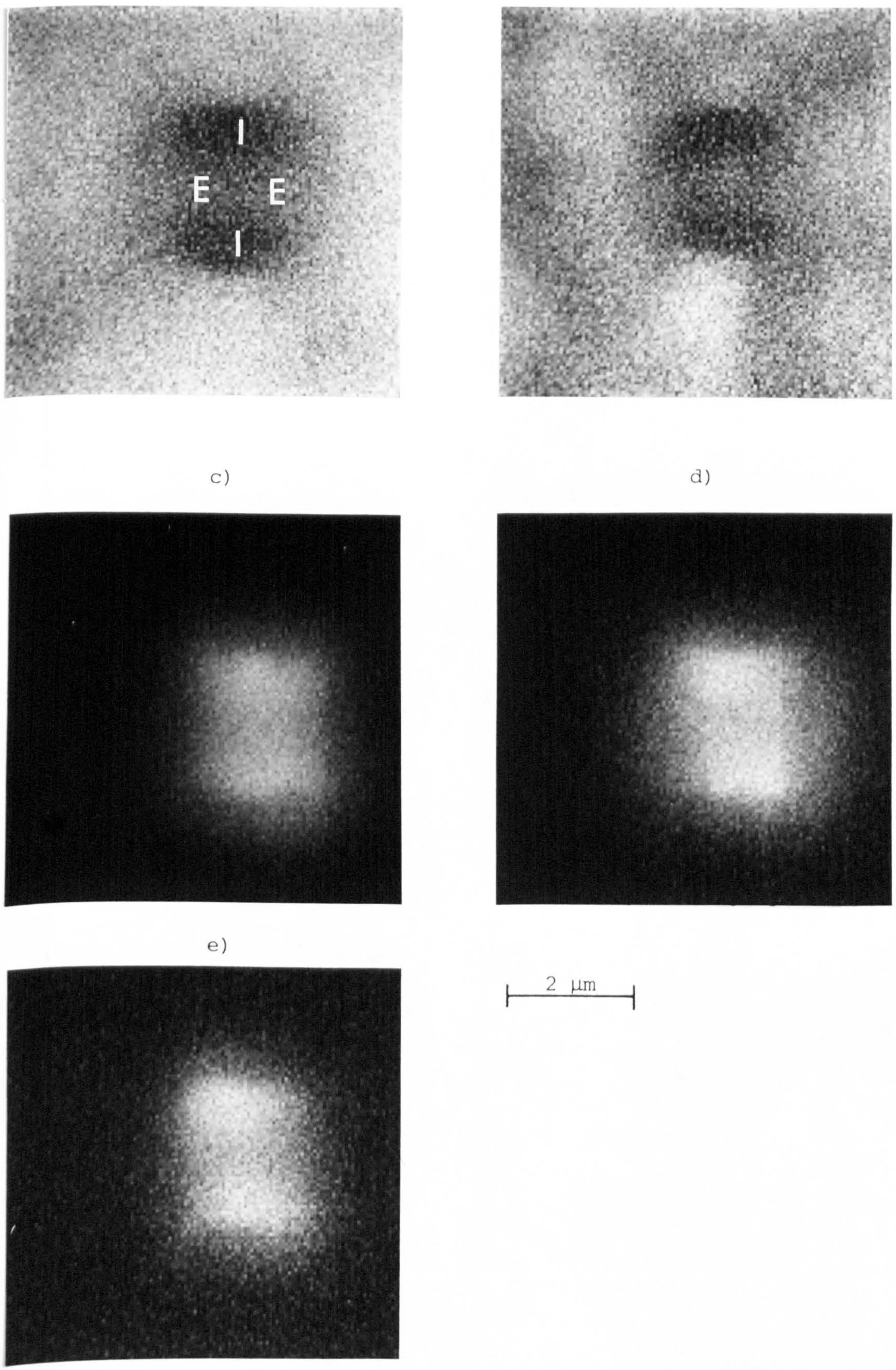

3.31 Monochromatic CL images of a pyramidal stacking fault in @1965 (piece 2). a) n=1(e-ℓh) emission b) n=1(e-hh) emission c), d) and e) 9,14 and 21 meV below the n=1(e-hh) emission. The position of the stacking fault is marked on a).

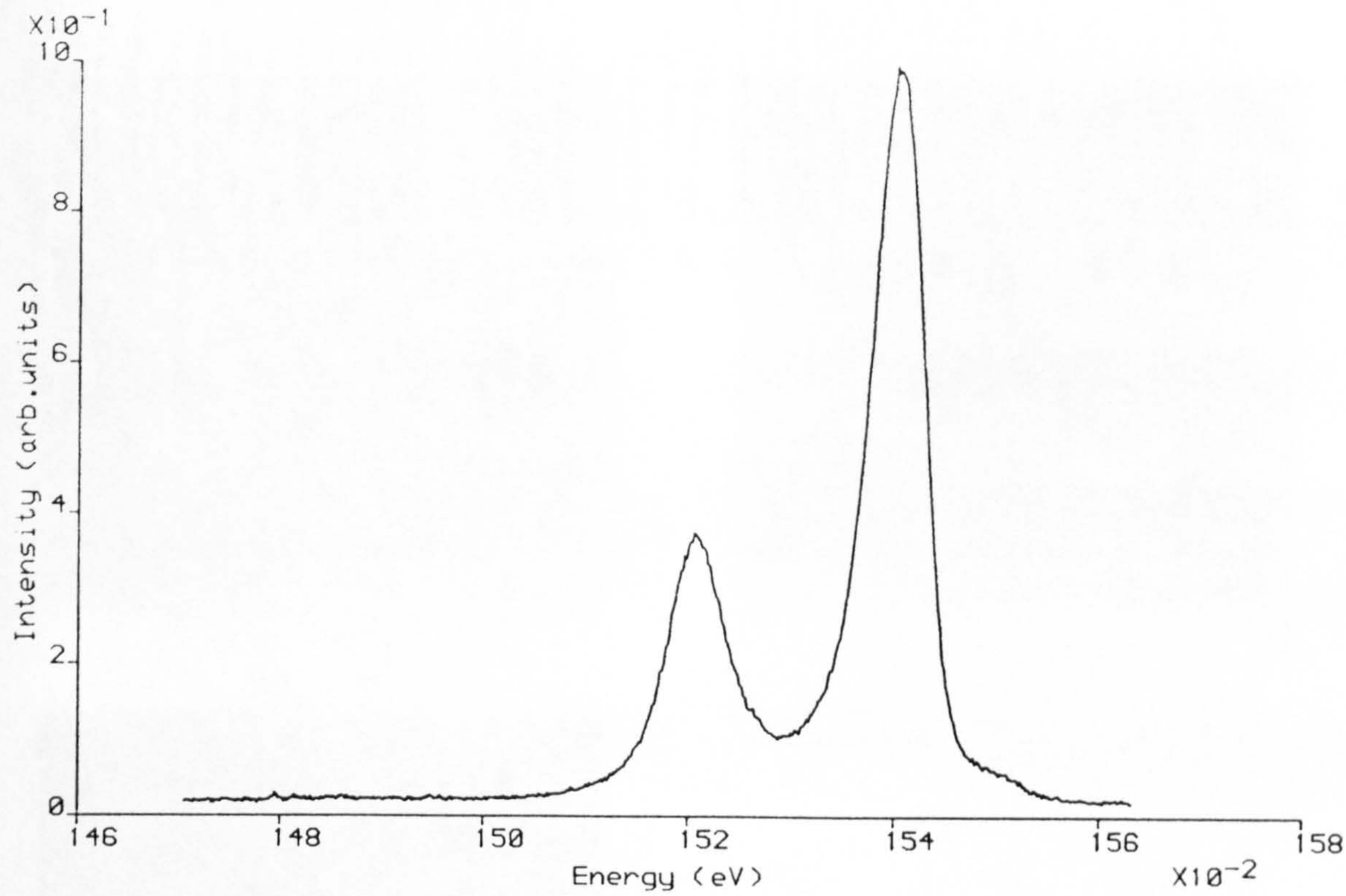

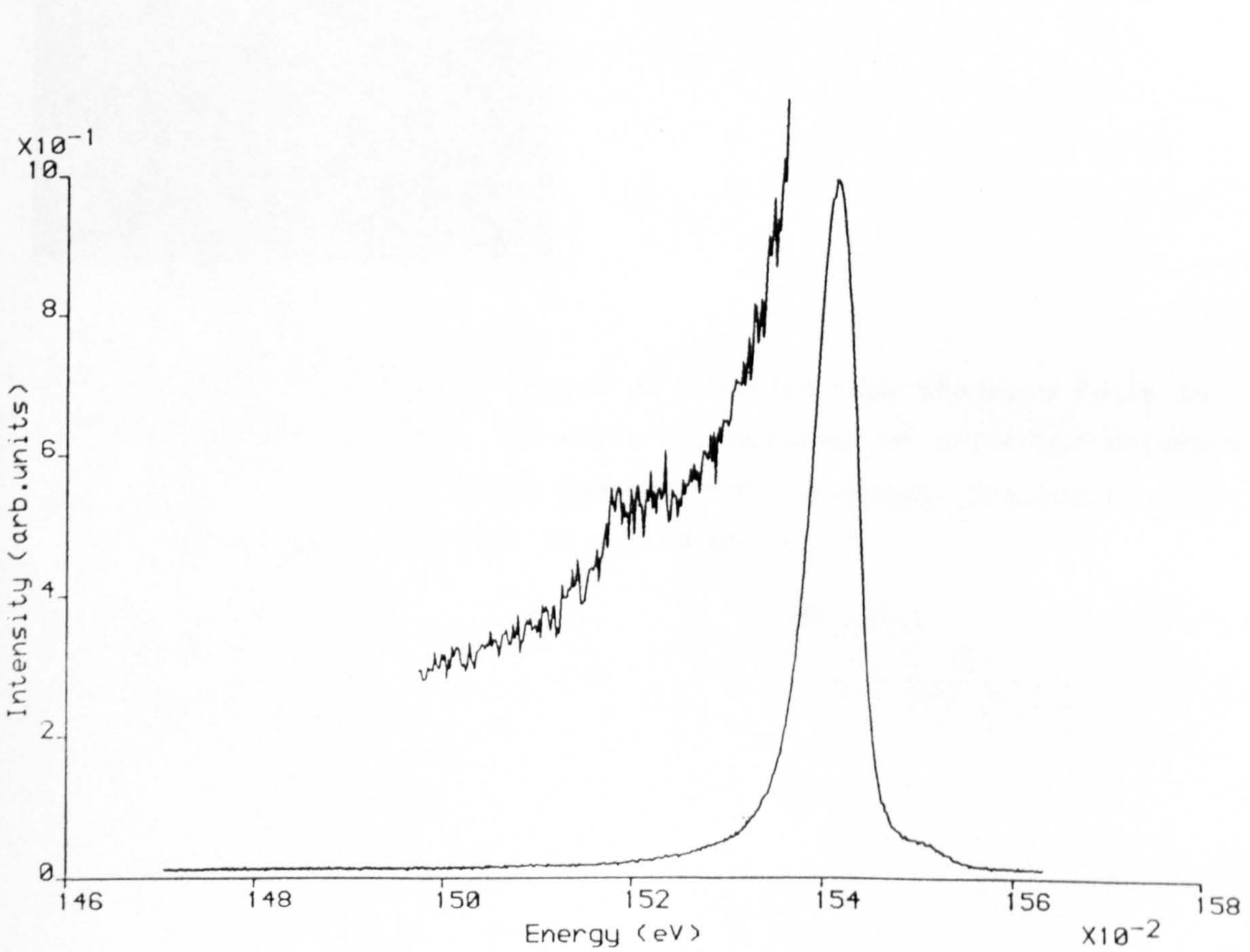

3.32 CL spectra from @1965 (piece 1). a) from a folded back stacking fault b) from adjacent unfaulted crystal.

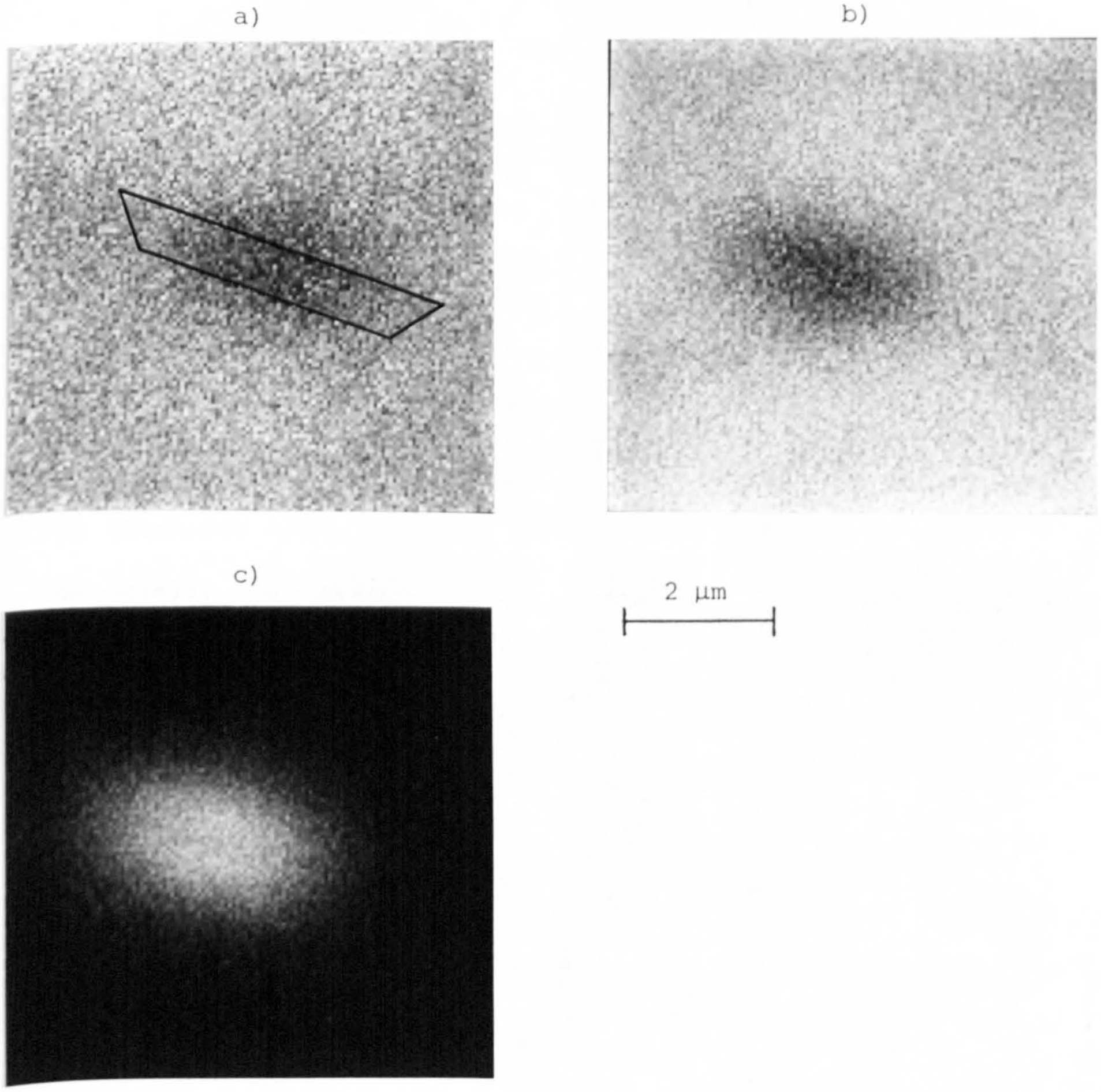

3.33 Monochromatic CL images of a folded back stacking fault in @1965 (piece 1). a) n=1(e-ℓh) emission b) n=1(e-hh) emission and c) 21 meV below the n=1(e-hh) emission. The position of the stacking fault is marked on a).

CHAPTER FOUR

OVAL DEFECTS

4.1. Introduction

MBE has been used to grow GaAs and $A\ell_xGa_{1-x}As$ layers for a number of novel electronic and optoelectronic devices such as quantum well lasers and high electron mobility transistors. Due to the high precision with which MBE can be used to control the thickness and doping of epitaxial layers, the technique is potentially very useful for the fabrication of integrated circuits. However, for applications involving large scale integration, the number of surface morphological defects must be kept to a minimum in order to obtain a high yield of functional devices. For the $GaAs/A\ell_xGa_{1-x}As$ system a number of different defects have been observed in MBE material, including stacking faults, oval defects, whiskers and polycrystalline growth. Whiskers and polycrystalline growth have been attributed (Bachrach and Krusor, 1981) to mechanical damage of the substrate and gross contamination of the substrate respectively. Neither whiskers nor polycrystalline growth were observed in this study and so will not be discussed further. Many authors have included stacking faults in the category of oval defects but in this study they have been considered separately (Chapter 3).

Oval defects are essentially macroscopic defects found in MBE epilayers and range in size from 1-10 μm. A typical oval defect consists of an oval shaped depression or hillock on the epilayer surface, orientated with the long axis along a <110>

direction. Sometimes a small inclusion is present at the centre of the defect. Figures 4.1 and 4.2 show scanning electron microscope images of two oval defects, with and without an inclusion respectively, observed in sample @ 1965. While oval defects have been reported in $In_xGa_{1-x}As$ (Tsang, 1985) and InP (Saito et al., 1983) MBE grown epilayers, most reports have concentrated on the GaAs/Al_xGa_{1-x} system. Oval defects are not normally found in material grown by MOCVD although low densities have been observed in layers grown by gaseous source MBE (Ishikawa et al., 1986) in which the gallium metal source was replaced by a trimethyl-gallium gas source.

4.2. Review of Previous Work

Since oval defects were first reported by Wood et al. (1981) they have been extensively studied by many workers in order to establish both their causes and methods of reducing their density. Factors such as gallium flux, growth time, substrate preparation and arsenic flux have all been investigated. As a result, several different and sometimes contradictory mechanisms have been proposed for oval defect formation. It seems likely that there are several different types of oval defect whose numbers vary according to the individual growth system and growth conditions. To date, reported densities of oval defects have varied from about 100 to 100,000 cm^{-3}. Several attempts have been made to classify oval defects into different types. Fukiwara et al. (1987) distinguished defects primarily by shape while Nanbu et al. (1986) used a combination of shape and size.

Wood et al. (1981) found that the oval defect density in

their system increased with the growth time. Using energy dispersive X-ray analysis, the cores of oval defect were found to contain anomalously high concentrations of gallium. The excess gallium was attributed to the spitting of gallium from the Knudsen effusion cell. This conclusion was reached due to the observation that gallium droplets condensed near the orifice of the effusion cell. At arbitrary times these droplets fell back into the main body of gallium at the bottom of the cell causing rapid ejection of small gallium droplets. Completely filling the gallium cell prior to growth and applying additional heating to the exit orifice substantially reduced the incidence of oval defects. Kirchner et al. (1981) first identified Ga_2O as a major contaminant of the gallium growth flux and suggested that Ga_2O_3 might be formed by the reaction,

$$4GaAs_{(c)} + Ga_2O_{3(c)} \rightleftharpoons 3Ga_2O_{(v)} + 2As_{2(v)} \qquad (4.1)$$

with incorporation of the Ga_2O_3 on the growth surface giving rise to defects. Chai and Chow (1981) observed a grey scum forming on the gallium melt when oval defect densities were high. Under these conditions Ga_2O was detected in the gallium growth flux by use of a quadrupole mass analyser. Cleaning the Knudsen cell with acid and recharging it with gallium taken from nitrogen filled packages greatly reduced the oval defect density (to around 2,000 cm^{-2}). The remaining defects were thought to originate at the substrate-epilayer interface. Bafleur, Munoz-Yague and Rocher (1982) investigated oval defects using both SEM and TEM techniques. Use of an electron microprobe did not show

any departures from stoichiometry either at the polycrystalline cores of the defects or in the surrounding hillock. For larger defects a high density of dislocations and some microtwinning were observed in the region immediately outside the core. As carbon contamination exceeding 20% of a monolayer has been implicated in surface facetting and twinned growth (Cho and Arthur, 1975) substrates were intentionally contaminated with carbon prior to growth. This gave a marked increase in oval defect density, the defects being indistinguishable from those grown on normal wafers. Saito et al. (1983) reported oval defects in MBE grown $InP/In_xGa_{1-x}As$ multilayers, similar to those found in $GaAs/Al_xGa_{1-x}As$. TEM revealed that the larger defects consisted of a central inclusion surrounded by an oval hillock with the long axis parallel to the $<1\bar{1}0>$ direction. Dislocations and stacking faults were found near the central inclusion although no signs of twinning were observed. Smaller defects did not have either the inclusion or the crystallographic defects. Pettit et al. (1984) reported the elimination of oval defects by p-type doping to high levels ($10^{18}cm^{-3}$) using magnesium as the dopant. They suggested that, if the oval defects were caused by gallium agglomeration around a Ga_2O_3 precipitate, then the high levels of magnesium would give rise to MgO on the substrate, rather than Ga_2O_3. As gallium does not wet MgO under vacuum conditions, the nucleation sites for gallium agglomeration are removed, thus preventing oval defect formation. Suzuki et al. (1984) used TEM and selective etching of $GaAs/Al_xGa_{1-x}As$ multilayers to determine the origins of oval defects. For high defect densities, most defects originated in the epitaxial layers. More

uniform heating of the arsenic cell eliminated many of these defects. The remaining defects originated at the substrate-epilayer interface, implying substrate contamination as the cause. While stacking faults and dislocations were found in the hillock region of the defects, substrate dislocations did not give rise to oval defects. Bafleur et al. (1984) cooled GaAs epilayers to 77K and performed spatially resolved photoluminescence (PL) with a resolution of 2 μm. A marked decrease in PL intensity occurred at oval defects and also over a larger surrounding area. Within the affected area,emissions involving point defect-impurity complexes dominated the luminescence. Suza and Okamoto (1984) reported the effects of oval defects on discrete devices-superlattice avalanche photodiodes. Diode performance was correlated with the number of visible oval defects. Only when a diode contained two or more defects was there an appreciable degradation of device performance. For field effect transistors, Shinohara et al. (1984) showed that oval defects increased leakage currents but did not degrade the breakdown voltage unless the defect was situated at or near the edge of the gate electrode.

Weng et al. (1985) identified particulates adhering to the substrate surface as the cause of oval defects in their system. Careful substrate preparation reduced the defect density by an order of magnitude to approximately 300 cm^{-2}, Watanabe et al. (1985) deliberately contaminated substrates with Ga, In and particles of both diamond and Al_2O_3. GaAs layers grown on these substrates contained oval defects indistinguishable from those grown on nominally clean substrates. Akimoto et al. (1985) contradicted these results due to the linear increase of defect

density with epitaxial layer thickness observed in their study. Further, they measured the oval defect density as a function of T, the temperature of the gallium cell, showing that the oval defect density was proportional to $e^{-\frac{1}{kT}}$. This suggested a formation mechanism involving gallium oxides. Matheson and Shih (1986) clarified the two contradictory mechanisms when they identified two discrete types of oval defect. The first due to particulate matter on the substrate surface, the second due to gallium agglomeration on the surface during growth and presumably nucleated by gallium oxides. The density of the latter type varied considerably according to the growth conditions. Fujiwara et al. (1986) also identified two types of oval defect but divided them into those with and those without a discrete particulate core. However, both types were associated with substrate contamination-macroscopic and microscopic contamination respectively. Nanbu et al. (1986) identified a total of nine different oval defects, distinguished by a combination of shape and size. Of the four most common defects, two varied according to the growth conditions and were ascribed to gallium oxides or gallium spitting.Of the remaining two types, only one was formed because of substrate contamination. The second was identified with substrate dislocations - in contrast to the results of Suzuki et al. (1984). Ishikawa et al. (1986) identified a further two types of defect for GaAs grown by gas source MBE but still obtained defect densities as low as 21 cm^{-2} (for defects greater than 5 μm in diameter). Fujiwara et al. (1987) also extended their classification scheme to distinguish between six types of coreless defect due to either microscopic substrate contamination or gallium agglomeration. Finally, Weng

(1987), who had earlier grown wafers with oval defect densities of about 300 cm^{-2} by careful substrate preparation, identified the sources of the remaining defects. Approximately half were incurred by particulates adhering to the substrate during transfer of the wafer through load-locks into the vacuum chamber. The remainder were attributed to Ga_2O_3 via the following mechanism. Firstly, Ga_2O_3 in the gallium melt is reduced by Ga_2O

$$Ga_2O_{3(s)} + 4Ga_{(l)} \rightleftharpoons 3Ga_2O_{(g)} \qquad (4.2)$$

Ga_2O has a much higher vapour pressure than Ga_2O_3 and effuses to the epilayer. At the epilayer this reaction reverses, leaving Ga_2O_3 to act as a nucleation centre for gallium agglomeration. Analysis of the rate of oval defect formation for different gallium cell temperatures provided evidence that equation (4.2) was valid. Additionally, careful elimination of Ga_2O_3 from the gallium melt prevented formation of the oxide induced defects.

To summarise, extensive research by many workers has suggested two separate mechanisms for oval defect formation. Firstly, microscopic or macroscopic contamination of the substrate prior to growth. Secondly, Ga_2O_3 present in the gallium melt, details of defect formations being ambiguous. Both types of defect are elongated in the $[1\bar{1}0]$ direction, possibly due to the faster development of the growth step in the $[1\bar{1}0]$ as compared to the [110] direction, J.H. Neave et al. (1983). Although the electrical properties of oval defects have been studied, little work has been done on their optical properties.

4.3. Results

In this study oval defects were investigated in samples G43 and @1965 using TEM, CL and EDX. In order to distinguish between the orthogonal [110] and $[1\bar{1}0]$ directions the method of Tafto and Spence (1982) was used. This determination was kindly performed by A.R. Preston. Oval defects were also found in samples KLB116 and KLB121, although no CL measurements were made - these samples were of lower quality so that interpretation of CL data would have been even more difficult.

In addition to the QW samples, an MBE grown GaAs epilayer sample (KLB358), grown at the Philips Research Laboratories in Surrey, was also examined by TEM and CL. This sample was Si doped (10^{17} cm^{-3}) and grown on an (001) GaAs substrate. Prior to the growth of this sample the Ga effusion cell was loaded with Ga that had been deliberately contaminated with gallium oxide.

4.3.1. Oval Defects in G43

TEM examination of sample G43 revealed an oval defect density in the region of 500-1000 cm^{-2}. Figure 4.3 shows a typical oval defect in this material. The main feature of this defect is an oval pit with the long axis parallel to the [110] direction. Almost all the observed oval defects were from 2-4 microns long, although both larger and smaller defects were observed. Simple TEM tilting experiments and SEM examination showed that the deepest region of the pit was closest to the substrate side of the foil. For most of the oval defects examined, the pit did not perforate the TEM foil. This conclusively showed that the pit was not produced by the chemical etchants used during

specimen preparation (for these etchants the rate of attack can be affected by impurities or defects in the crystal). Consequently, the pit must have been formed during sample growth. No thickening of the epilayer (overgrowth) was observed outside the core of any oval defect in G43. In contrast to the results of some earlier workers (for example, Suzuki et al., 1983) no stacking faults, twins or dislocations were found associated with oval defects.

A substantial proportion of oval defects incorporated a small particulate near the centre of the pit. EDX analysis and convergent beam electron diffraction revealed that the particulate consisted of misoriented and imperfect GaAs or $Al_xGa_{1-x}As$. Due to the proximity of the Al Kα and As Lα X-ray emission lines no attempt was made to quantify the Al content of the particulates. In some cases, however, EDX showed that the particulates were slightly Ga rich.

At the centre of several defects (both with and without central particulates) small amounts of impurities were detected by EDX, including silicon, calcium, iron, potassium and chlorine.

Low temperature TEM CL was performed on a number of oval defects in G43, including those with and without central particulates. No CL was ever detected from any particulate despite the use of the highest readily obtainable beam current. No significant differences were found between CL spectra obtained from oval defects with and without the central particulate. Figure 4.5 shows a CL spectrum from an oval defect (with particulate) with the electron beam illuminating the whole of the oval defect. Figure 4.6 shows an equivalent spectrum for an oval defect

without the particulate. Also included are control spectra acquired from regions of unfaulted crystal adjacent to the defects. The intensity of the n = 1 X(e - hh) QW luminescence decreases at the defects but the energy of this emission is unaffected. In both cases the normal weak background emission between 1.55 and 1.60 eV is replaced by stronger emissions. The energies of these features varied from defect to defect. These peaks did not correspond in energy to the weaker features observed from adjacent unfaulted crystal. Figures 4.7 and 4.8 show monochromatic CL images and TEM micrographs acquired from the same oval defects used to obtain the spectra shown in figures 4.5 and 4.6 respectively. For figure 4.7 the CL images a) to f) were acquired at the energies of the emission features marked A to F in figure 4.5. Similarly, the CL images a) to e) in figure 4.8 correspond to the features marked A to E in figure 4.6.

4.3.2. Oval Defects in@ 1965

Sample @ 1965 contained a considerably higher density of oval defects than G43, in the range 2,000 - 5,000 cm^{-2}. Unlike G43 sample @ 1965 was difficult to make into large area TEM samples. Possibly due to the slightly different sample preparation technique (see Chapter 2) TEM foils prepared from @ 1965 frequently perforated at oval defects, producing a microscopic hole. Such holes readily initiated the formation of cracks. Stresses were always present in TEM foils due to the lattice mismatch between GaAs and $Al_xGa_{1-x}As$ but were generally not sufficient to cause crack propagation. However, any additional mechanical stresses, such as those incurred while mounting the specimen for TEM

examination, frequently resulted in the destruction of the TEM specimen. Thus TEM samples of @1965 were extremely fragile and required great care when being handled. Unfortunately, cooling of the TEM specimen for CL studies frequently generated sufficient thermal stresses to distintegrate the electron transparent area. Due to this problem and the limited supply of material available only the most common types of oval defect could be examined using low temperature CL.

Sample @ 1965 contained several different types of oval defect ranging in size from 1-10 μm. Figure 4.9 shows a representative selection of oval defects from @1965. A typical oval defect consists of a pit (similar to those in G43) or a simple hole. In both cases the longest axis is parallel to the [110] direction. Although particulates were found at the centre of some defects in @ 1965 they were not present for most defects. As for G43 these particulates were examined using EDX analysis and convergent beam electron diffraction and found to consist of imperfect and misoriented GaAs or $Al_xGa_{1-x}As$. Immediately around the pit or hole at the core of the oval defect, a thickening of the epilayer (overgrowth) was generally observed. SEM of oval defects in bulk material showed hillocks around oval defects indicating that this overgrowth forms during MBE growth and was not formed during TEM sample preparation. This region of overgrowth is the oval shaped feature responsible for the name 'oval defect' and in this study was always found to have the long axis parallel to the $[1\bar{1}0]$ direction, in agreement with most other workers.

EDX analysis was used to study a number of oval defects in @ 1965. Regions of overgrowth did not show any detectable

departures from stoichiometry nor were any impurities detected. Similar results were obtained for the pit forming the core of some oval defects, but only when no central particulate was present. For oval defects with a simple hole at the core TEM micrographs frequently showed a thin layer of material partially or totally occluding the hole (Figure 4.9). This layer was determined to be Ga rich GaAs containing impurities. Sulphur, silicon, calcium, iron, potassium and chlorine were all detected, although sulphur was the most common impurity. EDX of the particulates at the cores of some oval defects revealed the same impurities, with the exception of sulphur which was not detected, with the particulate sometimes being slightly Ga rich. However, it should be stressed that the majority of particulates did not show any impurities or departures from stoichiometry.

CL was performed on a number of different oval defects in @1965. Figures 4.10, 4.12 and 4.14 show CL spectra acquired from three different oval defects (all without central particulates). The defects were a pit without overgrowth, a hole without overgrowth and a hole with overgrowth respectively. For comparison each of these figures also includes a control spectrum taken from unfaulted crystal adjacent to the relevant oval defect. In all three cases the control spectra are dominated by the n = 1 X(e - hh) QW emission, with the n = 1 X(e - ℓh) emission appearing as a weak shoulder at slightly higher energy. On the low energy side of the main peak is a weak feature probably due to an n = 1 (e - a) transition. The most likely acceptor is carbon due to residual hydrocarbons in the MBE growth system (see Chapter 3). For the simple pit the control spectra and the spectra from the oval defect

(Figure 4.11) are virtually identical. Figures 4.11a), b) and c) show three monochromatic CL images acquired at the energies marked A, B and C on Figure 4.10. A TEM micrograph of the oval defect is shown in Figure 4.11(d). The light hole and heavy hole CL images acquired at 1.547 and 1.540 eV respectively are almost identical. Both images show a marked decrease in intensity around the centre of the defect. The n = 1 (e - a) CL image (1.508 eV) also shows a marked decrease in intensity around the core of the defect but in addition shows a slight enhancement of intensity over a small region on one side of the defect (just outside the central pit). Careful examination of the light and heavy hole CL images reveals that both these images show a light decrease in intensity over the same region.

For the hole without overgrowth, the spectrum(Figure 4.12) show similar behaviour to the pit except that the spectrum from the hole shows a slight broadening and loss of resolution of the acceptor emission. Figures 4.13a) and b) show CL images acquired at the energies of the heavy hole and acceptor luminescence while Figure 4.13c) shows a TEM micrograph of this defect. As before the CL images show decreased intensity at the core of the defect with enhanced acceptor emission around the outside of the core. However, the acceptor luminescence shows an anomlous bright spot to the right of the oval defect. TEM did not reveal any crystallographic defect at this position. This bright spot was observed for several oval defects. Several TEM specimens were carefully examined by CL in an attempt to locate bright spots which were not associated with oval defects. However, such bright spots were only observed when associated specifically with the hole type of

oval defect. Note that in Figure 4.13 the light hole image is not included as it was identical to the heavy hole image.

To illustrate the effect of overgrowth on luminescence, Figure 4.14 shows a CL spectrum from a hole type defect with overgrowth as compared with a control spectrum from adjacent crystal. A relatively weak low energy shoulder can be seen in the spectrum from the defect. Figures 4.15a) and b) show monochromatic CL images at the energies of the heavy hole and low energy shoulder emissions respectively while Figure 4.15c) shows a TEM micrograph of the oval defect. The hole at the centre of the defect obviously does not give any CL. The region of overgrowth appears dark in the n = 1 X(e - hh) image while it gives enhanced emission at the energy of the weak shoulder. The heavy hole emission intensity is depleted over a considerable area outside the oval defect. This particular oval defect is a reasonably typical example of an oval defect surrounded by an overgrowth region, although the strength and energies of the defect related emissions varied considerably between different defects. Figure 4.16 compares a CL spectrum from another oval defect (with overgrowth) with a control spectrum from adjacent unfaulted crystal. These spectra are included to indicate the variability of the oval defect luminescence features. In this example the main QW peak shifts to lower energy in the region around the oval defect and decreases in intensity. When a more intense electron beam was used to illuminate the oval defect the shifted QW luminescence peak moved to slightly higher energy, indicating that the QW emission at the oval defect has probably changed character from the normal n = 1 X(e - hh) transition to an n = (e - a) transition (Lambert et al., 1982). Two weaker

peaks at lower energy can also be seen in Figure 4.16. It should be stressed that by far the majority of oval defects in @1965 were surrounded by an overgrowth region.

4.3.3. Results from KLB358

Preparation of TEM specimens of KLB358 was performed in the same way as for the QW structures (Chapter 2) except that the GaAs selective NH_4OH/H_2O_2 etchant was not employed. Instead, specimens were kept immersed in the non-selective H_2SO_4/H_2O etchant until the centre of the sample was optically transparent,at which point this region of the specimen is also electron transparent. The normal procedure was then used to prepare the specimens for TEM examination.

KLB358 contained a high density of oval defects (approximately $5 \times 10^6 cm^{-2}$). A typical example is shown in Figure 4.17. This defect shows a roughly oval region of overgrowth surrounding a thinner core region. The particulates sometimes observed at oval defects in @1965 and G43 were not seen in this sample. EDX analysis of oval defects in this material did not reveal any departures from stoichiometry nor were any impurities detected.

CL spectra from oval defects in this material were compared with spectra from defect free regions. The only difference observed was that the luminescence from the oval defects was more intense but this was almost certainly due to the increased crystal thickness in the overgrowth region of the defects.

To check that the overgrowth observed in the TEM was not a product of the specimen preparation, a bulk sample of KLB358 was examined in an SEM. The oval defects observed were surrounded

by hillocks, showing that the overgrowth is not a product of the TEM specimen preparation.

4.4. Discussion

4.4.1. Impurities Detected by EDX

In sections 4.3.1 and 4.3.2, results from EDX analysis of oval defects in @ 1965 and G43 were presented. In both materials, impurities were sometimes detected when a particle was present at the core of the defect. Surprisingly, the same impurities were detected for both materials - calcium, iron, silicon and potassium being the most common. The particles at the cores of oval defects were determined to be imperfect GaAs (or $A\ell_xGa_{1-x}As$), misoriented with respect to the substrate, a slight excess of gallium being present in some cases. The presence of impurities initially suggests that the oval defects may have been caused by substrate contamination, the excess Ga being generated by Ga agglomeration during growth of the epilayers (as suggested by Pettit et al., 1984). Substrate contamination has been linked to oval defect formation by a number of workers, for example Weng et al. (1987). Werner et al. (1987) examined oval defects using EDX analysis in an SEM and detected calcium and iron at the cores of some defects. They also detected barium, an element not found in the current work. However, SEM EDX analysis of oval defects in bulk samples of G43 and @ 1965 did not detect any impurities at all. The difference in results from TEM foils and bulk SEM specimens suggests that the impurities detected at oval defects might originate with the TEM sample preparation rather than the MBE growth. The final stage of sample preparation (see Chapter 2) was removal of the wax used to protect the epilayer surface during chemical etching. This was

accomplished by multiple rinsing in analar 1-1-1 trichloroethane followed by rinsing in analar acetone. For both these solvents the manufacturers quote sodium, calcium, iron and potassium as major non-volatile contaminants (in order of decreasing concentration). Of these elements only sodium was not detected at oval defects in TEM foils. However, it is difficult to detect sodium by EDX when gallium is present, owing to the overlap of the sodium Kα and gallium Lα X-ray emission lines, although this might be possible using some form of deconvolution. Thus the impurities detected at oval defects are the same as the impurities in the solvents used in the final stages of TEM specimen preparation. It is worth noting that for oval defects the relative amount of each impurity, as crudely judged by the intensity of the X-ray emission lines, normally followed by the sequence calcium, iron and potassium (in order of decreasing X-ray intensity). This is the same sequence as for the contaminants in the solvents. Therefore it seems likely that solvent gets trapped in the pit accompanying oval defects. On evaporation of the solvent, contaminants are left behind giving rise to the impurities detected by EDX.

So far the presence of chlorine, sulphur and silicon at some oval defects have not been accounted for. None of these are listed as contaminants in the acetone used for the final specimen rinse. Chlorine was only detected very occasionally and only gave very weak X-ray emission lines when it was present. It is believed that this chlorine can be traced to the 1-1-1 trichloroethane used for the penultimate specimen rinse as in this solvent, chlorides are the major contaminants. The silicon detected is also easy to

account for - during specimen preparation samples were mounted on glass slides, etched in glass beakers and rinsed in glass petrie dishes. Traces of silicon are therefore unsurprising. Sulphur was only detected for the hole type of oval defect in @ 1965 and then was only found in the thin layer of material occluding the hole. This layer was determined to be gallium rich GaAs. For @ 1965, the final etchant used in specimen preparation was $H_2SO_4:H_2O_2:H_2O$. This etchant is commonly used to produce a passivating gallium oxide layer on substrates prior to MBE growth and has been linked as leaving residual sulphur on the substrate surface (Chai et al., 1985). Thus it seems likely that both the sulphur and the excess gallium detected by EDX originate at this stage. The final sulphuric acid based etchant was not used for TEM specimens of G43 so that the lack of sulphur at oval defects in G43 supports the above interpretation. However, excess gallium was still detected at oval defects in G43. The final etchant (H_2O_2/NH_4OH) used on this material attacks GaAs by the growth of a gallium oxide film which breaks into small fragments, thereby exposing fresh surfaces to the etchant (Logan and Reinhart, 1973). Thus, as for @1965, it seems possible that the excess gallium detected at oval defects is due to a residue of gallium oxide.

The above discussion strongly suggests that all the impurities detected by EDX could originate with the TEM sample preparation so that the EDX results cannot be used to draw any conclusions about the cause of oval defects. If impurities do originate with the chemical etchants it is not clear why the impurities are only observed at the oval defects.

4.4.2. Discussion of CL Results

Low temperature CL was performed on oval defects in G43 and @ 1965. For both materials, CL spectra acquired from oval defects revealed normally weak features on the low energy side of the dominant exitonic QW emission. Similar but much weaker features were observed in unfaulted crystals. These features are thought to be extrinsic in character, due to impurities in the crystal and are probably generated by n = 1 (e - a) transitions. For both G43 and @ 1965 monochromatic CL images acquired at the energies of the impurity emissions showed a clear enhancement of intensity in the vicinity of oval defects. Comparison of spectra acquired at and adjacent to oval defects in both G43 and @ 1965 showed that the energies of the enhanced emissions did not normally correspond to the energies of the weak background luminescence features observed in unfaulted crystal. This suggests that oval defects may be caused by substrate contamination. However, it is quite possible that the luminescence features observed at oval defects are completely spurious, due to optical interference, absorption or surface structure.

To demonstrate that optical interference and absorption effects are not responsible for the observed CL features, oval defects in bulk samples of @ 1965 and G43 were studied using CL (see Chapter 7). The results obtained were qualitatively similar to the results from thin foils so it is believed that neither interference nor absorption are responsible for the luminescence features observed at oval defects.

The pits and holes found at the centres of oval defects are expected to modify the CL images in the following way. Most of

the light generated in a TEM foil made from GaAs or $Al_xGa_{1-x}As$ undergoes total internal reflection. A hole or pit creates a new surface from which extra light can escape. This effect is illustrated in Figure 4.18 for a simple facet. The critical angle for total internal reflection is dependent on refractive index which does not vary significantly over the energy range of interest in this study, so that as an electron beam is scanned towards a facet, CL of all wavelengths should be emitted more strongly. Examination of, for example, Figure 4.7 reveals that the intensity of the heavy hole QW emission does not increase near oval defects even though the CL images of the weaker, lower energy emissions do show a marked increase in intensity. Thus it seems likely that any additional light escaping around oval defects does not have a significant effect on CL images, possibly due to dirt on or roughness of the surfaces exposed around oval defects.

In addition to the enhanced impurity luminescence observed in the vicinity of oval defects, the intrinsic QW luminescence intensity always decreased at the core of the oval defect and sometimes over a large surrounding area. Obviously at the core this is partly due to the crystal becoming thinner. Non-radiative surface recombination will also become more important where the QW's are perforated by an oval defect as carriers (normally confined to the QW's) can then reach a surface. Outside the core, loss of intensity probably occurs due to an increase in the number of competing carrier recombination routes due to the radiative transitions observed by CL and probably due to additional non-radiative transitions.

An interesting effect can be observed in monochromatic CL images acquired at the energies of the weak low energy emission features. Images acquired at progressively lower energies show the regions of enhanced intensity around oval defects contracting towards the core of the defect. In other words, the lowest energy luminescence emanates from the region of crystal closest to the oval defect. This effect was normally much more marked in G43 than in @ 1965. As the low energy features are believed to be due to impurities it is thought that this effect reflects the distribution of impurities within the QW's. It seems reasonable to suppose that the highest concentration of impurities occurs closest to the oval defect. Normally impurities in QW's are incorporated at the edges of the wells (Miller et al., 1982). However, as the impurity concentration increases it is possible that more impurities become incorporated near the centre of the well. Masselink et al. (1984) have shown that the binding energies of acceptors are highest at the centre of the well. Therefore the emission energy of an acceptor at the centre of a QW will be lower than the emission energy of an acceptor at the edge of the well. Thus it appears that the increase in low energy emission close to an oval defect may be due to more impurities being incorporated near the centre of the well.

4.4.3. General Discussion

The structures of oval defects observed in this study correlate well with the results of previous workers. Sample KLB358 was deliberately grown using a Ga source contaminated with gallium oxide. The oval defects in this material were noticeably different

from those in @ 1965 and G43. This implies that the defects in KLB358 were generated by gallium oxide but that those in the QW samples were formed via a different mechanism. The defects in KLB358 did not show any changes in CL spectra as compared to unfaulted crystal. However, this may simply be due to the relatively high doping of this material obscuring any effects from small concentrations of impurity. Comparison of oval defects in KLB358 with the classification schemes developed by Fujiwara et al. (1987) and Nanbu et al. (1986) showed that defects in KLB358 did not correspond to any of the defects classified by Fujiwara et al., but were very similar to the type C defect observed by Nanbu et al. However, none of the oval defects identified by Fujiwara et al. were ascribed to gallium oxide. Nanbu et al. determined that type C oval defects are generated by gallium oxide, in agreement with the current work.

Oval defects in G43 were unusual in that TEM micrographs did not show any obvious overgrowth around the core of the defect, but this may simply be because any change in thickness was too small to detect on a simple TEM micrograph. In all other respects these defects are similar to those classed as type B by Fujiwara et al., or as type B by Nanbu et al., and ascribed to substrate contamination. As for oval defects in G43, Fujiwara et al. and Nanbu et al. observed this type of defect both with and without a particulate at the core.

A number of different oval defects were observed in @ 1965. However, careful examination of a number of defects suggested that they were all essentially similar but that the degree of overgrowth

varied. Again these defects appear to correspond to type B or β which are caused by substrate contamination. Fujiwara et al. also identified oval defects (type α) that did not have a particulate core and ascribed them to microscopic (as opposed to macroscopic) substrate contamination. However in the current work it was not felt this distinction was needed.

Perhaps the most thorough study of the origins of oval defects has been reported by Weng (1987). He concluded that oval defects such as those in KLB358 were caused by Ga_2O_3 while defects like those in the quantum well structures were caused by substrate contamination.

The luminescence features observed at oval defects in both G43 and @1965 were thought to be due to the presence of impurities. As the energies of these features varied from defect to defect the luminescence is consistent with the formation of oval defects via substrate contamination. The CL results for G43 and @ 1965 are also in qualitative agreement with the results of Bafleur et al. (1984) obtained using spatially resolved photoluminescence. However, considerably greater spatial resolution was obtained using CL, so that even the smallest oval defects could be examined.

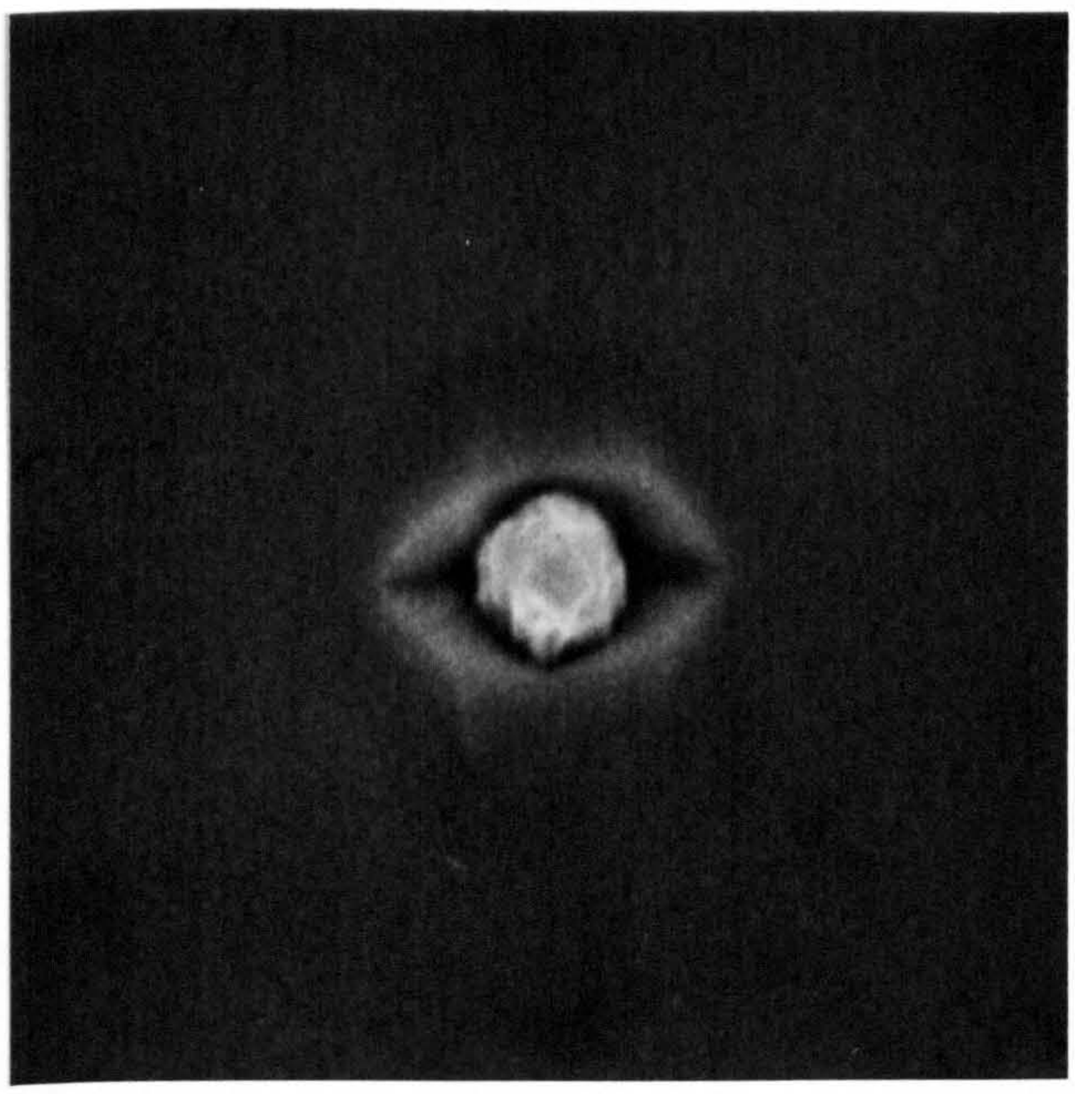

4.1 SEM image of an oval defect in G43 (with central particulate).

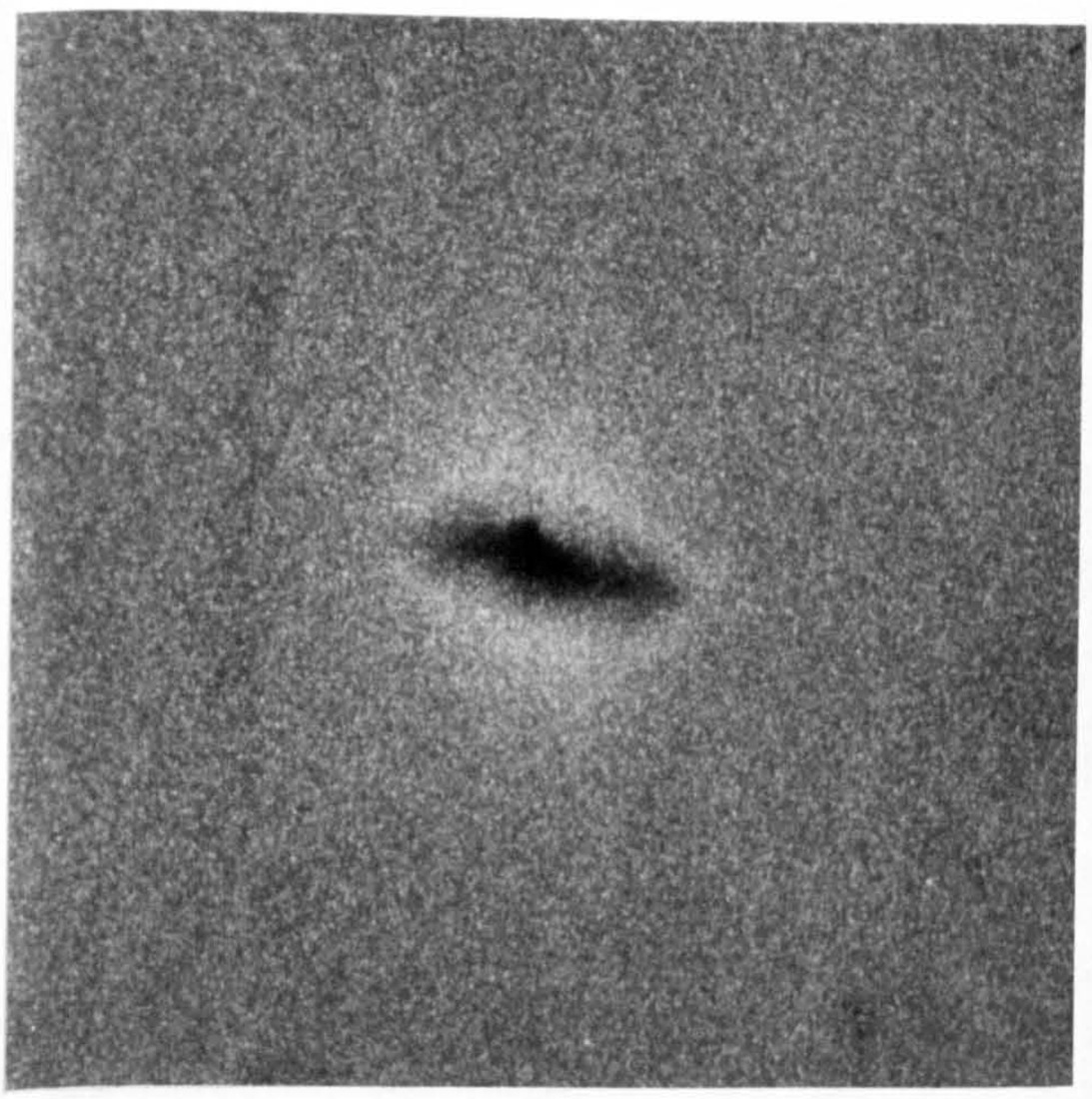

4.2 SEM image of an oval defect in G43 (without central particulate).

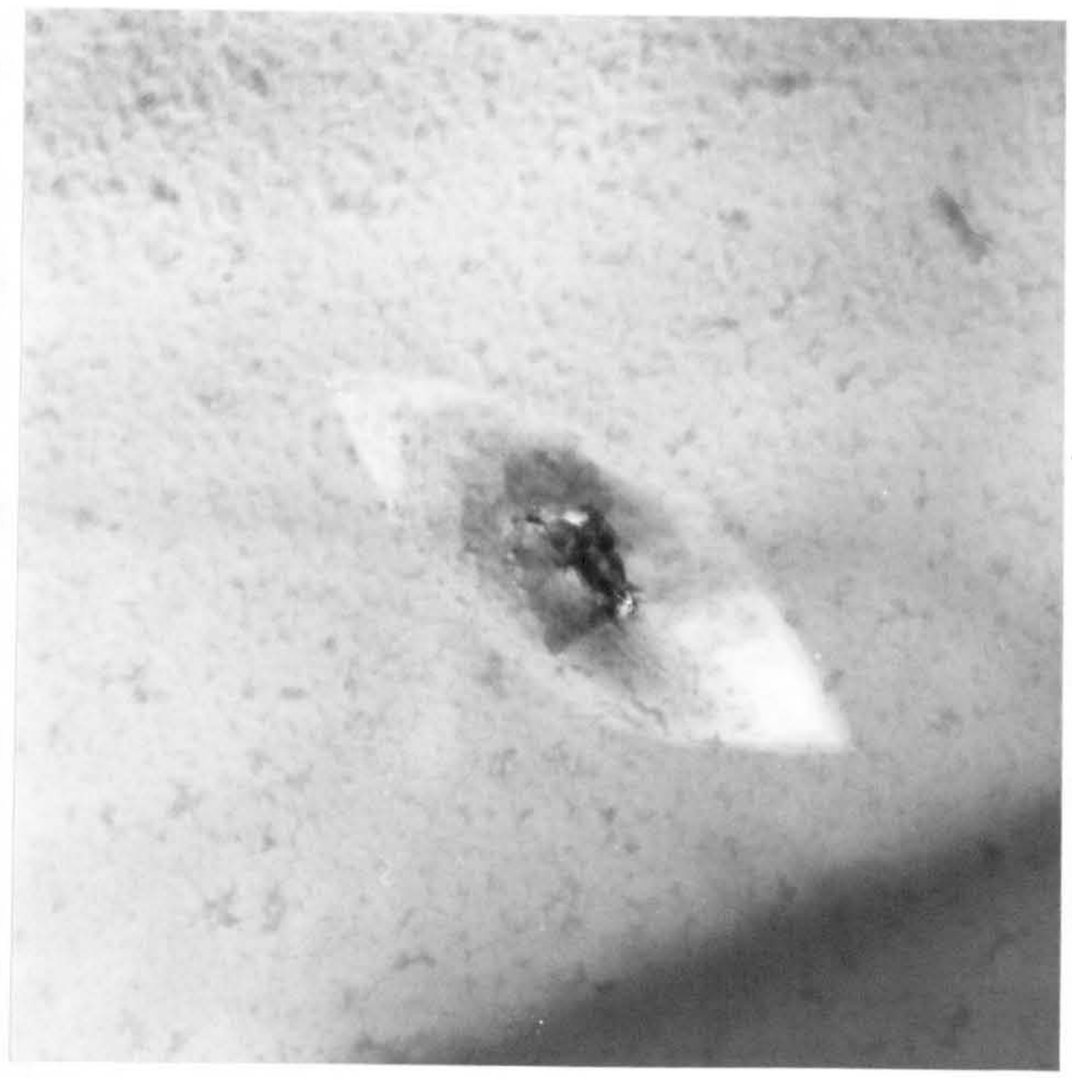

4.3 BF TEM micrograph of an oval defect in G43 (without central particulate).

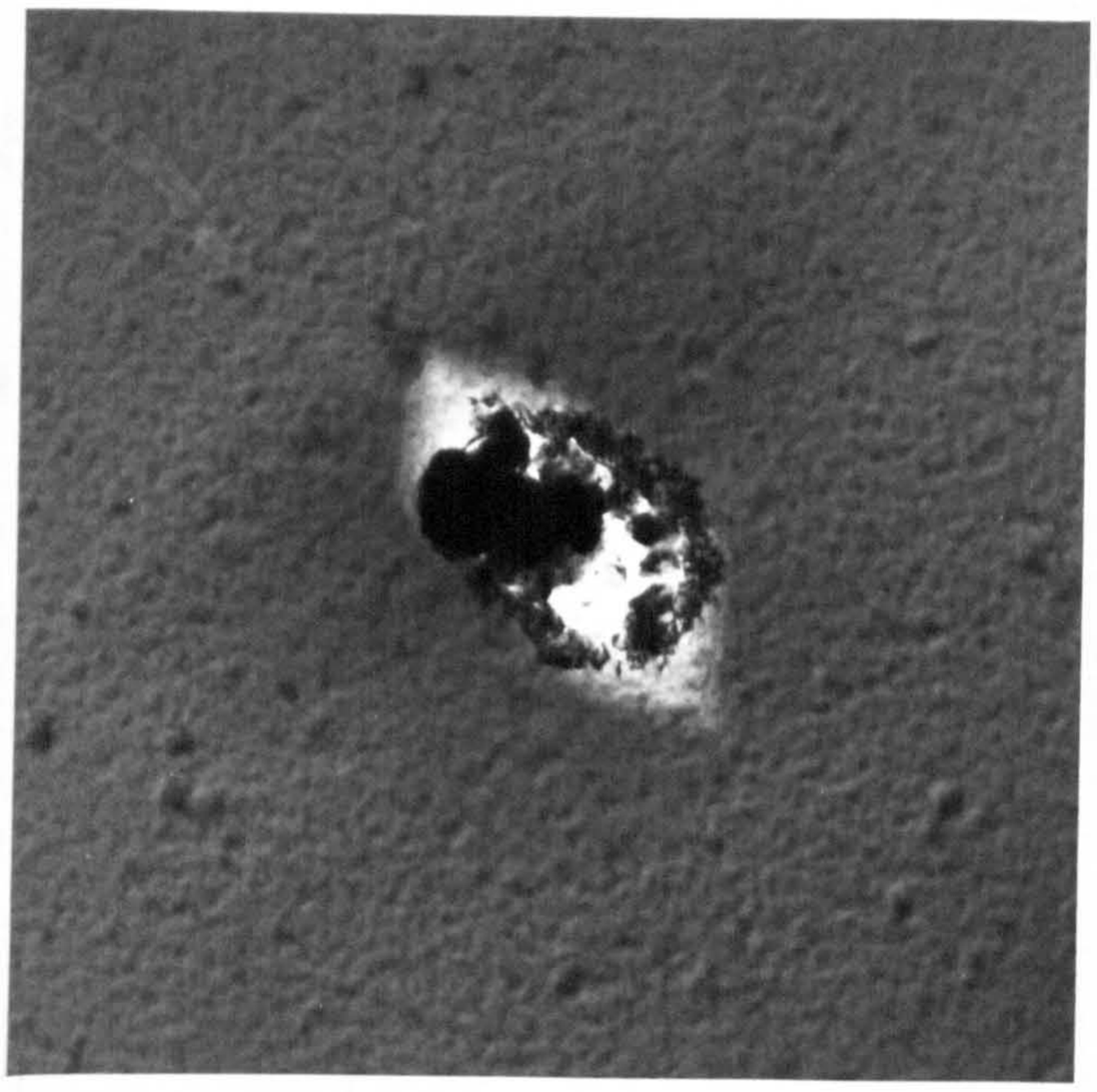

4.4 BF TEM micrograph of an oval defect in G43 (with central particulate).

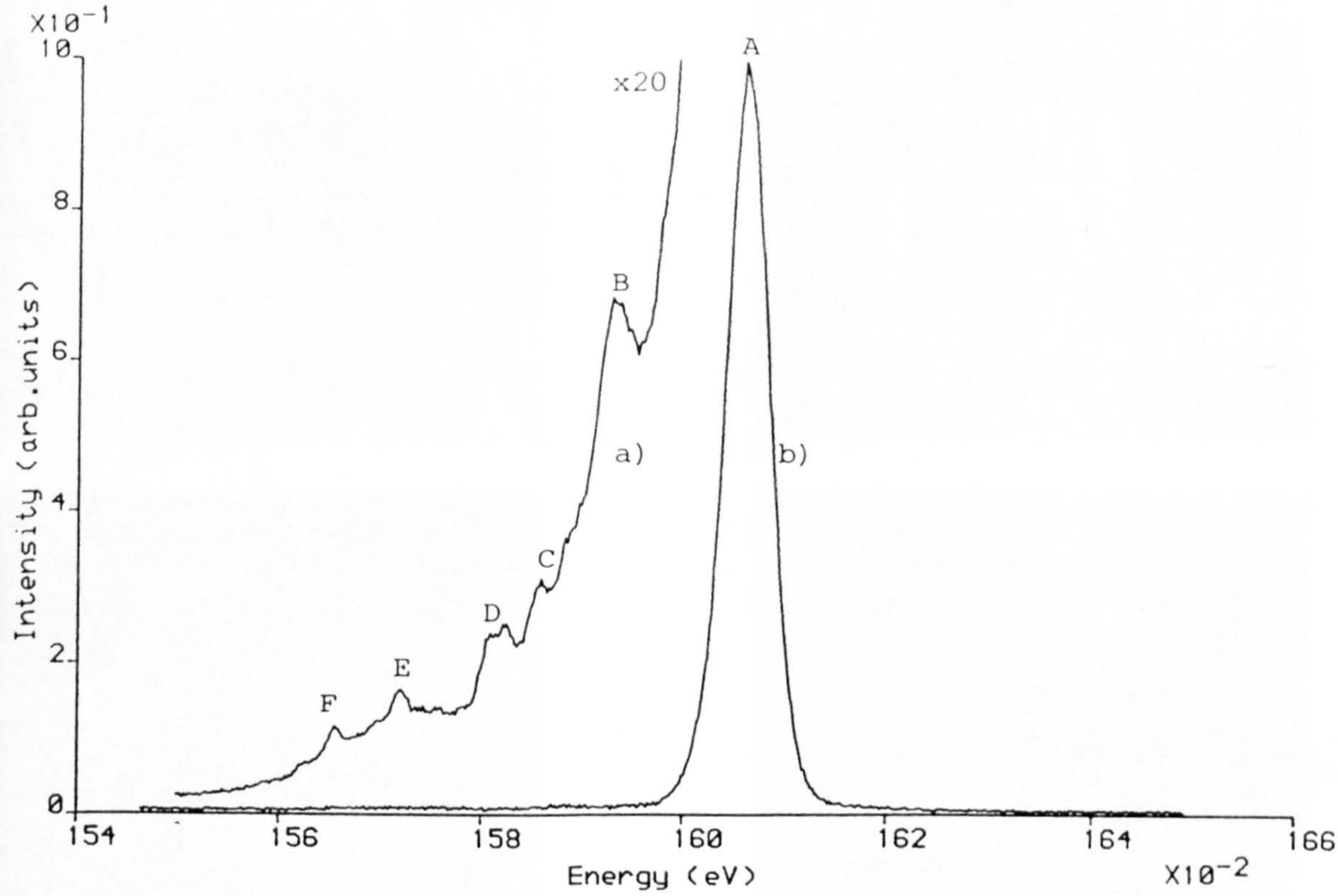

4.5 Comparison of CL spectra from a) an oval defect and b) adjacent unfaulted crystal (sample G43).

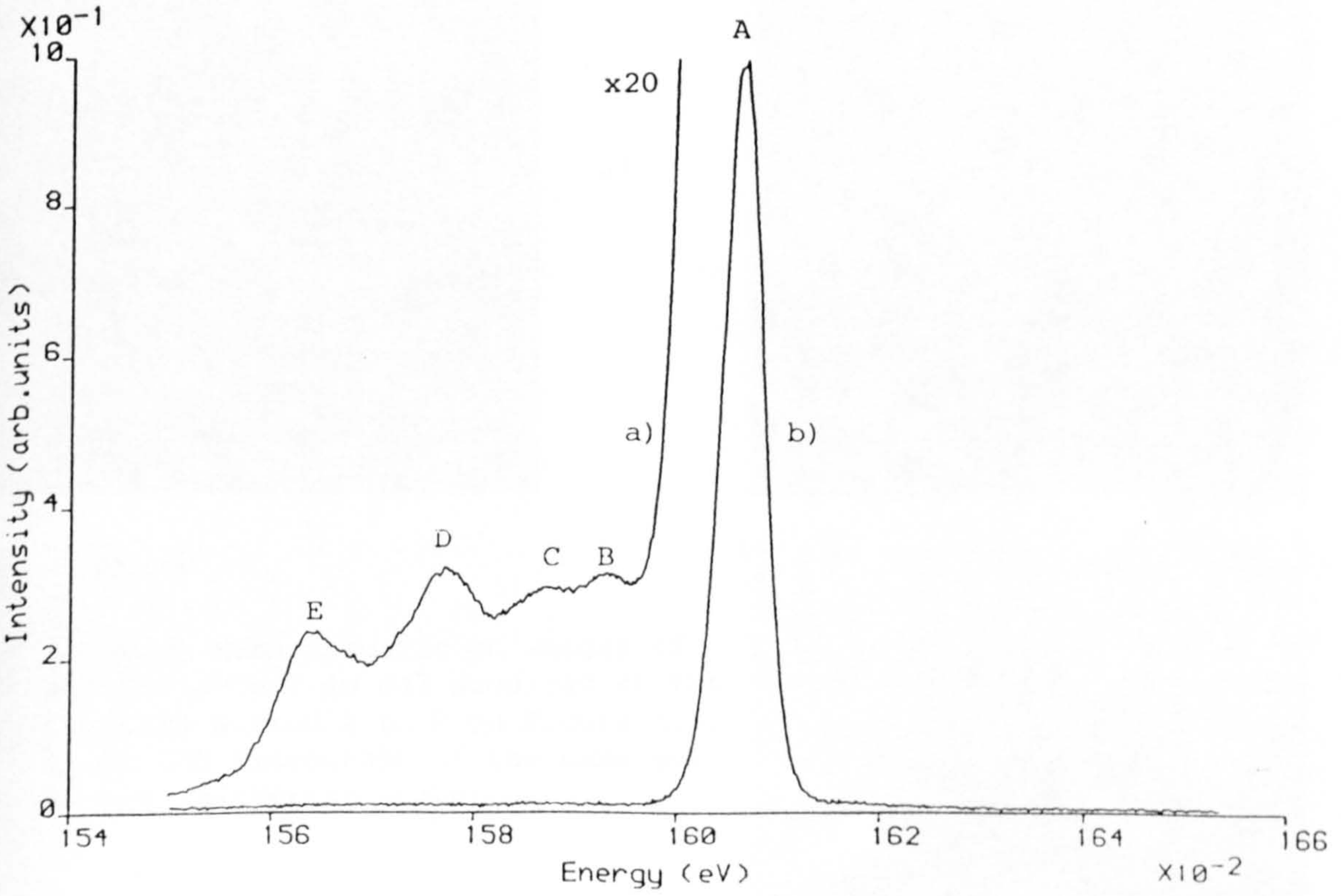

4.6 Comparison of CL spectra from a) an oval defect and b) adjacent unfaulted crystal (sample G43).

a)

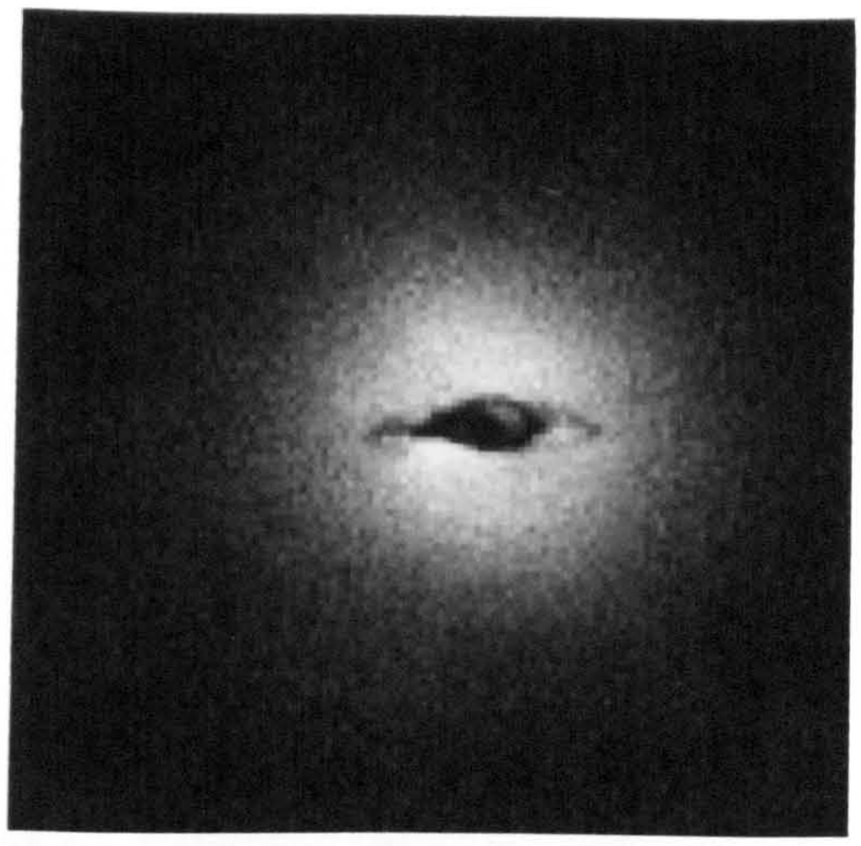

b)

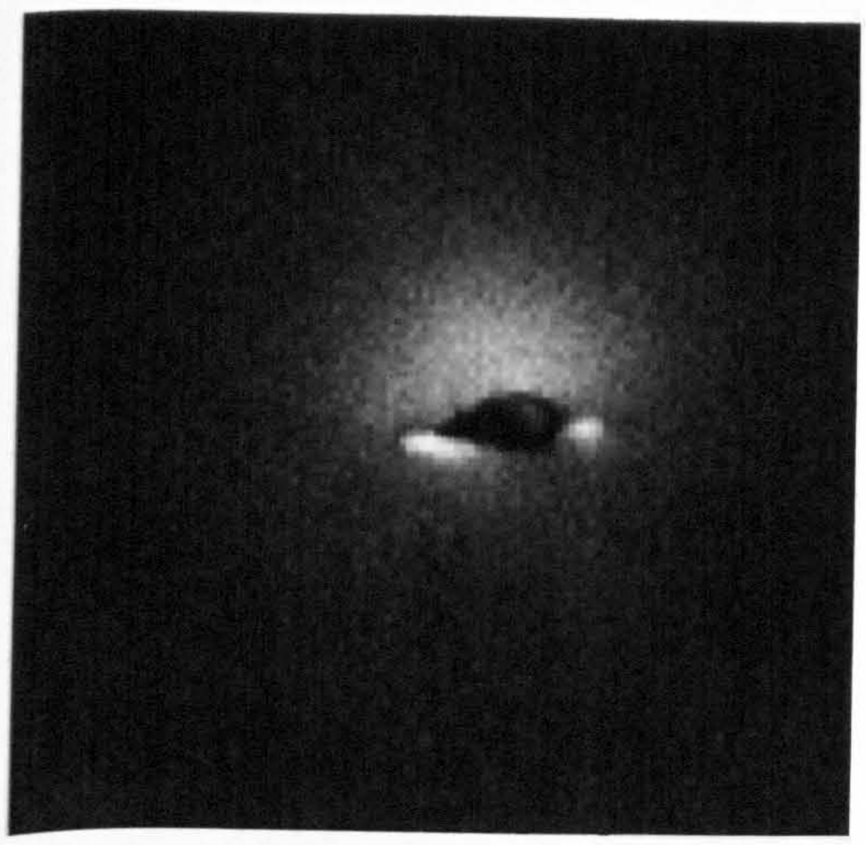

c)

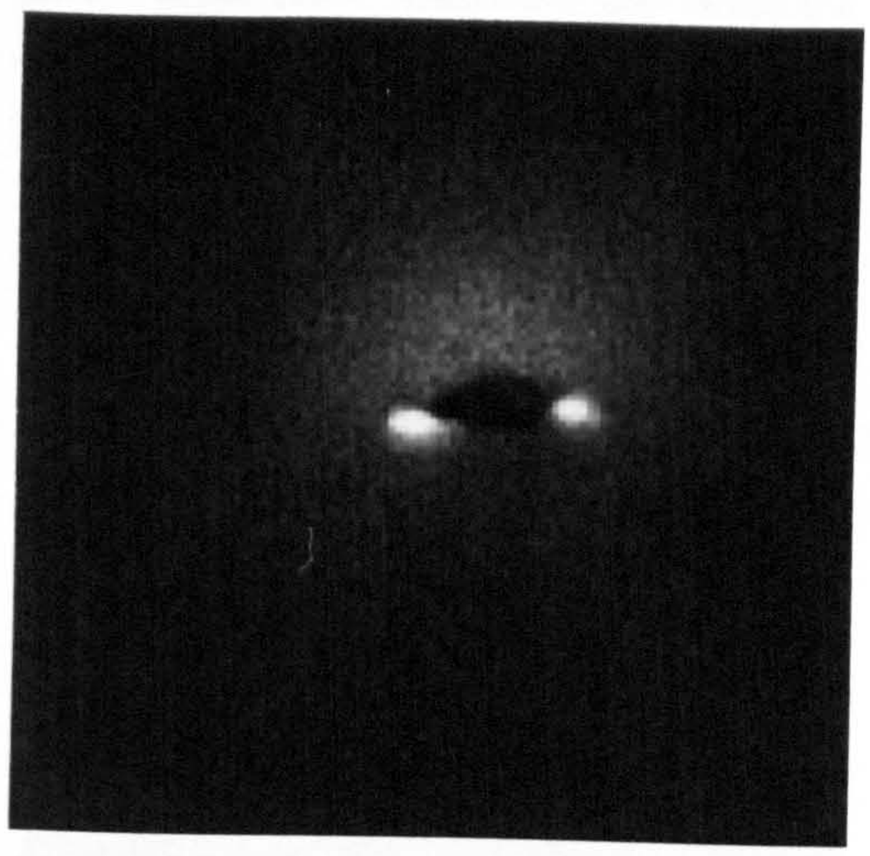

d)

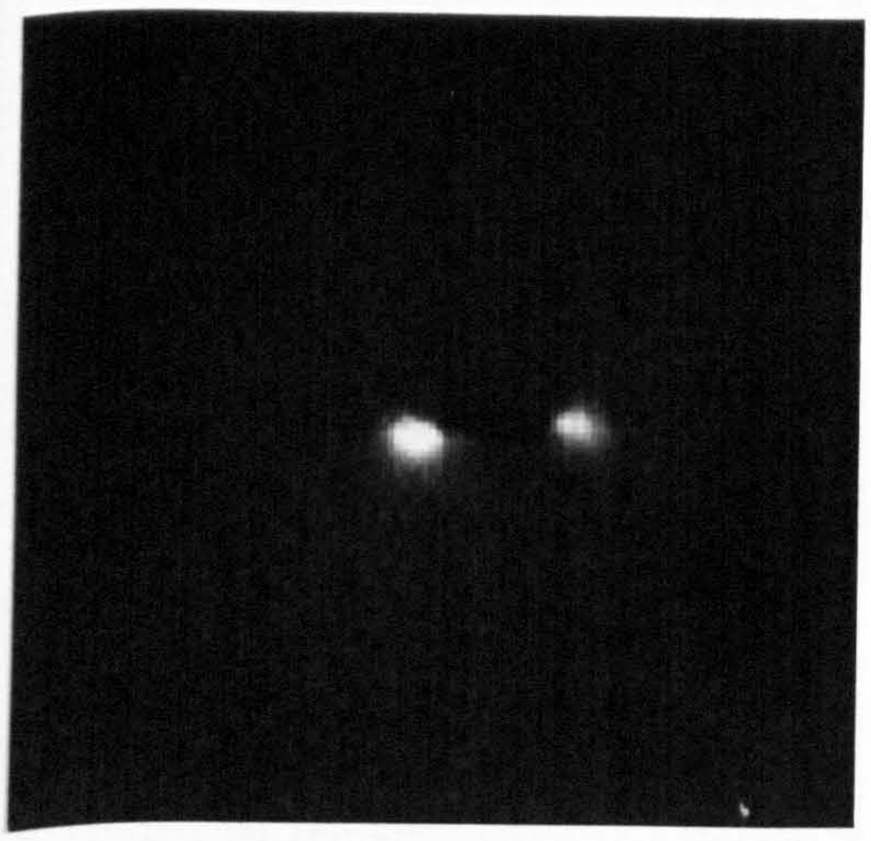

e)

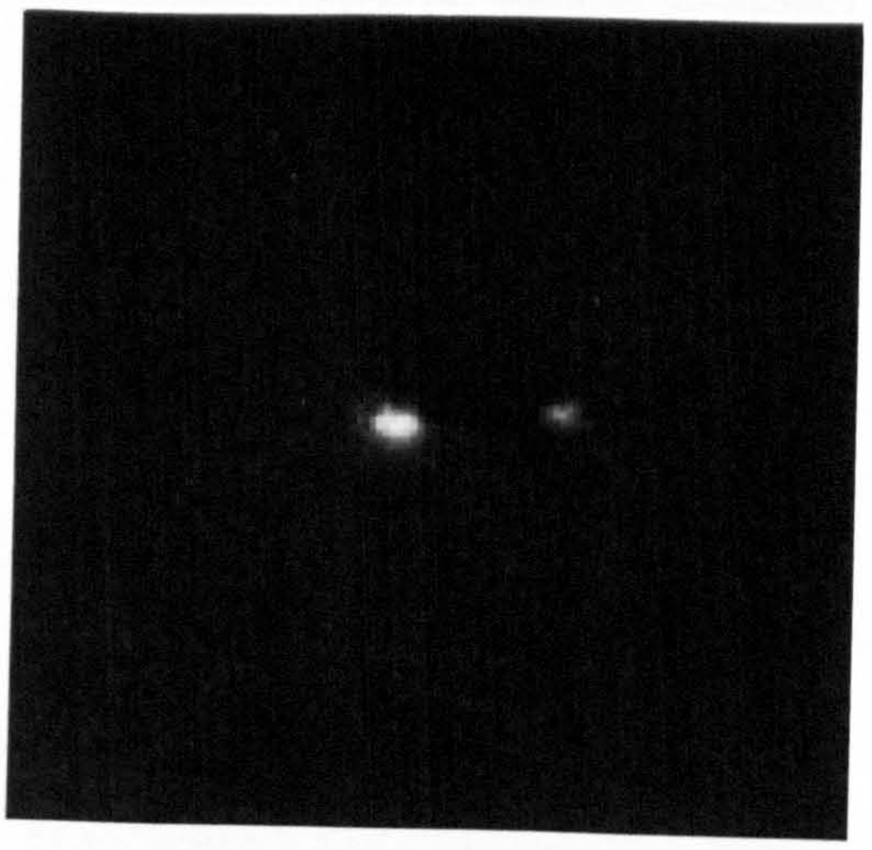

f)

2 µm

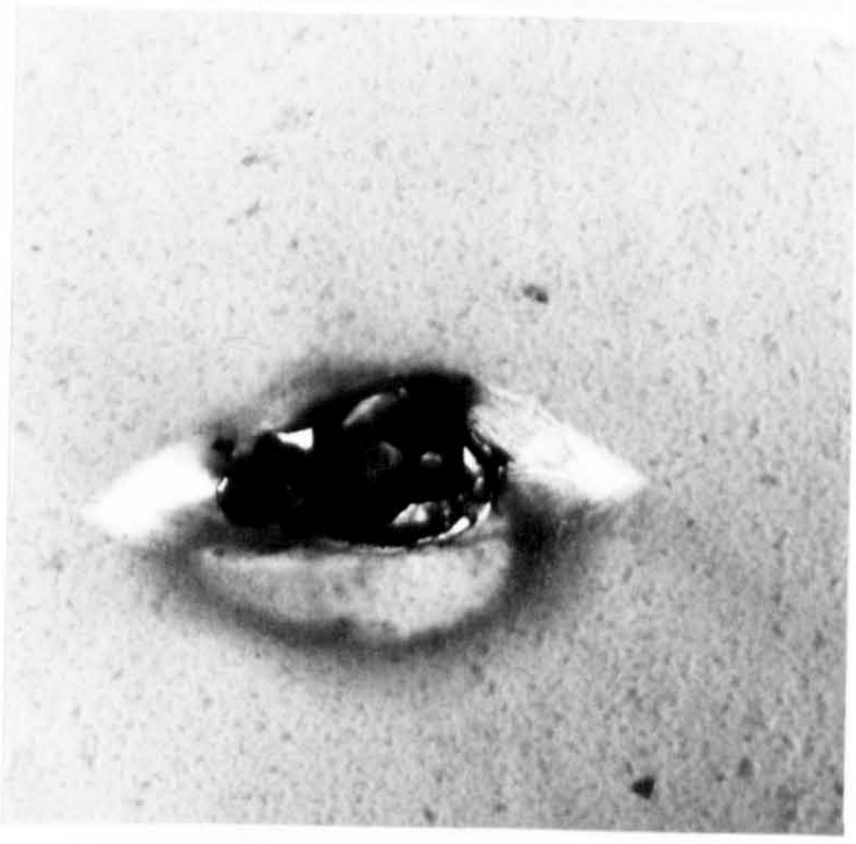

g)

1 µm

g=220

4.7 a) to f) Monochromatic CL images of an oval defect in G43 acquired at the energies marked A to F on Figure 4.5. g) BF TEM micrograph of the same oval defect (different scale).

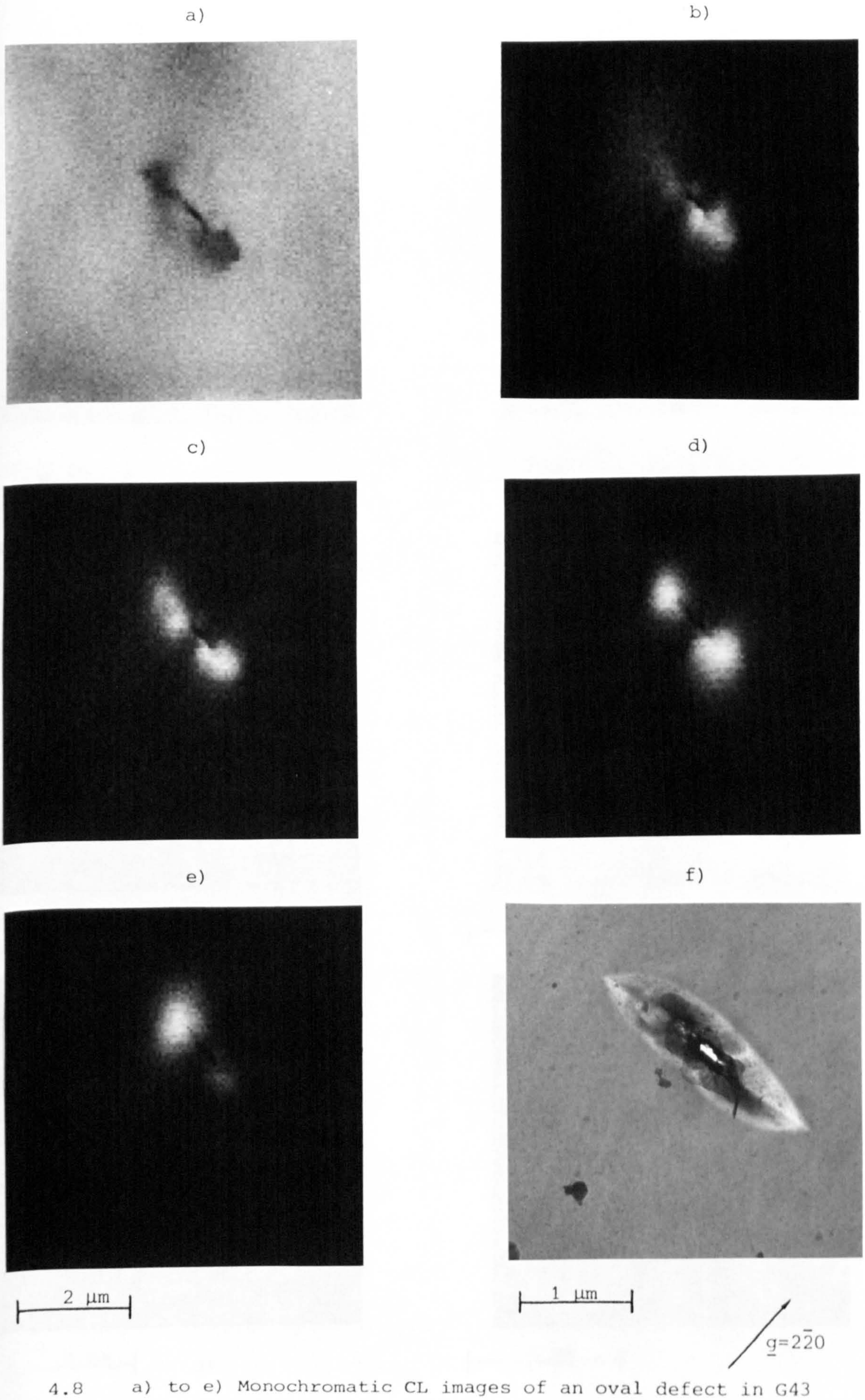

4.8 a) to e) Monochromatic CL images of an oval defect in G43 acquired at the energies marked A to E on Figure 4.6.
f) BF TEM micrograph of the same oval defect (different scale)

2 µm a)

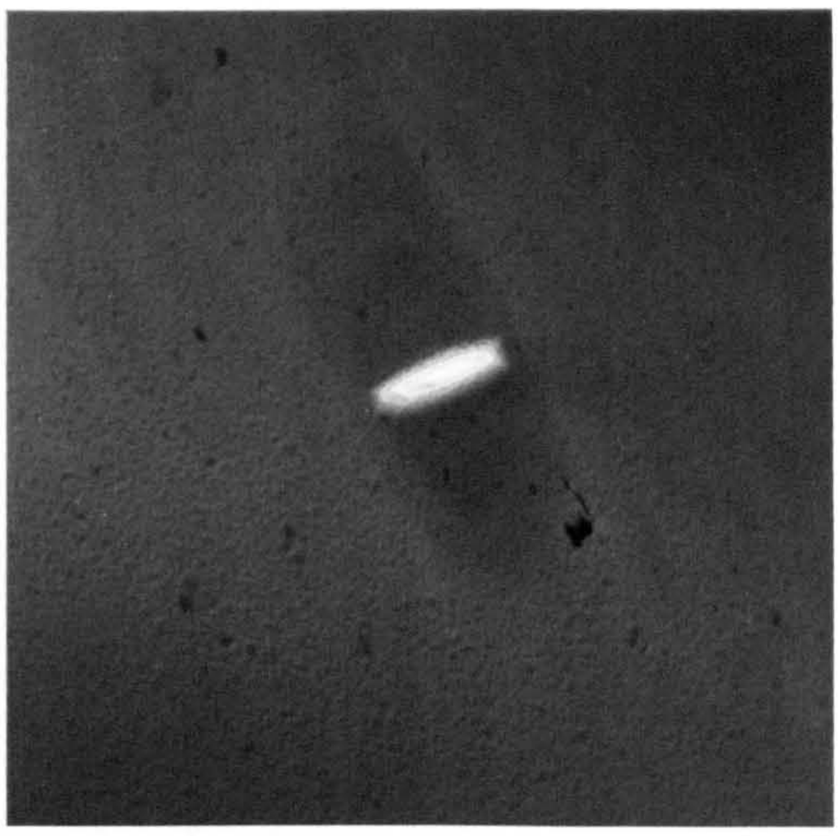

3 µm b)

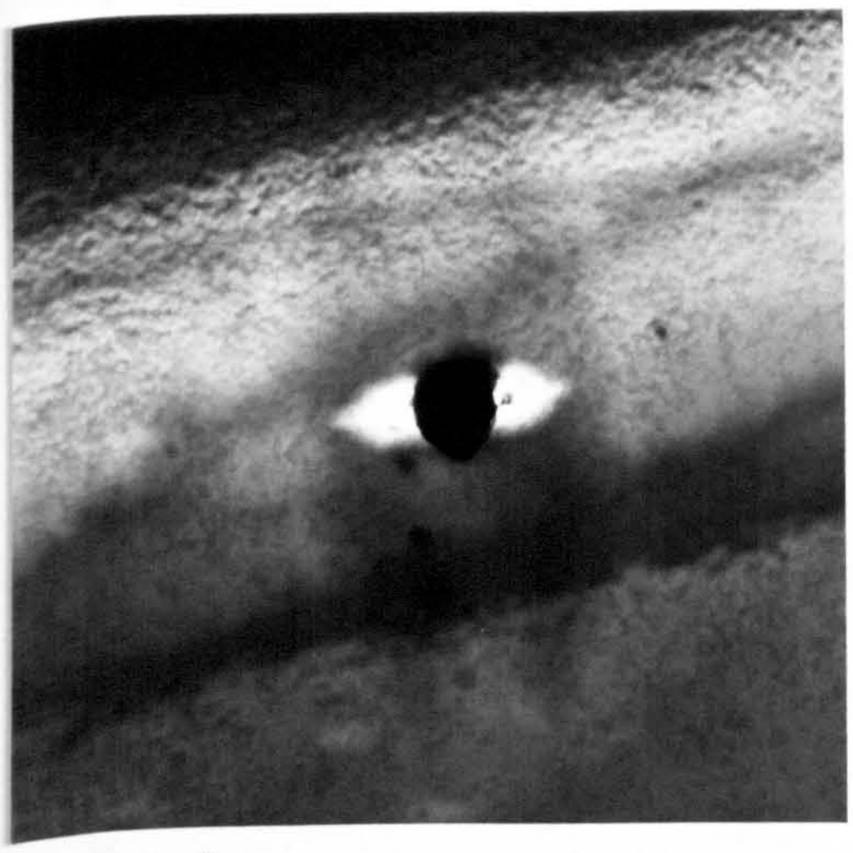

3 µm c)

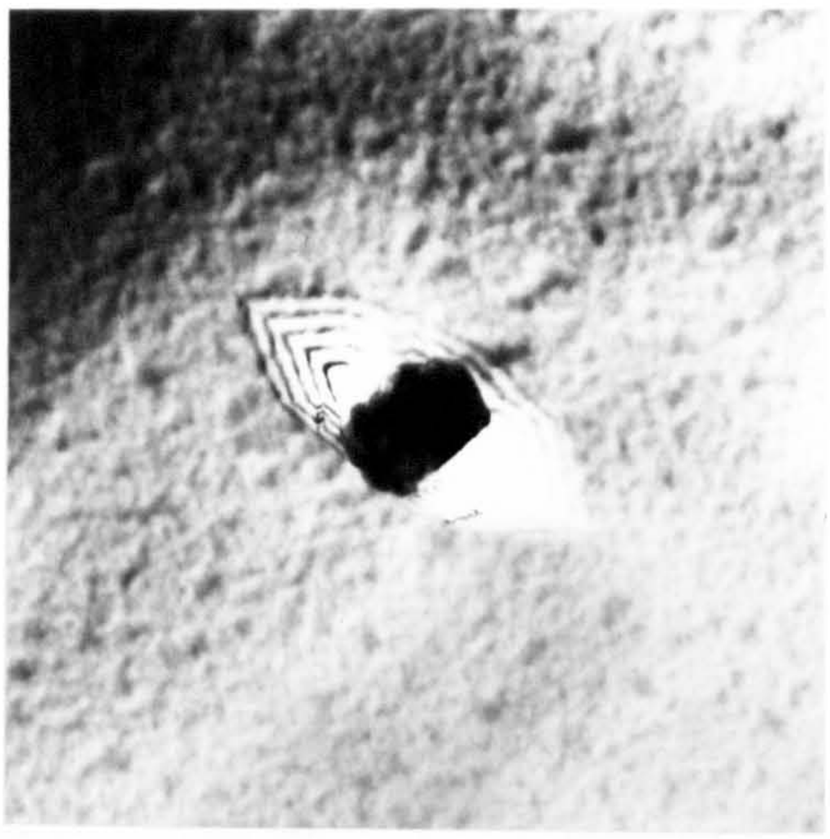

2 µm d)

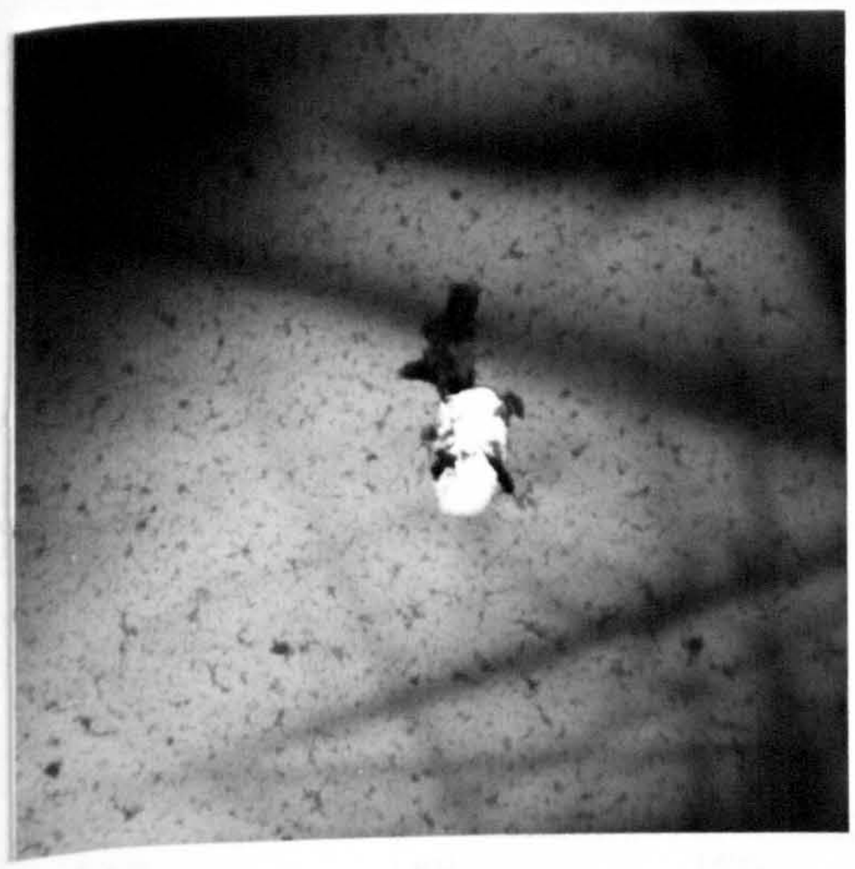

5 µm e)

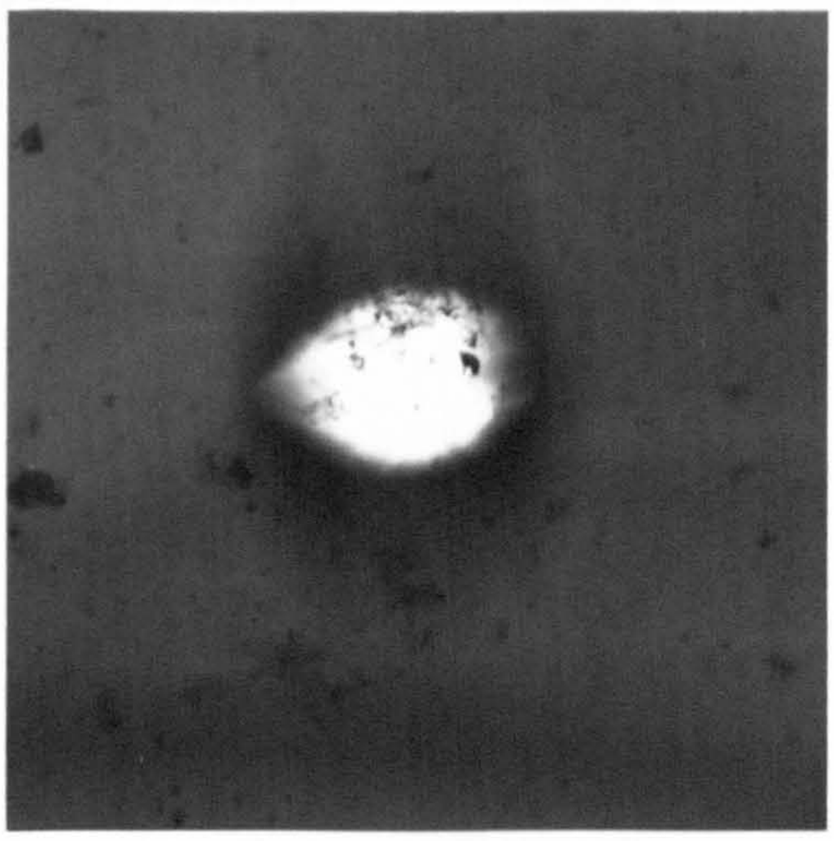

4 µm f)

4.9 BF TEM micrographs of typical oval defects in @1965.

a)

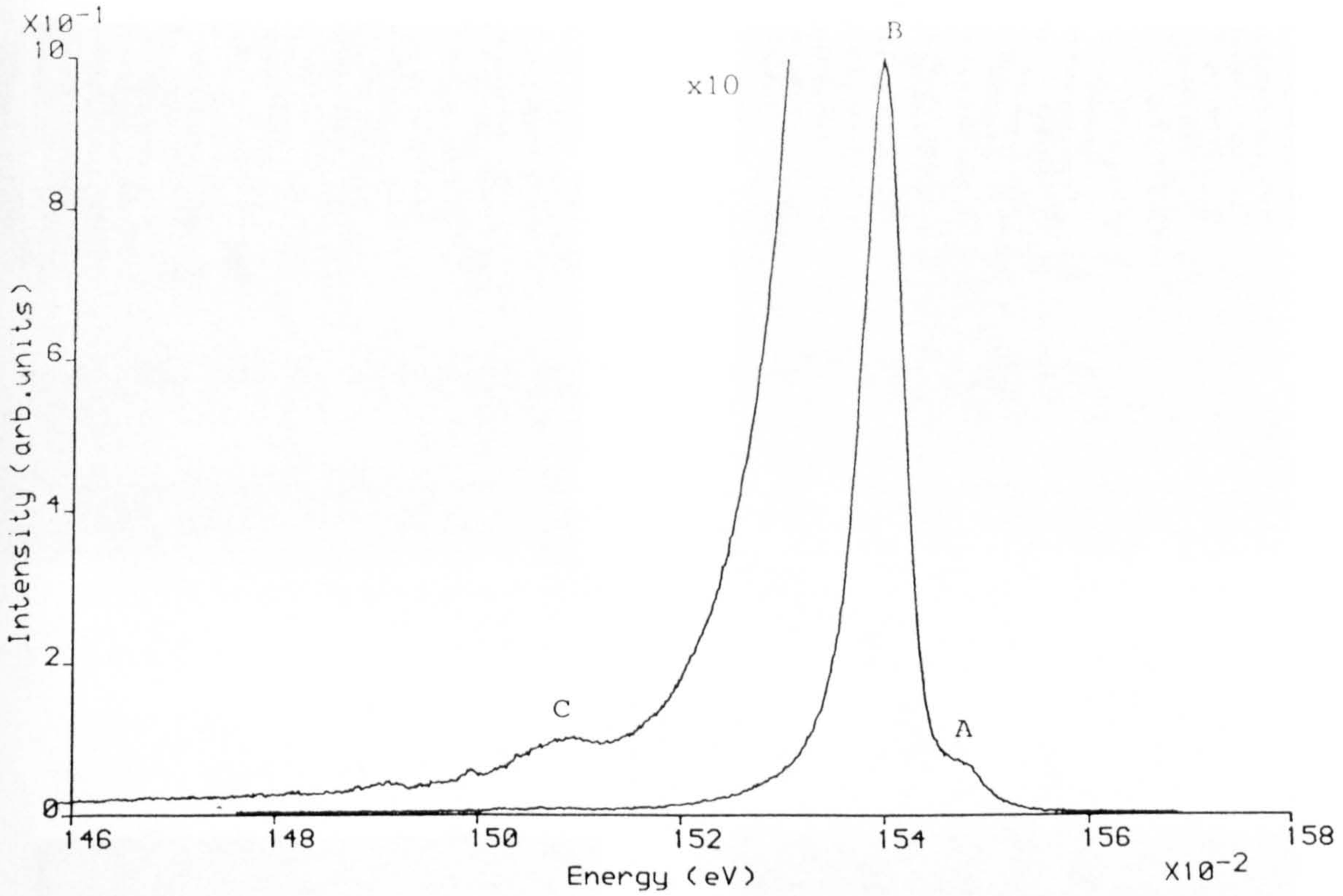

b)

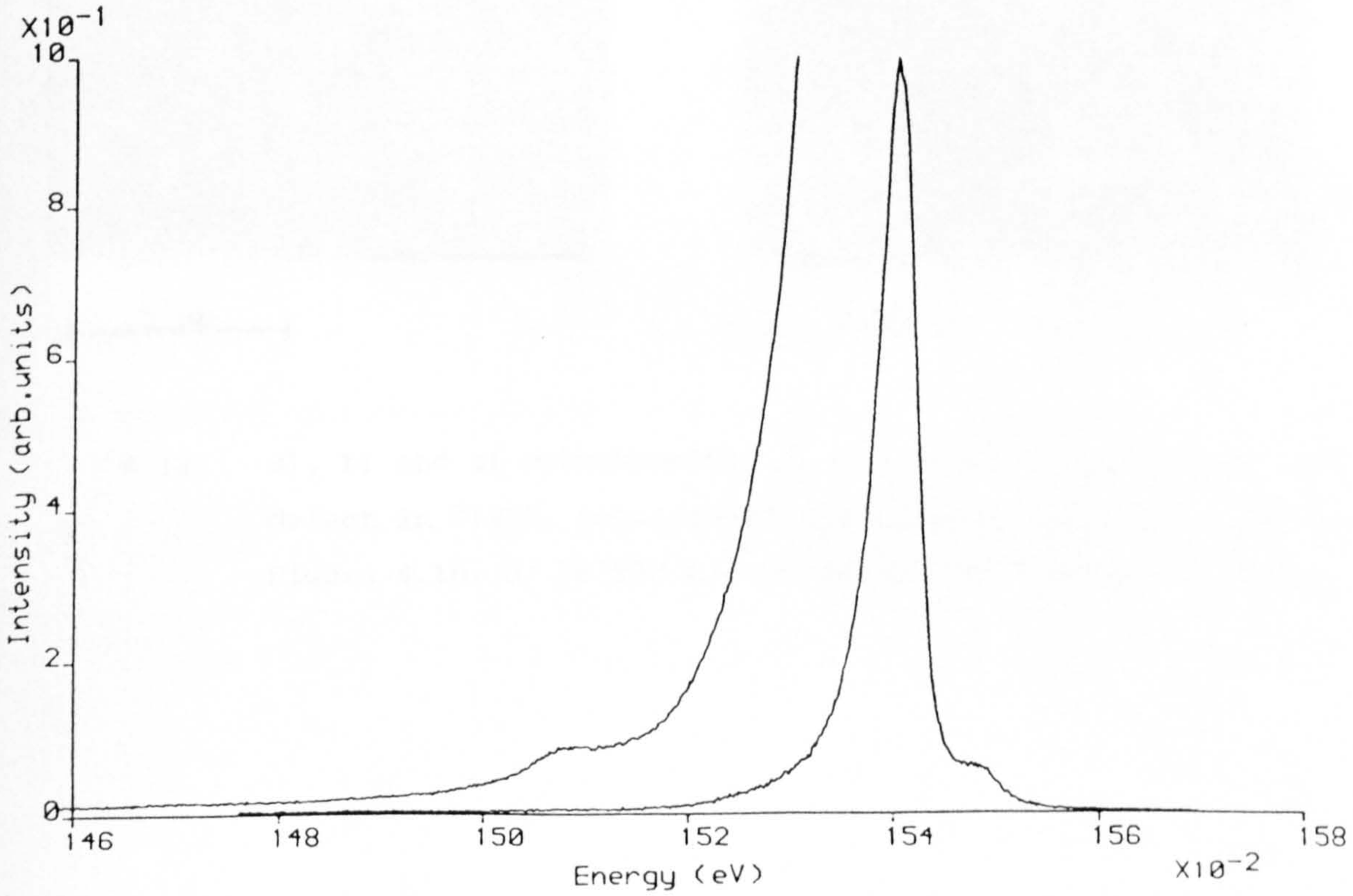

4.10 a) CL spectrum from a "pit" like oval defect b) CL spectrum from adjacent unfaulted crystal.

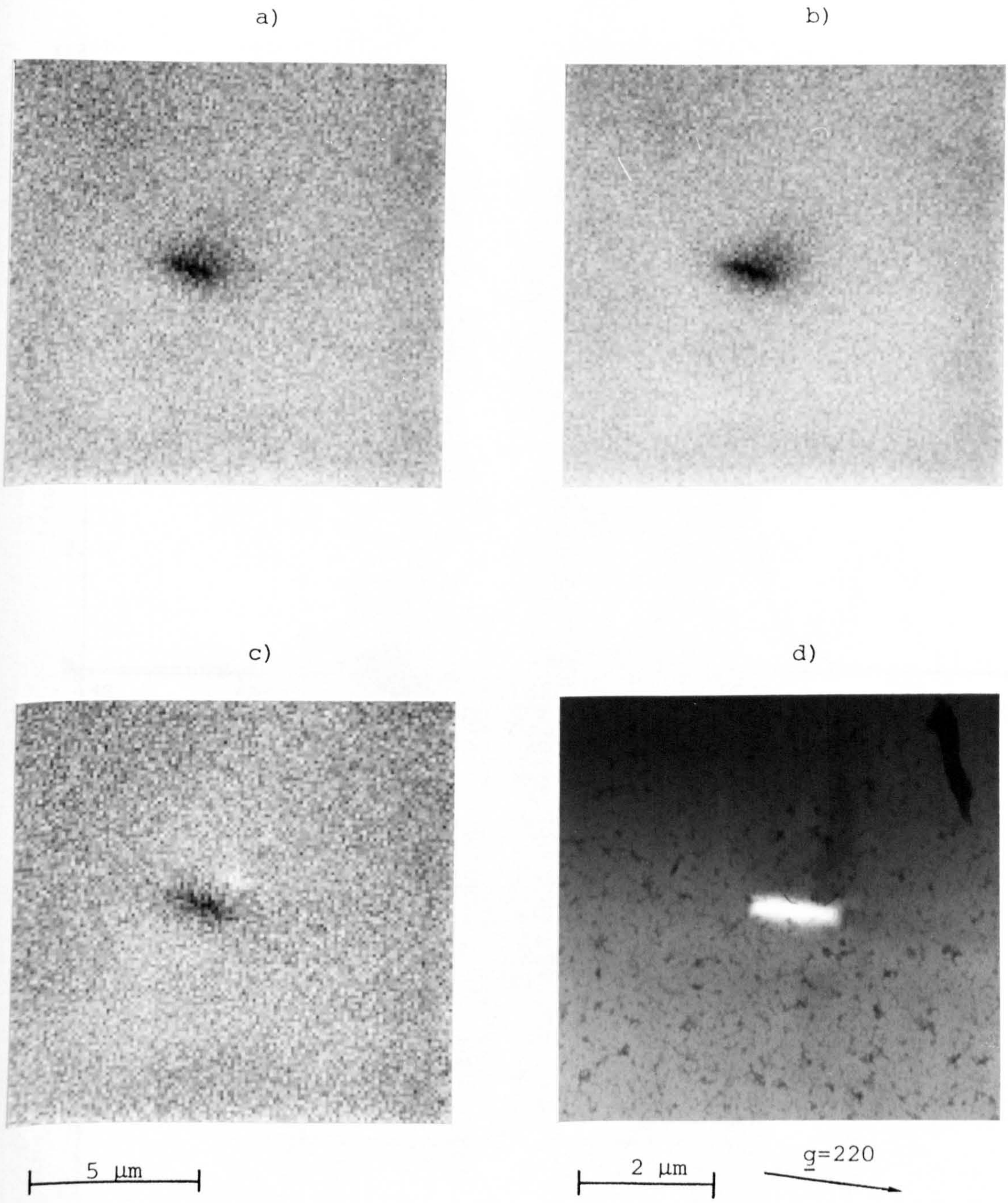

4.11 a), b) and c) Monochromatic CL images of a "hole" type oval defect in @1965, acquired at the energies marked A,B and C on Figure 4.10. d) BF TEM micrograph of the same oval defect.

a)

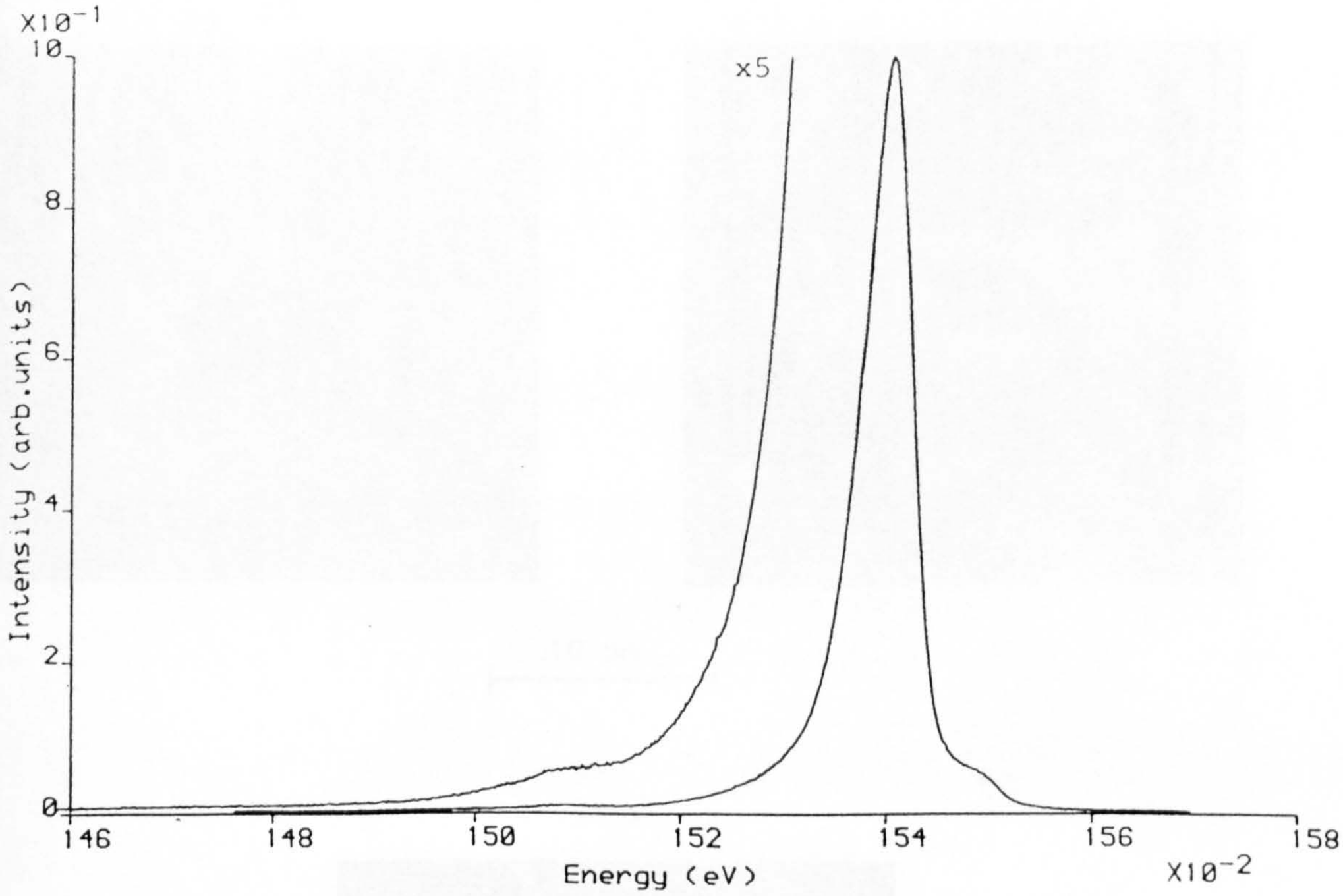

b)

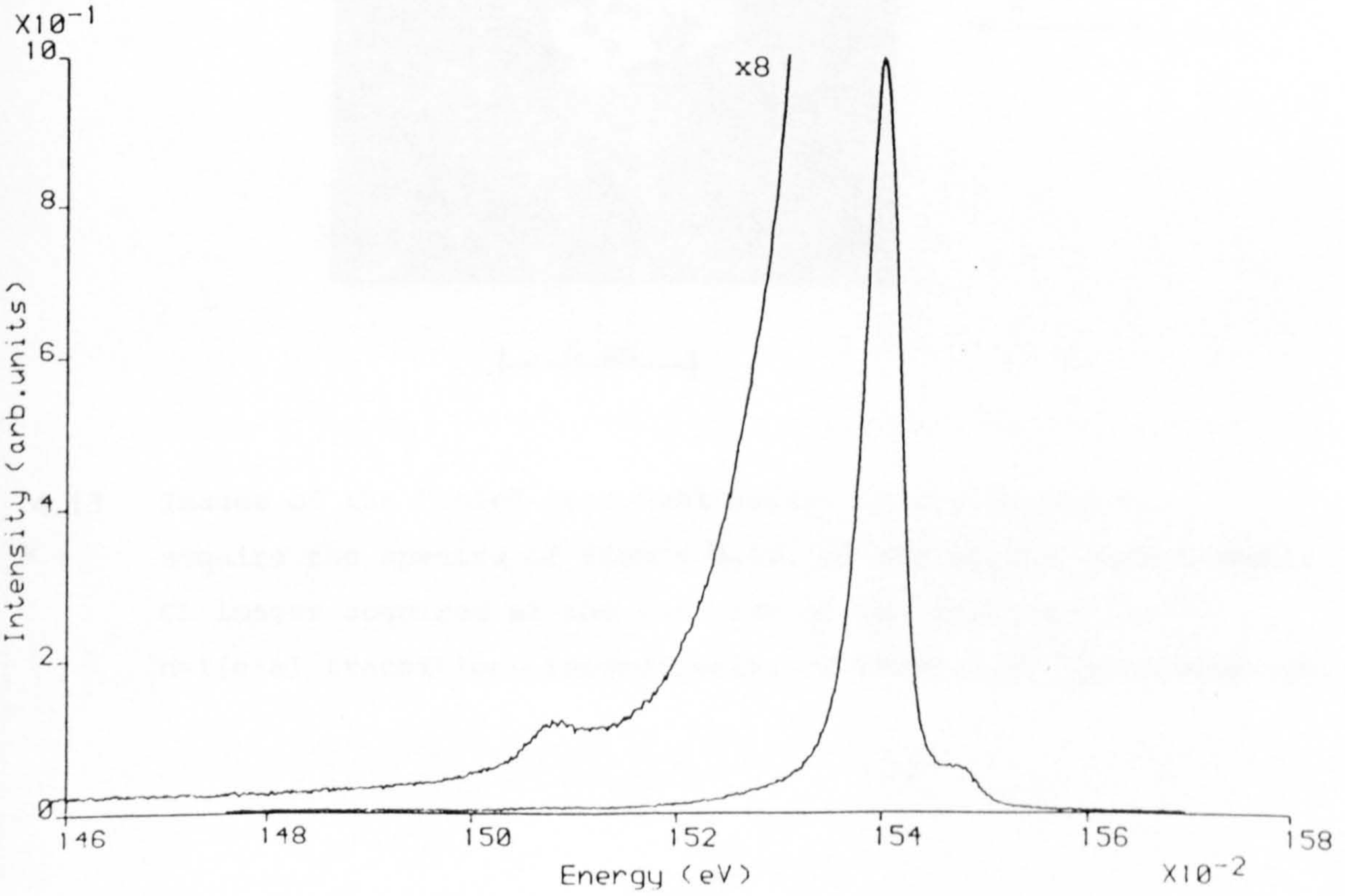

4.12 a) CL spectra from a "hole" type oval defect in @1965.

b) CL spectra from adjacent unfaulted crystal.

a)

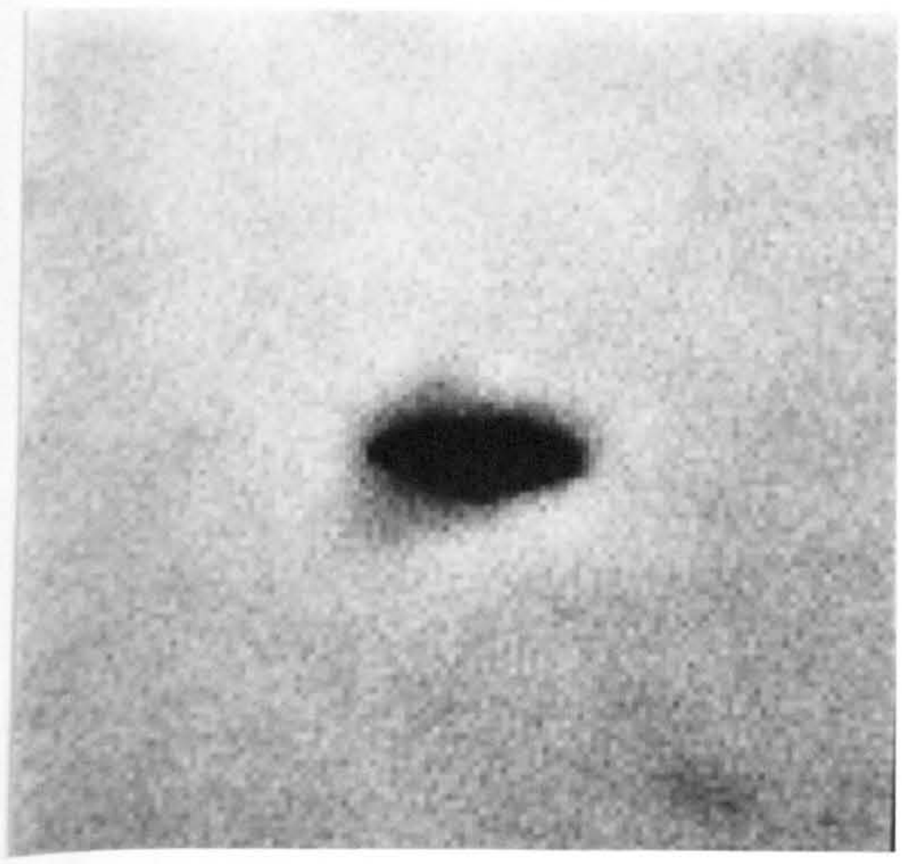

10 μm

b)

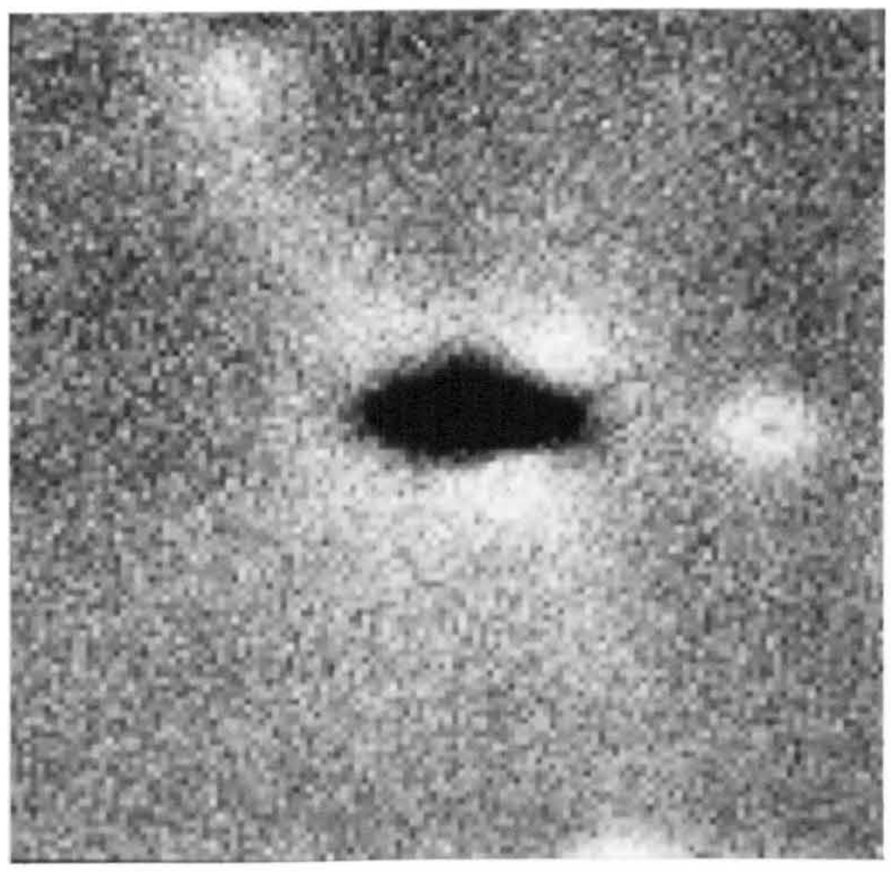

c)

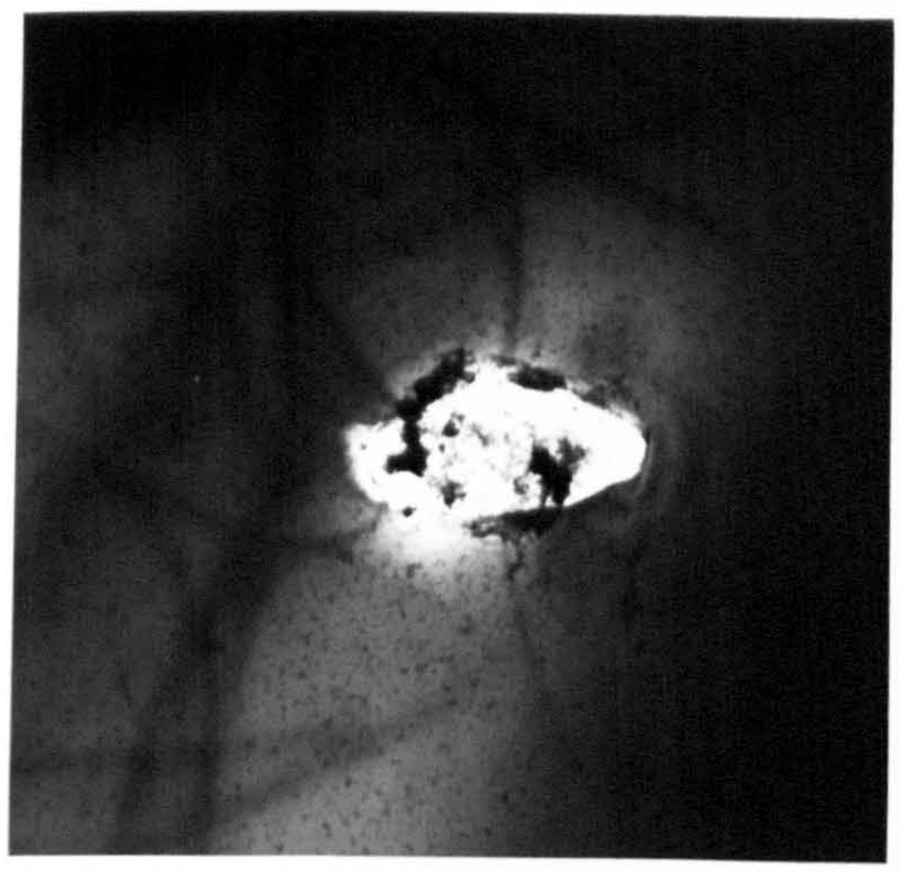

6 μm

g=220

4.13 Images of the "hole" type oval defect in @1965 used to acquire the spectra of Figure 4.12. a) and b) are monochromatic CL images acquired at the energies of the n=1(e-hh) and n=1(e-a) transitions respectively. c) shows a BF TEM micrograph.

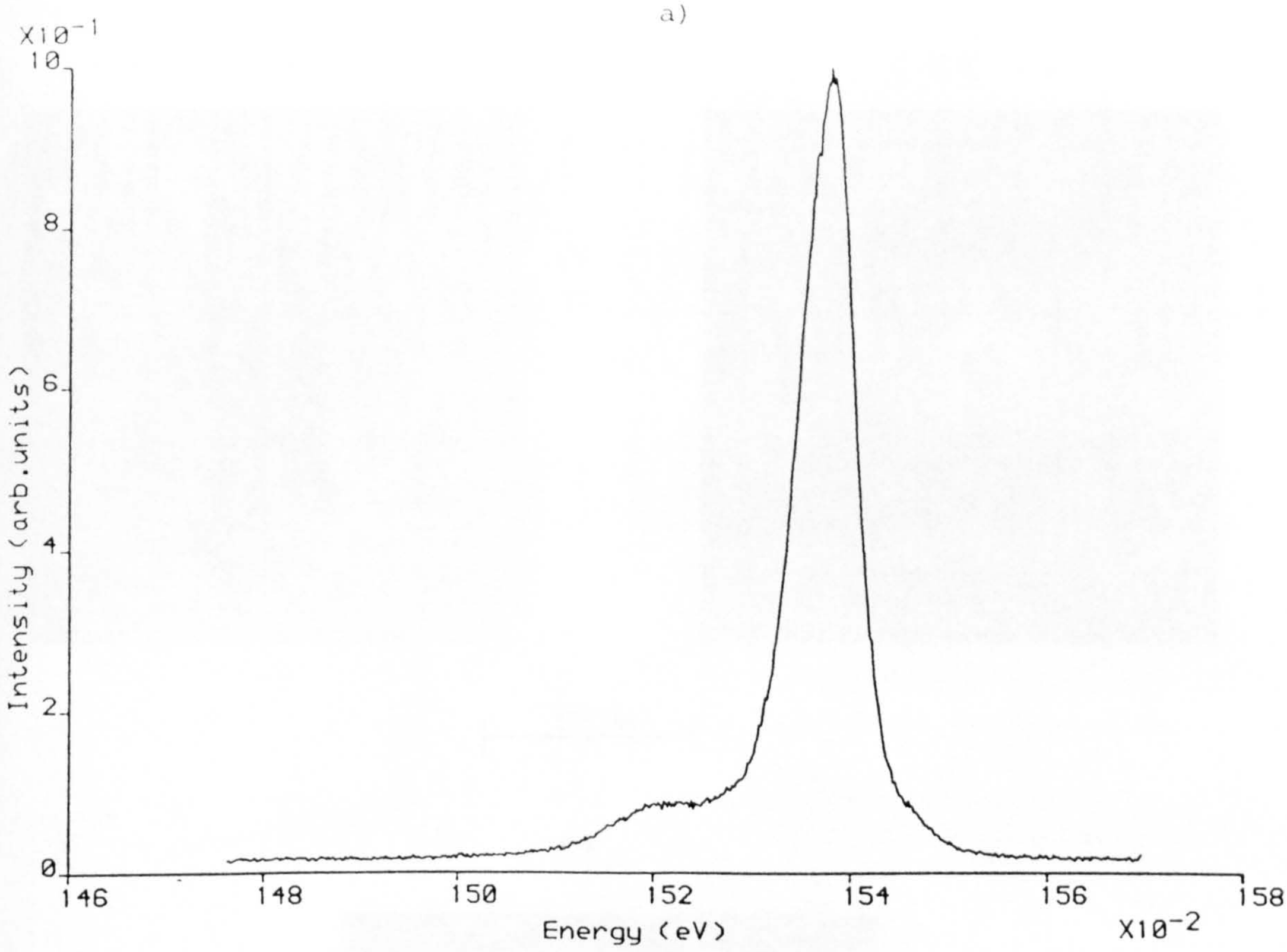

4.14 a) CL spectrum from a "hole" type oval defect (with over-growth) in @1965. b) CL spectrum from adjecent unfaulted crystal.

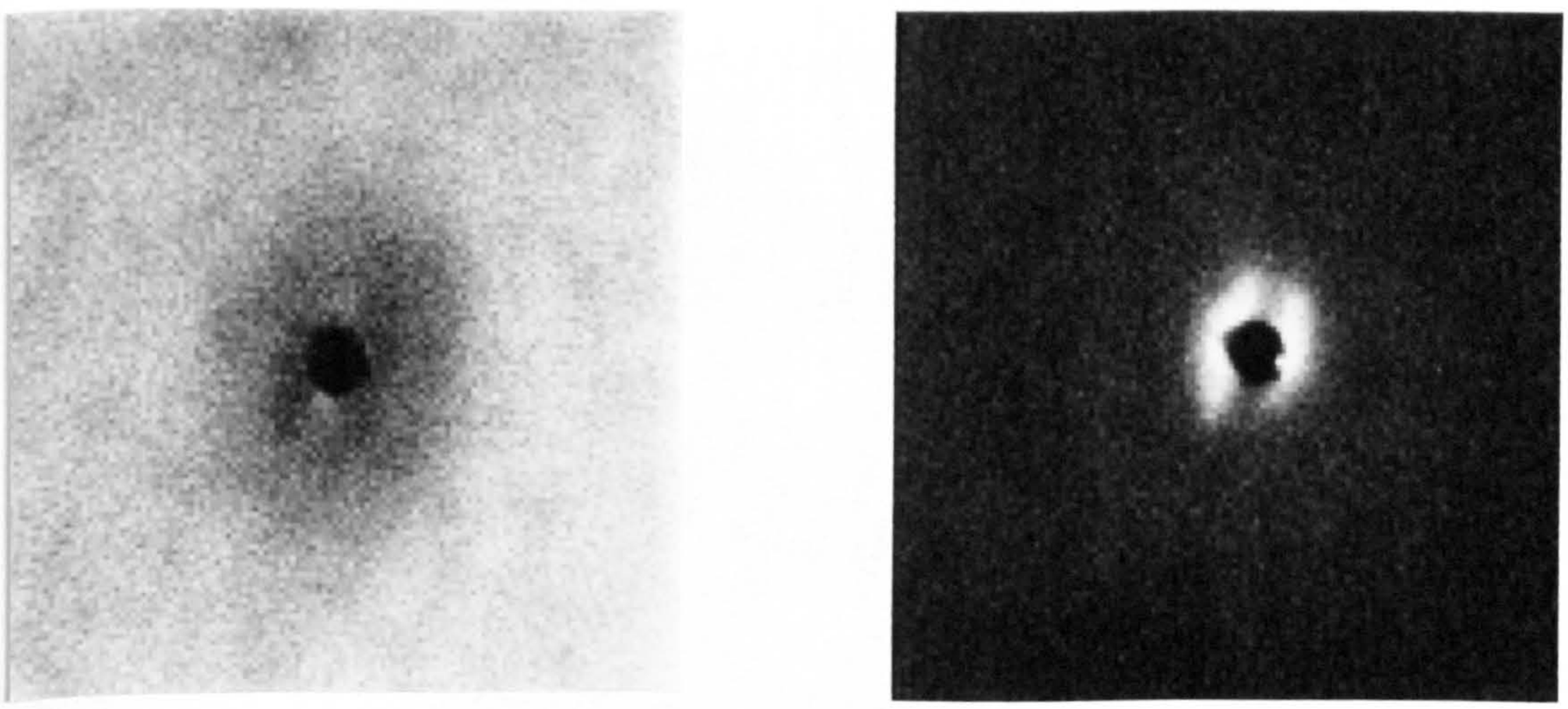

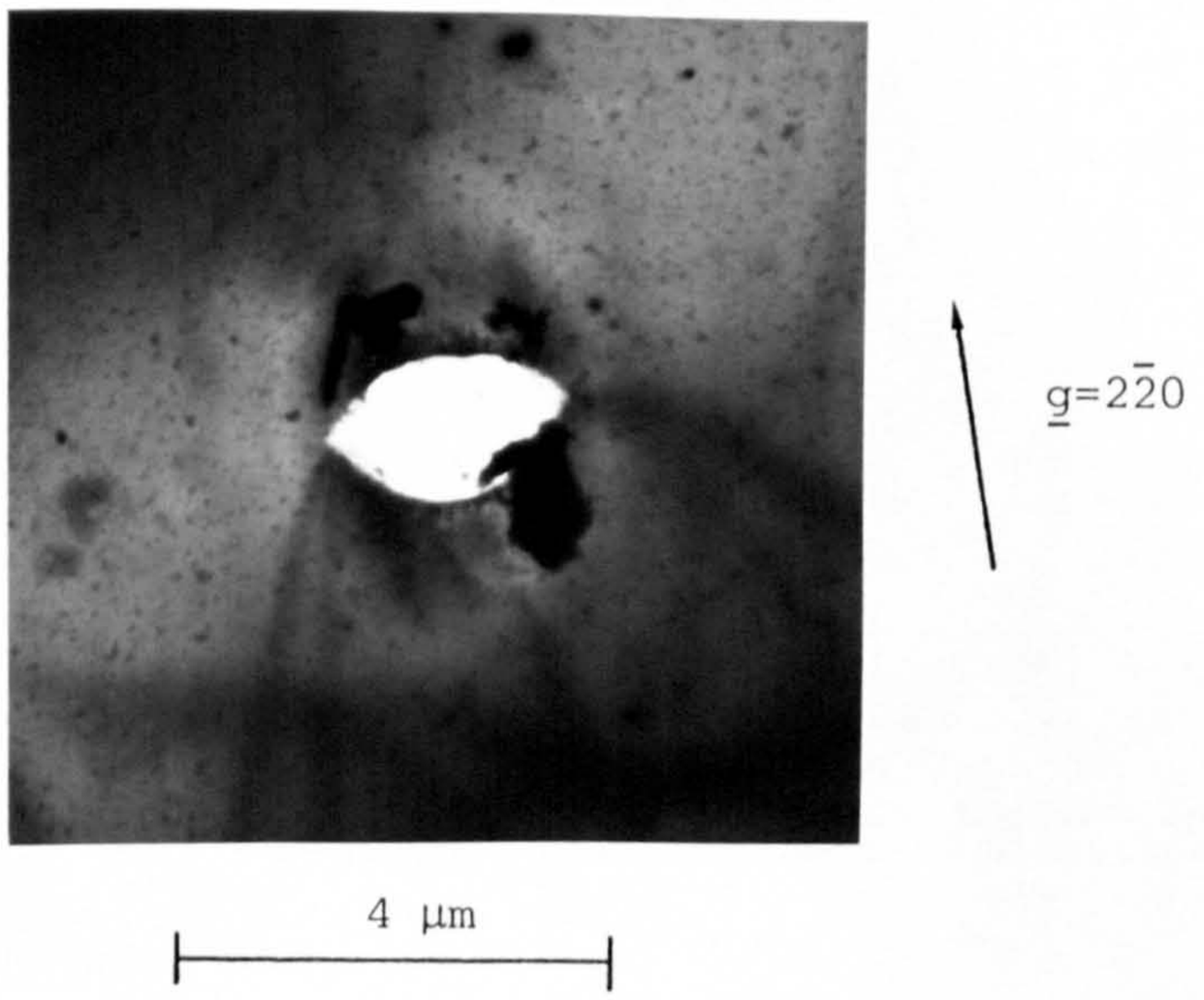

4.15 Images of the oval defect used to acquire the spectrum of Figure 4.14. a) and b) monochromatic CL images acquired at the energies of the n=1(e-hh) and n=1(e-a) transitions. c) BF TEM micrograph.

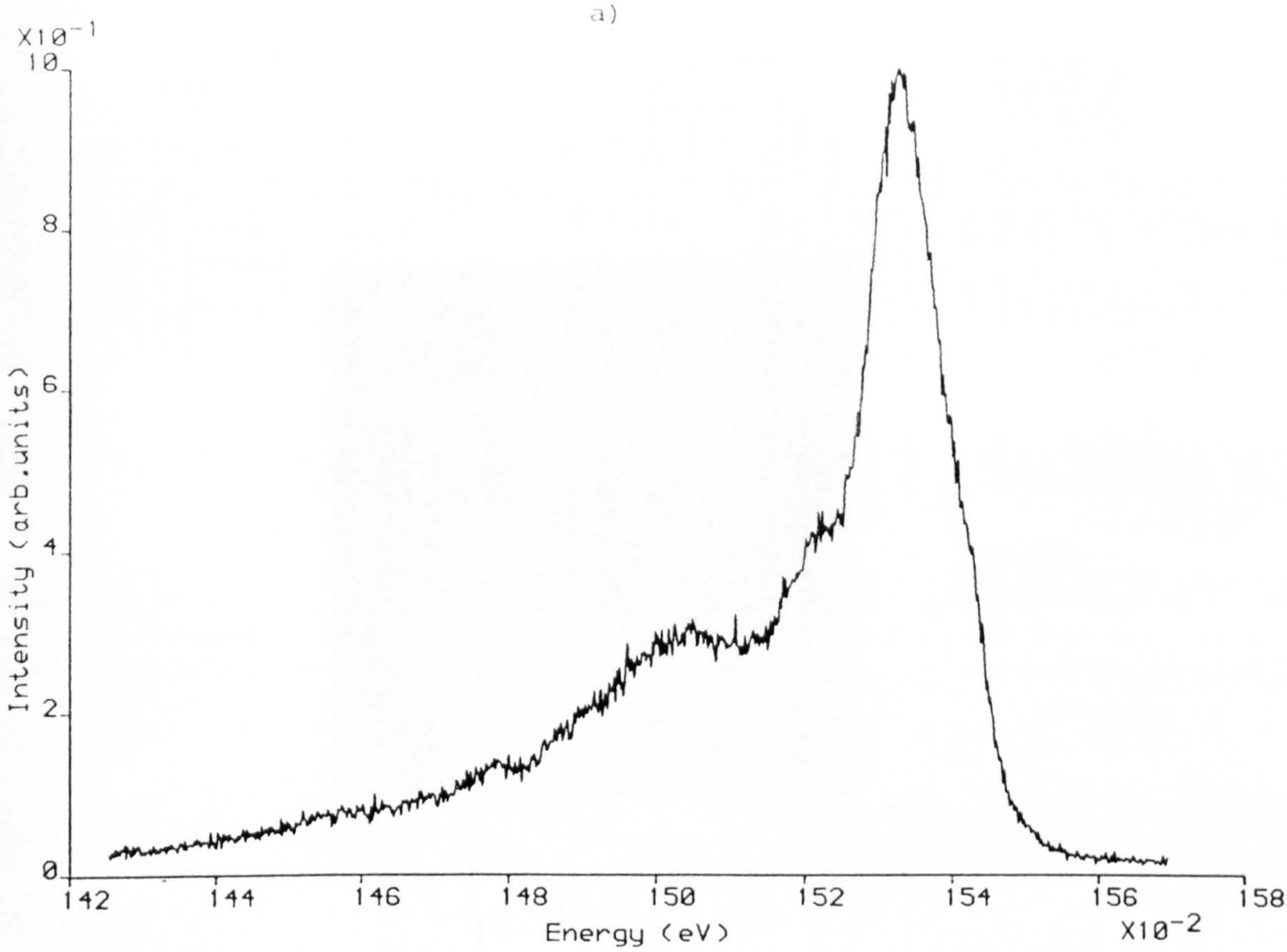

4.16 CL spectra from a) an oval defect in @1965 b) adjacent unfaulted crystal. Note that the peak intensity in a) is approximately 20 times weaker than in b).

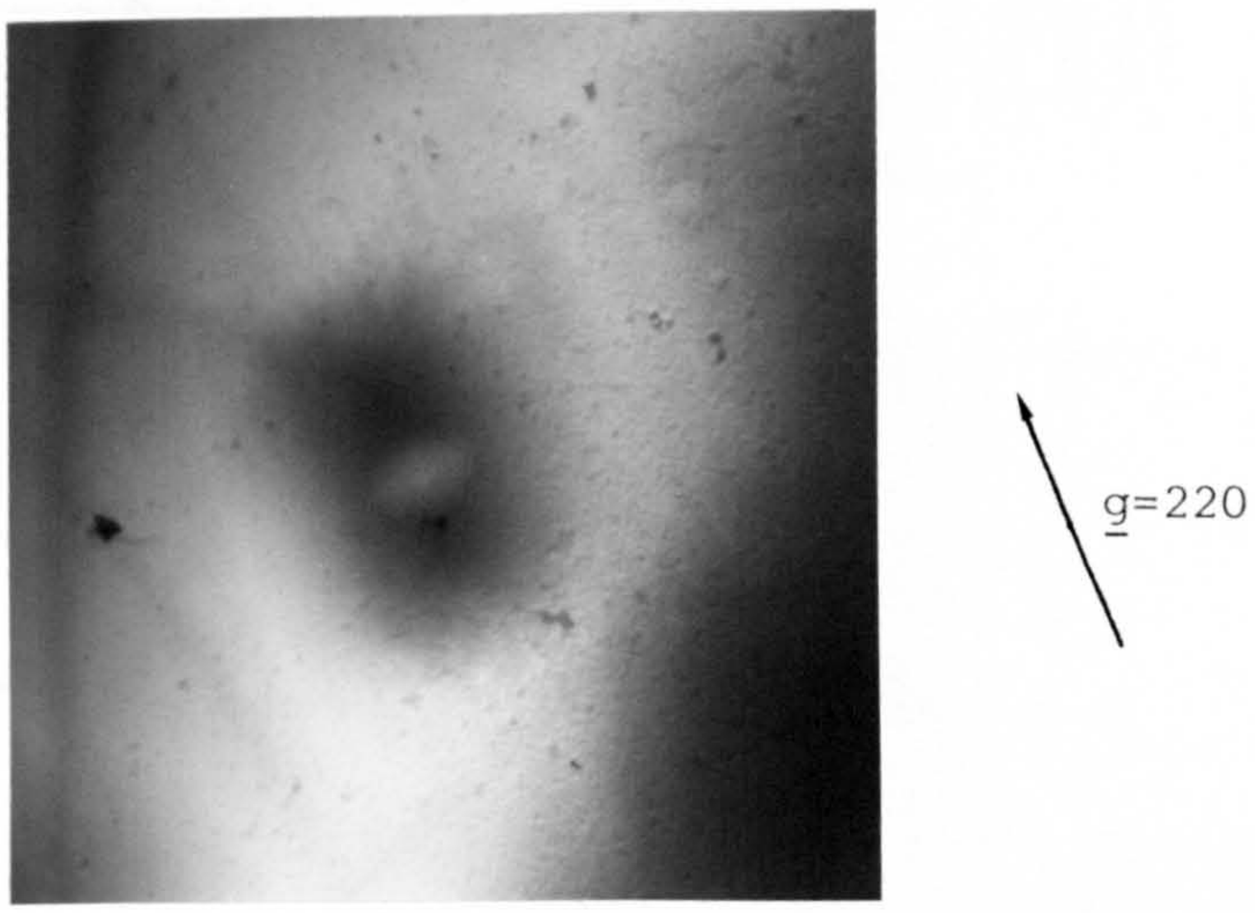

4.17 BF TEM micrograph of a typical oval defect in KLB358.

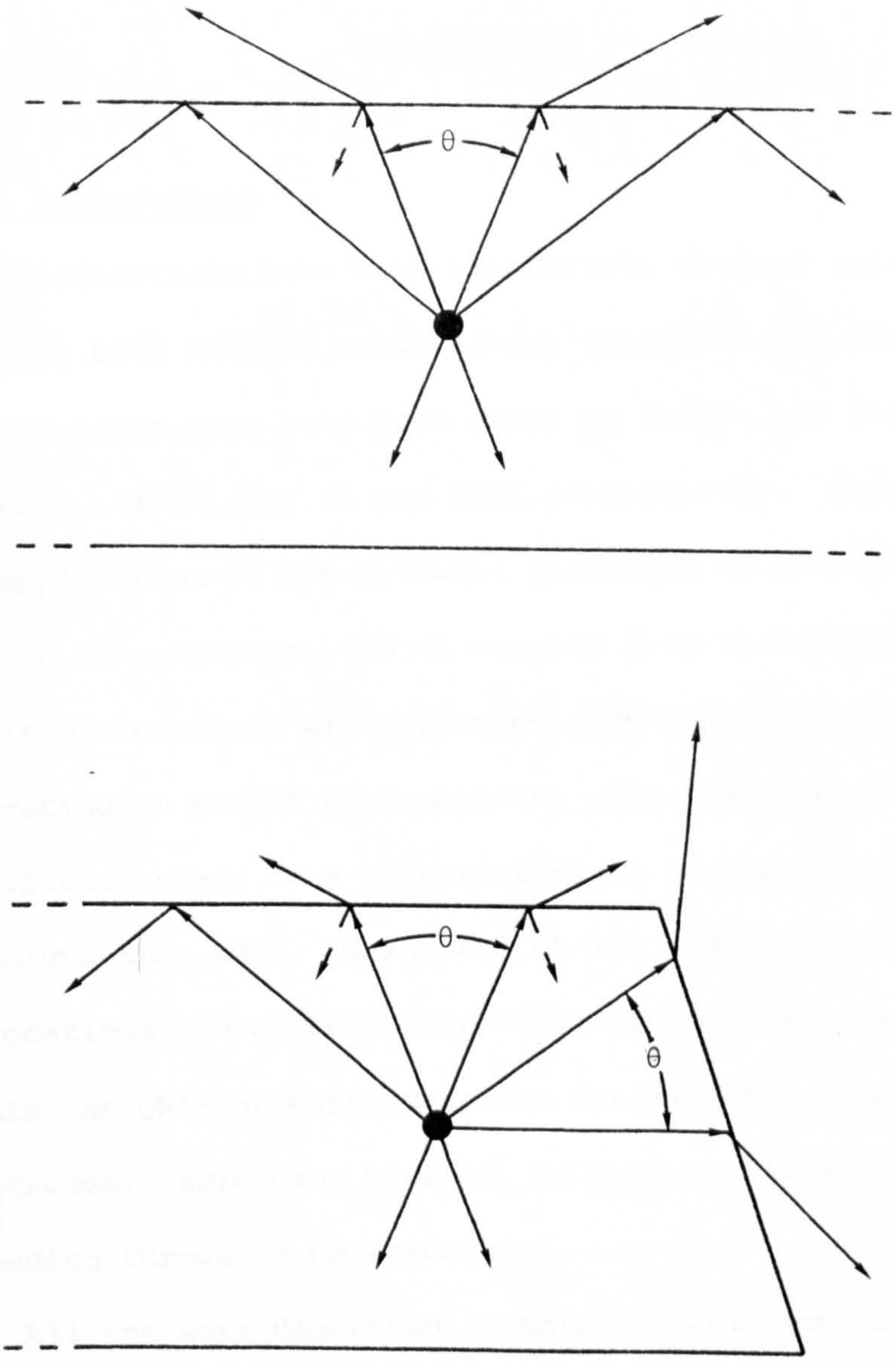

4.18 Schematic diagram illustrating how an increase in surface area of a TEM specimen might allow more CL to escape. θ is the critical angle for total internal reflection.

CHAPTER FIVE

DISLOCATIONS

5.1. Introduction

Dislocations have been extensively studied using both CL and electron beam induced conductivity (EBIC) in the SEM. Reviews for the two techniques have been given by Yacobi and Holt (1985) and by Leamy (1982) for CL and EBIC respectively. Both reviews discuss the application of the relevant technique to the study of dislocations.

In this Chapter, TEM CL results from threading dislocations and misfit dislocations are presented, the majority of the work concentrating on misfit dislocations. For misfit dislocations in the interfacial plane of a QW structure CL is a more useful analytical technique than EBIC. Shinohara et al. (1985) have shown that such dislocations cannot be detected by EBIC because carrier confinement within the QW's prevents carriers reaching the charge collection electrodes. EBIC can, however, be used to study dislocations threading through a QW structure.

All the work described in this Chapter was carried out on specimens of G43. This was the only quantum well material available which contained misfit dislocations. Although threading dislocations were found in other material they were normally associated with stacking faults or oval defects and could not be studied independently.

A theoretical treatment of CL intensity around such dislocations is presented in Chapter Six.

5.1.1. Crystallography

Dislocations in the sphalerite structure are normally formed by slip on {111} glide planes, forming either pure screw or 60° dislocations. Due to the large Peierls barrier with deep troughs along <110> directions, glide dislocations usually lie along <110> directions. For the diamond structure, two types of dislocation can form, termed the glide set and the shuffle set. However, the sphalerite structure is polar so that dislocations can terminate on either of the two sublattices. This is illustrated for GaAs in Figure 5.1, following the model proposed by Hornstra (1958). Removing the slab of material ABCD and displacing the sides of the cut to rejoin these sides will form a 60° dislocation of the glide set. Performing the same operation on slab EFGH produces another 60° dislocation of the glide set but with opposite Burgers vector. The first 60° dislocation with positive Burgers vector terminates on an As surface and is termed an α dislocation. The second 60° dislocation with negative Burgers vector terminates on a Ga surface and is termed a β dislocation. Obviously the core of the α dislocation will be Ga rich with dangling Ga bonds at the core, while the β dislocation will have an As rich core with dangling As bonds. In Figure 5.1, if slabs AJKD or ELMH are removed, then 60° dislocations of the shuffle set are formed. The α or β nature of the dislocations is unchanged.

5.1.2. Extended dislocations

Glide set and shuffle set dislocations can both dissociate into partial dislocations. A 60° glide set dislocation dissociates

into two glissile Shockley partials (Figure 5.2). A typical dislocation reaction being

$$\frac{a}{2}[110] = \frac{a}{6}[\bar{1}12] + \frac{a}{6}[12\bar{1}].$$

A 60° shuffle set dislocation cannot dissociate directly as a high energy stacking fault would have to be created in the process. However, Hornstra (1958) devised a mechanism by which shuffle set dislocations can dissociate via nucleation of a pair of partial dislocations in the adjacent glide set. For example,

$$\frac{a}{2}[1\bar{1}0] + \frac{a}{6}[\bar{1}2\bar{1}] + \frac{a}{6}[1\bar{2}1] = \frac{a}{6}[2\bar{1}\bar{1}] + \frac{a}{6}[1\bar{2}1]$$

The degree of dissociation of a dislocation in the sphalerite structure is dependent on the energy of the stacking fault between the two partials. The higher the stacking fault energy the narrower the separation between the partials. For GaAs the stacking fault energy (per unit area) is of the order $50mJm^{-2}$ (Gomez and Hirsch, 1978) giving an equilibrium dissociation width of 30 - 70Å.

5.1.3. Lomer-Cottrell Locks

A Lomer-Cottrell lock is formed by the interaction of two perfect dislocations gliding on two different {111} planes. The two perfect dislocations dissociate into Shockley partials, two of which (one from each perfect dislocation) can combine to form the Lomer-Cottrell lock. An example of this is the reaction;

$$\frac{a}{2}[0\bar{1}\bar{1}] \rightarrow \frac{a}{6}[1\bar{1}\bar{2}] + \frac{a}{6}[\bar{1}\bar{2}\bar{1}] \text{ on } (\bar{1}1\bar{1}) \qquad (5.1)$$

$$\frac{a}{2}[101] \rightarrow \frac{a}{6}[211] + \frac{a}{6}[1\bar{1}2] \text{ on } (1\bar{1}\bar{1}) \qquad (5.2)$$

Adding 5.1 and 5.2 then gives

$$\frac{a}{2}[0\bar{1}\bar{1}] + \frac{a}{2}[10\bar{1}] \rightarrow \frac{a}{6}[1\bar{1}0] + \frac{a}{6}[1\bar{1}\bar{2}] + \frac{a}{6}[1\bar{1}2]$$

The $\frac{a}{6}$ <1$\bar{1}$0> stair-rod dislocation has edge character and as such does not lie in the glide plane of either of the two perfect dislocations. The {001} plane containing both the Burgers vector and the line direction of the Lomer-Cottrell lock is not a slip plane for the sphalerite structure so the dislocation is sessile. The two partial dislocations left over from the dislocation reaction are repelled from the stair-rod dislocation so that the whole structure is stable.

5.1.4. Misfit Dislocations

Although the lattice match between GaAs and $Al_xGa_{1-x}As$ is small, particularly at the growth temperatures used for MBE, there will be a small mismatch which will create strain across the layers of a GaAs/$Al_xGa_{1-x}As$ QW structure. The lattice parameter of $Al_xGa_{1-x}As$ is slightly greater than that of GaAs so that an $Al_xGa_{1-x}As$ layer grown on a GaAs substrate will be in compression. When the $Al_xGa_{1-x}As$ layer exceeds a critical thickness (Matthews et al., 1976) it becomes energetically favourable for part of the strain to be accommodated by misfit dislocation generation. For epitaxial layers grown on (001) substrates (using semiconductors with the sphalerite structure), two sets of dislocations along the orthogonal <110> directions are required to relieve the misfit strain.

The existence of misfit dislocations was first predicted by Frank and van der Merwe (1949), who considered strain relief due to edge dislocations with Burgers vectors in the interfacial plane. However, in practice it is easier to generate dislocations with Burgers vectors at an angle to the interface, usually 60^{o} dislocations, even though each of these dislocations relieves less of the misfit.

For the diamond structure the number of misfit dislocations in the [110] and [1$\bar{1}$0] directions should be equal. For the sphalerite structure the mechanical properties in the [110] and [1$\bar{1}$0] directions are different because of the polarity of the structure. Asymmetric misfit dislocation formation in these two directions has been observed by Abrahams et al. (1972) and by Petroff et al. (1980). Booker et al. (1978) have reviewed the misfit dislocations found in III-V compound epilayer structures. Lattice mismatch can either generate new dislocations or modify existing ones. Two mechanisms for the generation of lengths of misfit dislocation from threading dislocations have been demonstrated by Matthews (1975) and are illustrated in Figures 5.3 and 5.4. Figure 5.3 shows the elongation of a dislocation threading the interface. As the thickness of the epilayer increases the dislocation bends along the interface creating a length of misfit dislocation. It is possible for the top end of the dislocation to run completely out to the edge of the wafer. Figure 5.4 shows a similar effect occurring via dissociation of a perfect threading dislocation. When the epilayer exceeds the critical thickness, one partial glides along the interface leaving a misfit dislocation in the interface and a stacking fault that extends from the interface to the surface of the epilayer. Note that screw dislocations do not relieve misfit strain. Misfit dislocations in GaAs/$Al_xGa_{1-x}As$ layers have been found to nucleate at the growth surface (Booker et al., 1978) when the final layer of a multilayer structure was $Al_xGa_{1-x}As$ rather than GaAs. Misfit dislocations formed in this way were always 60° type. Booker et al. (1978) also observed misfit dislocations generated at the surface

where a threading dislocation emerged, the generated dislocation running down the threading dislocation until it reaches the interface and then generates a length of misfit dislocation in the interface. Misfit dislocations can also be generated by climb (Cherns and Stowell, 1975).

5.1.5. CL Contrast from Dislocations

CL and EBIC investigations of dislocations in semiconductors have been performed by many authors. For threading dislocations several different types of CL contrast have been observed and have been reviewed by Dupuy (1983). The normal form of CL contrast is black dot contrast where the CL intensity decreases near the dislocation due to enhanced non-radiative recombination at the dislocation core. Black dot CL contrast in GaAs has been observed by, for example, Schiller and Boulou (1975). Titchmarsh et al. (1977) attempted to correlate the magnitude of black dot contrast at dislocations in GaP with the nature of the dislocation. All the dislocations studied, including screw, edge and 60° types gave similar black dot contrast so that the different types of dislocation could not be distinguished by CL.

CL images of dislocations can also show what is known as dot and halo contrast where the dark core of the dislocation is surrounded by a region where the CL intensity is greater than the normal background level. This form of contrast is usually only observed in highly doped material as reported by Balk et al. (1976) and by Chu et al. (1981) for Se doped GaAs. Balk et al. concluded that Se precipitation at the dislocation created a region

denuded of Se around the dislocation, leading to increased radiative recombination efficiency in this region and thus giving rise to the observed halo. Davidson and Dimitriadis (1980) observed dot and halo contrast in GaP but concluded that the halo was due to a Cotrell atmosphere of impurities. A third type of CL contrast from dislocations has been observed by Petroff et al. (1981) in monochromatic CL images. In addition to the dark contrast observed at the energy of the GaAs $(D^{o}x)$ line, bright contrast was detected at the energy of a second unidentified emission line. This report by Petroff et al. is unusual in that monochromatic imaging was used - most authors simply image with the integrated CL signal.

5.1.6. CL of Misfit Dislocations

CL and EBIC have been performed on misfit dislocations in a number of III-V semiconductor multilayer structures. InGaAs layers on InP and GaAs substrates were examined by Franzosi et al. (1986) and Argunova et al. (1985) respectively, both observing dark CL contrast from 60^{o} misfit dislocations. Petroff et al. (1980) also observed 60^{o} misfit dislocations in $Ga_{1-x}A\ell_{x}As_{1-y}P_{y}$ epitaxial layers grown on GaAs substrates by MBE and again found dark contrast. However, Lomer-Cottrell dislocations did not show any CL contrast at all. This was interpreted in terms of a core reconstruction. Shinohara et al. (1985) studied misfit dislocations in $GaAs/A\ell_{x}Ga_{1-x}As$ MQW structures using EBIC but concluded that for these dislocations the technique was of limited use due to carrier confinement within the QW's. Only dislocations

threading through the structure could be detected. Although CL does not suffer from this limitation it has not been applied to misfit dislocations in GaAs/$A\ell_xGa_{1-x}$ QW structures.

5.2. TEM Results

As stated earlier, G43 was the only quantum well material examined which contained significant numbers of dislocations. In other samples dislocations were only found when associated with oval defects, stacking faults, scratches or dislocation tangles. CL was not performed on these dislocations due to the superposition of effects from the other defects which would have made interpretation of results more complicated.

TEM analysis of dislocations in G43 was performed on the EM430 using the conventional $\underline{g}.\underline{b} = 0$ criterion given that $\underline{g}.\underline{b} \times \underline{u}$ was normally non zero for the same $\underline{g}$ (see Thomas and Goringe, 1979).

5.2.1. Misfit Dislocations

TEM specimens of G43 consisted of a central circular region of uniformly thick (0.4 μm) material where the substrate and GaAs buffer layer had been completely removed leaving just the 5 QW's and the 2 $A\ell_xGa_{1-x}As$ cladding layers intact. Outside this central region the crystal thickness increased until the material was no longer electron transparent (Figure 5.5). Thus there was a circular ring, outside the thinnest part of the specimen, where TEM micrographs could be taken such that the electron beam passed through both the QW's and the interface between the GaAs buffer layer and the first $A\ell_xGa_{1-x}As$ cladding layer. Figure 5.6 shows a

typical BF TEM micrograph taken from this region. A network of misfit dislocations can be clearly seen. These dislocations run parallel to both of the orthogonal <110> directions. No signs of preferential dislocation orientation (with respect to the <110> directions) were observed. The separation of the dislocations varied considerably, but parallel dislocations were usually separated by 1-5 μm. These dislocations were found to be 60^{o} type, formed when threading 60^{o} dislocations elongated along the interface between the GaAs buffer layer and the first $Al_xGa_{1-x}As$ cladding layer. Lomer-Cottrell dislocations were not observed at this interface.

Misfit dislocations were also observed in the central region of specimens where the GaAs buffer layer had been completely removed. Two different types of misfit dislocations were observed in this region. Firstly the 60^{o} dislocations already discussed, and secondly dislocations with pure edge character. Stereomicroscopy indicated that both types of dislocations formed in the middle of the TEM foil and ran along the QW interfaces. TEM examination of the ends of the edge character dislocations showed that each end of a given dislocation split into two dislocations that threaded out of the specimen. Analysis of TEM micrographs showed that the end dislocations were 60^{o} $\frac{a}{2}$ <110> dislocations. Using the Burger vectors of the end dislocations it was shown that the edge character misfit dislocation was a sessile Lomer-Cottrell lock. Figure 5.7 shows a TEM micrograph of such a dislocation showing the end dislocations. Using stereomicroscopy the configuration of this dislocation was found to be as illustrated in Figure 5.8.

Both Lomer-Cottrell locks and 60^{o} dislocations running along the QW interfaces were much rarer than the 60^{o} dislocations running

along the interface between the GaAs buffer layer and the first $A\ell_xGa_{1-x}As$ cladding layer. A typical TEM specimen of G43 with $1mm^2$ of thin area contained less than 5 misfit dislocations at the QW interface, although one sample contained more than 10. Eight TEM specimens were carefully examined and all the misfit dislocations running along the QW interface classified as Lomer-Cottrell or 60^o dislocations. The lengths of these dislocations varied from less than 1 μm to over 50 μm. In the same survey the line directions ([110] or $[1\bar{1}0]$) of the dislocations were found. As a quick means of distinguishing the [110] and $[1\bar{1}0]$ directions oval defects were examined in each of the eight specimens. As the orientation of the oval defects was known (Chapter Four) this allowed the line directions of the dislocations to be determined. The results of this survey are tabulated in Figure 5.9. Obviously Lomer-Cottrell dislocations greatly outnumbered 60^o dislocations but formed preferentially along the $[1\bar{1}0]$ direction. 60^o dislocations did not show any statistically significant signs of preferential orientation.

5.2.2. Threading Dislocations

Threading dislocations in G43 were only studied in the thinnest, central region of TEM specimens. The density of threading dislocations was normally around $10^4 - 10^5 cm^{-2}$. However, the density of threading dislocations was frequently higher in the immediate vicinity (within 5 μm) of misfit dislocations. In addition, samples containing low densities of misfit dislocations also contained lower densities of threading dislocations. All the threading dislocations were found to be perfect screw dislocations.

5.3. CL Results

5.3.1. Unfaulted Crystal

Before presenting results from dislocations in G43 a few spectra typical of unfaulted crystal will be presented. Figure 5.10 shows the quantum well emission from a typical region of unfaulted crystal. The only observable feature on this spectrum is the n = 1 X(e - hh) peak at 1.606 eV. The energy of this peak was constant (within the accuracy of the EM400 CL system) both across individual specimens and between different specimens. Figure 5.11 shows the low energy side of the QW emission plotted on expanded intensity and energy scales. Two weak broad peaks can be seen at approximately 1.586 and 1.566 eV respectively. In this example the two peaks are of approximately equal intensity, although the lower energy peak was generally the weaker of the two. The two peaks were observed at approximately the same energy for all the specimens examined, although variations of up to ± 3 meV about the most common values (1.587 and 1.568 respectively) did occur. However, in some cases only a very broad, very weak low energy shoulder was observed which could not be resolved into discrete peaks. When acquiring spectra to study these low energy peaks it was found that for typical experimental conditions (120 kV, 0.1 to 0.5 μm radius electron beam) low electron beam currents were required. For beam currents above 2 nA the low energy tail of the n=1 X(e - hh) becomes stronger than the weak subsidiary peaks such that these peaks could no longer be resolved.

Although the $Al_xGa_{1-x}As$ emission from G43 could be detected the signal was very weak and could only be observed for high electron beam currents where contamination effects become severe.

As a result the $Al_xGa_{1-x}As$ emission was not studied for G43.

5.3.2. Misfit Dislocations

60° misfit dislocations in the interface between the GaAs buffer layer and the first $Al_xGa_{1-x}As$ cladding layer were not studied in TEM specimens, although they were examined in bulk specimens (Chapter Seven). Due to the changes of specimen thickness in the region of TEM specimens where these dislocations could be observed, interference effects would have made interpretation of results even more difficult than usual.

A number of misfit dislocations running along the QW interfaces were examined by CL. Both 60° and Lomer-Cottrell misfit dislocations parallel to both the [110] and $[1\bar{1}0]$ directions were studied. No correlation was found between CL spectra (or images) and either the type or orientation of the dislocations. However, it should be stressed that Lomer-Cottrell dislocations parallel to $[1\bar{1}0]$ were studied most, simply because they were most common. Only six 60° dislocations (three parallel to each <110> direction) and only three Lomer-Cottrell dislocations parallel to [110] were examined, which is not sufficient to draw any meaningful conclusions. The spectra and images for these dislocations fell within the range of behaviour observed for the Lomer-Cottrell dislocations parallel to $[1\bar{1}0]$.

The energy and width of the n=1 X(e - hh) emission peak was completely unaffected by the presence of misfit dislocations, although the intensity was generally slightly decreased. As a consequence the spectra shown in this Chapter will only show the low energy side of this peak - no structure was ever detected on

the high energy side.

Figure 5.12 shows a CL spectrum acquired from a typical misfit dislocation located approximately 10 μm from the region used to acquire the spectrum of Figure 5.11. The two spectra are virtually identical. Figure 5.13 shows three monochromatic CL images acquired at the energies of the n=1 X(e - hh) emission and the two weaker low energy peaks. The dislocation appears as a dark line in the heavy hole emission image but appears as a pair of closely spaced bright lines in the low energy images.

The images and spectra shown in Figure 5.12 and 5.13 are typical of the most common behaviour observed at different misfit dislocations. However, considerable variations were observed between different dislocations. The general behaviour of misfit dislocations in G43 was as follows. For most misfit dislocations the low energy peaks corresponded in energy to the peaks observed in unfaulted crystal but were simply more intense. In some cases the peaks at the dislocations were shifted to slightly lower energy by 1-2 meV. The two low energy peaks were not always affected equally at misfit dislocations as for some dislocations only the higher energy of the two peaks noticeably increased. Additional low energy peaks that were not seen in unfaulted crystal were seen occasionally for misfit dislocations, the most common occurring at approximately 1.595 eV, while another was observed at 1.576 eV. For the majority of misfit dislocations (particularly those less than 20 μm in length) the low energy peaks did not vary in energy along the length of the dislocation. CL images acquired at the energy of the n=1 X(e - hh) transition nearly always showed a dark line

at the position of the dislocation, although in a few cases the contrast was extremely low. In general, as the electron beam was scanned towards a misfit dislocation the intensity of the heavy hole emission increased until the immediate vicinity of the dislocation when it dropped sharply. Monochromatic images acquired at the energies of the lower energy features normally showed two bright lines either side of a misfit dislocation. Usually the image acquired at the lowest energy showed 'sharper' lines, although the separation of the lines did not vary appreciably.

For unfaulted crystal the low energy peaks were typically over 100 times weaker than the heavy hole emission. At misfit dislocations the low energy peaks were typically between 10 and 50 times weaker than the heavy hole emission. When the low energy peaks were relatively strong at a misfit dislocation monochromatic images did not usually show a double bright line but instead showed a single broader bright line.

It should be stressed that a number of misfit dislocations deviated considerably from the above description. For example, Figure 5.14 shows three spectra from the same misfit dislocation. Figure 5.14a) shows a spectrum from one end, Figure 5.14b) shows a spectrum from near the middle and Figure 5.14c) shows a spectrum from the other end of the dislocation. For comparison Figure 5.14d) shows a spectrum from nearby unfaulted crystal. These spectra show variations in the energy of the weaker peaks occurring along the length of the dislocation. Figures 5.15a) to d) show monochromatic CL images acquired from this dislocation. Figure 5.15a) was acquired at the energy of the heavy hole emission while Figures

5.15b) to d) were acquired at the energies marked A, B and C on Figures 5.14a) and b). Note that spectrum 5.14a) was acquired from the end of the dislocation at the lower left of the images. The images clearly show that for this example the low energy emission originates primarily from one end of the dislocation with particularly weak emission arising from the middle.

A number of attempts were made to study the effects of temperature and electron beam intensity on the energy and intensity of the low energy emission peaks. This work proved unsuccessful for several reasons. Firstly, contamination produced irreversible changes in the energies and intensities of the low energy peaks, although only the intensity of the heavy hole peak was affected. Secondly, when varying the temperature these weak peaks rapidly decreased in intensity so that they were no longer resolvable. Thirdly, when varying the electron beam current the heavy hole emission increased in intensity more rapidly than the lower energy peaks. As a result the low energy tail of the heavy hole peak obscured the subsidiary peaks.

5.3.3. Threading Dislocations

CL results from screw threading dislocations were much simpler than for the misfit dislocations. No increase in the intensity of the low energy peaks was ever observed at any screw dislocation, either when taking spectra or images. On scanning the electron beam towards a threading dislocation the n=1 X(e - hh) emission did not show the increased intensity observed (relative to unfaulted, distant crystal) for misfit dislocations. The only effect observable

at threading dislocations was a relatively weak decrease in emission at all photon energies. Figures 5.16a), b) and c) show three monochromatic CL images acquired at the energies of the heavy hole, first (1.585 eV) low energy and second (1.569 eV) low energy peaks respectively. In all three images the dislocation appears as a dark spot. These images also show that the spatial variations in the heavy hole emission occur over a larger scale than the spatial variations in the lower energy peaks. This observation will be discussed in Chapter Six.

5.4. Discussion

The 60° misfit dislocations observed between the GaAs buffer layer and the first $Al_xGa_{1-x}As$ cladding layer were generated by 60° threading dislocations bending along the interface (Figure 5.3) due to misfit strain. The critical thickness h_c, above which bending can occur, has been derived theoretically by Matthews et al. (1976) and is given by the equation

$$h_c = \frac{b(1 - \nu \cos^2\alpha)\ \ln(h_c/b)}{8\pi f\ (1 + \nu)\ \cos\lambda}$$

where b is the strength of the dislocation, ν is Poisson's ratio, f is the misfit between the stress-free lattice parameters of epi-layers and the substrate, α is the angle between the Burgers vector $\underline{b}$ and the length of the dislocation line that lies in the interfacial plane. Finally, λ is the angle between $\underline{b}$ and the direction in the interfacial plane which is perpendicular to the line of intersection of the slip plane and the interface. Using

parameters quoted in Adachi (1985) then h_c for sample G43 is 0.33 μm at room temperature. This is less than the epilayer thickness so bending of threading 60° dislocations along the interface is expected. At the temperatures used for MBE growth (500 - 750°C) the critical thickness h_c exceeds the epilayer thickness for G43. It is possible that as a result misfit dislocations are only generated when the sample is being cooled subsequent to growth. However, this is not certain as Shinohara et al. (1975) observed the dislocation bending mechanism operating in AlAs-GaAs epilayers for thicknesses below h_c.

The mean spacing, L_d, between misfit dislocations that accommodate all the misfit strain is given (Frank and van der Merwe, 1949) by

$$L_d = Kb/f$$

where K is the ratio of the edge component of the Burgers vector in the interfacial plane to the total Burgers vector. For 60° dislocations in (001) films K = 0.5. Thus for the 60° misfit dislocations in G43, L_d = 0.5 μm. This theoretical value will only be approached given sufficient numbers of threading 60° dislocation. This may explain why the observed misfit dislocation spacing in G43 is greater than the theoretical value.

In contrast to the results of, for example, Booker et al. (1978) or Rozgonyi et al. (1974) 60° misfit dislocations did not show any signs of non-uniform distribution in the orthogonal <110> directions. This may be due to the extensive cross-slip of dislocations between the two <110> directions or due to interactions between dislocations.

It is surprising that out of the three QW samples grown at the Philips Research Laboratories and examined in this study, only one contained misfit dislocations even though for all three samples the epilayer thickness exceeded the critical thickness h_c. None of the observed 60^o misfit dislocations in G43 were formed by the surface or interfacial generation mechanisms proposed by Booker et al. (1978), so they must all have been formed by bending of 60^o threading dislocations along the interface. This mechanism cannot operate if no 60^o threading dislocations are present. Threading dislocations normally originate within the substrate and are incorporated in the epilayers during growth. Only in G43 were threading dislocations observed and then only screw rather than 60^o dislocations were found. Thus it seems likely that the misfit dislocations reflect a high dislocation density in the substrate on which G43 was grown, although impurity effects and the growth conditions may also be important. The absence of 60^o threading dislocations was presumably due to the formation of misfit dislocations allowing the threading dislocations to glide to the edge of the wafer. It is perhaps significant that sample G43 was grown on a GaAs substrate provided by a different manufacturer than supplied the substrates for the two SQW structures.

The presence of 60^o misfit dislocations at the QW interfaces is surprising given the narrowness of the QW layers. However, 60^o misfit dislocations in superlattice structures have been observed previously (Shinohara et al., 1985). It is not clear why Lomer-Cottrell misfit dislocations should greatly outnumber the 60^o misfit dislocations. In order to generate a 60^o misfit dislocation from a 60^o threading dislocation energy is required. Firstly, to bend

the threading dislocation into the interfacial plane and secondly, to extend the resultant misfit dislocation along the interface. It is conjectured that the interaction between the two 60^{o} misfit dislocations that combine to form the Lomer-Cottrell allows this process to occur more readily than bending of a single dislocation. As the edge component (in the interfacial plane) of a Lomer-Cottrell lock is greater than that of a single 60^{o} misfit dislocation a Lomer-Cottrell relieves more misfit strain and can extend more easily. In order for a Lomer-Cottrell lock to form two 60^{o} threading dislocations must be close enough to interact, which may explain why Lomer-Cottrell dislocations are found in regions with above average threading dislocation densities. Assuming Lomer-Cottrell locks can form at lower misfit strains than 60^{o} misfit dislocations, for the reasons outlined above, then presumably they can form during cooling subsequent to MBE growth but at higher temperatures than for 60^{o} misfit dislocations. At elevated temperatures climb may allow the Lomer-Cottrell dislocations to move from the interface between the GaAs buffer layer and the first $Al_xGa_{1-x}As$ cladding layer to the QW interface, possibly aided by the presence of impurities. Of course the Lomer-Cottrell locks may form at the QW interface but the higher strain at the earlier interface suggests that this does not happen.

The preferential orientation of Lomer-Cottrell locks parallel to the $[1\bar{1}0]$ direction is ascribed to asymmetries between the orthogonal <110> directions due to the polar nature of the sphalerite structure, although it is not clear why 60^{o} misfit dislocations do not show the same behaviour.

CL of unfaulted regions of G43 showed the normal n=1 X(e - hh) emission but also revealed two weaker, lower energy peaks that were usually observed approximately 18 and 37 meV below the energy of the heavy hole transition. The latter peak was at approximately the energy of the longitudinal optical (LO) phonon in GaAs (36 meV) and so could conceivably be due to an LO phonon replica. Phonon replicas are frequently observed in PL of III-V bulk semiconductors but their presence in QW structures is disputed. Holonyak et al. (1980) observed lasing in a QW device at an energy 36 meV below the heavy hole emission and attributed it to stimulated emission via a phonon assisted transition. However, other workers have failed to duplicate this result, and in most cases have failed to identify an emission line at the appropriate energy. Fouquet and Burnham (1986) did observe an emission peak 36 meV below the heavy hole emission when using PL to investigate MBE grown MQW structures. Time resolved PL demonstrated that this peak could not be a phonon replica. Therefore it seems unlikely that the emission in G43 occurring 37 meV below the heavy hole transition is a phonon replica. Experiments where spectra were acquired from G43 using a range of electron beam currents were hampered by irreversible changes produced by contamination effects. Even so it was apparent that increasing the electron beam intensity produced a far greater increase in the heavy hole emission than in either of the lower energy peaks. An LO phonon replica would be expected to increase in proportion to the increase in the heavy hole emission. Therefore this result confirms that the peak observed 37 meV below the heavy hole emission is most unlikely to be a phonon replica. In addition a phonon replica would

not be expected to show the significant variations in emission energy observed in this study.

At high electron beam currents it was observed that both the low energy peaks were obscured by the low energy tail of the much stronger heavy hole emission, suggesting that these peaks are caused by limited numbers of impurity atoms which become saturated at high currents (Lambert et al., 1982). Comparison with the theoretical calculations of Green and Bajaj (1985) suggests that these peaks are not due to donors but are probably due to n = 1(e - a) transitions. Bimberg and Christen (1985) used time resolved CL to identify two weak peaks in 55Å thick QW's occurring at the same energies (relative to the heavy hole emission) as the two peaks observed in G43. Both peaks were ascribed to carbon acting as an acceptor, the difference in energy being due to the position of the carbon atoms - either at the centre of the QW's (lower energy) or at the interfaces (higher energy). Therefore it seems likely that the two peaks observed in G43 at energies 18 and 38 meV below the heavy hole emission can be similarly ascribed. Henceforth these two peaks will be termed the $n = 1(e - A_C)$ and $n = 1(e - A_I)$ emissions respectively. Spectra acquired from misfit dislocations in G43 usually showed only the carbon impurity emission but on occasion other emission features were also observed. The most common of these was observed approximately 11 meV below the heavy hole emission. The calculations of Greene and Bajaj (1985) suggest that this emission is due to an n = 1(d - hh) transition with the donors sited at the edge of the wells. For unfaulted crystal, emission at this energy was only observed once. Possibly this emission is due to a low background

level of donors throughout the crystal but which can only be detected at higher levels owing to the proximity of the heavy hole peak. The other common low energy peak in G43 (30 meV below the heavy hole emission) is probably due to an acceptor but the nature and position of the impurity are unknown.

Threading dislocations in G43 showed only the weak black dot contrast similar to that which has been observed previously by a number of workers. For example, Petroff et al. (1981) observed this type of contrast in MBE grown GaAs/$Al_xGa_{1-x}As$ double hetereostructures using STEM CL. However, for undoped MQW structures the same workers did not observe any contrast from threading dislocations, in contrast to the results presented in this study. This discrepancy is probably due to the fact Petroff et al. examined relatively thick (2-3 μm) MQW specimens. The reduced spatial resolution from such specimens may have made the weak contrast at threading dislocations difficult to detect. Black dot contrast at dislocations is usually interpreted (Davidson and Dimitridias, 1980) as being due to non-radiative recombination occurring either because of dangling bonds at the dislocation core or a Cottrell atmosphere of point defects or impurities surrounding the dislocation. In G43 only screw threading dislocations were observed. As screw dislocations do not generate long range dilatational strain fields to cause impurity diffusion it seems likely that the black dot contrast at threading dislocations in G43 is due to the core structure of the dislocations and not a Cottrell atmosphere. However, screw dislocations do generate long range shear stresses which can attract certain impurities so that an impurity atmosphere might still be present.

In general misfit dislocations at the QW interfaces in G43 showed enhanced luminescence at the energies tentatively ascribed to the n = 1(e - A_c) and n = 1(e - A_I) transitions. Presumably this is due to Cottrell atmospheres of impurities being attracted to the dislocation because of the long range dilatational strain field associated with the edge component of the dislocation (Hirth and Lothe, 1968). The obvious source of impurities is the crystal surrounding the dislocation, so that the same spectral features were observed for dislocations as for the surrounding crystal. At some dislocations the impurity emissions shifted to slightly lower energies, possibly because the impurity distribution at the dislocations is shifted slightly towards the centre of the QW's.

Misfit dislocations appeared as dark lines in monochromatic images acquired at the energy of the heavy hole luminescence, although the observed contrast was sometimes very weak. The dark line implies that, in the vicinity of the dislocations, transitions are occurring which are non-radiative at this energy. Some of these transitions are obviously giving rise to the enhanced impurity luminescence at the dislocations. Dislocations where the impurity emission was relatively strong generally showed stronger contrast in the heavy hole emission. However, the dark contrast observed at screw threading dislocations suggests that non-radiative transitions might also occur at misfit dislocations. Outside the region of dark contrast in the immediate vicinity of misfit dislocations, monochromatic CL images showed that the heavy hole emission was stronger than for crystal a long way from the dislocation. This implies that impurity and non-radiative recombination

centres have diffused to the dislocation leaving a region in which the radiative efficiency of the heavy hole emission was increased. However, it is equally possible that this effect is simply due to contamination incurred when locating suitable dislocations using TEM as this procedure normally requires relatively high beam currents.

Monochromatic CL images acquired from misfit dislocations at the energies of the n = 1(e - A_C) and n = 1(e - A_I) luminescence peaks showed two distinct types of contrast depending on the strength of the impurity emission being imaged (relative to the heavy hole luminescence). For a relatively strong impurity emission, misfit dislocation images showed only a single bright line, while for a relatively weak impurity emission, images showed a pair of bright lines separated by a darker region where the intensity was still higher than normal background level. The former type of contrast is consistent with Cottrell atmospheres of impurities around misfit dislocations, with the impurity concentration reaching a maximum near the core of the dislocation. The latter type of contrast might be interpreted in terms of a reduction in impurity concentration close to the cores of misfit dislocations. However, the theory for the impurity distribution around dislocations (Hirth and Lothe, 1968) suggests that the impurity concentration should increase monotonically towards the core of a dislocation. A decrease in impurity concentration in the immediate vicinity of a dislocation therefore seems unlikely. Instead it is suggested that the dark line in the impurity luminescence CL images is simply due to non-radiative recombination in the region at or around the dislocation

core. This effectively reduces the radiative efficiency in this region and gives rise to the observed dark line in the impurity emission images. Obviously when the impurity luminescence is relatively strong this reflects a higher impurity concentration around the dislocation, which is sufficient to offset the increase in non-radiative recombination around the dislocation, so that only a single bright line is observed in monochromatic CL images.

Although much work has been published on the CL of misfit dislocations in the SEM, few workers have studied Lomer-Cottrell dislocations. In addition few authors have used (S) TEM CL or monochromatic imaging. The most notable exception is the work of Petroff et al. (1980), who performed similar experiments to those in the current study but on doped $Ga_xAl_{1-x}As_yP_{1-y}/Ga_zAl_{1-z}As$ layers grown on (001) substrates using LPE. The results from these layers differed in two respects from those obtained in the current study. Firstly, Lomer-Cottrell dislocations did not show any CL (or EBIC) contrast at any photon energy. Secondly, 60° misfit dislocations showed only non-radiative recombination. There are several possible explanations for these differences in results. Specimens examined Petroff et al. were four times thicker than samples of G43 and were relatively highly doped (3×10^{17} cm^{-3}, n or p-type). The increased thickness may have reduced the spatial resolution obtainable making detection of a Cottrell atmosphere more difficult. Also the Cottrell atmosphere around a dislocation may only contain a relatively low density of impurities (or dopants), which would be difficult to detect against the higher background dopant concentration. It is not clear why the Lomer-Cottrell misfit dislocations observed by Petroff et al. did not show any CL or EBIC contrast, while those

observed in the current study showed clear contrast. Possibly this may be due to the difference between the LPE and MBE growth processes, the considerably higher growth temperature used for LPE (1200^{o}C as opposed to 500-700^{o}C for MBE) may allow a dislocation core reconstruction which only occurs at higher temperatures. Other possible explanations include the effects of dopants, differences in the magnitude of the misfit strain causing the dislocations or the differences in the compounds used to grow the epilayers.

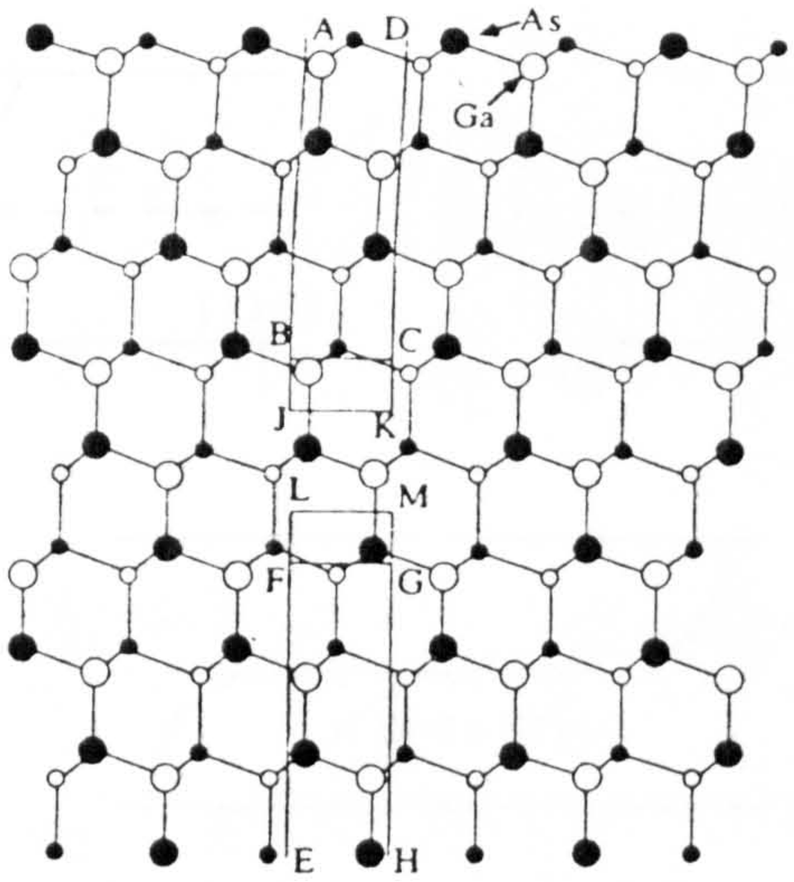

5.1 Illustration to show the atoms that must be removed to form glide set and shuffle set dislocations in GaAs (see text).

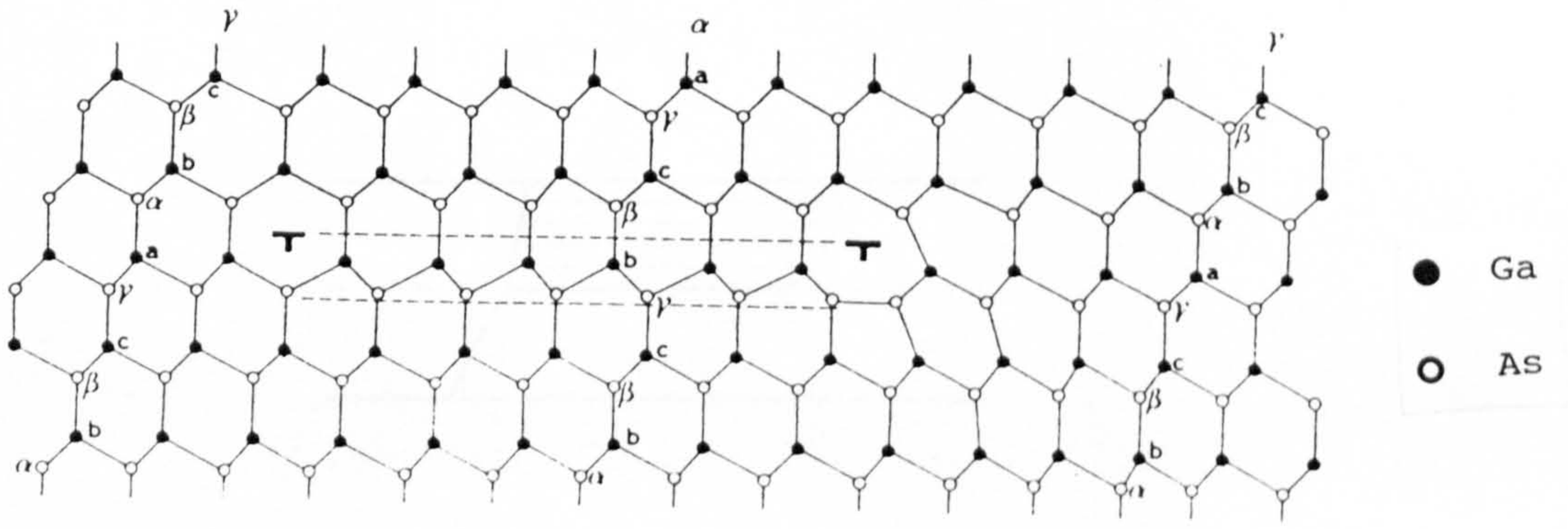

5.2 60° dislocation in the sphalerite structure, dissociated to form an intrinsic stacking fault (viewed along $[1\bar{1}0]$).

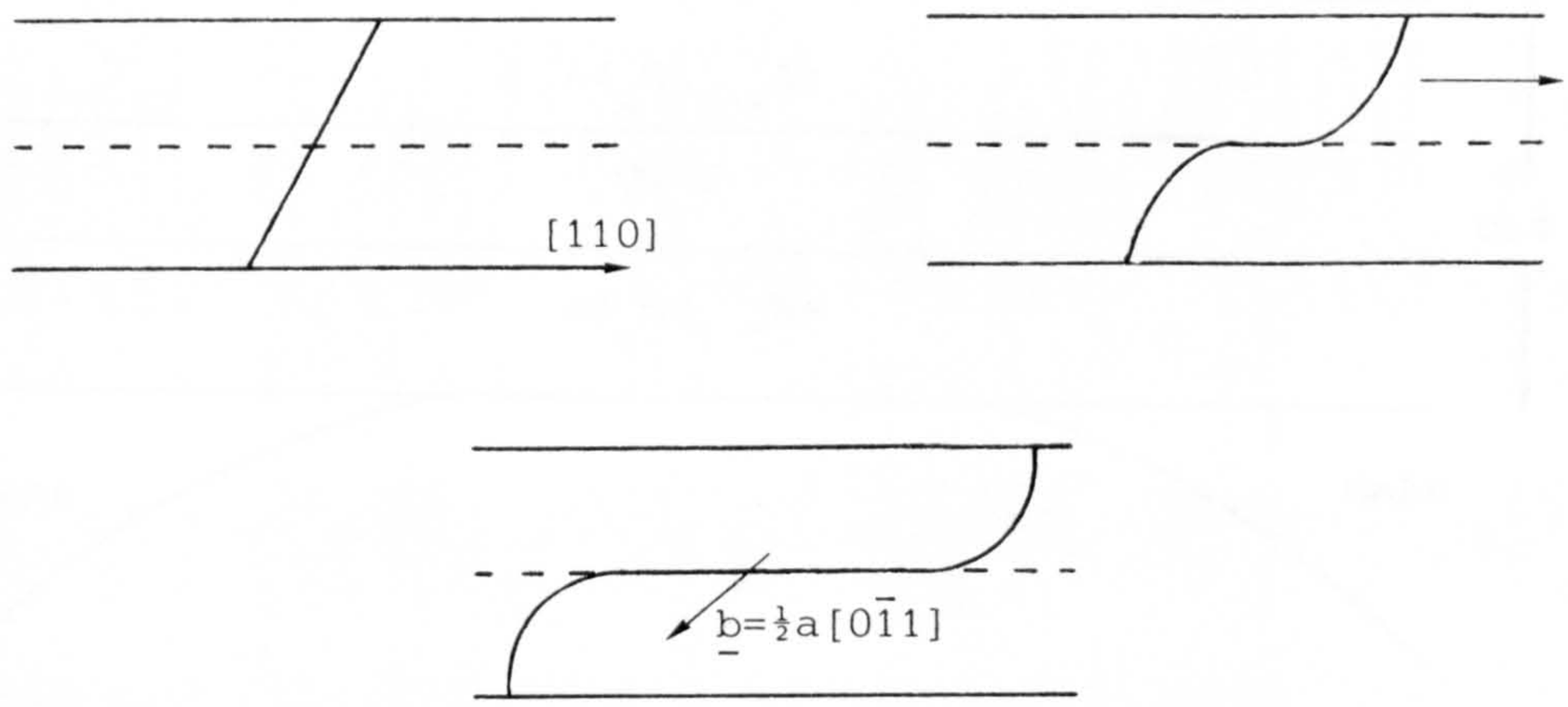

5.3 Formation of a length of misfit dislocation by elongation of a threading dislocation (after Matthews, 1975).

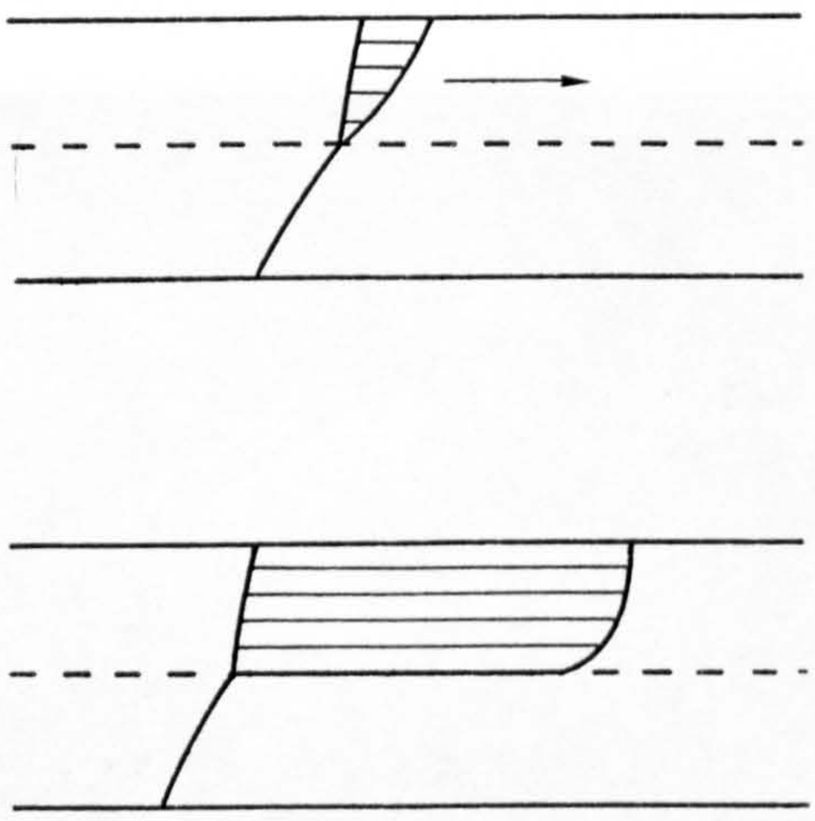

5.4 Misfit dislocation generation by dissociation of a threading dislocation (after Matthews, 1975).

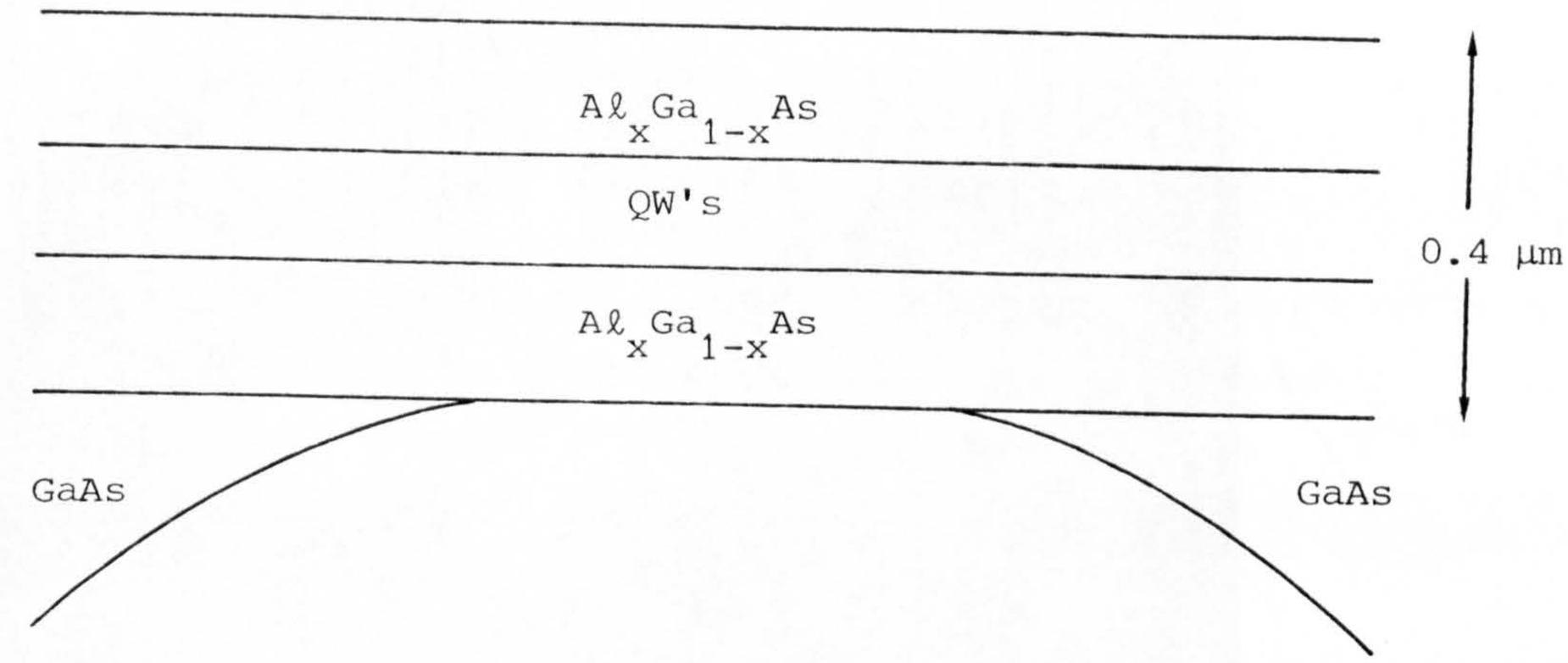

5.5 Schematic diagram of a typical TEM specimen of G43 showing the constant thickness central region surrounded by a region of varying thickness.

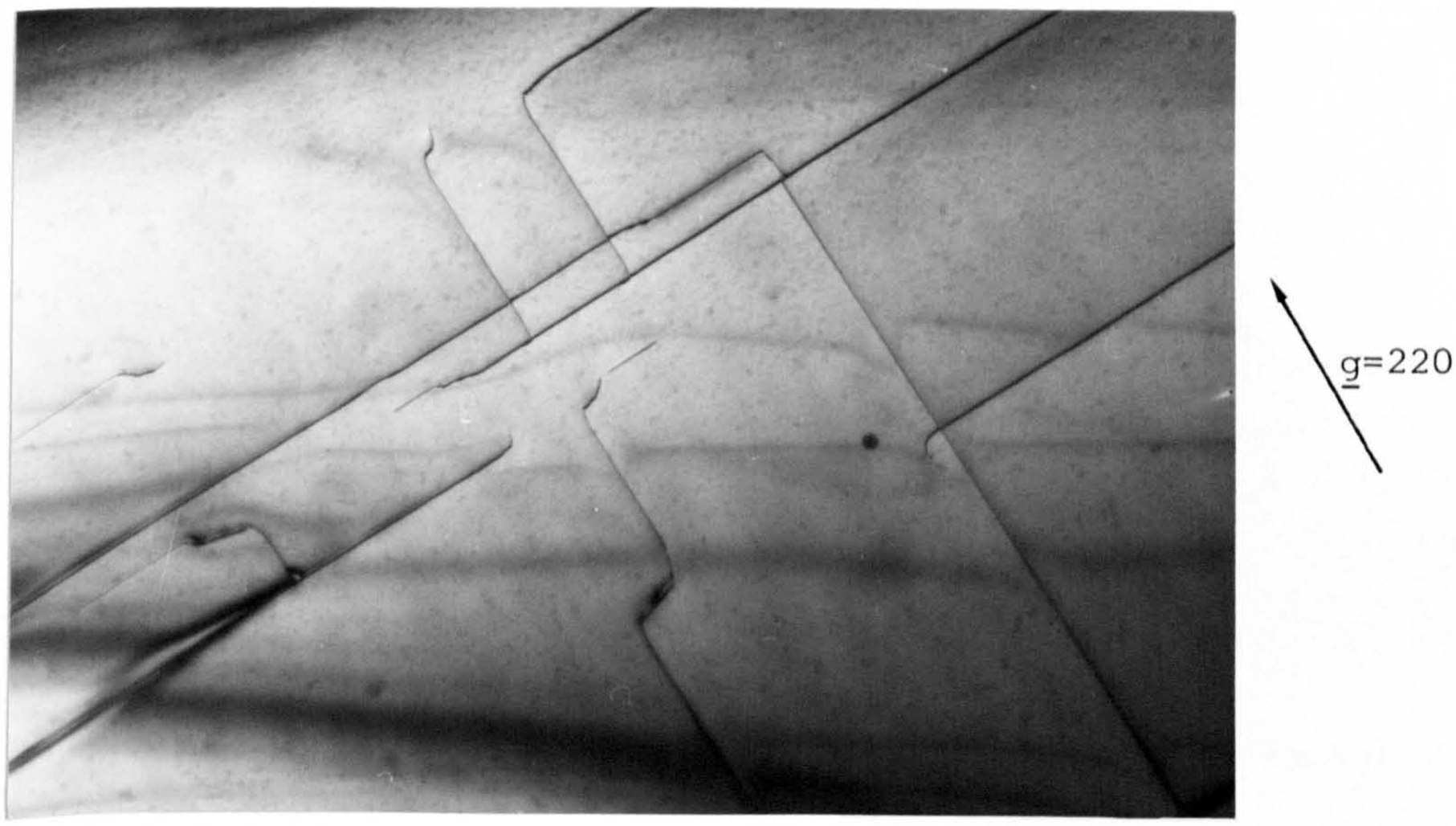

5.6 BF TEM micrograph showing 60° misfit dislocations in the interface between the first $Al_xGa_{1-x}As$ layer and the GaAs buffer layer (sample G43).

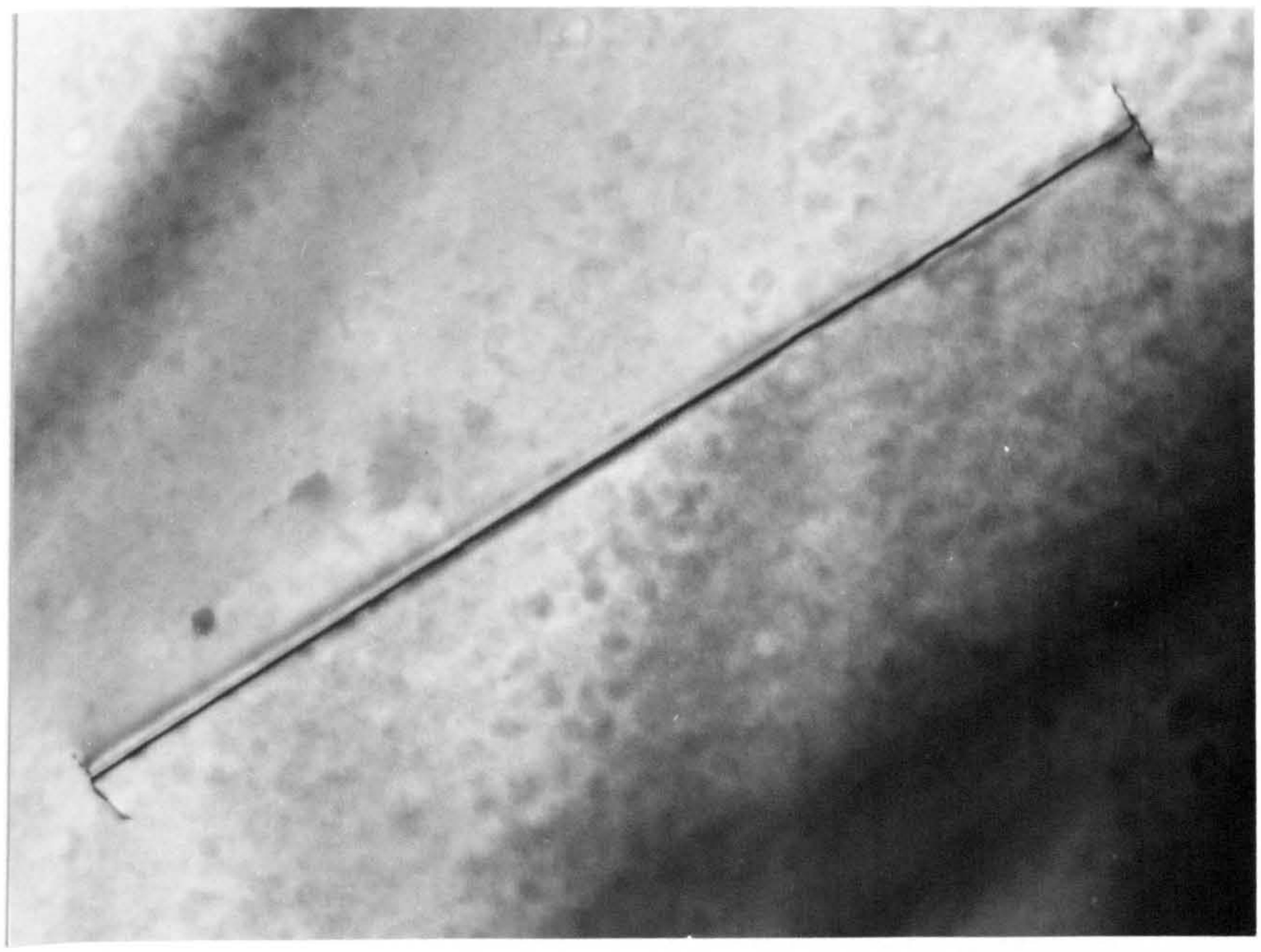

5.7 BF TEM micrograph of a Lomer-Cottrell lock in G43.

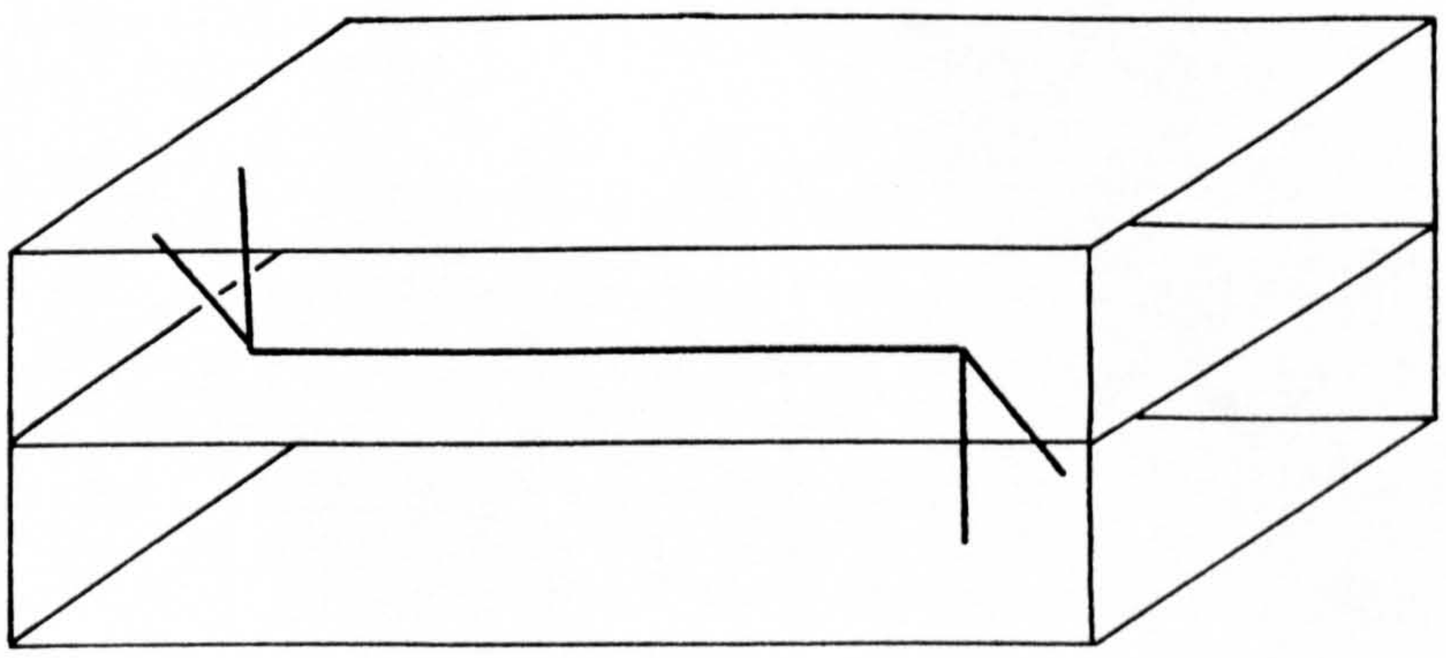

5.8 Schematic diagram illustrating the configuration of the 60° dislocations at either end of a Lomer-Cottrell lock.

	DIRECTION		
TYPE	[110]	[1$\bar{1}$0]	Total
Lomer-Cotrell	7	34	41
60°	8	5	13

5.9 Table giving the relative numbers of Lomer-Cottrell and 60° dislocations observed in a total of 8 TEM specimens of G43

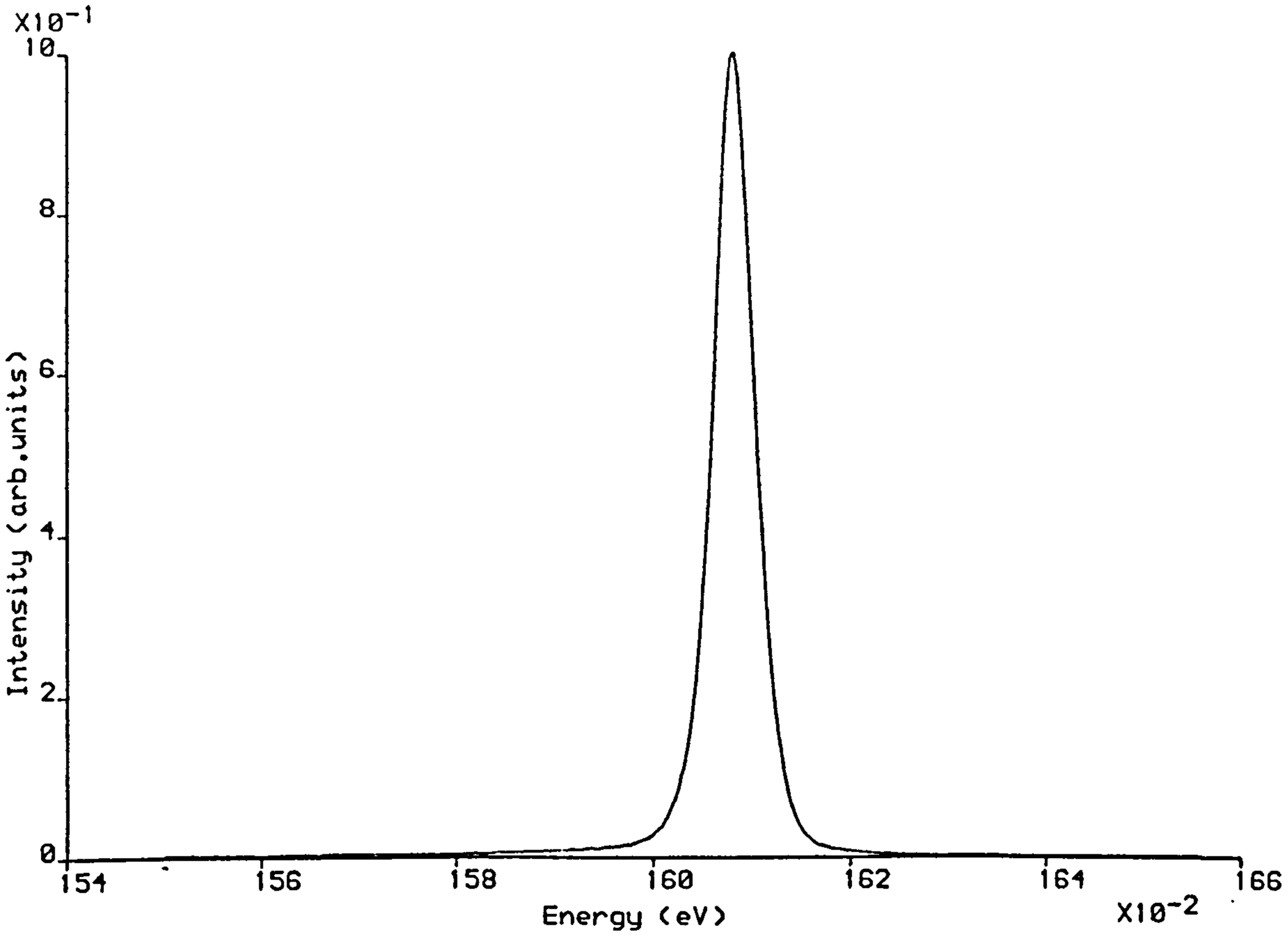

5.10 CL spectrum from an unfaulted region of G43 showing the n=1(e-hh) peak.

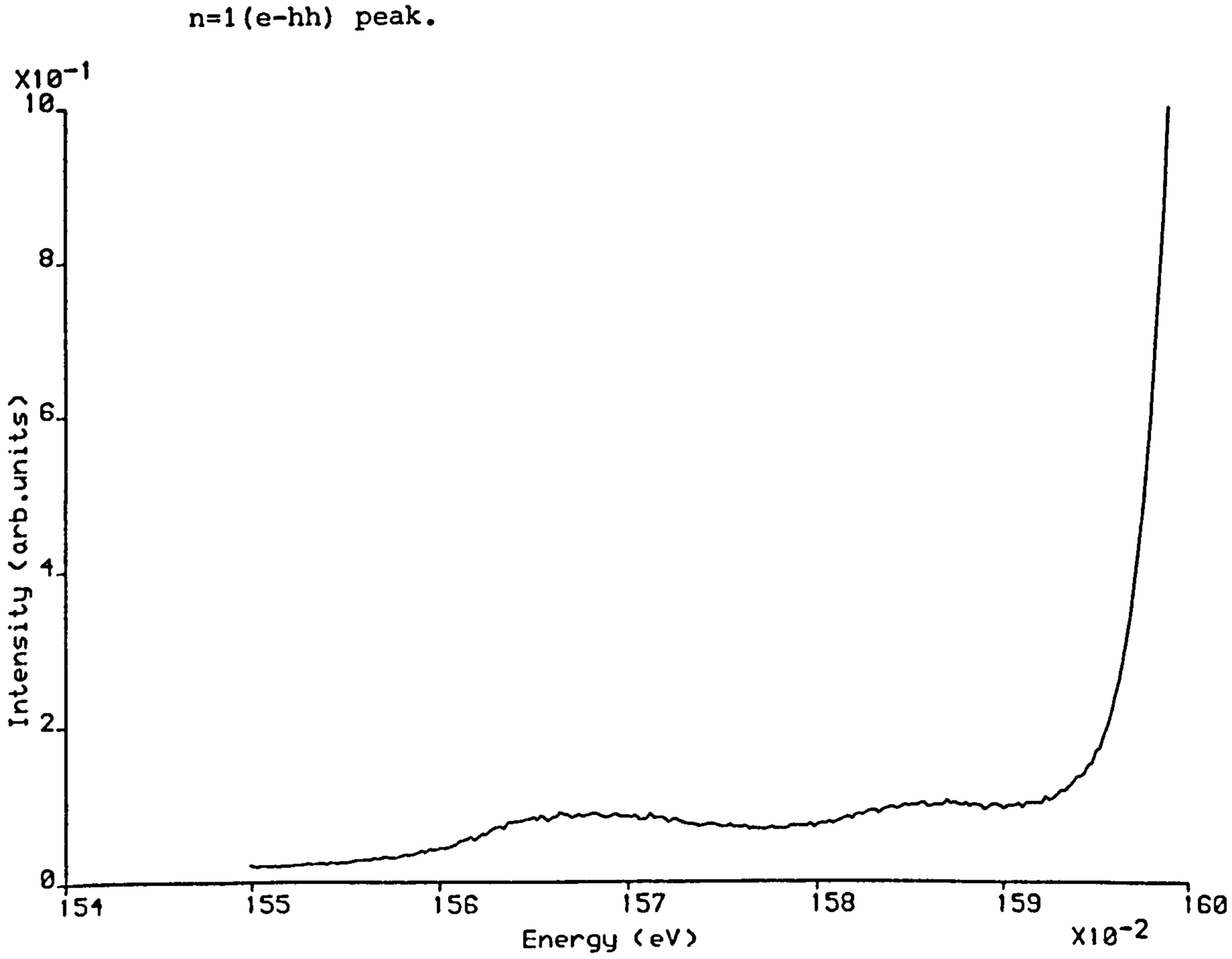

5.11 CL spectum from an unfaulted region of G43 showing the weak structure on the low energy side of the main peak.

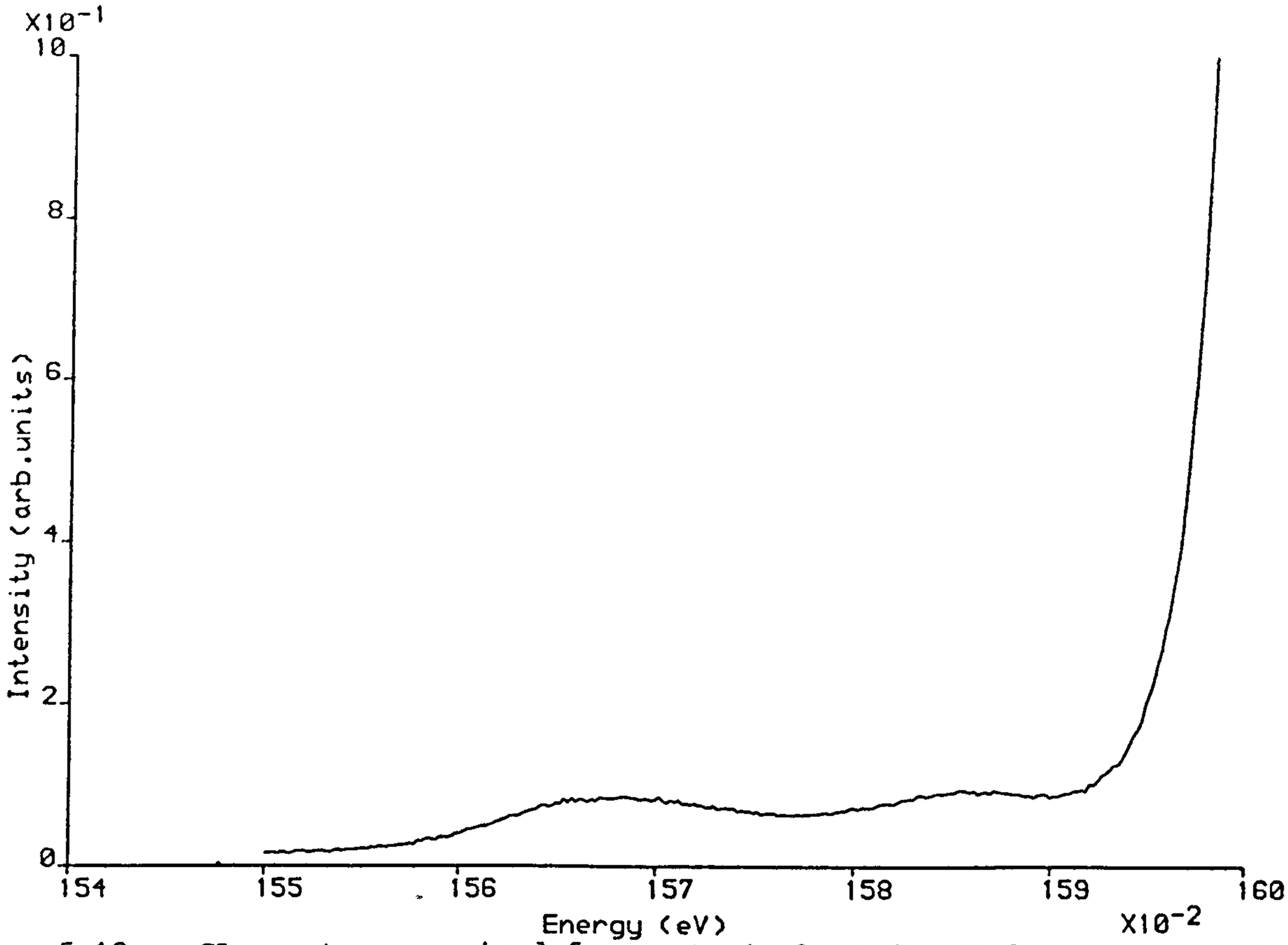

5.12 CL spectrum acquired from a typical misfit dislocation in G43 showing the same low energy structure as was observed for unfaulted crystal (Figure 5.11).

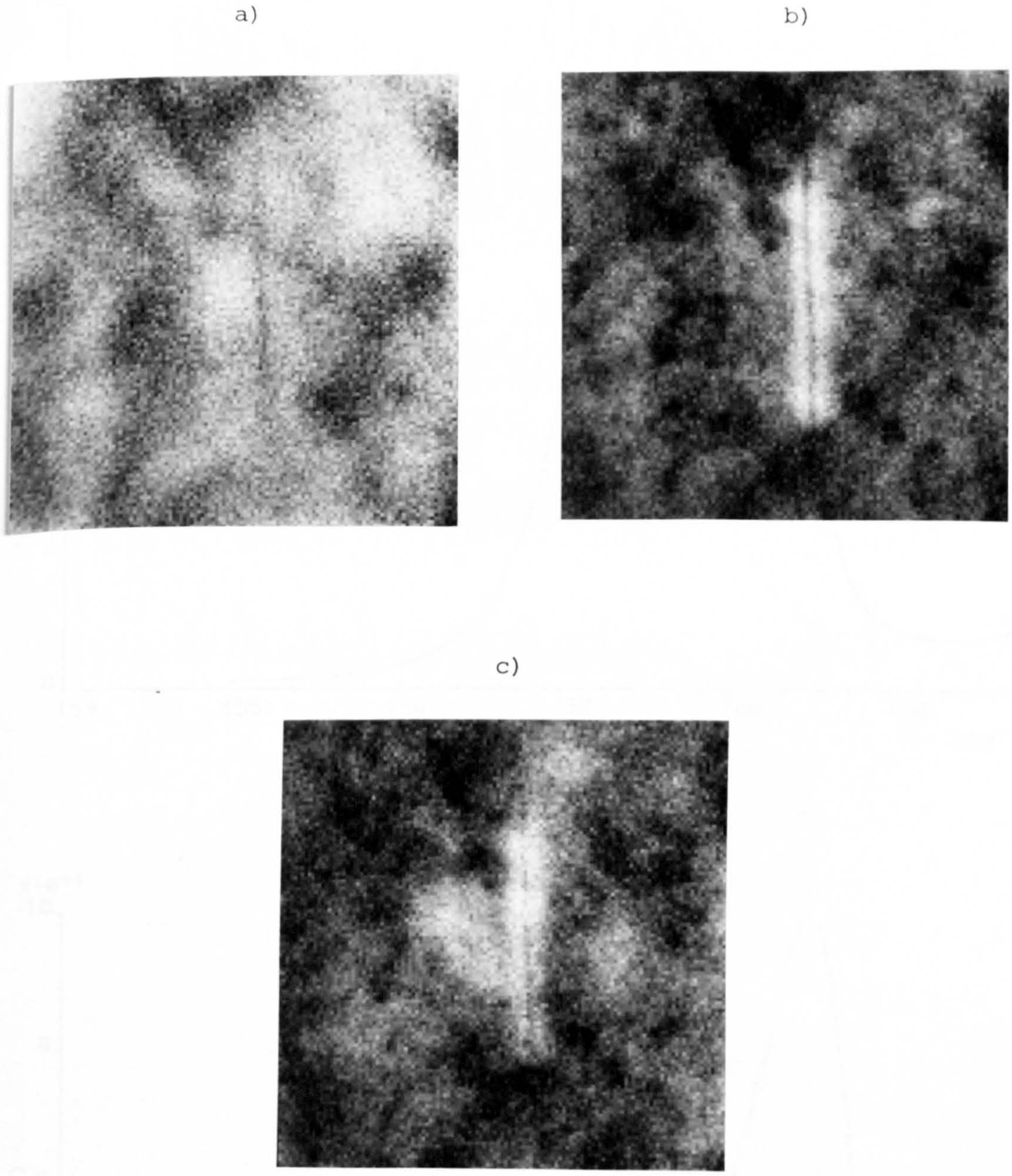

5.13 Monochromatic CL images of a typical misfit dislocation in G43. a) n=1(e-hh) emission b) 1.586 eV c) 1.566 eV (see Figure 5.12).

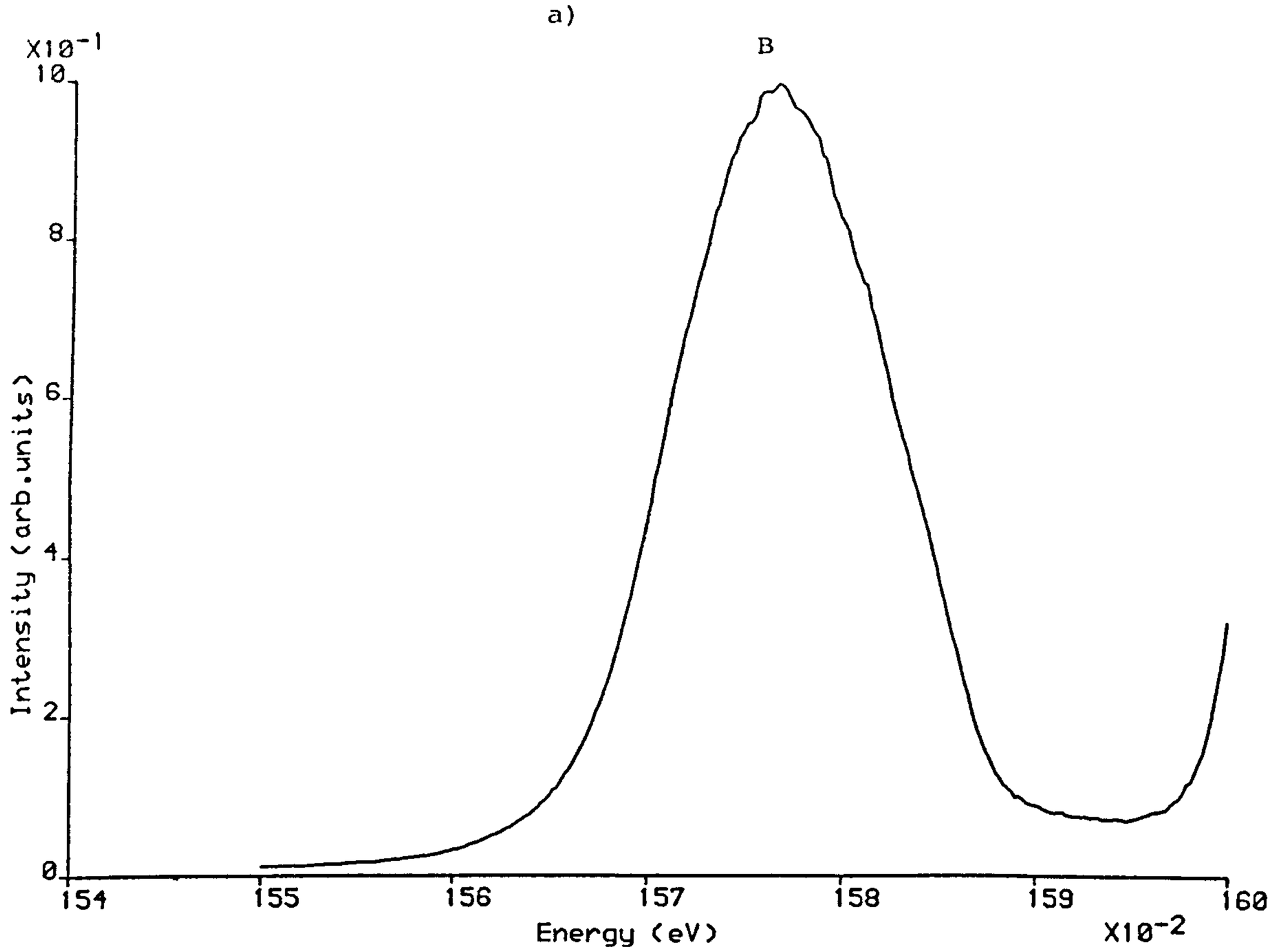

5.14 CL spectra from a slightly atypical misfit dislocation in G43.

a) Spectrum from one end ot the dislocation.

b) Spectrum from the middle of the dislocation.

c)

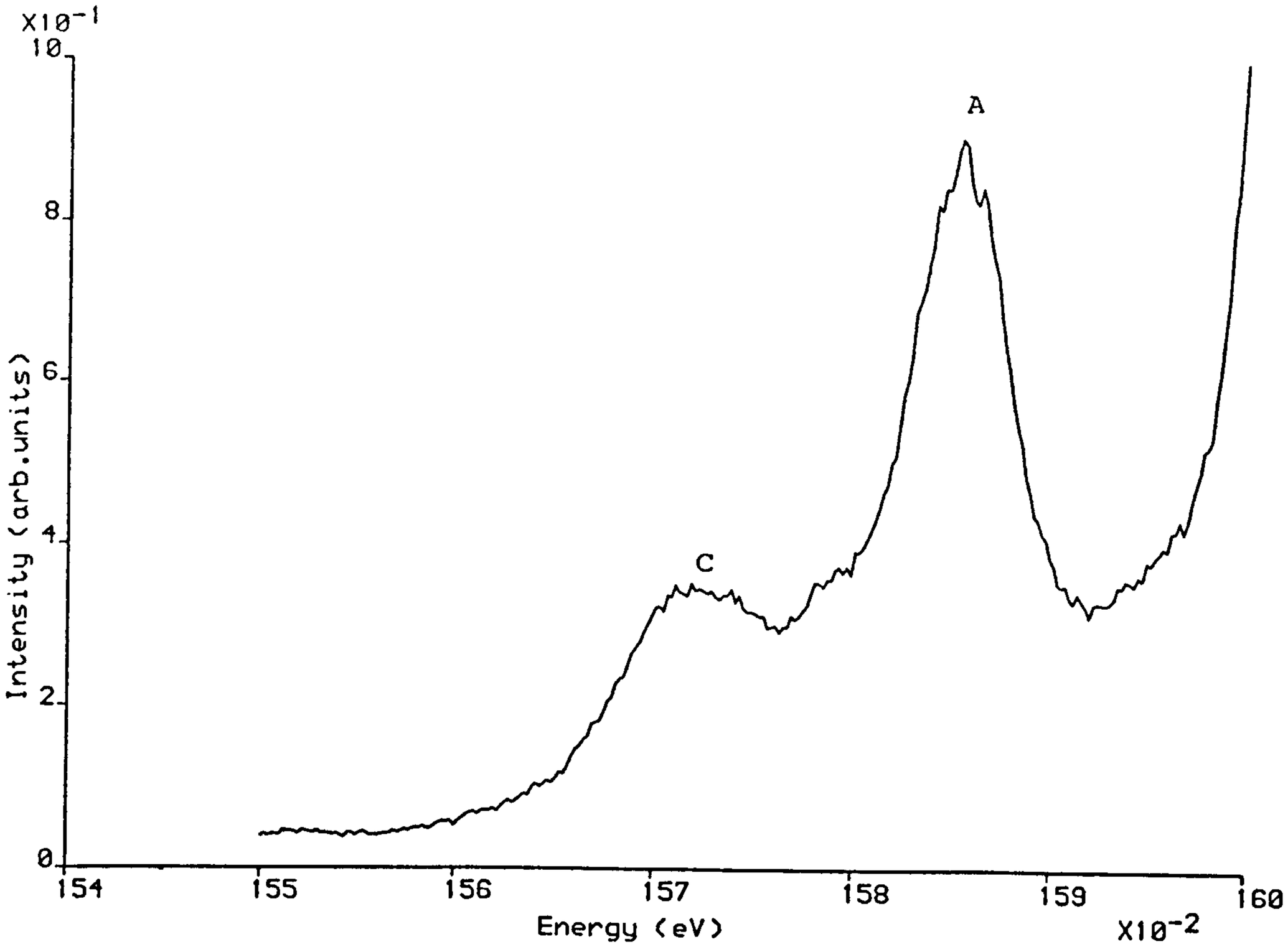

d)

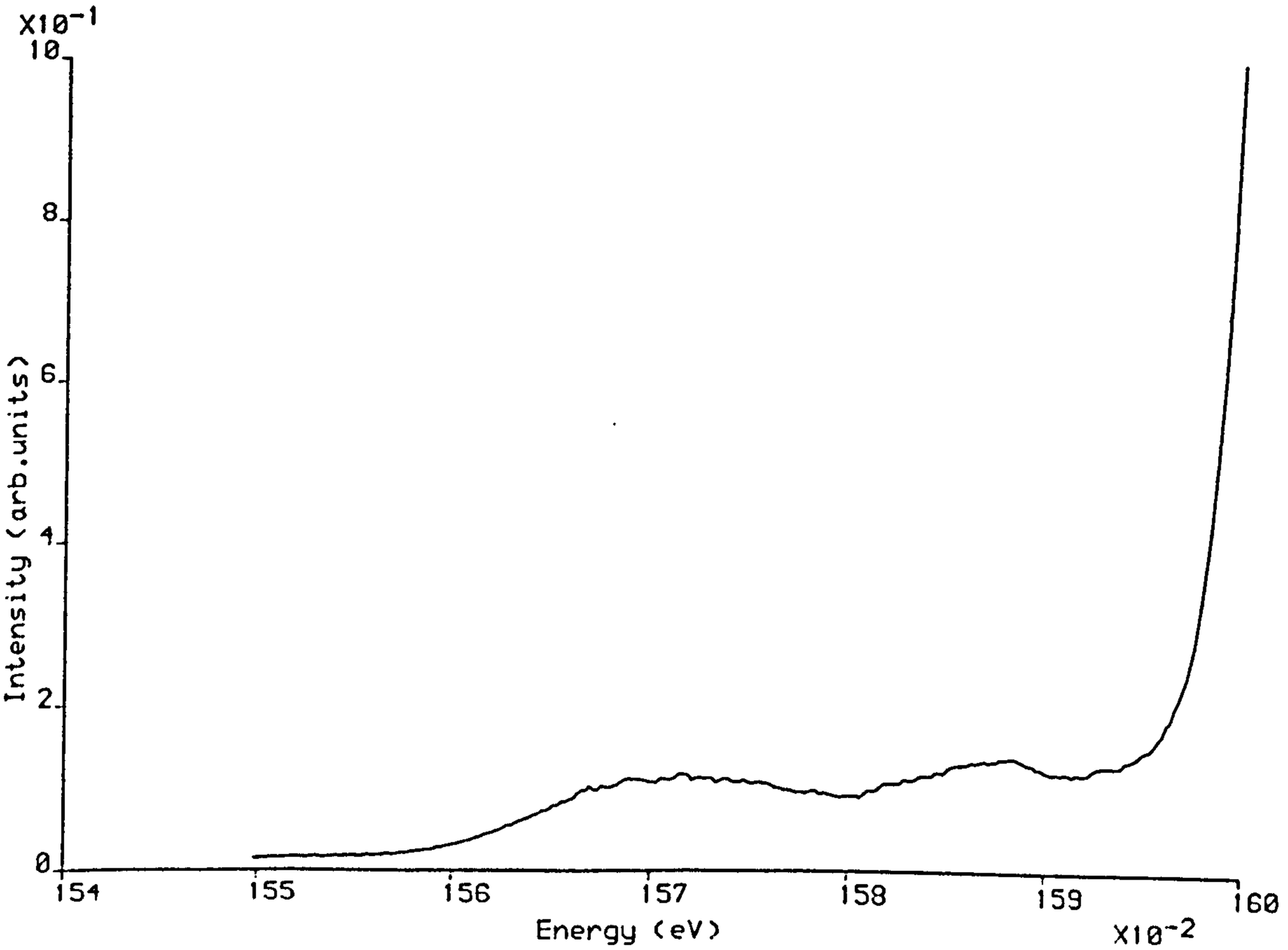

c) Spectrum from the second end of the dislocation.

d) Spectrum from unfaulted crystal adjacent to the dislocation.

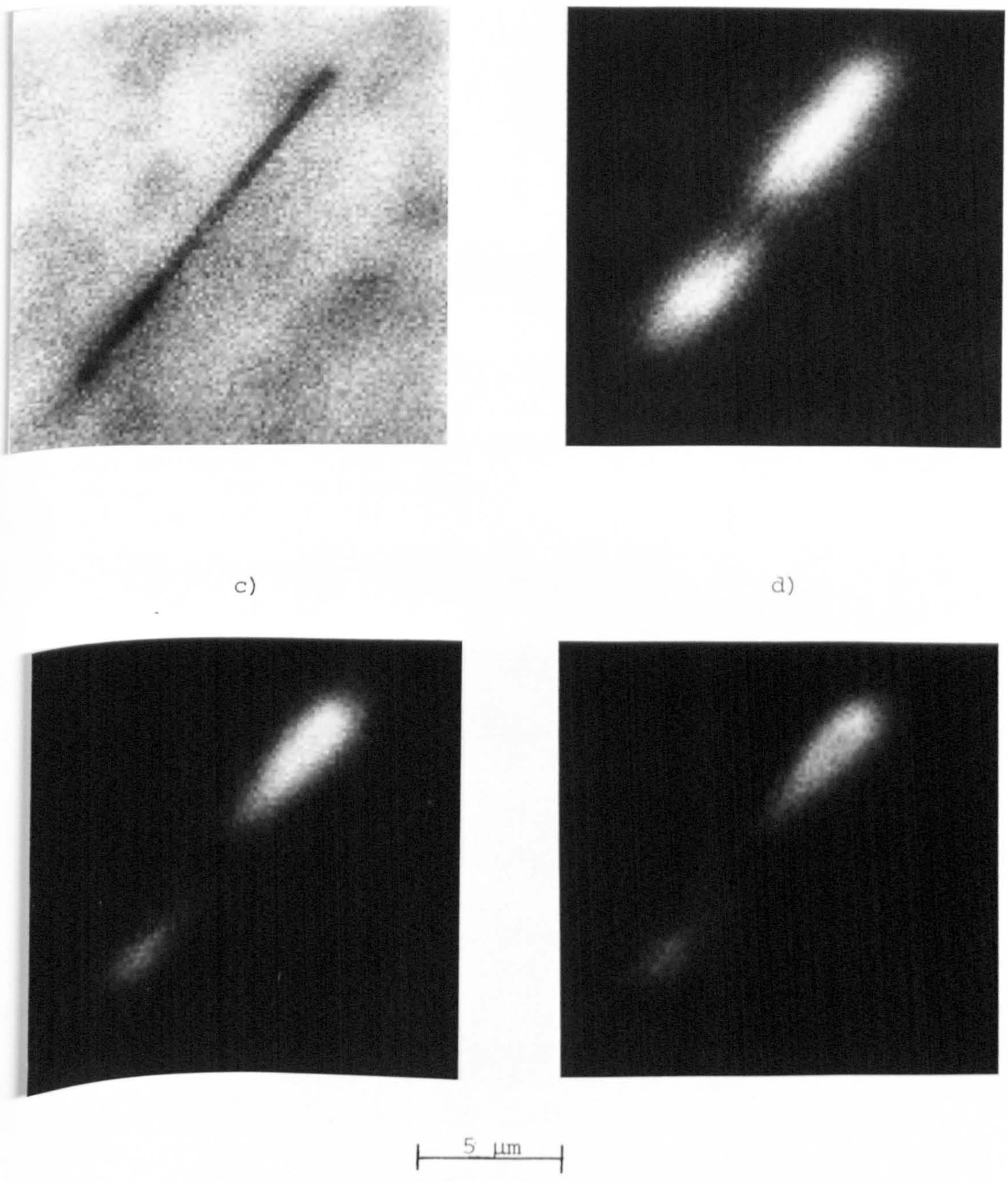

5.15 Monochromatic CL images of the misfit dislocation used to acquire the CL spectra shown in Figure 5.14. a) was acquired at the energy of the n=1(e-hh) emission while b), c) and d) were acquired at the energies marked A, B and C on Figure 5.14.

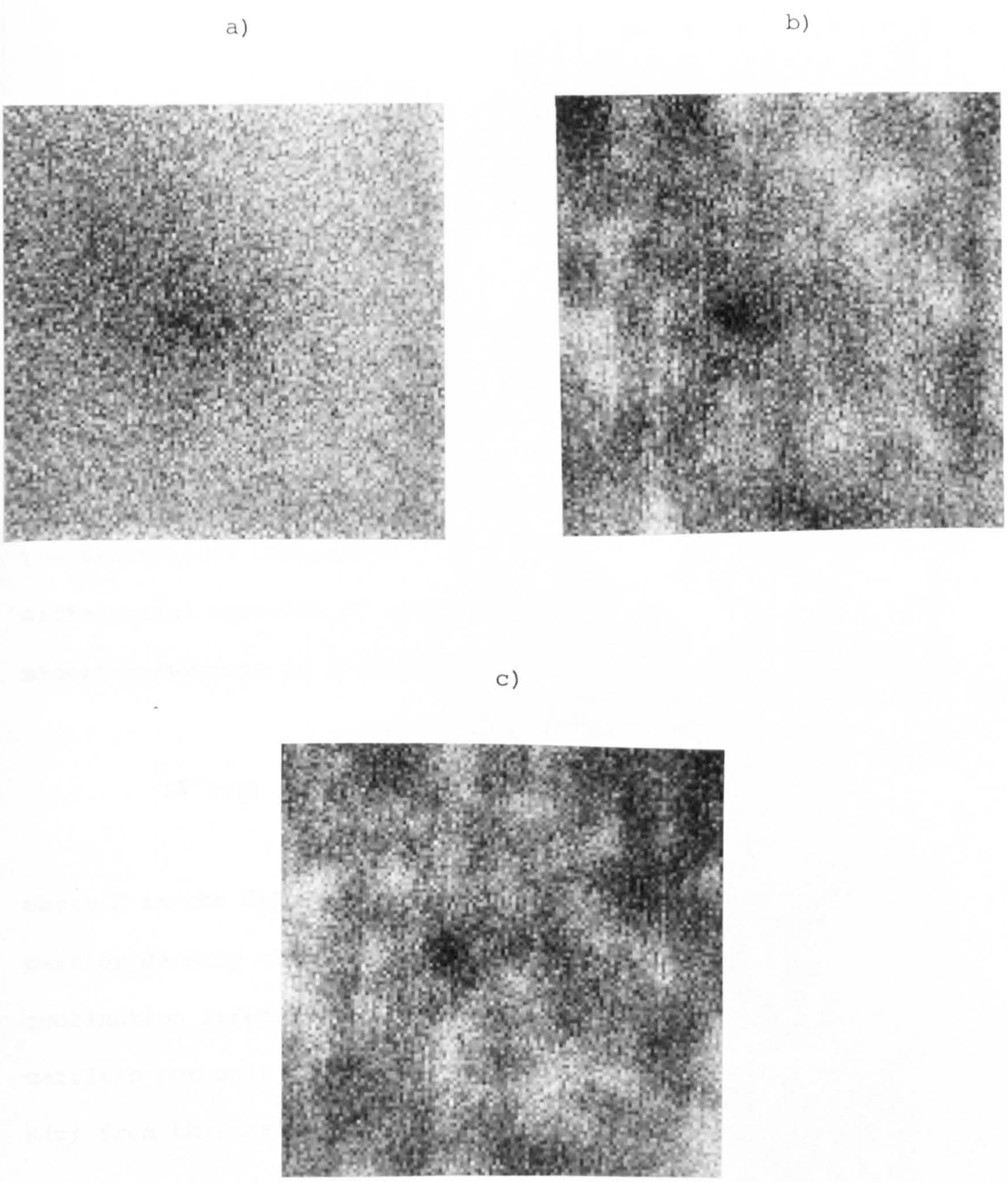

5.16 Monochromatic CL images of a threading dislocation in G43, acquired at the energies of a) the n=1(e-hh) b) 1.585 eV and c) 1.568 eV emissions.

CHAPTER SIX

THE THEORY OF CL PROFILES OF DISLOCATIONS

6.1. Introduction

In recent years considerable progress has been made towards an understanding of EBIC and CL contrast from dislocations in bulk semiconductors. The necessary theory has been derived primarily for EBIC but can in general be adapted for CL. The basis of all the theoretical calculations is the steady state, small signal differential equation of continuity for the diffusion of excess minority carriers in a semiconductor

$$D\nabla^2 P(\underline{r}) - \frac{P(r)}{\tau} - g(\underline{r}) = 0 \qquad (6.1)$$

where D is the diffusion coefficient, $P(\underline{r})$ is the excess minority carrier density at position $\underline{r}$, τ is the minority carrier recombination lifetime and $g(\underline{r})$ is the generation rate of excess carriers per unit volume (Kyser and Witry, 1964). Determining $P(\underline{r})$ from this calculation allows EBIC or CL signal intensities to be calculated. Applications of this theory include determinations of minority carrier diffusion lengths (Hackett, 1972) or recombination lifetimes (Zimmermann, 1972) from EBIC measurements. As written, equation 6.1 is only valid for doped semiconductors when the injected carrier density is less than the majority carrier density. When these conditions are not fulfilled, charge neutrality is maintained by diffusive motion of both electrons and holes, the resultant effective diffusion constant being $2D_eD_h/(D_e + D_h)$ where D_e and D_h are the diffusion coefficients for electrons and

holes respectively. The applicability of the diffusion equation (6.1) is discussed in more detail by Leamy (1982).

In order to calculate the CL or EBIC profiles of dislocations, the effect of the dislocation must be included in some fashion, most workers introducing a region of non-radiative recombination to model the dislocation. Donolato (1978/79) developed the first model for the EBIC contrast of dislocations by assuming a decrease in τ over a small region around the dislocation and using a perturbation theory approach to calculate the EBIC signal. Lohnert and Kubalek (1984) modified this approach to calculate the CL profiles of threading dislocations. The same theory has also been applied to EBIC images of oxygen induced stacking faults in silicon (Donolato and Klann, 1980). Most researchers have used the method of Donolato or modifications thereof. However, Jakubowicz (1985) and Castaldini et al. (1985) modelled dislocations as being surrounded by surfaces of infinite surface recombination velocity and then used the principle of mirror images to derive the EBIC signal. Jakubowicz considered the effects of point defects, with the defect being represented by a sphere of infinite surface recombination velocity. In a subsequent paper (Jakubowicz, 1986), threading dislocations were simulated as the sum of a series of point defects and the theory extended to allow both CL and EBIC profiles to be calculated. Castaldini et al. (1985) used a similar approach for calculating EBIC profiles of threading dislocations but modelled the dislocation as a cylinder with infinite surface recombination velocity.

Ourmazd et al. (1983) studied the EBIC contrast from dislocations as a function of temperature and compared their experimental

results with the modification of Donolato's work proposed by Pasemann (1981). Their experimental results obeyed the relation

$$\frac{dc}{dT} = \alpha C_{RT} + \beta$$

where C is the EBIC contrast of a dislocation at a temperature T, C_{RT} is the EBIC contrast at room temperature while α and β are constants. However, according to the theory the relation

$$\frac{dc}{dT} = \alpha C_{RT}$$

was expected. To explain this discrepancy, Ourmazd et al. suggested that the carrier diffusion length might vary around a dislocation. Several other explanations have been proposed by other authors including Donolato (1986) and Jakubowicz (1985) but none have achieved general acceptance.

Most workers calculating CL and EBIC profiles of dislocations have only considered dislocations in bulk semiconductors. In order to simplify the analytical solutions either a point like or spherical carrier generation volume are assumed, even though neither case accurately reflects the experimental generation volume. Additional inaccuracies are introduced because the depths and directions of the dislocations are unknown, although some authors obtained this information via TEM performed subsequent to SEM experiments. Few workers have attempted to calculate CL or EBIC profiles of dislocations in TEM samples. In addition no attempts have been made to include more than one radiative re-

combination route. In the current work, CL profiles for misfit dislocations were calculated using simplified versions of the work of both Donolato and Jakubowicz. These calculations are then compared with experimental results.

6.2. Simplifying Assumptions

As stated in the previous section the fundamental equation used in calculating CL profiles of dislocations is the diffusion equation which can be rewritten as

$$D\nabla^2 P(\underline{r},\underline{r}_o) - \frac{P(\underline{r},\underline{r}_o)}{\tau} + g(\underline{r},\underline{r}_o) = 0 \qquad (6.2)$$

where $\underline{r}_o$ is the position of the carrier generation source. The total minority carrier recombination lifetime, τ, can be written in terms of the various operative recombination processes $(\tau_1, \tau_2, \tau_3....)$ as

$$\frac{1}{\tau} = \frac{1}{\tau_1} + \frac{1}{\tau_2} + \frac{1}{\tau_3} \cdots$$

The CL intensity $I_n(\underline{r}_o)$ emitted via a radiative transition with recombination lifetime τ_n is given by

$$I_n(\underline{r}_o) = C \int_v \frac{P(\underline{r},\underline{r}_o)}{\tau_n} d^3r \qquad (6.3)$$

where v denotes integration over the whole sample and C is a proportionality factor to account for the light collection efficiency of the CL system. Obviously this equation neglects absorption and

internal reflection.

Before evaluating the integral of equation 6.3, $P(\underline{r}, \underline{r_o})$ must be determined. For sample G43, the material for which CL profiles of dislocations were studied experimentally, the layer structure was complicated, the 5 GaAs QW's being separated by 4 $A\ell_xGa_{1-x}As$ barriers and surrounded by two $A\ell_xGa_{1-x}As$ cladding layers. A full analysis of dislocation CL profiles in this material would require solutions for $P(\underline{r}, \underline{r_o})$ in each of the eleven layers taking into account the effects of surface and interfacial recombination, the finite size of the electron beam and broadening of the electron beam as it passed through the TEM specimen. This comprehensive approach was considered to be prohibitively complicated so a number of simplifying assumptions were made. As carriers in a QW are normally considered as a purely 2-dimensional system due to carrier confinement (Dingle, 1975) interfacial recombination can be neglected as its effects are incorporated in the 2-dimensional diffusion length. A further simplification is to consider the 5 separate QW's as a single effective QW. Using this approximation the presence of the $A\ell_xGa_{1-x}As$ cladding layers can also be neglected as their only action is to inject carriers into the QW's over a small area. For the misfit dislocations in G43, which were typically 20-50 μm long, it seems reasonable to assume that the dislocations have infinite length. In section 6.4 it is shown that the 2-dimensional diffusion length is typically 1-2 μm long, so that the above assumption is valid. Therefore CL profiles of misfit dislocations can be modelled in a single dimension. It should be stressed that this approach is almost certainly an over-simplification but that a more sophisticated approach would require highly complex analysis.

6.3.1. One-Dimensional Carrier Density - Unfaulted Crystal

Before calculating the carrier density in the presence of a dislocation the carrier density for unfaulted crystal is required. In one dimension the diffusion equation (6.2) can be written as

$$D \frac{d^2P(x,x_o)}{dx^2} - \frac{P(x,x_o)}{\tau} + g(x,x_o) = 0 \qquad (6.4)$$

This equation can be solved using a Green's function approach (Boas, 1983) where $P(x, x_o)$ is found for a point (delta function) source

$$g(x, x_o) = g_o \, \delta(x - x_o)$$

and g_o is the total number of minority carriers generated per second. Equation 6.4 can now be written as

$$D \frac{d^2P(x,x_o)}{dx^2} - \frac{P(x,x_o)}{\tau} = -g_o \delta(x-x_o)$$

The solution to this equation is obtained by solving for $x \neq x_o$ assuming that $P(x, x_o)$ tends to zero as x tends to plus or minus infinity. Imposing the boundary condition

$$\left.\frac{dP(x,x_o)}{dx}\right|_{x_o+\varepsilon} - \left.\frac{dP(x,x_o)}{dx}\right|_{x_o-\varepsilon} = -g_o \qquad \text{as } \varepsilon \to 0$$

and requiring that $P(x, x_o)$ is continuous at $x = x_o$ gives

$$P(x,x_o) = \frac{g_o L}{2D} e^{-|x-x_o|/L}$$

where $L = \sqrt{D\tau}$ is the minority carrier diffusion length. The

carrier density $P_a(x, x_o)$ due to an arbitrary minority carrier generation source can be found from

$$P_a(x,x_o) = \int_{-\infty}^{\infty} \frac{g(x,x_o)}{g_o} P(x,x_o)\, dx_o$$

although this was not performed in the current study.

6.3.2. Carrier Density in the Presence of a Dislocation

As stated in section 6.1, previous workers have modelled dislocations in terms of a region of reduced minority carrier lifetime (Donolato, 1978/9) or surfaces with high surface recombination velocity (Jakubowicz, 1985). Using the reduced lifetime model the simplest situation is to represent the dislocation as a region of width ω centred on $x = 0$, with reduced lifetime $\tau = \tau'$. The carrier density in each of the 3 regions can be found in the same way as for unfaulted crystal but with the additional boundary conditions that $P(x, x_o)$ and $\frac{dP}{dx}(x, x_o)$ must be continuous at $x = \pm \frac{\omega}{2}$. This procedure involves solving 8 simultaneous equations. The resultant expression for $P(x, x_o)$ is complex amd will not be included here. (See Appendix 1) Assuming that for sample G43 there are two recombination routes with lifetimes τ_{hh} and τ_{im} due to the n = XX(e - hh) and impurity QW luminescence respectively, and that τ_{im} decreases in the region $-\frac{\omega}{2} < x < \frac{\omega}{2}$, then the resultant expression for $P(x, x_o)$ can be substituted into equation 6.3 to derive the CL profiles of the dislocation at the energies of the heavy hole and the impurity luminescence. For $x_o > \frac{\omega}{2}$ then $I_{hh}(x_o)$ and $I_{im}(x_o)$, the CL intensities at the energies of the heavy hole and impurity luminescence respectively, can be written

as

$$I_{hh}(x_o) = a - be^{-x_o/L} \qquad (6.5)$$

$$I_{im}(x_o) = c + de^{-x_o/L} \qquad (6.6)$$

where a, b, c and d are all real, positive constants with a always greater than b. Equations 6.5 and 6.6 are only valid when the electron beam is outside the region in which the dislocation affects the recombination lifetime. To overcome this limitation a slightly more complex model was incorporated into a computer program. In this model the dislocation was represented by n regions of variable width, with each region containing an arbitrary number of independent radiative or non-radiative recombination routes. In the i^{th} region the carrier density $P_i(x, x_o)$ given by

$$P_i(x, x_o) = A_i e^{\frac{x}{L_i}} + B_j e^{\frac{-x}{L_i}}$$

where L_i is the diffusion length in the region. The coefficients A_i and B_i were evaluated numerically using the boundary conditions outlined previously, and the CL signal for each radiative recombination route evaluated (Appendix 1).

If dislocations in 3-dimensions are represented by a surface of high surface recombination velocity then in 1-dimension the dislocation can be represented by a point with high 'point' recombination velocity. For this situation $P(x, x_o)$ can be

found using the principle of mirror images (Morse and Feshbach, 1953). This method will not be discussed in detail here. For a dislocation at x = 0 and for x_o > 0 the CL signals $I_{hh}(x_o)$ and $I_{im}(x_o)$ have the same form as in equations 6.5 and 6.6, although the coefficients a, b, c and d are determined differently. Although the dislocation could be modelled in terms of a number of points with differing recombination velocities this was not done. However, a computer program was written which calculated the CL profiles assuming 3 equally spaced points, centred about the origin, with the 2 outer points having equal recombination velocities (see Appendix 1).

6.3.3. Threading Dislocations

To calculate the CL profile of threading dislocation 2-dimensional carrier diffusion and a point generation source were again assumed. However, assuming infinite dislocation length is no longer valid. As for misfit dislocations, threading dislocations were again modelled in terms of either a decrease in minority carrier lifetime or a surface of high surface recombination velocity. The diffusion equation is much harder to solve in 2 dimensions than in 1 dimension, so that approximations were needed in order to obtain the carrier density.

As a first step to modelling threading dislocations the 2-dimensional carrier density, for unfaulted crystal, was needed. Following the method of Donolato (1981) the Green's function equation corresponding to the 2-dimensional diffusion equation was written as

$$\frac{d^2G(\underline{r}:\underline{r}')}{dr^2} + \frac{1}{r}\frac{dG(\underline{r}:\underline{r}')}{dr} - \frac{G(r:r')}{L^2} = -\frac{\delta(\underline{r}-\underline{r}')}{2\pi r}$$

where $G(\underline{r}:\underline{r}')$ is the appropriate Green's function. The solution for $G(\underline{r}:\underline{r}')$ is (Morse and Feshbach, 1953)

$$G(\underline{r}:\underline{r}') = \frac{1}{2\pi} K_o(|\underline{r}'-\underline{r}|/L)$$

where K_o is the zero-th order modified Bessel function of the 2nd kind.

For a point generation source at r_o given by

$$g(\underline{r},\underline{r}_o) = g_o \frac{\delta(\underline{r}-\underline{r}_o)}{2\pi r}$$

where g_o is the carrier generation rate per second, then the carrier density for unfaulted crystal, $P_o(\underline{r}, \underline{r}_o)$, is given by

$$P_o(\underline{r},\underline{r}_o) = \frac{1}{D} \int_s g(\underline{r}',\underline{r}_o)G(\underline{r}:\underline{r}')d\underline{r}'$$

where s denotes integration over the whole area of the sample. Therefore $P_o(\underline{r}, r_o)$ can be written

$$P_o(\underline{r},\underline{r}_o) = \frac{g_o}{2\pi D} K_o(|\underline{r}-\underline{r}_o|/L)$$

If a dislocation is represented as a region F, of reduced carrier lifetime, then Donolato (1978) has shown that the carrier density $P(\underline{r}, \underline{r}_o)$, can be written as

$$P(\underline{r},\underline{r}_o) = P_o(\underline{r},\underline{r}_o) - \int_F \gamma P_o(\underline{r}',\underline{r}_o)G(\underline{r}:\underline{r}')d\underline{r}' \qquad (6.7)$$

The integral in this equation represents a first order perturbation

theory approximation and referred to as the Born approximation by analogy with quantum mechanics. The term γ is included to account for the dislocation 'strength' and is given by

$$\gamma = \frac{1}{L'^2} - \frac{1}{L^2}$$

where L' is the minority carrier diffusion length in the region of the dislocation. Substituting from equation 6.7 into equation 6.3 gives the dislocation CL profile as

$$I(\underline{x}_o) = g_o C - \frac{\gamma g_o C}{2\pi} \int_F K_o(|\underline{r}-\underline{x}_o|/L) \, d\underline{r} \qquad (6.8)$$

In the current study the region F was assumed to be circular. As the integral in equation 6.8 is difficult to solve analytically for this situation numerical solutions were calculated using a Simpson's rule approximation to the integral.

If a dislocation is modelled as a surface (or closed loop in 2 dimensions) with high surface recombination velocity then a different approximation is needed to calculate the minority carrier density. Following the method of Jakubowicz (1985) and using the principle of images (Feynman, 1964) applied to a dislocation modelled as a circle of infinite 'surface' recombination velocity, then the dislocation can be approximated by an image of the generation source situated at the centre of the dislocation. The carrier density can then be written as

$$P(\underline{r},\underline{r}_o) = \frac{g_o}{2\pi D} K_o(|\underline{r}-\underline{r}_o|/L) - \frac{g_o \, K_o(r_o/L)}{2\pi D \, K_o(a/L)} K_o(r/L) \qquad (6.9)$$

where a is the dislocation radius. For a dislocation of finite strength then a can be replaced by an effective radius γa where γ is a constant such that $0 < \gamma < 1$. Note that this expression for $P(\underline{r}, \underline{r}_o)$ is only valid outside the circle representing the defect. To obtain $I(x_o)$ the equation

$$I(x_o) = \frac{1}{\tau} \int_S P(\underline{r},\underline{r}_o)d\underline{r} - \frac{1}{\tau} \int_F P(\underline{r},\underline{r}_o)d\underline{r}$$

can be evaluated using equation 6.12. The integral over F must be included because the carrier density is zero within the circle representing the dislocation. The final result for $I(x_o)$ is

$$I(x_o) = g_oC - \beta g_oC - \frac{g_oC}{2\pi L^2} \int_F \left[K_o(\underline{r}-\underline{x}_o /L) - \beta K_o(\underline{r} /L)\right] d\underline{r} \quad (6.10)$$

where $$\beta = \frac{K_o(x_o/L)}{K_o(\gamma a/L)}$$

Note that if a is small this expression for $I(x_o)$ is equivalent to equation 6.9.

Again this equation is difficult to evaluate analytically so that numerical solutions were obtained using a Simpson's rule approximation to the integral. It is worth mentioning that this method involves integration in 2 dimensions and requires a significant amount of computer time to obtain simulations of the required accuracy, particularly since the function K_o must also be evaluated iteratively.

6.4. Results and Interpretation

6.4.1. Unfaulted Crystal

Figures 6.1 a), b), and c) show three monochromatic CL images acquired from a defect free region of G43. The images were acquired at the energies of the luminescence peaks ascribed to the n = 1X(e - hh), n = 1(e - A_I) and n = 1(e - A_C) transitions respectively (Chapter Five). Two important features are illustrated by these images. Firstly, all three images show gradual variations in intensity over distances of 2 - 5 μm, the spatial resolution probably being limited by the 2-dimensional diffusion length. In the impurity CL images this effect is partly obscured by intensity variations over a submicron scale, probably limited in spatial resolution by broadening of the electron beam as it passes through the TEM specimen. These two effects will be discussed in greater detail in section 6. However, it is obvious that these essentially random intensity variations will complicate the interpretation of results from dislocation. In an attempt to minimise this effect CL profiles of dislocations were not normally obtained from linescans. Instead CL images were processed using the image analysis program, SEMPER. To obtain 1-dimensional profiles from images, columns of pixels parallel to the dislocations were summed together and stored as a single channel.

6.4.2. Misfit Dislocations

Figure 6.2 shows a typical dislocation profile from an approximately 50 μm long misfit dislocation, and produced by image processing as outlined above. This profile was acquired at the energy of the heavy hole emission. The dislocation position

corresponds to the position of mininum intensity. This figure illustrates two phenomena that complicate comparisons between theory and experiment. Firstly, the CL intensity either side of the dislocation is asymmetric,possibly due to the TEM foil bending around the dislocation. To compensate for this, CL profiles were further processed to obtain a profile showing the average behaviour of the two sides of the dislocation. All subsequent CL profiles from misfit dislocations have been processed in this way but have also been mirror reflected about the line of the dislocation. Figure 6.2 also shows that the heavy hole luminescence intensity reaches a maximum value some 8 - 12 μm from the dislocation. As discussed in Chapter Five it is not clear whether this effect reflects a genuine increase in intensity or is merely due to contamination. Owing to this uncertainty, no attempt was made to include this behaviour in theoretical calculations of CL profiles. Instead, only dislocations where this behaviour was weakest were compared with theory, the full width of CL profiles being restricted to less than 10 μm. Figure 6.2 has been rescaled such that the maximum CL signal is unity. Most previous workers have plotted the contrast function $C(x_o)$, defined as

$$C(x_o) = \frac{I(\infty) - I(x_o)}{I(\infty)}$$

rather than the CL signal. In the current work $I(\infty)$ was difficult to determine due to the spatial variations in the CL signals from unfaulted crystal, particularly for the impurity emission where $I_{im}(x_o)$ is normally small. Therefore, CL profiles of dislocations in this Chapter have been plotted with the maximum signal normalised to unity.

Figure 6.3 shows two dislocation profiles acquired from the same dislocation at the energies of the heavy hole and impurity luminescence. For this 30 μm long misfit dislocation, only a single impurity luminescence peak was detected, the energy being 1.586 eV. In this Figure the heavy hole luminescence decreases to a minimum at the dislocation while the impurity luminescence increases to a maximum at the same point. The impurity luminescence is actually about 30 times weaker than the heavy hole luminescence. For purposes of comparison Figure 6.4 shows the same two dislocation profiles but with the heavy hole emission signal subtracted from a constant and rescaled. After this operation it can be seen that the two profiles are very similar. These experimental results agree well with theoretical profiles generated using equations 6.5 and 6.6 except when the electron beam is close to the dislocation. If the dislocation is modelled as a narrow region of width w, inside which two radiative recombination routes, corresponding to the heavy hole and impurity transitions, and outside which only the heavy hole recombination route is present then a better fit is obtained. Figure 6.5 compares a CL profile calculated using this model with the experimental heavy hole emission profile and shows good agreement between the two. The calculated profile used a diffusion length of 1.4 μm and a dislocation width of 0.4 μm. The dislocation could also be modelled as two surfaces of high surface recombination velocity separated by 0.4 μm, and which radiate at the energy of the impurity emission. Again, this model shows good agreement with the experimental results (Figure 6.6) for a diffusion length of 1.4 μm. The impurity luminescence CL profiles also show

good agreement with the calculated profiles. However, the intensity of the impurity luminescence is not sufficient to account for the observed change in intensity of the heavy hole emission. Therefore a third non-radiative recombination route must also be present at the dislocation.

Figure 6.7 shows a CL dislocation profile acquired at the energy of the heavy hole luminescence, from a different dislocation. Also shown is the theoretical profile calculated for a diffusion length of 1.6 μm and assuming that a region of width 0.4 μm, centred on the dislocation, contains two recombination routes as opposed to only the heavy hole recombination route outside this region. As before good agreement is obtained between the theoretical and experimental curves. As in the previous example only one impurity luminescence peak was detected for this dislocation. Figure 6.8 shows a CL profile acquired from this dislocation at the energy of the impurity luminescence, compared with the profile calculated using the same model as for Figure 6.7. As before, good agreement between the experimental and calculated curves was obtained but only when diffusion length of 0.7 μm was used in the calculation as compared to the value of 1.6 μm used to simulate the heavy hole CL profile. This type of behaviour was observed at by far the majority of the misfit dislocations observed in this study, the diffusion length needed to simulate the impurity luminescence CL profiles always being less than or equal to the diffusion length needed to simulate the heavy hole luminescence profiles. For misfit dislocations which showed more than one impurity luminescence peak, good agreement was again obtained between calculated and experimental

results but the lower the energy of the emission the lower the diffusion length needed to simulate the experimental data. Misfit dislocations where CL profiles acquired at the energies of the impurity luminescence showed local maxima either side of the dislocation (Figure 6.8) were not studied extensively but could be simulated as before except for values of x_o between ± 1.0 μm.

6.4.3. Threading Dislocations

Experimental results from threading dislocations were much harder to obtain than for misfit dislocations. In the latter case CL images were acquired by scanning the electron beam perpendicular to the dislocation, so that any specimen drift or vibration was easy to detect. For threading dislocations specimen drift was harder to detect. In addition, as the contrast from threading dislocations was generally weak, they could only be studied at relatively high magnifications when well separated from other crystal defects. The impurity luminescence around threading dislocations could not be studied. Unlike misfit dislocations, threading dislocations did not show enhanced impurity luminescence but gave reduced intensity as compared to the surrounding unfaulted crystal. To study this luminescence would have required long acquisition times resulting in unacceptable levels of specimen drift.

As for misfit dislocations, CL profiles of threading dislocations were obtained by processing monochromatic CL images using the image analysis program SEMPER. As monochromatic images of threading dislocations were radially symmetric, SEMPER was used to take radial averages around the dislocation. The procedure

used produced a CL profile equivalent to that which would have been produced by scanning an electron beam across a threading dislocation. Figure 6.9 shows a CL profile of a threading dislocation produced as outlined above and acquired at the energy of the heavy hole luminescence. The image used to obtain this profile was the only example acquired in the current study which could be analysed. Although the same experiment was performed a number of times this example was the only one for which no significant specimen drift occurred during acquisition of the image. Figure 6.10 shows the same dislocation profile calculated using Donolato's method (equation 6.9) for a diffusion length of 4 μm and assuming the dislocation has an effective radius of less than 0.01 μm, with the constant γ adjusted so that the contrast levels of the experimental and calculated profiles are approximately equal. Except for a narrow region close to the dislocation the two profiles are in good agreement. Figure 6.11 compares the same experimental data with the profile calculated using the method of Jakubowicz (equation 6.10), again assuming a diffusion length of 4 μm and a small effective radius for the dislocation. Note that this method cannot be used to evaluate the CL signal for $x_o \approx 0$ as the model used requires the CL signal to be zero on the 'surface' used to represent the dislocation. Except for the region close to the dislocation this model again produces good agreement with the experimental data.

6.5 Discussion

In general the calculated CL profiles for dislocations agree

well with the experimental results, despite the simplifications used. CL profiles calculated using two different models to represent the effects of the dislocations gave very similar results except in the immediate vicinity of the dislocation. For this situation the method of Donolato appeared to match the experimental data more closely than the method of Jakubowicz. However, no attempt was made to include the effects of a finite generation volume so that this result is not conclusive. Comparison of theory and experiment for misfit dislocations revealed two interesting features. Firstly, in addition to the enhanced impurity related luminescence observed for all misfit dislocations, there must also be enhanced non-radiative recombination at or near to the dislocation, possibly due to a space charge region around the dislocation core or impurity decoration. Secondly, although both the heavy hole and impurity luminescence near dislocations appear to obey the equations (6.5 and 6.6) derived from the diffusion equation, the diffusion length required to simulate the impurity luminescence dislocation profiles was generally shorter than for the heavy hole luminescence. CL images from unfaulted crystal showed similar behaviour in that spatial variations in the intensity of the heavy hole luminescence occurred over a larger length scale than for the impurity luminescence. There are a number of possible explanations for this behaviour. It is possible that the diffusion length varies significantly both in unfaulted crystal and around misfit dislocations. As both the heavy hole and impurity luminescence appear to obey equations 6.5 and 6.6 it seems more likely that two or more diffusion processes may be operating. For nominally undoped quantum

well structures the heavy hole luminescence is due to free excitons while the impurity luminescence is due to an electron to acceptor transition (Balkan et al., 1986). The intensity of the heavy hole emission is therefore related to the exciton density while the impurity emission intensity is related to the density of free electrons. This may account for the different diffusion lengths observed for the two recombination routes.

There are a number of aspects to the work described in this Chapter which merit further investigation. Dislocation CL profiles were calculated assuming a point like generation source. This assumption is physically unrealistic due to broadening of the electron beam as it passes through the TEM foil. Modifying the theory to include this effect might improve the accuracy of calculated dislocation CL profiles for small values of x_o. For some misfit dislocations, where the impurity luminescence was relatively weak, CL images acquired at the energy of this luminescence showed two local maxima either side of the dislocation. It is believed that this effect can be modelled in terms of a narrow region of enhanced non-radiative recombination around the dislocation core. If this region is surrounded by a wider region of less strongly enhanced radiative impurity luminescence it may be possible to simulate the observed dislocation profiles. This effect was briefly investigated in the current work but further study was frustrated by the lack of reliable experimental data. The relative weakness of the impurity luminescence necessitated the use of long image acquisition times for which specimen drift became significant.

Although the theory outlined in this Chapter was only applied

to dislocations in a QW structure it could easily be applied to other defects such as stacking faults or to simpler layer structures, particularly for samples where the diffusion length could be determined independently. The effects of temperature on the CL contrast of dislocations might also be investigated.

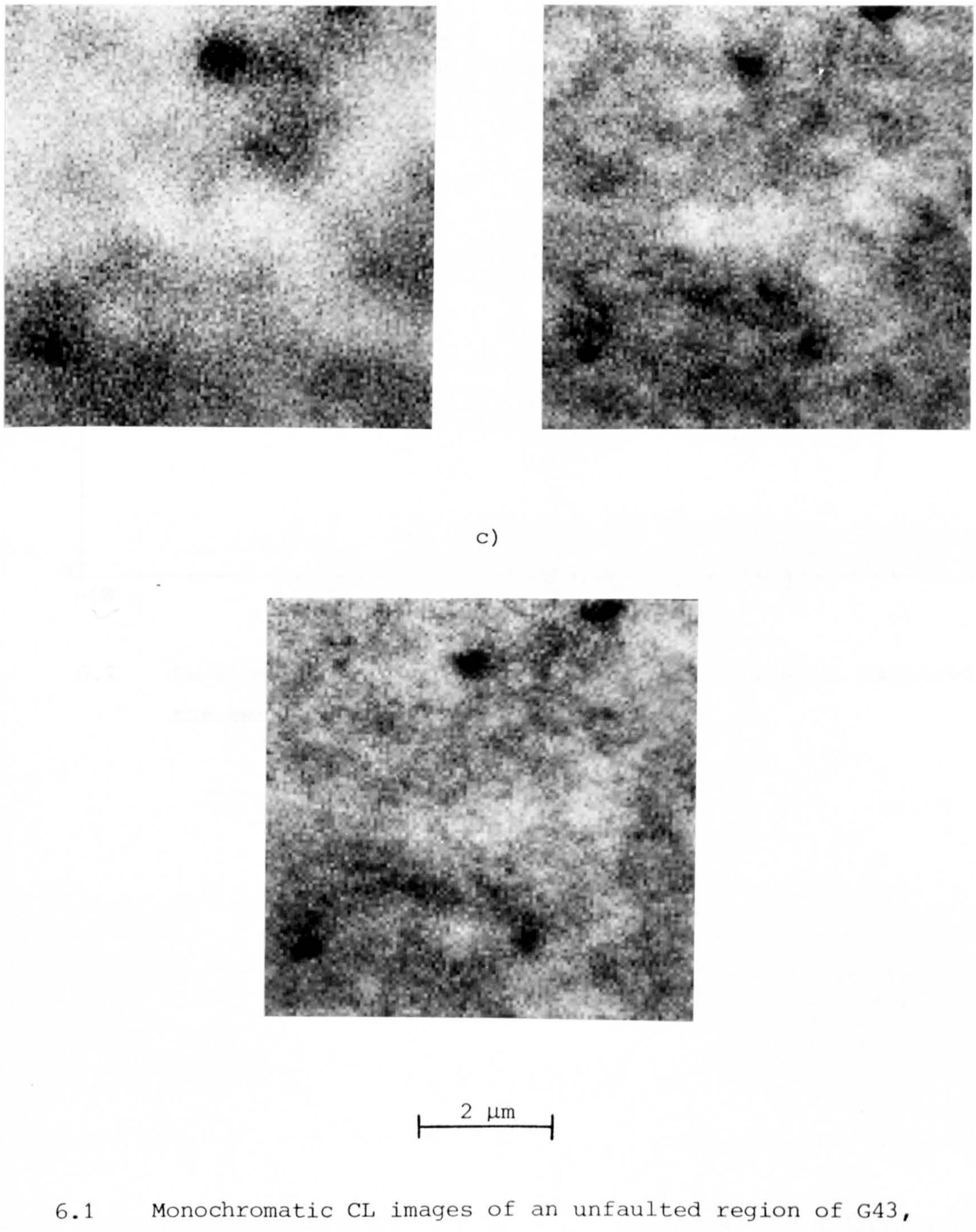

6.1 Monochromatic CL images of an unfaulted region of G43, acquired at the energies of a) n=1(e-hh) b) n=1(e-A_I) and c) n=1(e-A_C) emissions (see Chapter 5).

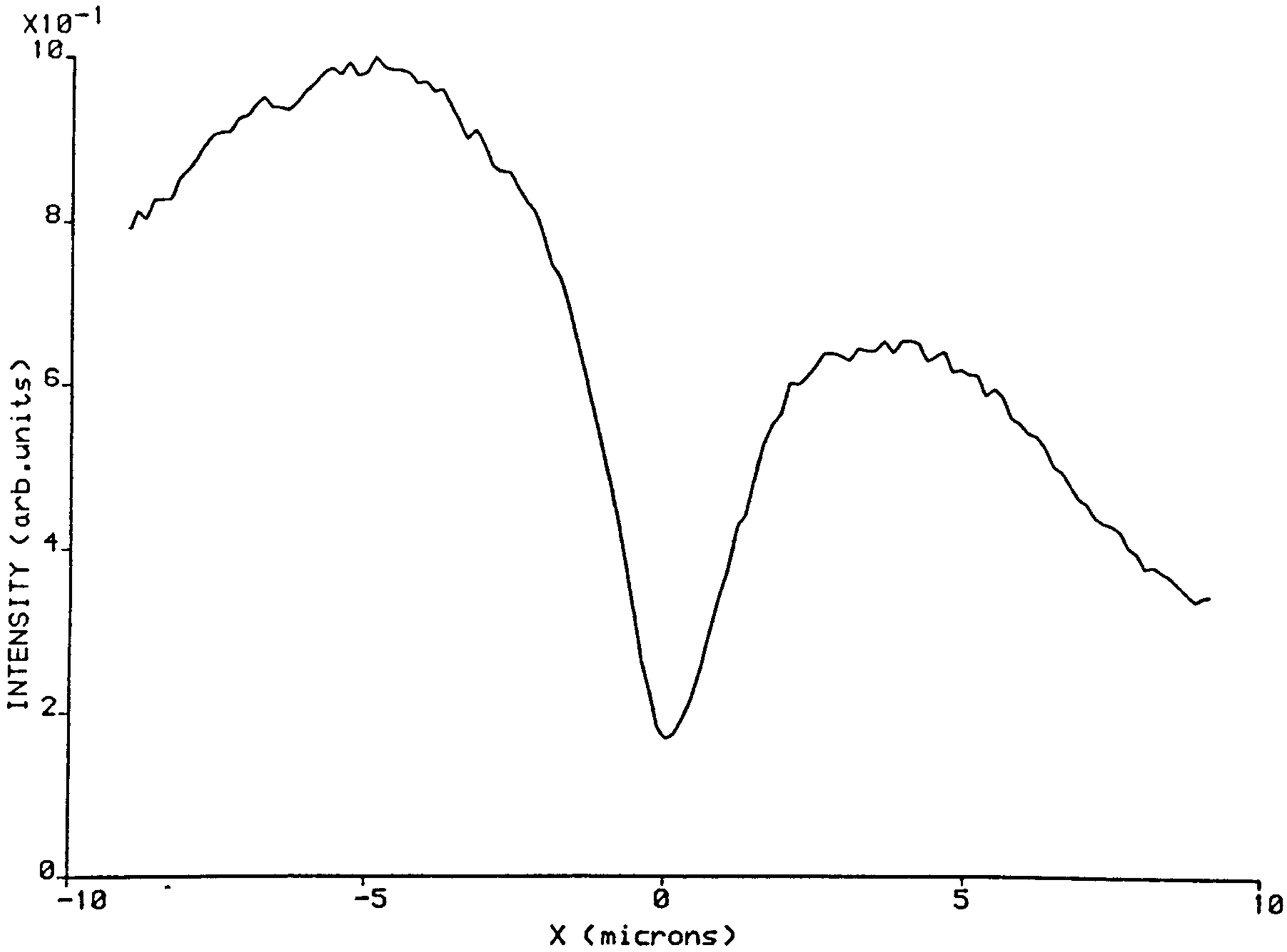

6.2 CL linescan across a typical misfit dislocation, acquired at the energy of the n=1 (e-hh) emission.

a)

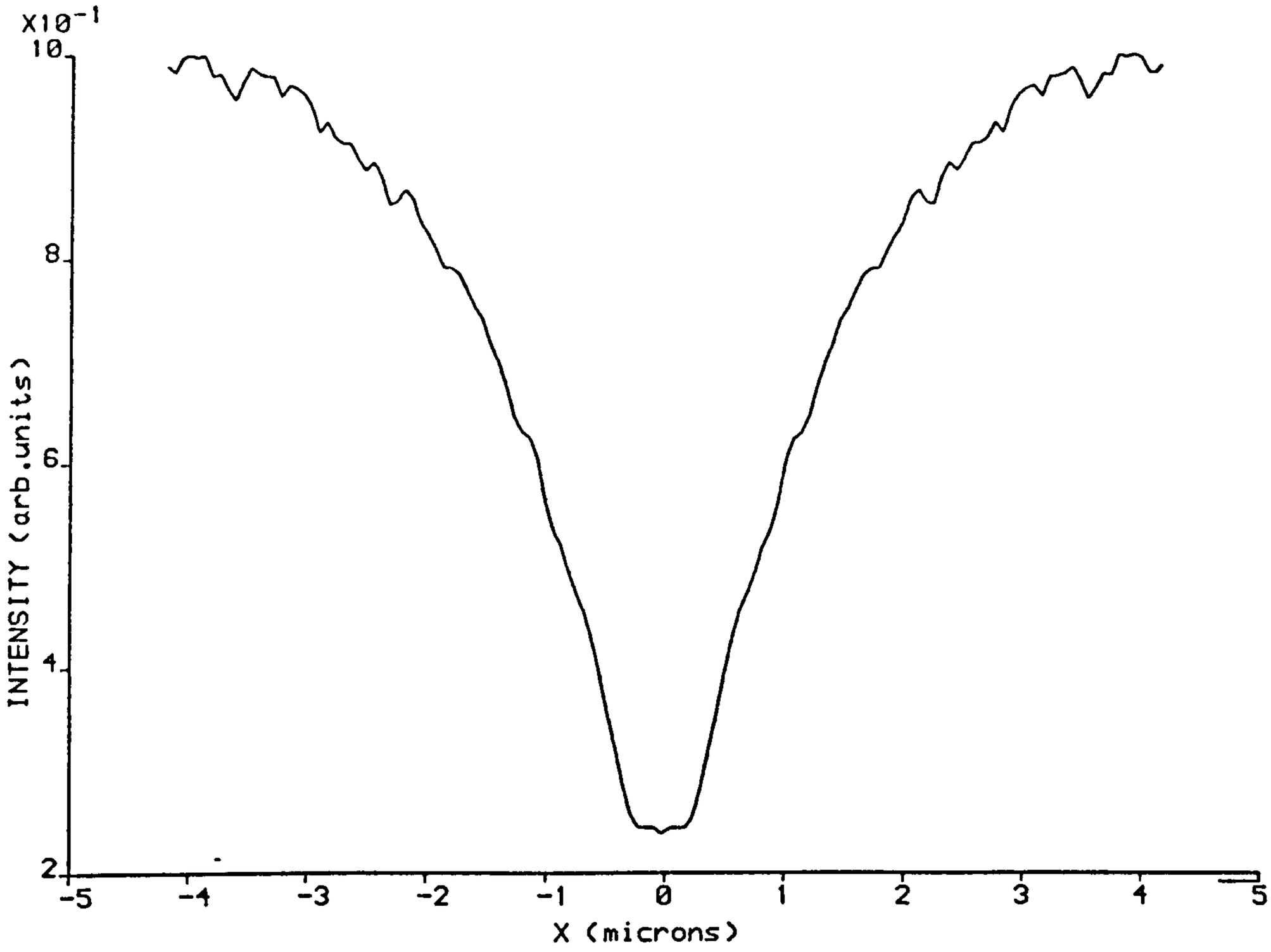

b)

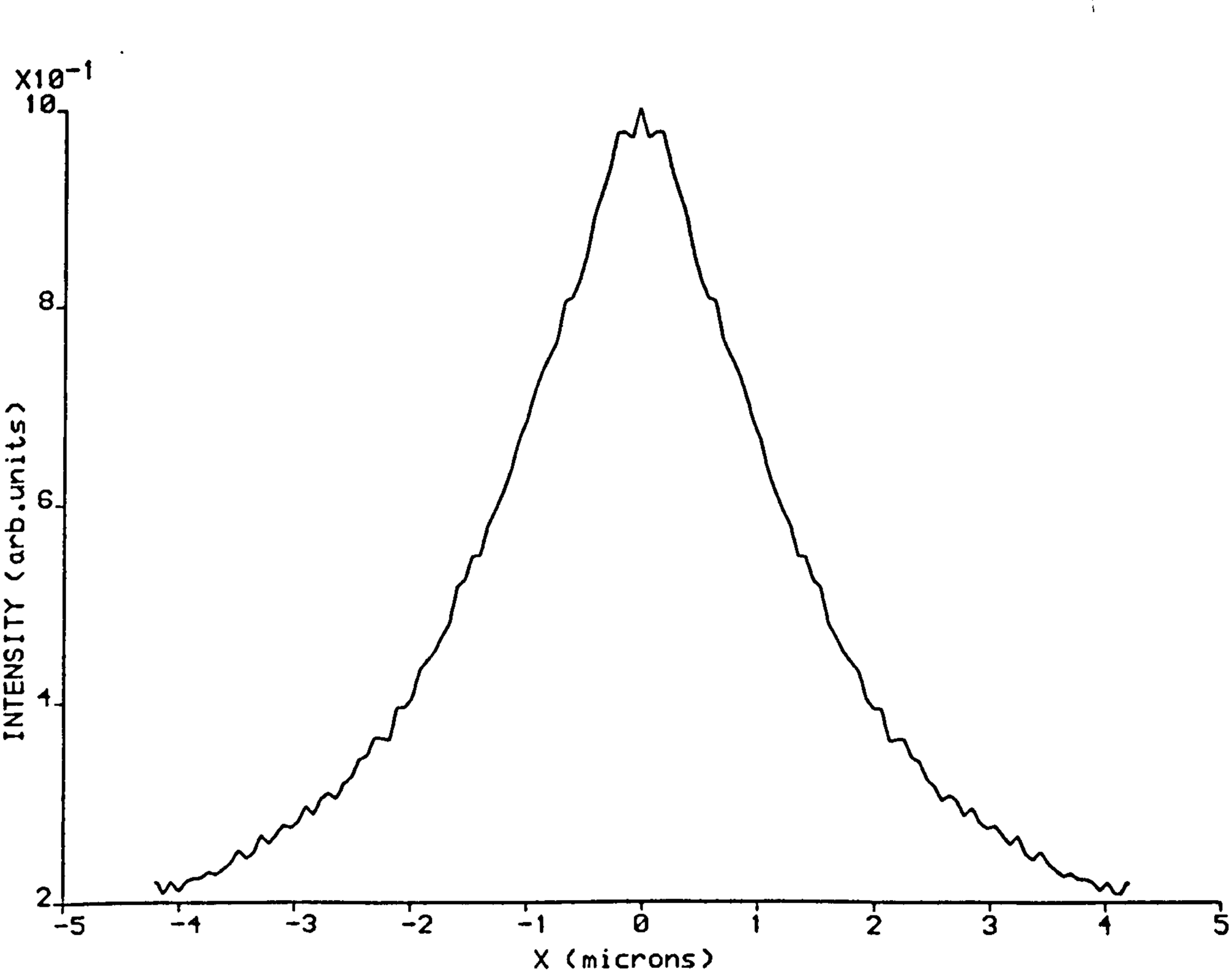

6.3 Two CL linescans across the same misfit dislocation, acquired at the energies of a) the n=1(e-hh) emission and b) the n=1(e-a) emission.

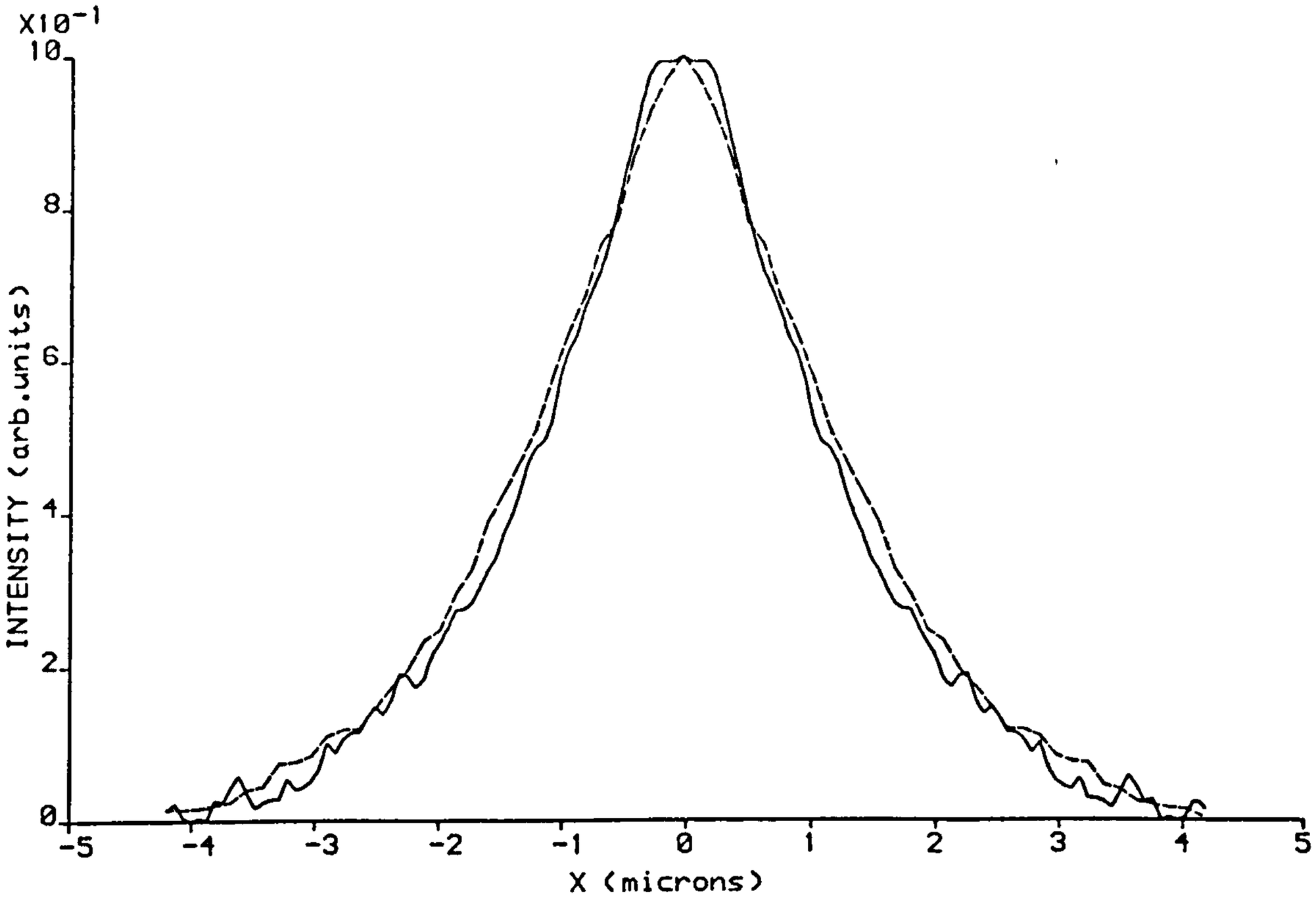

6.4 Comparison of two CL linescans across the same misfit dislocation, acquired at the energies of the n=1(e-hh) (solid line) and n=1(e-a) (broken line) emissions. The n=1(e-hh) data has been subtracted from a constant and rescaled.

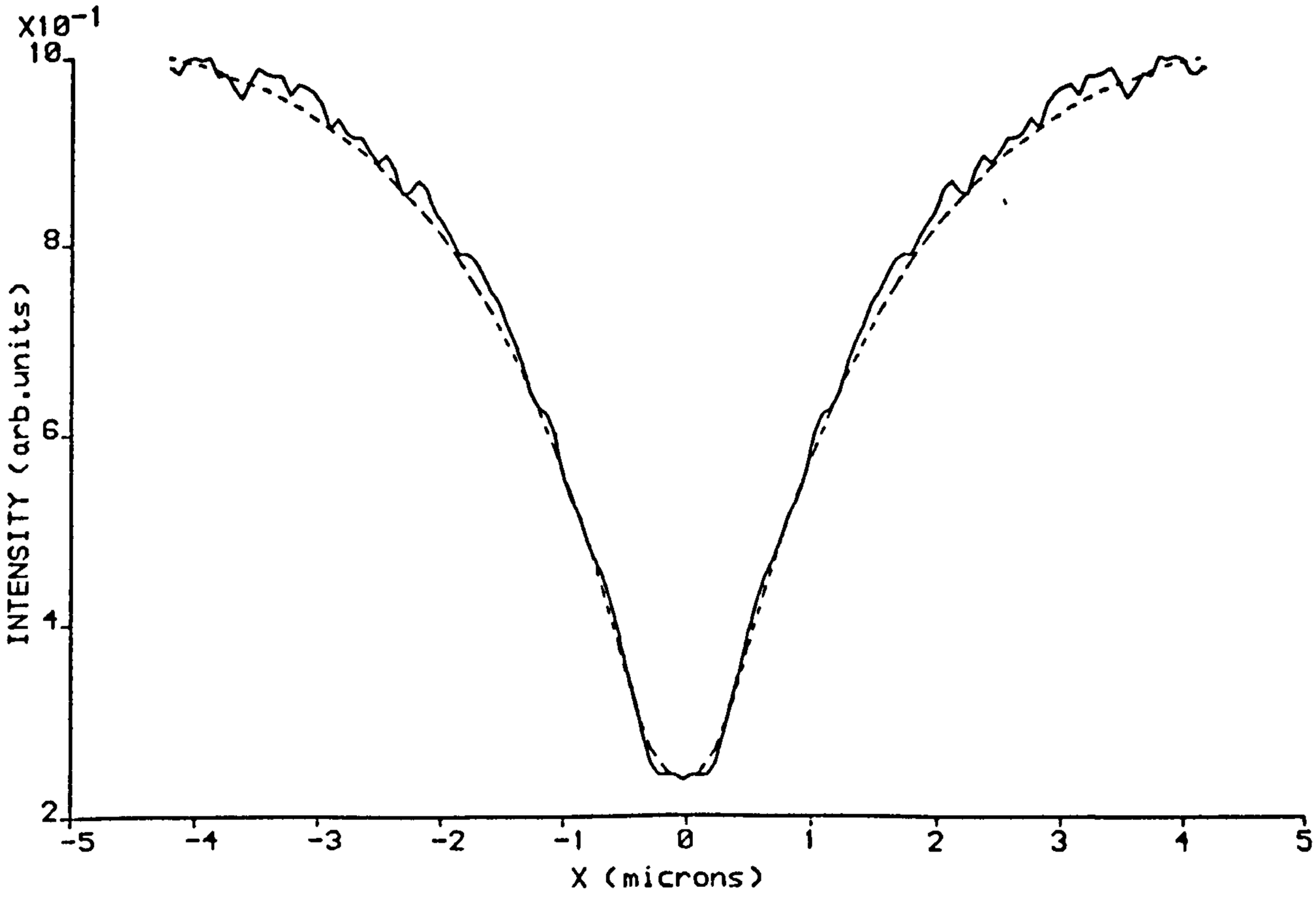

6.5 Comparison of experimental (solid line) and calculated (broken line) linescans across a dislocation. The experimental data was acquired at the energy of the n=1(e-hh) emission (see text).

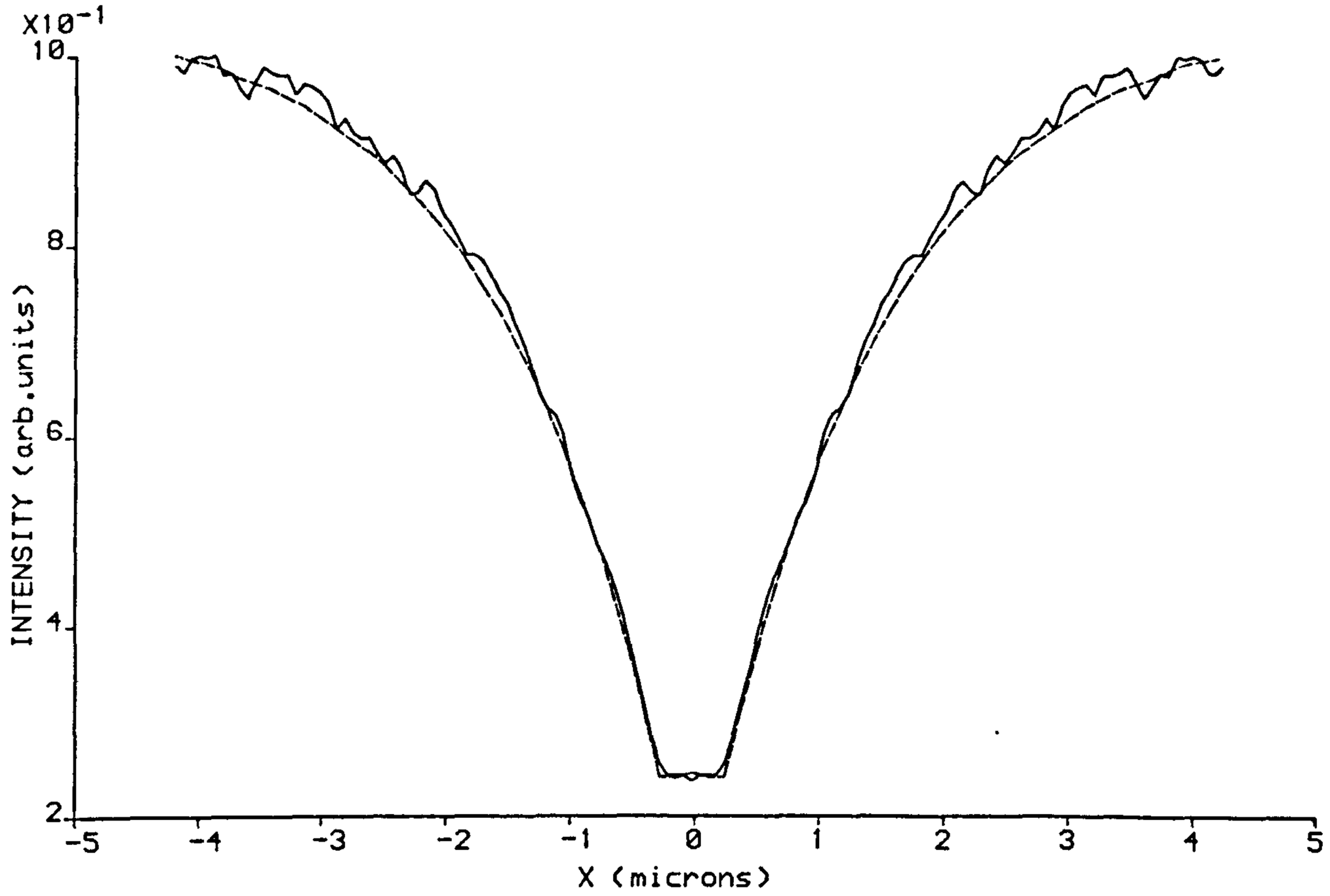

6.6 Comparison of experimental (solid line) and calculated (broken line) CL linescans across a misfit dislocation for the n=1(e-hh) emission (see text).

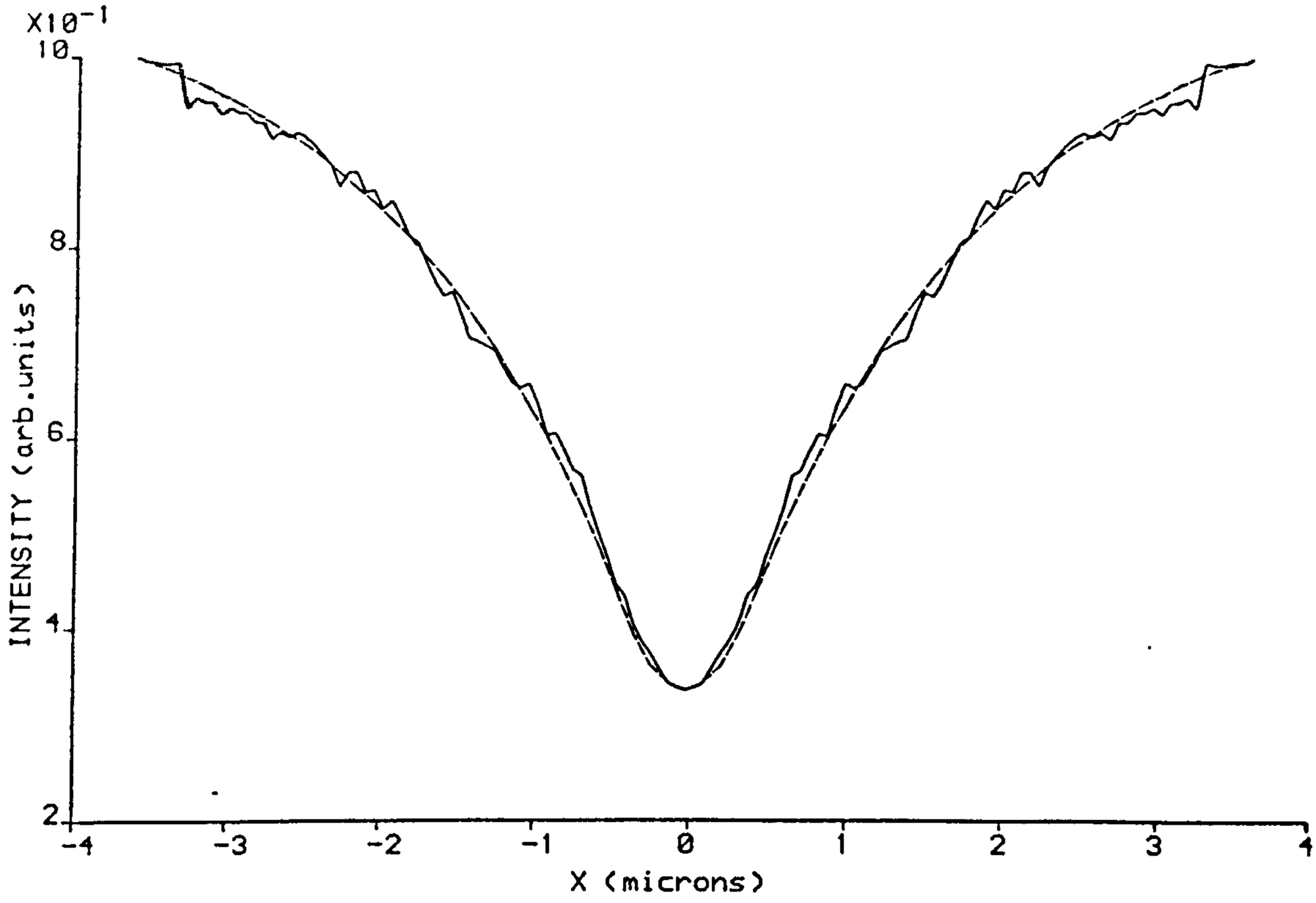

6.7 Experimental (solid line) and calculated (broken line) CL line-scans across a misfit dislocation. The experimental data was acquired at the energy of the n=1(e-hh) emission (see text).

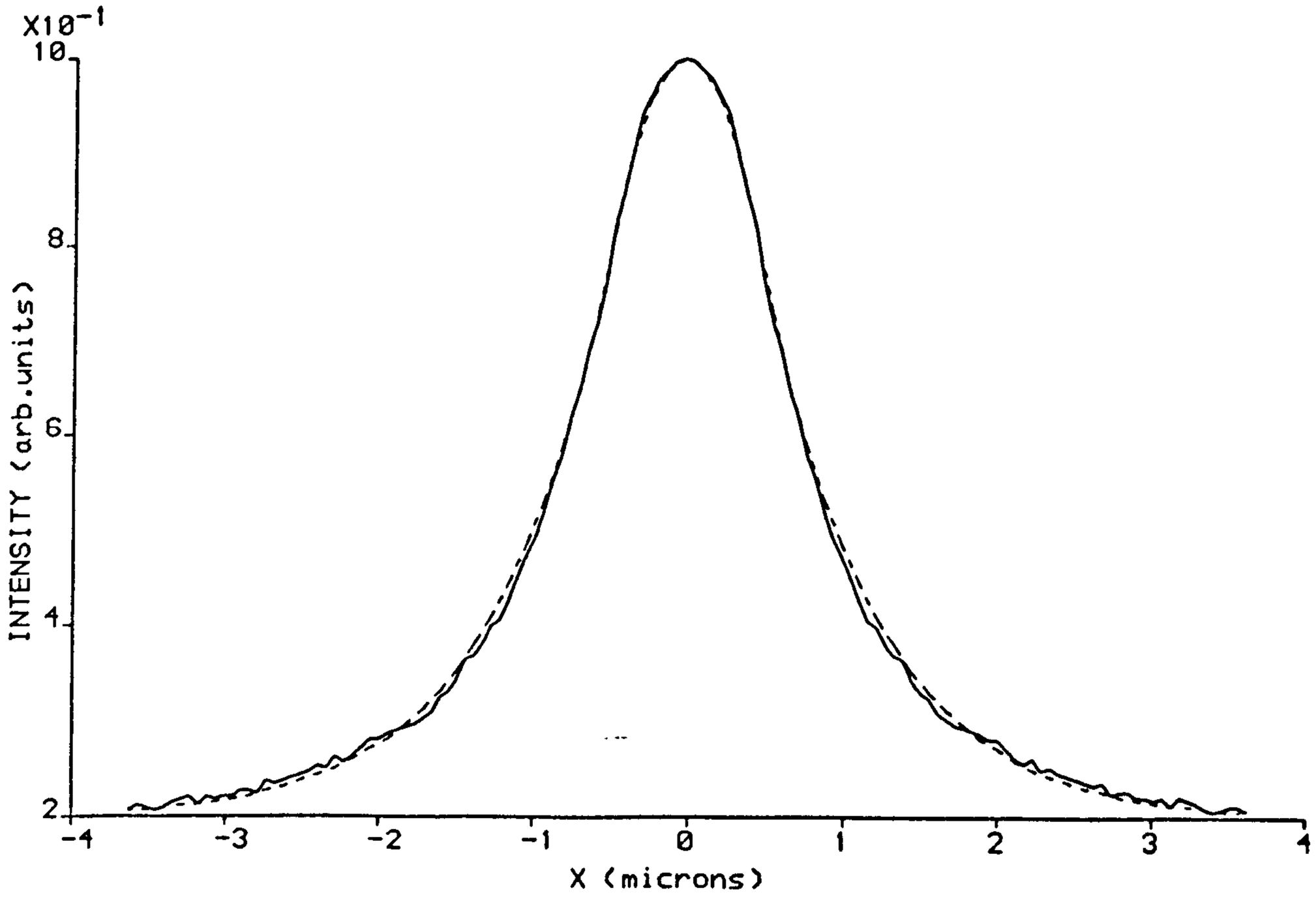

6.8 Experimental (solid line) and calculated (broken line) CL linescans across a misfit dislocation. The experimental data was acquired at the energy of the n=1(e-a) emission (see text).

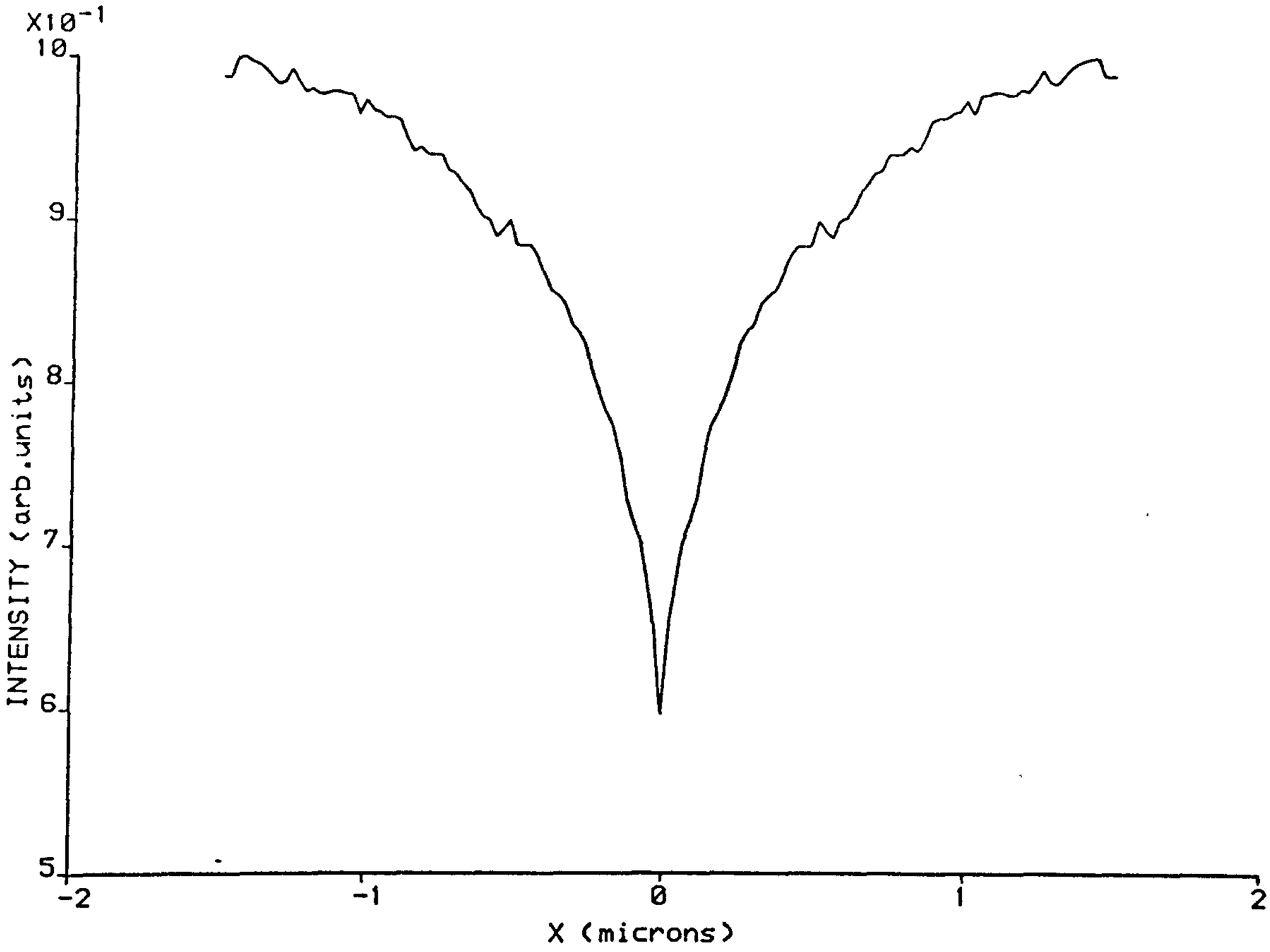

6.9 CL linescan across a threading dislocation, acquired at the energy of the n=1(e-hh) emission.

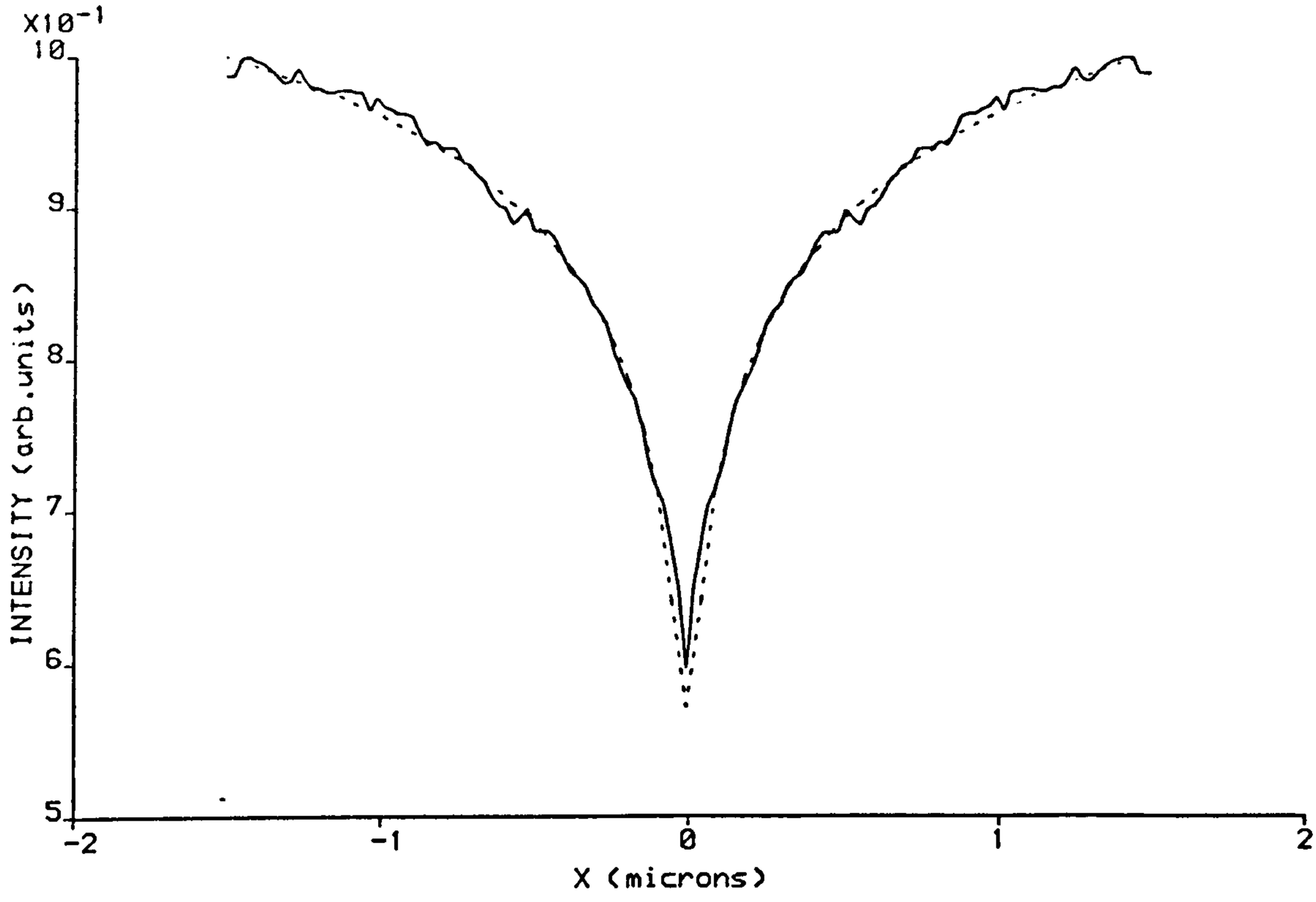

6.10 Comparison of experimental (solid line) and calculated (broken line) CL linescans across a threading dislocation. Experimental data acquired at the energy of the n=1(e-hh) emission (see text).

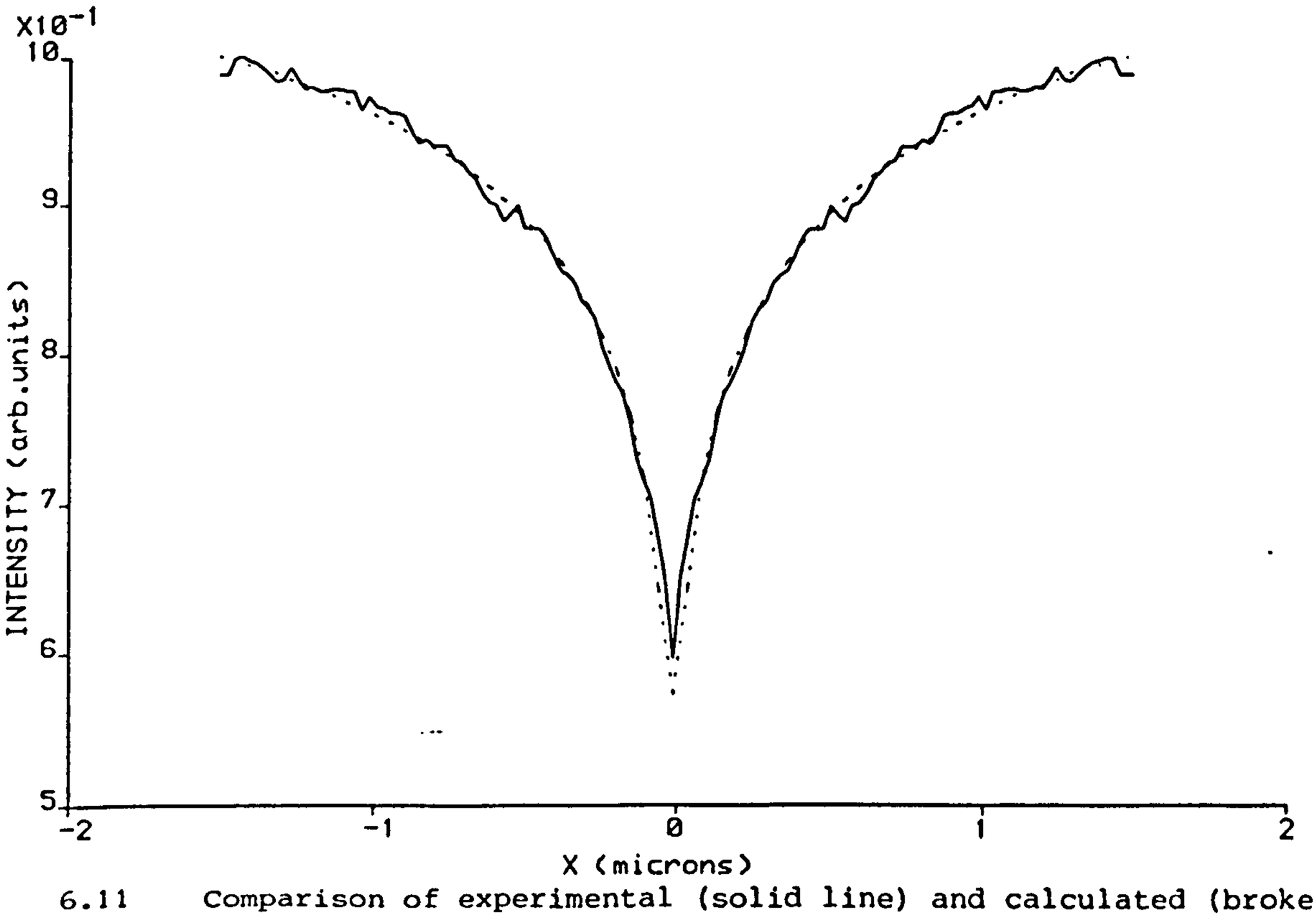

6.11 Comparison of experimental (solid line) and calculated (broken line) CL linescans across a threading dislocation. Experimental data acquired at the energy of the n=1(e-a) emission (see text).

CHAPTER SEVEN

CATHODOLUMINESCENCE FROM BULK SAMPLES

TEM CL is a destructive technique requiring time consuming specimen preparation. SEM CL is much more attractive as a routine characterization technique as it is non-destructive, requires minimal specimen preparation and can be used to examine relatively large specimens. In the current Chapter an attempt was made to use the information obtained from TEM CL as a means of determining defect densities and identifying defects in bulk, undoped GaAs/$A\ell_xGa_{1-x}As$ QW specimens using SEM CL. Comparison of TEM CL and SEM CL results also demonstrates that absorption and interference effects can safely be neglected for the structures investigated in the current work. SEM CL was performed on the EM400 microscope used to obtain TEM CL results as this instrument was equipped with electron beam scanning facilities and a secondary electron detector.

For simplicity,results in this Chapter will be presented according to the material investigated rather than according to defect type.

7.1. G43

Figure 7.1 shows a typical CL spectrum acquired from a bulk sample of G43. This spectrum was acquired from a region of sample which showed uniform emission in an integrated CL image. As for TEM samples (See Chapter Five) of G43 this spectrum shows only the n=1 X(e - hh) peak. Figure 7.2 shows a CL spectrum acquired over a narrower energy range on the low energy side of the

n=1 X(e - hh) peak. This spectrum shows the same weak structure observed in spectra acquired from TEM specimens and nominally ascribed to n = 1(e - a) transitions, the acceptor possibly being carbon. Figure 7.3a) shows a monochromatic CL image acquired at the energy of the n=1 X(e - hh) emission. The loss of CL intensity at the lower left of this image is an artefact due to the way the sample was mounted. The most obvious feature of Figure 7.3a) is the dark spot near the centre of the image. Figure 7.3b) shows another monochromatic CL image of the same area as for Figure 7.3a) but acquired at the energy of 1.568 eV. This energy corresponds to one of the weak spectral features observed on Figure 7.2. Figure 7.3b) shows much more structure than Figure 7.3a). In particular the network of misfit dislocations between the GaAs buffer layer and the first $A\ell_xGa_{1-x}As$ cladding layer can clearly be distinguished (see Chapter Five). The dark spot observed in Figure 7.3a) appears bright in Figure 7.3b) suggesting that this may be due to a crystallographic defect in the QW layers. Figure 7.4 shows a CL spectrum acquired from this supposed defect. The weak spectral features observed in Figure 7.2 are considerably enhanced in Figure 7.4, behaviour characteristic of misfit dislocations running along the QW interfaces. Figure 7.5 shows a lower magnification monochromatic CL image of the same region, again acquired at 1.586 eV. A misfit dislocation running along the QW interfaces can be seen as a short bright line near the top of the image. Comparison of this bright line with the feature observed in Figure 7.3 suggests that this feature is unlikely to be a misfit dislocation. SEM did not show any significant contrast at or near this feature so it is unlikely to be an oval defect.

The nature of the defect responsible for this feature will be discussed in more detail in section 7.4.

Figures 7.6a), b) and c) shows 3 monochromatic images acquired at energies of 1.606, 1.586 and 1.568 eV respectively, corresponding to the heavy hole transition and the two most common impurity transitions, all acquired from the same region of crystal. Comparison with the TEM results presented in Chapter Four indicates that the structure near the centre of all 3 images is an oval defect. SEM was subsequently used to confirm this conclusion. Threading dislocations in bulk specimens of G43 could not be identified by SEM CL, possibly because of the weakness of the contrast.

7.2. @ 1965

Figure 7.7 shows a monochromatic CL image acquired at the energy of the n = 1 X(e - hh) transition from a bulk specimen @ 1965. This image has been computer processed in order to minimise non-uniformities generated due to misalignment of the CL mirror. Only one feature can easily be distinguished on this image, a small dark spot towards the lower right of the image. By contrast Figure 7.8, acquired at an energy 20 meV below the n = 1 X(e - hh) transition, clearly shows a number of bright spots, only one of which (the brightest) shows appreciable contrast in the heavy hole emission.

Figure 7.9 shows a CL spectrum acquired from one of the bright spots visible in Figure 7.8. This spectrum shows a single weak peak on the low energy side of the heavy hole peak. This peak is approximately 21 meV below the heavy hole peak and is characteristic

of folded back stacking faults in sample @1965 (Chapter Three).

7.3. KLB116 and KLB121

Figure 7.10 shows a monochromatic CL image acquired from a bulk specimen of KLB116, at an energy 21 meV below the main QW emission. A considerable number of small bright spots can be seen in this image. Figure 7.11 shows a CL spectra acquired from one such spot. Comparison with the results presented in Chapter Three again suggests that the defect responsible for this spot is a stacking fault. The most obvious feature on Figure 7.10 is the bright band running across the image. This band appears similar to the cellular structure observed in TEM samples of KLB121 and is presumably due to impurities, although the origin of the impurities is not known.

Figure 7.12a) shows a monochromatic CL image from a bulk specimen of KLB121, acquired at the energy of the n = 1 (e - hh) transition. Although the CL intensity shows variation over distances of approximately 5 μm no obvious crystal defects can be distinguished. Figures 7.12b) and c) show two monochromatic images acquired from the same region as Figure 7.12a) but at energies 30 and 50 meV below the heavy hole respectively. Note that in Figure 7.12b) four bright spots appear but in Figure 7.12c) an additional bright spot can be seen. Spectra from all five bright spots showed the low energy, impurity related QW emission characteristic of stacking faults.

7.4. Discussion

In the previous 3 sections CL results from bulk specimens

of all the QW structures examined by TEM CL are presented. Only results from the QW luminescence have been included. Most of the monochromatic images show considerably reduced spatial resolution as compared to images taken from TEM specimens, due to the larger minority carrier generation volume in bulk specimens. Better spatial resolution might be obtained using a lower accelerating voltage. This could not be done on the EM400 as this microscope will not operate below 20 keV, the voltage used to obtain all the results presented in this Chapter. As a result of degraded spatial resolution most of the defects detected in SEM CL images appeared simply as bright or dark spots with consequent loss of spatial information. There are no differences between CL images from bulk and TEM specimens which cannot be directly ascribed to the degraded spatial resolution in bulk samples.

CL spectra from bulk specimens were not absolutely identical to CL spectra from TEM specimens, except for nominally unfaulted crystal in G43 and @1965. However, the only differences observed were fully consistent with the variations observed between different defects using TEM CL. If absorption or interference effects were appreciably distorting CL results from TEM specimens then it is most unlikely that this would be true.

In section 7.1 monochromatic CL imaging was used to locate a supposed defect in a bulk specimen of G43 which did not appear to be either a dislocation or an oval defect. As the stacking fault density in G43 was found to be very low, then this defect is also almost certainly not a stacking fault. A CL spectrum acquired from this defect showed that the weak impurity luminescence

observed in unfaulted crystal was considerably enhanced around this defect. This behaviour is characteristic of misfit dislocations in G43. This defect is probably a dislocation cluster such as the one shown in Figure 7.13.

Dislocation clusters varied in size from 0.5 μm to 5 μm and were relatively common (density 10^2 - 10^4 cm^{-2}) in all the QW structures examined in this study. The origin of this type of defect is not known but may be due to mechanical substrate damage prior to MBE growth.

The results obtained using TEM CL on defects in QW structures suggest a simple technique whereby defect densities in undoped QW structures might be measured using monochromatic CL imaging in an SEM. The results presented in the previous sections show that the heavy hole QW luminescence is relatively insensitive to the presence of crystallographic defects. For QW structures of reasonable quality, the heavy hole luminescence is by far the strongest emission so that integrated CL images are virtually identical to monochromatic CL images acquired at the energy of the heavy hole transition. Therefore integrated CL imaging is not a reliable technique for assessing defect densities in bulk $GaAs/Al_xGa_{1-x}As$ QW structures. A more suitable characterization technique is as follows. Firstly, acquire a CL spectrum, preferably from a region of uniform CL intensity (as judged by integrated CL imaging), in order to determine the energy of the heavy hole luminescence, and to identify any structure on the low energy side of this peak. Secondly, acquire a monochromatic CL image either at the energy of any emission observed on the low energy side of the heavy hole peak, or at an arbitrary energy

10 - 50 meV below the heavy hole emission. The majority of defects will appear as small regions of significantly enhanced intensity on such an image. To ensure that the maximum number of defects are detected several similar images should be acquired at energies separated by 10 - 20 meV. As illustrated in section 7.3 this procedure is necessary to identify defects which only luminesce over a narrow energy range. Note that this technique was used to locate all the features discussed in previous sections.

In the current study defects were easily located using the technique outlined above but defects could not be identified unambiguously, although some tentative identifications were made. The characteristic features of CL images acquired from different defects are summarised below.

Misfit dislocations appeared as dark lines in integrated CL images. If these dislocations ran along (or close to) the QW interfaces then monochromatic CL images acquired at energies less than that of the heavy hole transition showed a corresponding bright line (or pair of lines). Threading screw dislocations appeared dark in monochromatic CL images, irrespective of the acquisition energy, but showed only weak contrast. Regions of mechanical damage, such as scratches, behaved similarly but with greater contrast, usually over a larger area of the sample. Large (> 1 μm) dislocation clusters could also be distinguished by their dark contrast in integrated CL images but in monochromatic CL images acquired at energies less than that of the heavy hole emission appeared as a dark central region surrounded by a brighter halo. Oval defects showed similar effects but could be identified using

conventional SEM. Stacking faults proved difficult to distinguish from the smaller (< 1 μm) dislocation clusters but generally showed stronger impurity related luminescence.

In the current study only undoped GaAs/$A\ell_xGa_{1-x}As$ QW structures were investigated. It is believed that defect densities in doped QW structures cannot be determined as outlined in this Chapter because the weak impurity related luminescence will be difficult to detect against the background luminescence due to the dopants. However, there seems no reason that the technique could not be applied to undoped QW structures grown from other III-V semiconductors.

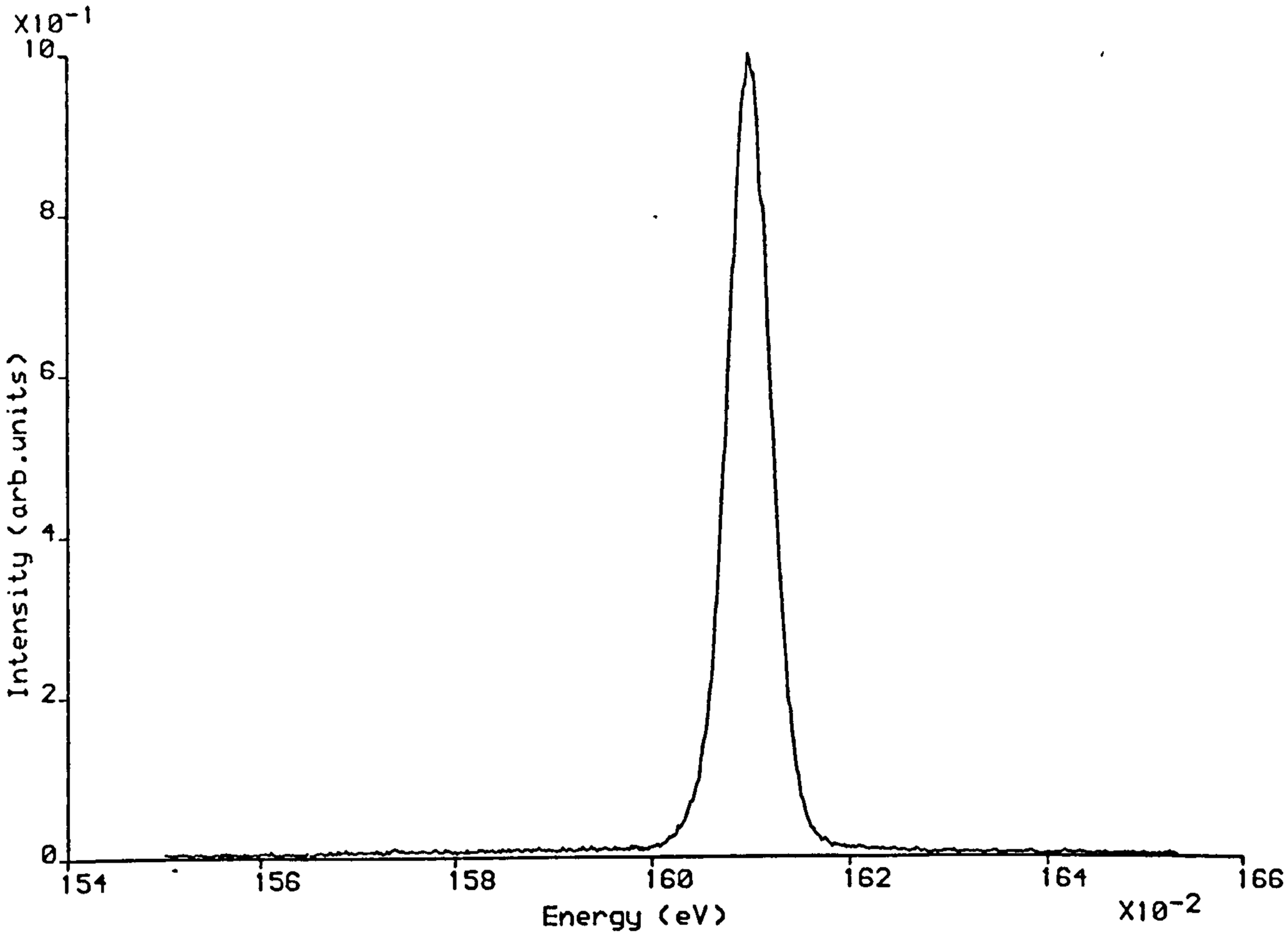

7.1 CL spectrum from bulk G43 showing only the n=1(e-hh) emission.

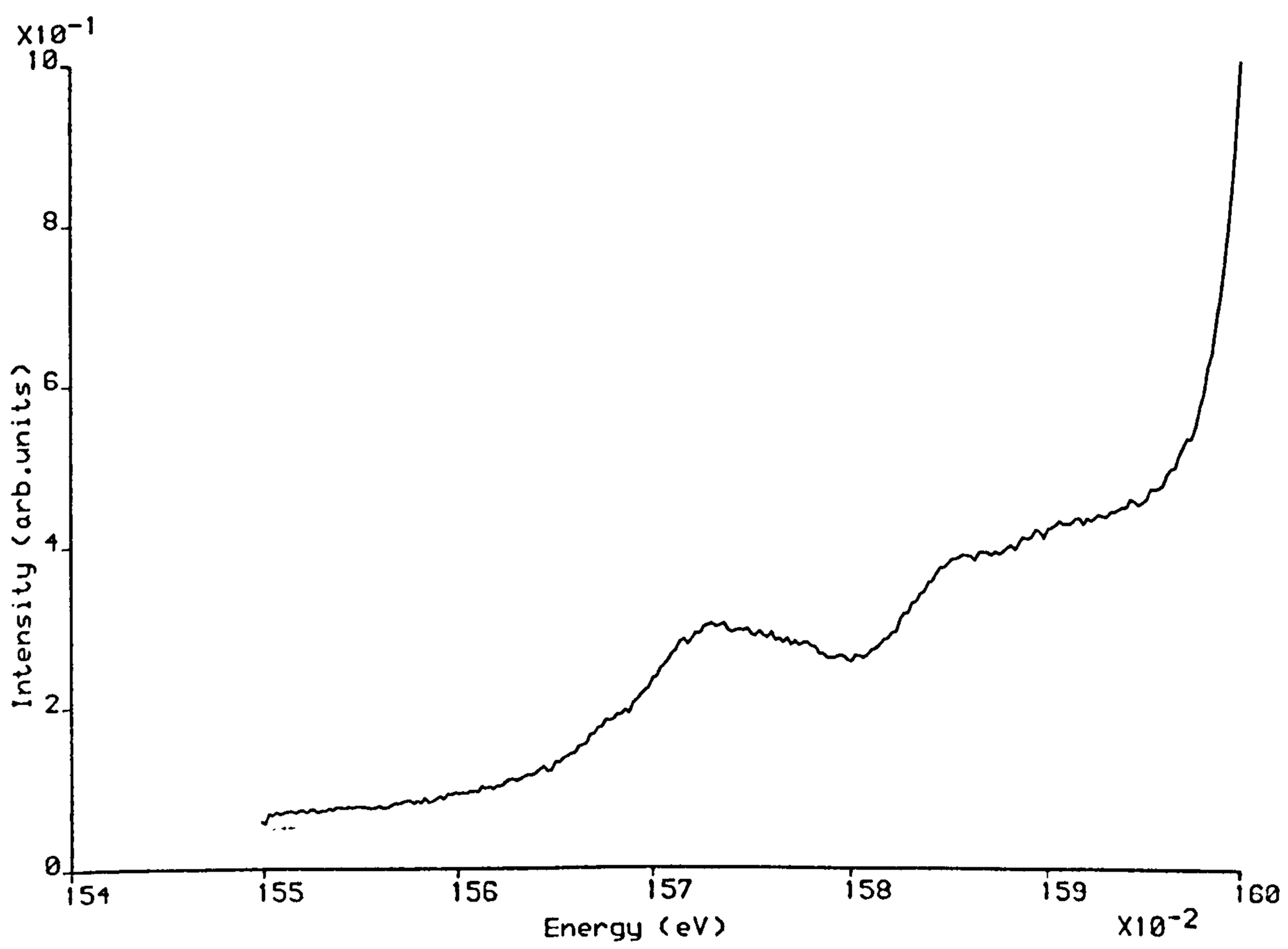

7.2 CL spectrum from bulk G43 showing the weak low energy peaks.

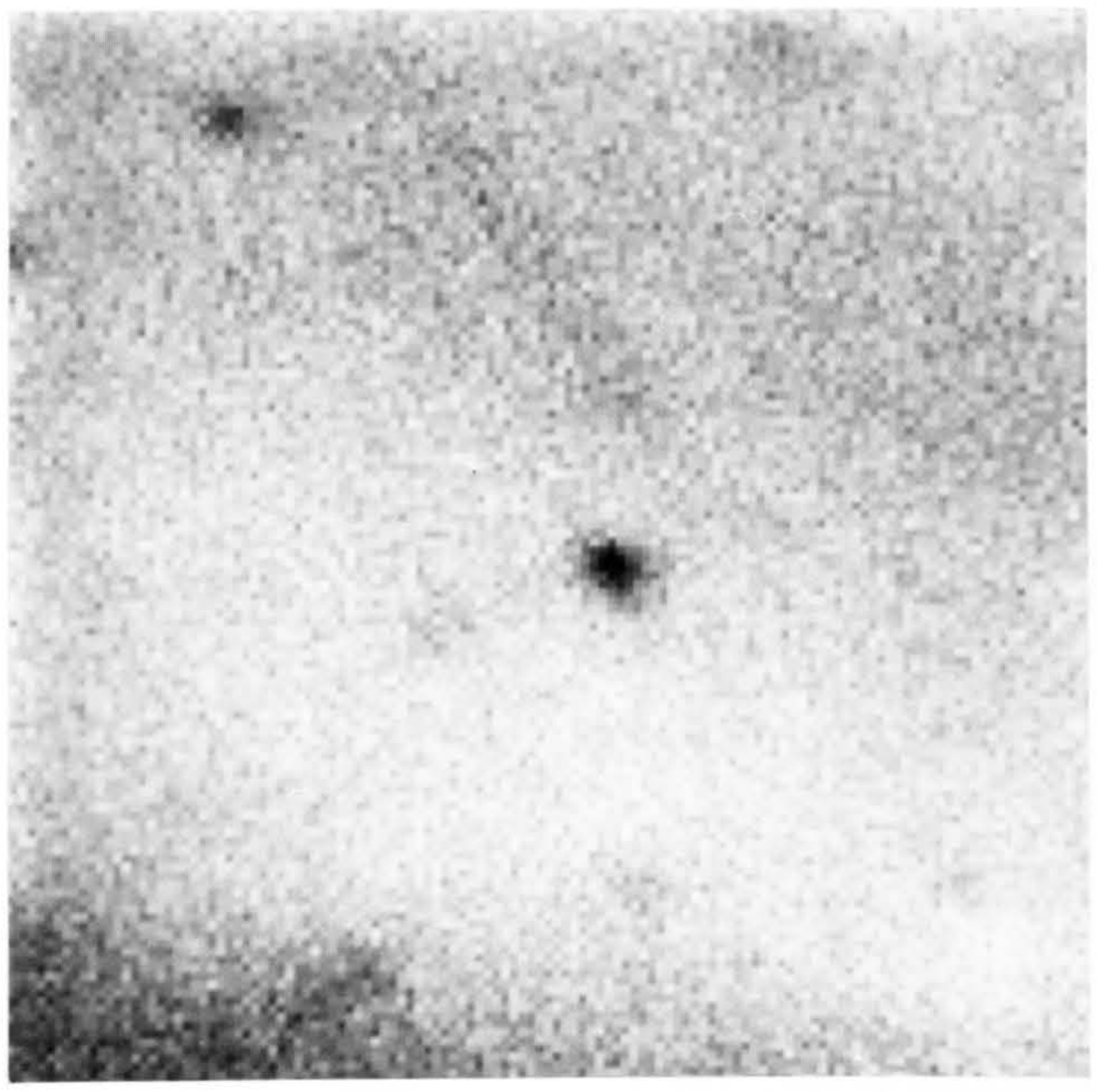

a)

b)

20 μm

7.3 Monochromatic CL images from bulk G43. a) n=1(e-hh) emission b) lower energy emission (1.568 eV).

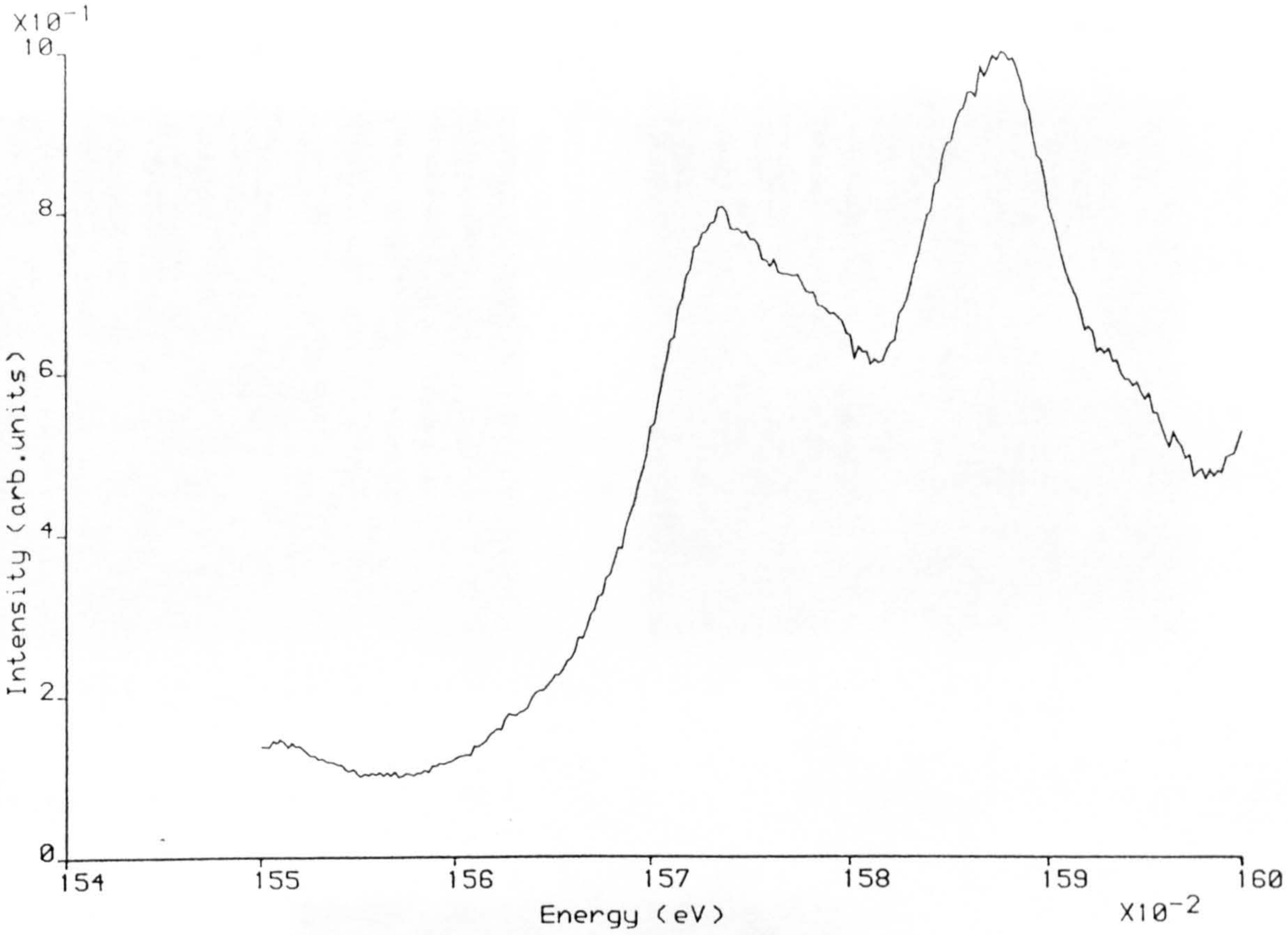

7.4 CL spectrum from the bright spot visible in Figure 7.3 b).

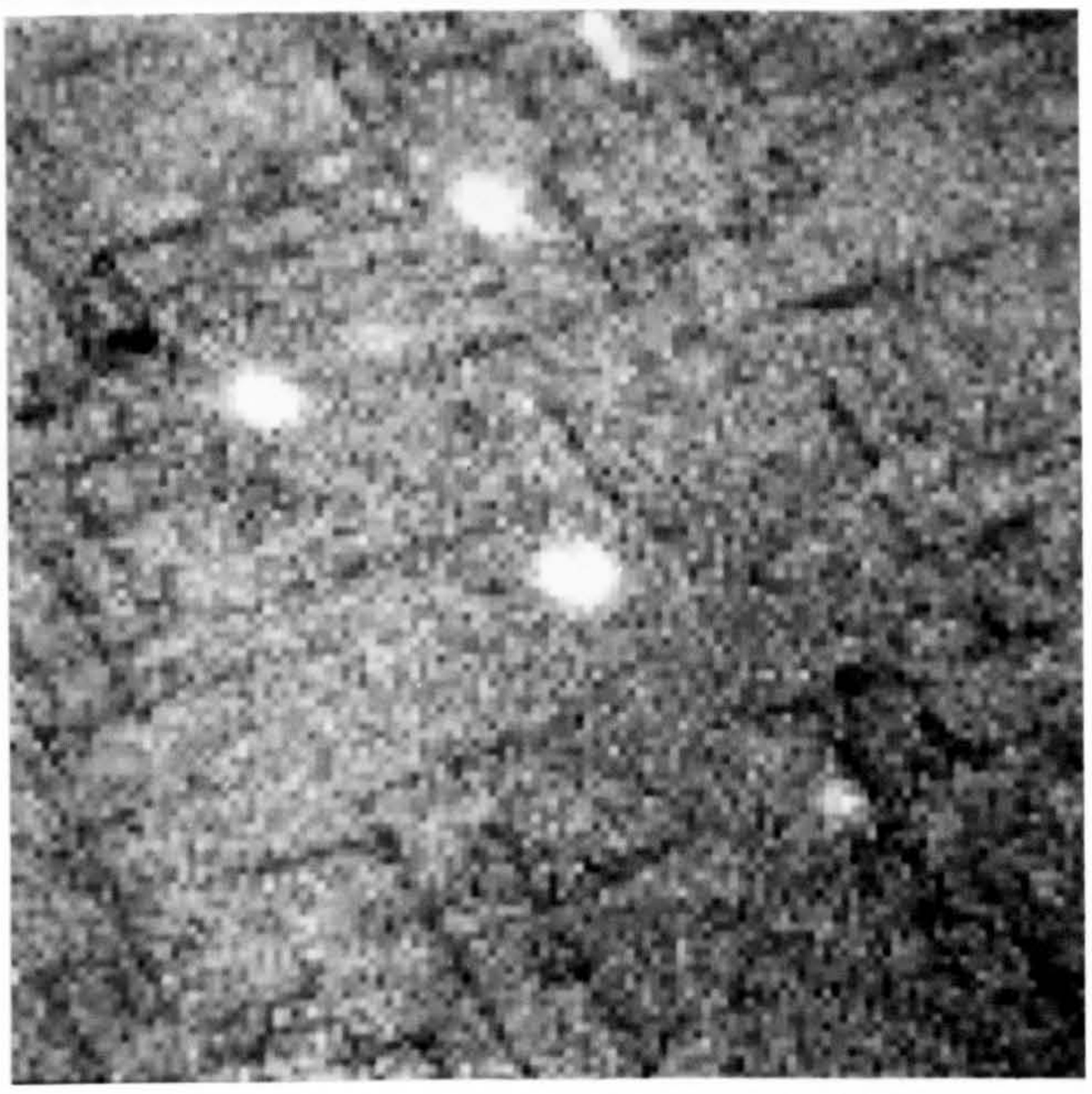

7.5 Monochromatic CL image from bulk G43 acquired at 1.586 eV using lower magnification than for Figure 7.3 b).

a)

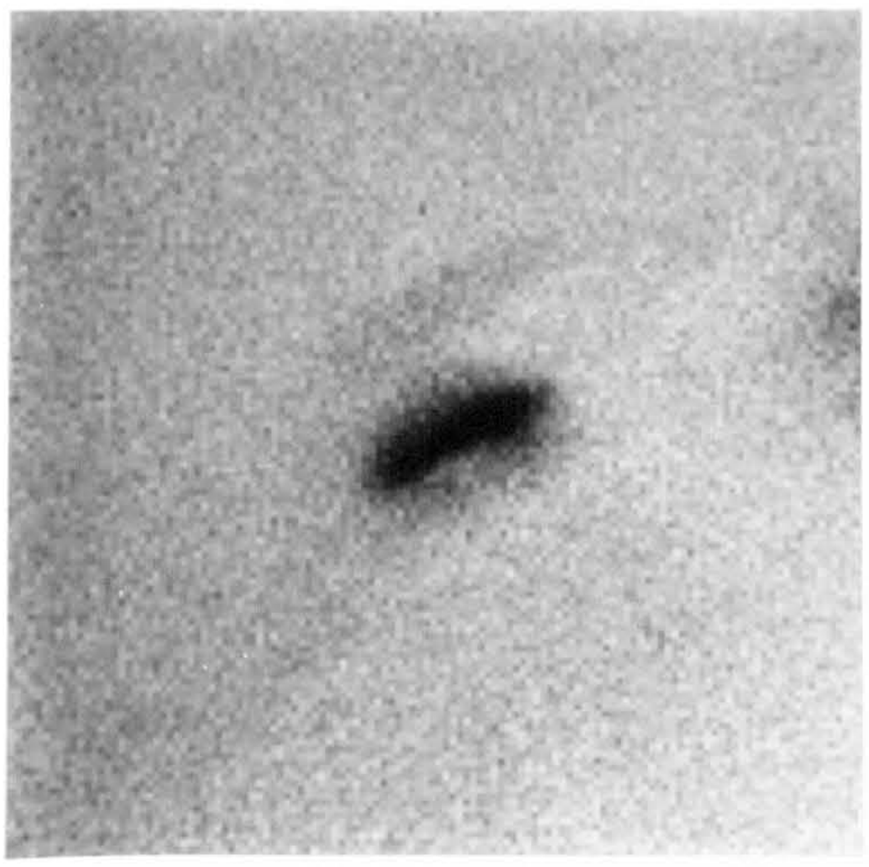

b)

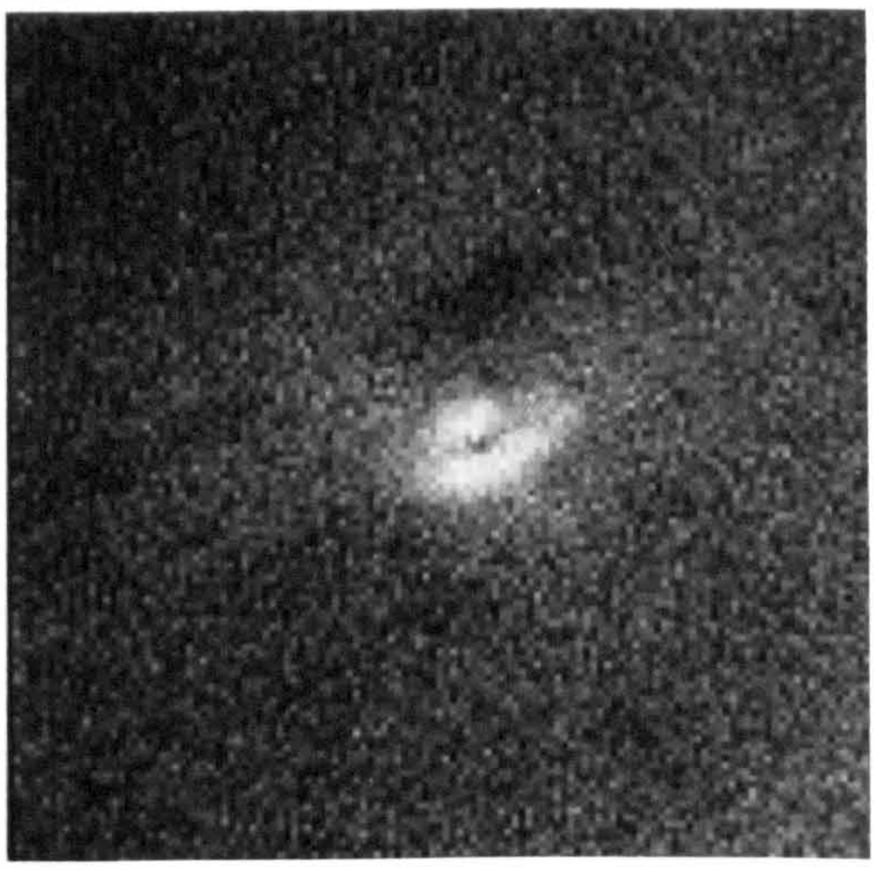

c)

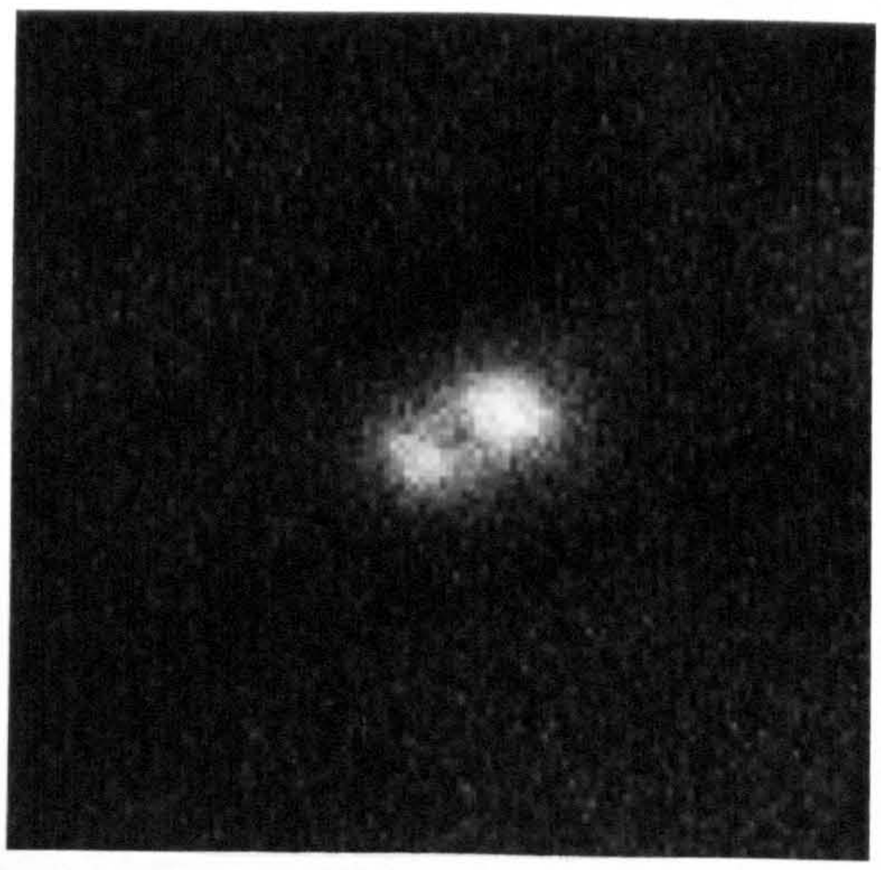

7.6 Monochromatic CL images of an oval defect in bulk G43. a) n=1(e-hh) b) 1.586 eV and c) 1.568 eV emissions respectively.

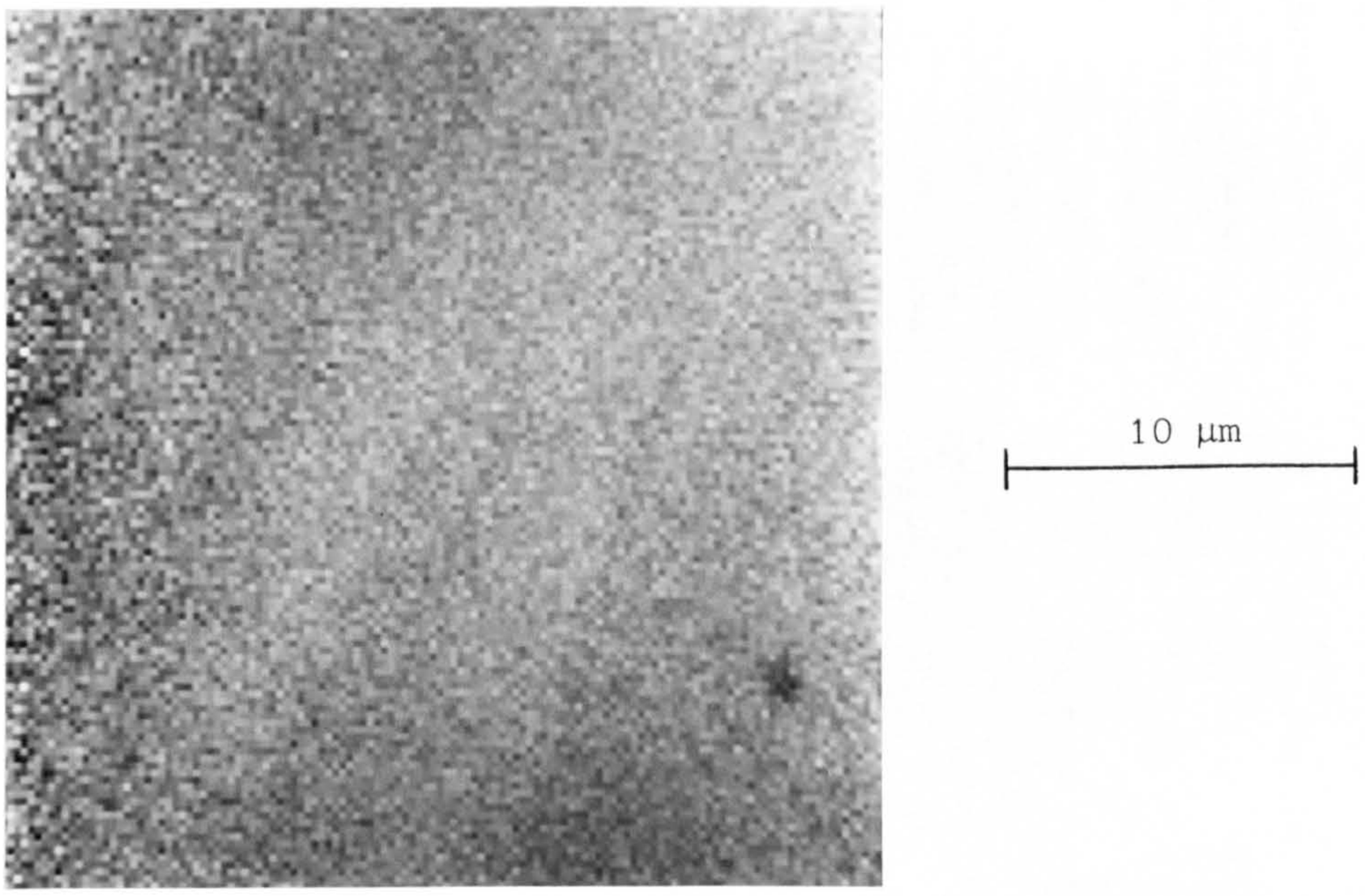

7.7 Monochromatic CL image from bulk @1965 acquired at the energy of the n=1(e-hh) emission.

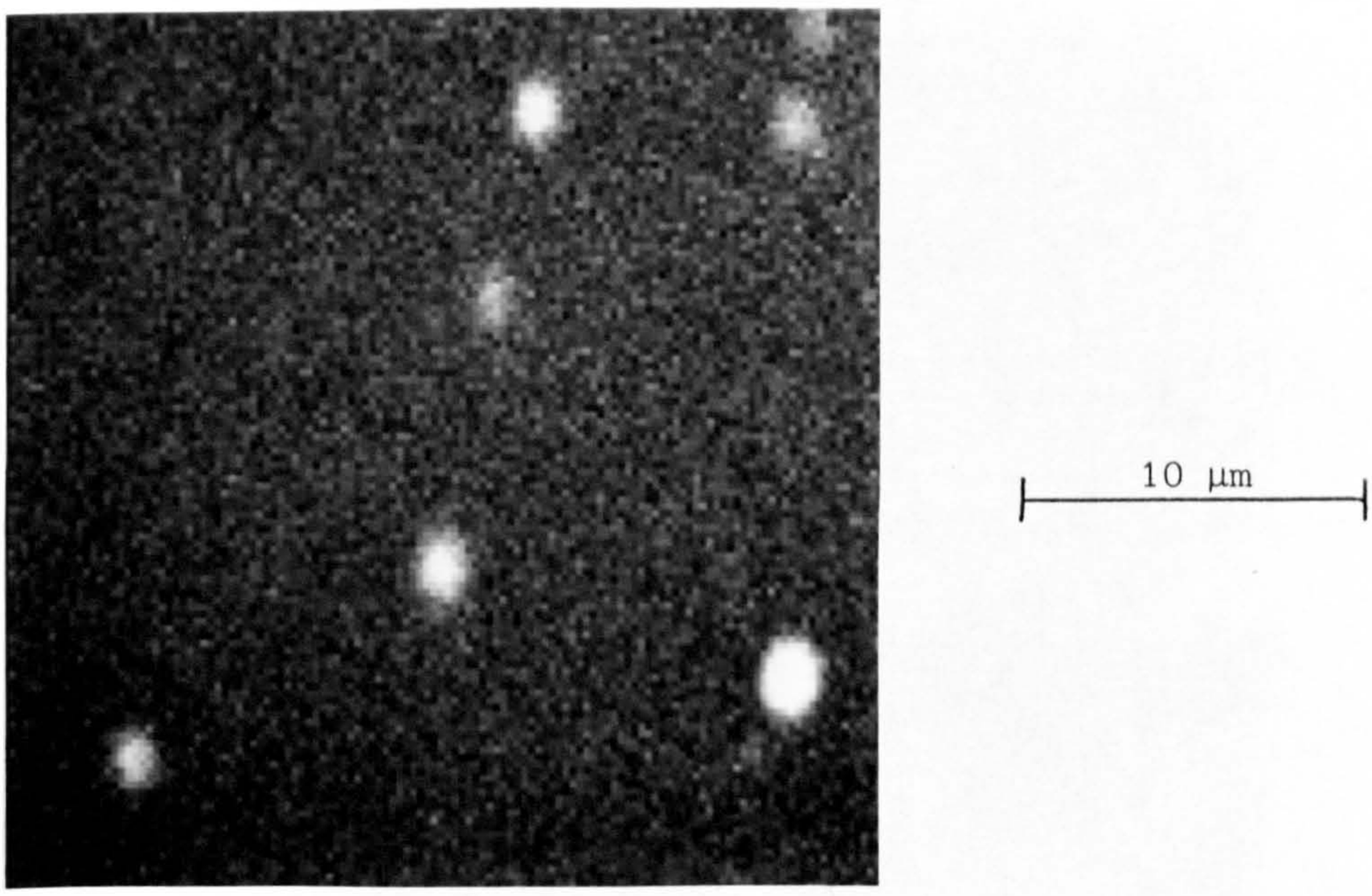

7.8 Monochromatic CL image from bulk @1965 acquired at an energy 20 meV below the n=1(e-hh) emission (same region as Figure 7.7).

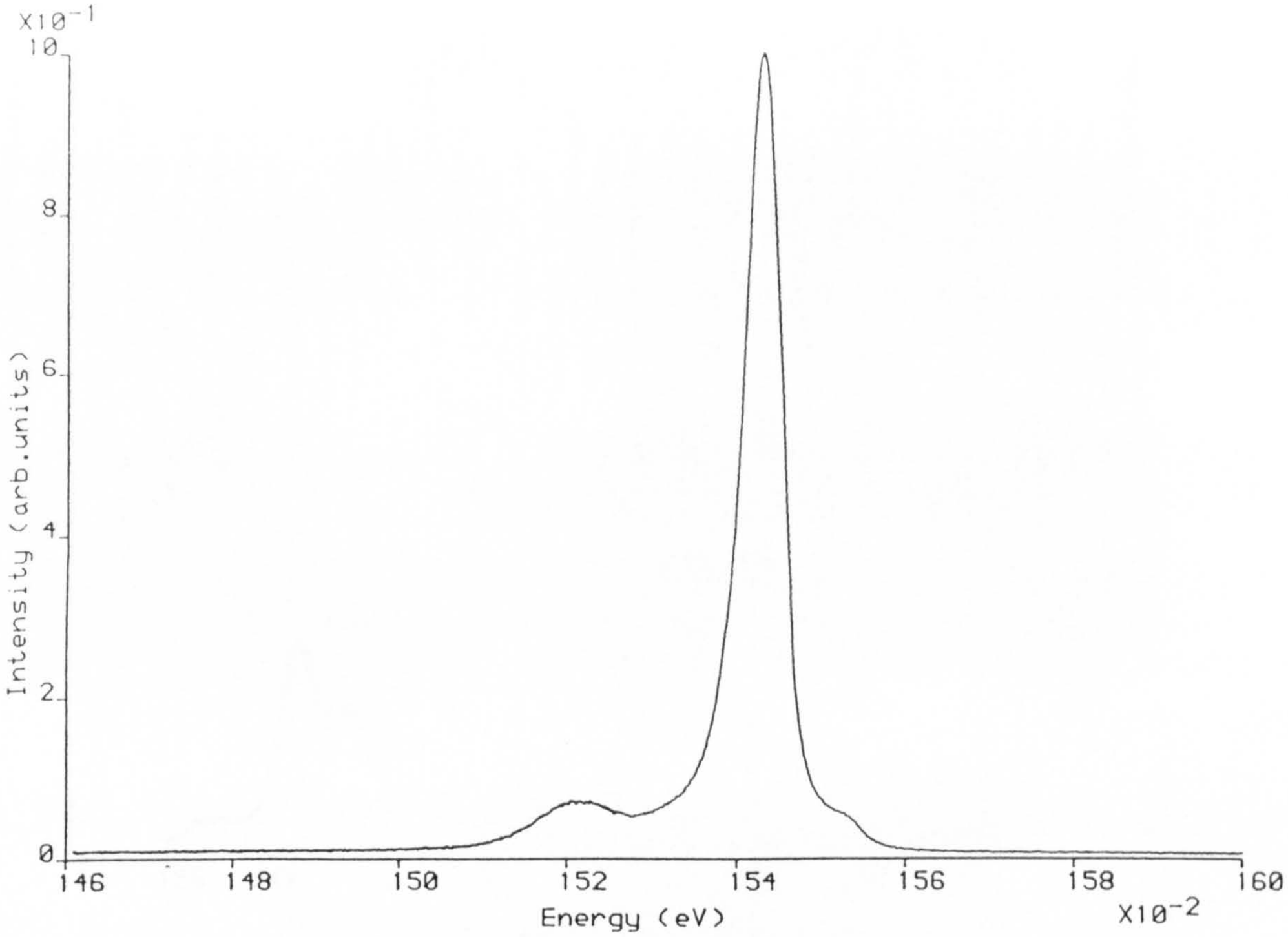

7.9 CL spectrum acquired from one of the bright spots visible in Figure 7.8.

7.10 Monochromatic CL image from bulk KLB116 acquired at an energy 20 meV below the main QW emission.

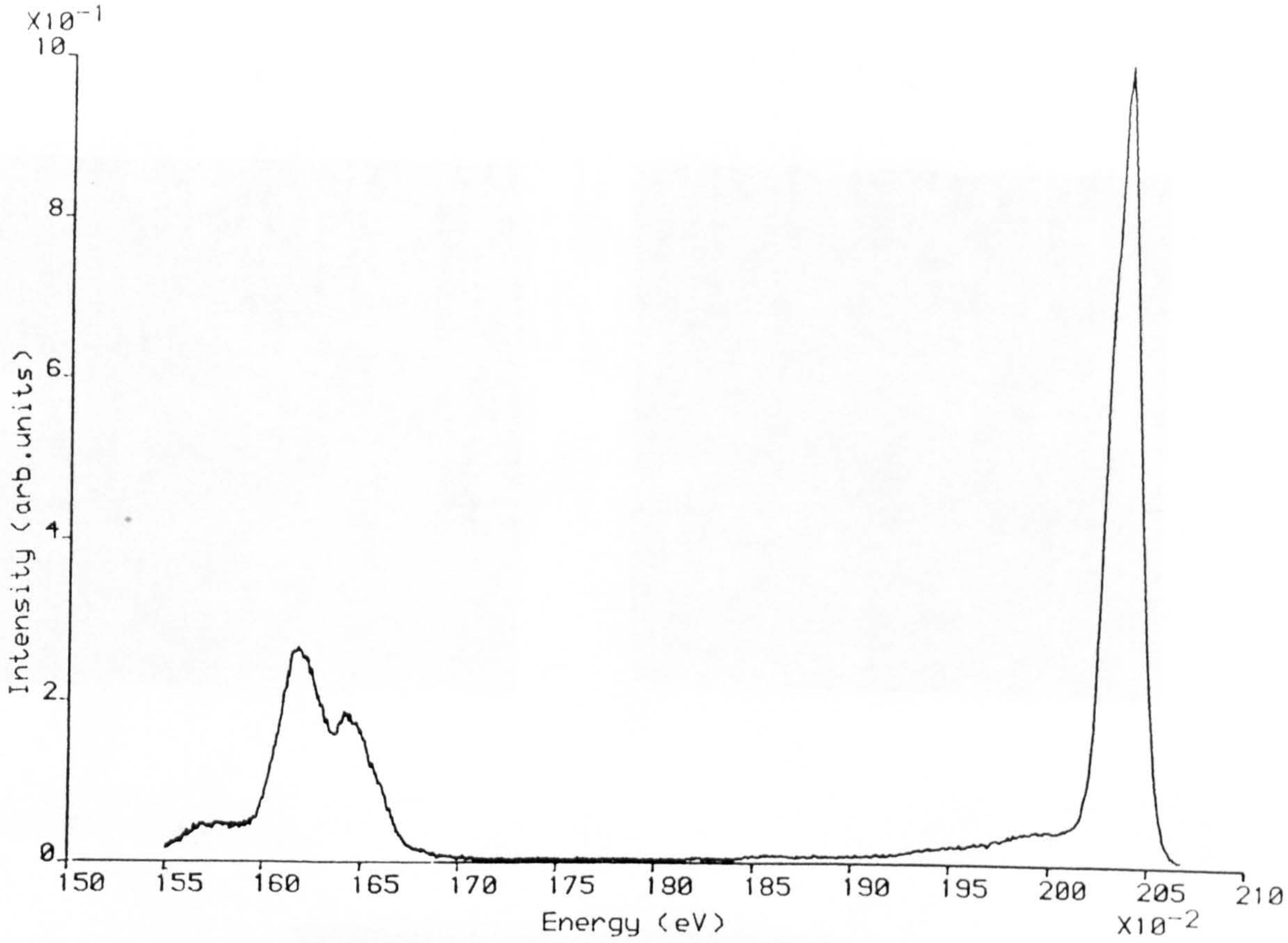

7.11 CL spectrum from one of the bright spots shown in Figure 7.10.

a)

b)

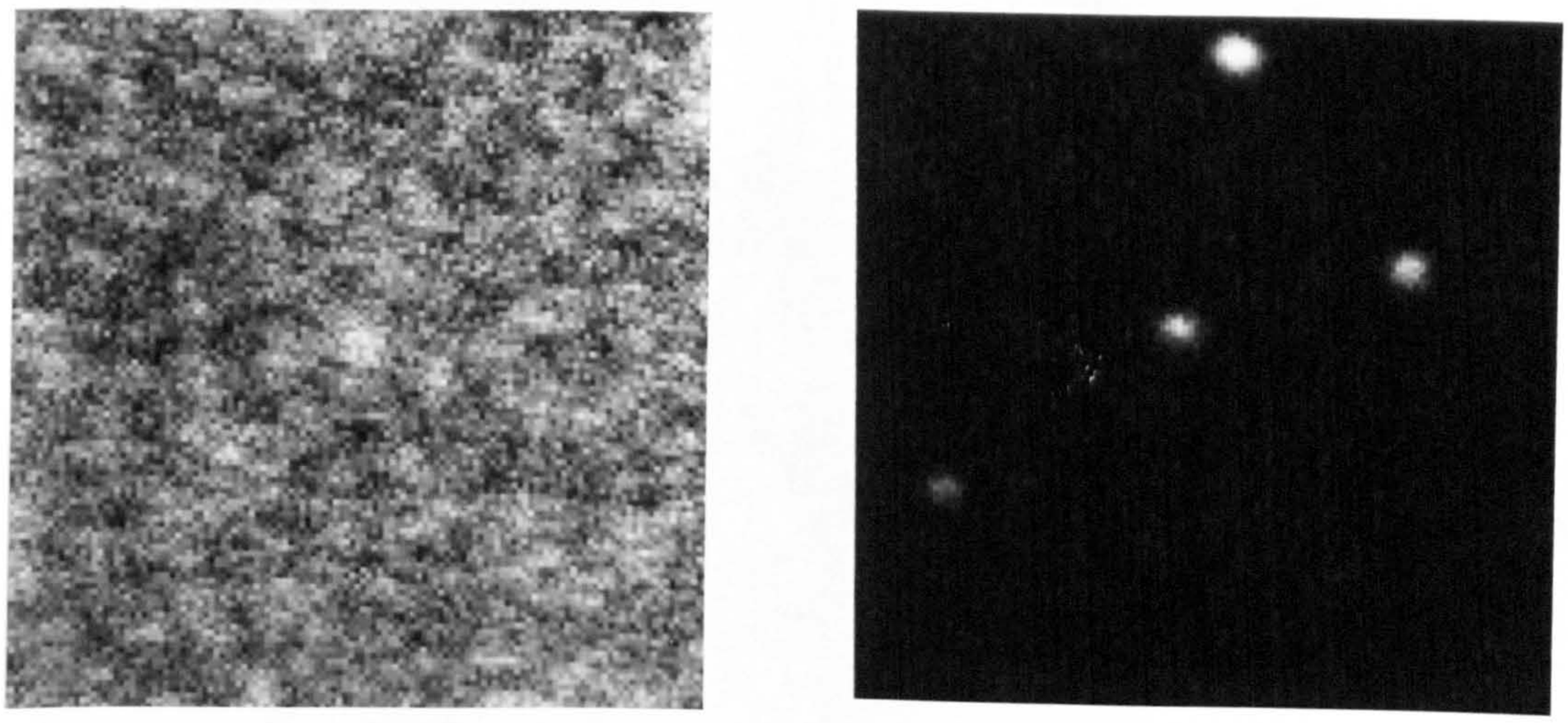

c)

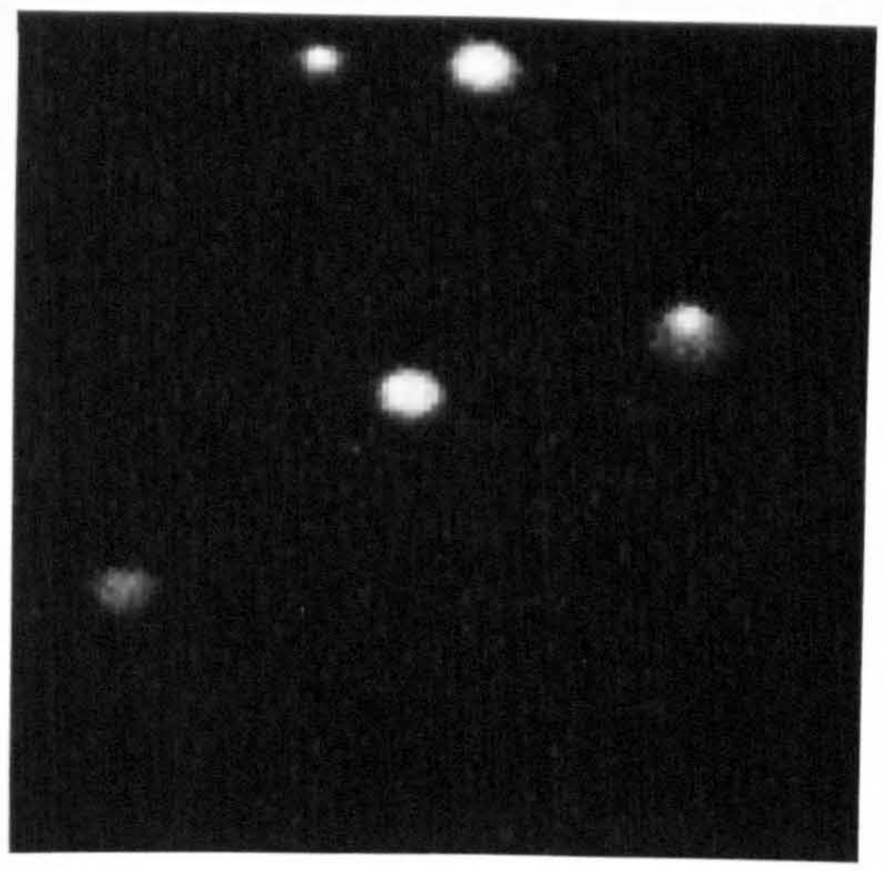

20 μm

7.12 Monochromatic CL images from bulk KLB121. a), b) and c) were acquired at, 20 meV below and 50 meV below the energy of the n=1(e-hh) QW emission.

7.13 BF TEM micrograph of a dislocation cluster in G43.

CHAPTER EIGHT

CONCLUSIONS

This Chapter outlines the major conclusions drawn from this investigation. More detailed discussions of the experimental results have been included in the relevant chapters.

Low temperature TEM CL was used to investigate the optical properties of defects in undoped GaAs/$A\ell_xGa_{1-x}As$ SQW and MQW structures grown by MBE. In Chapter Three stacking faults were examined. Stacking fault densities in samples of low optical quality were found to be higher than for better quality material. All the stacking faults were found to nucleate at or near to the substrate interface. Stacking faults were found to degrade the QW luminescence and give rise to extra emission features at energies up to 50 meV below the main QW emission. These features were ascribed to impurity related transitions. Monochromatic CL images on TEM micrographs of stacking faults were used to infer that the stacking faults were caused by substrate contamination. Pyramidal stacking faults in both QW samples and a simple $A\ell_xGa_{1-x}As$ epilayer were found to form only in one orientation with intrinsic character faults on {111}Ga planes.

In Chapter Four results were presented from oval defects, a type of defect which is usually only found in MBE grown epilayers. These defects were oriented with the long axis parallel to a <110> direction and appeared similar to those previously reported in the literature. In most cases oval defects severely reduced the intensity of the QW luminescence in the immediate

vicinity of the defect. CL spectra from oval defects showed emission features at energies up to 50 meV below the dominant n = 1 X(e - hh) QW luminescence. These features were again ascribed to impurity related transitions and suggesting that the cause of oval defects is substrate contamination, as proposed by a number of other workers.

Isolated dislocations suitable for CL studies were only observed in one QW sample (Chapter Five). Screw dislocations threading through the QW's produced weak dark contrast in monochromatic images irrespective of the photon energy used to acquire the image. Petroff et al. (1981) performed a similar study of dislocations in GaAs/$A\ell_xGa_{1-x}As$ QW structures but did not observe any contrast. This discrepancy may be due to differences in doping or because thinner samples (allowing higher spatial resolution) were examined in the current work. Misfit dislocations also gave dark CL contrast when imaged at the energy of the n = 1 X(e - hh) transition. CL spectra acquired from misfit dislocations generally showed an enhancement of the normal background impurity related QW luminescence. Monochromatic CL images acquired at the energy of this luminescence showed either a single or double band of higher intensity centred on the dislocation. This was interpreted as being due to a Cottrell atmosphere of impurities around the dislocation with non-radiative recombination occurring at the dislocation core. Two types of misfit dislocation were observed, thought to be formed by elongation along the QW interface of either a 60° threading dislocation or a Lomer-Cottrell lock. The two types of dislocation could not be distinguished by CL. The results obtained for the

60° misfit dislocations agree with the results of a number of other workers although to the author's knowledge impurity related luminescence around misfit dislocations has not previously been reported. Petroff et al. (1980) could not detect any CL or EBIC contrast from Lomer-Cottrell locks in $Al_xGa_{1-x}As/Al_xGa_{1-x}As_yP_{1-y}$ layer structures grown by LPE and postulated a core reconstruction to explain the lack of non-radiative recombination. It is not clear why different results were obtained in the current study although growth conditions, doping, specimen thickness and the material grown may all be important. A theoretical treatment of CL intensity around dislocations was presented in Chapter Six, based on the minority carrier diffusion equation. Good agreement was obtained between theory and experiment and allowed the minority carrier diffusion length to be estimated. In order to simulate the CL intensity around a given misfit dislocation two different diffusion lengths were normally required, one to model monochromatic images acquired at the energy of the n = 1 (e - hh) transition and a shorter diffusion length to describe images acquired at the energy of the impurity related luminescence. It was suggested that this could be because the two different transitions are governed by different diffusion processes.

SEM CL was performed on bulk samples on the same QW structures used for TEM CL (Chapter Seven). Results from SEM CL were very similar to those obtained by TEM CL demonstrating that the TEM CL results were not significantly distorted by interference or absorption effects. It was concluded that CL imaging is an

efficient technique for detecting defects in undoped QW structures provided monochromatic imaging at energies 10 - 50 meV below the main QW peak is used. Integrated CL images are considerably less sensitive to the presence of defects.

None of the defects investigated in this study showed any signs of fluctuations in the QW width.

Suggestions for Further Work

The current work suggests a number of avenues for further study. A major limitation of this investigation was that only undoped MBE grown GaAs/$A\ell_xGa_{1-x}As$ QW structures were available for study. CL results from doped GaAs and $A\ell_xGa_{1-x}As$ epilayers, presented briefly in Chapters Three and Four, suggest that impurities (as opposed to dopants) may not significantly effect doped QW structures. It would also be of interest to examine MOCVD grown QW structures and establish any differences in the types of defect found. Similar studies could also be performed on QW structures grown using different semiconductor systems, such as $In_xGa_{1-y}As/A\ell_xIn_{1-x}As$.

SEM CL was demonstrated to be a useful technique for locating defects in QW structures and allowed most defects to be identified. However, SEM CL was only used to examine material which had previously been characterized by TEM CL. Ideally, SEM CL should be used to locate and if possible identify defects in bulk QW samples before TEM CL characterization. This would allow an unbiased assessment of SEM CL as a QW characterization technique.

Although the most common types of defects in QW structure were studied, defects such as dislocation clusters merit further

study.

Comparisons between experimental results and calculations of the CL intensity around dislocations were hampered by the nonuniformity of luminescence observed even for unfaulted crystal. This work could be furthered if more uniform QW samples (also containing dislocations) were examined. The same calculations could also be applied to simple epilayer structures and compared with experimental results obtained at different temperatures.

Appendix 1

The Minority Carrier Density in the Presence of a Misfit Dislocation

In Chapter Six dislocations were modelled in terms of a region of reduced minority carrier recombination lifetime (Donolato model) or in terms of surfaces with high surface recombination velocity (Jakabowicz model). This appendix gives more details of the methods used to calculate the minority carrier density using these models. The approximations to one-dimensional behaviour have already been discussed in Chapter Six.

Considering the Donolato model first. The one-dimensional diffusion equation can be written as

$$D\frac{d^2P(x)}{dx^2} - \frac{P(x)}{\tau(x)} = -g\delta(x-x_o)$$

where $P(x)$ is the minority carrier density at position x, D is the diffusion coefficient, $\tau(x)$ is the minority carrier recombination lifetime, g is the number of minority carriers generated per second and x_o is the position of the electron beam. To allow $P(x)$ to be calculated for an arbitrary function $\tau(x)$ the following approximation can be used. Considering the dislocation as n regions, each with a constant value for $\tau(x)$, then $\tau(x)$ in region i can be denoted by τ_i and letting the boundary between region i and region i + 1 be at x_i. Note that region 1 extends from $-\infty$ to x_1 and region n extends from x_n to ∞. The minority carrier density $P_i(x)$ in region i must satisfy the equation

$$\frac{D d^2P_i(x)}{d^2x} - \frac{P_i(x)}{\tau_i(x)} = 0$$

where $x \neq x_o$ and $x_{i-1} \leqslant x \leqslant x_i$. Therefore $P_i(x)$ can be written as

$$P_i(x) = A_i e^{-x/L_i} + B_i e^{x/L_i}$$

with the same constraints on x. $L_i = \sqrt{D\tau_i}$ is the minority carrier diffusion length in region i. In the region q where $x_{q-1} \leqslant x_o \leqslant x_q$ the coefficients A_q and B_q for $x \leqslant x_o$ are not the same as for $x \geqslant x_o$, so for clarity the coefficients A_i and B_i for $i \geqslant q$ and $x \geqslant x_o$ will be denoted A_i' and B_i' respectively. All these coefficients can now be determined as follows. P(x) must be finite for all x, therefore $A_1 = 0$ and $B_n' = 0$. Imposing the boundary conditions

$$P_i(x) = P_{i+1}(x)$$

and

$$\frac{dP_i(x)}{dx} = \frac{dP_{i+1}(x)}{dx}$$

at $x = x_{i-1}$ gives the equations

$$A_i = \tfrac{1}{2}A_{i-1}\left[\frac{L_{i-1}+L_i}{L_{i-1}}\right]e^{-x_{i-1}(1/L_i - 1/L_{i-1})} + \tfrac{1}{2}B_{i-1}\left[\frac{L_{i-1}-L_i}{L_{i-1}}\right]e^{x_{i-1}(1/L_i + 1/L_{i-1})} \qquad \text{(A1)}$$

and

$$B_i = \tfrac{1}{2}A_{i-1}\left[\frac{L_{i-1}-L_i}{L_{i-1}}\right]e^{-x_{i-1}(1/L_i + 1/L_{i-1})} + \tfrac{1}{2}B_{i-1}\left[\frac{L_{i-1}-L_i}{L_{i-1}}\right]e^{x_{i-1}(1/L_i + 1/L_{i-1})} \qquad \text{(A2)}$$

The coefficients A_q and B_q can be evaluated in terms of B_1 as $A_q = aB_1$ and $B_q = bB_1$ where constants a and b are found by iterative use of equations A1 and A2. A similar procedure can be used to determine A_q' and B_q' in terms of A_n such that $A_q' = cA_n$ and $B_q' = dB_n$ where constants c and d are determined by iterative use of the equations

$$A'_i = \tfrac{1}{2}A'_{i+1}\left[\frac{L_{i+1}+L_i}{L_{i+1}}\right]e^{-x_i(1/L_i-1/L_{i+1})} + \tfrac{1}{2}B'_{i+1}\left[\frac{L_{i+1}-L_i}{L_{i+1}}\right]e^{x_i(1/L_i+1/L_{i+1})} \quad \text{(A3)}$$

and

$$B'_i = \tfrac{1}{2}A'_{i+1}\left[\frac{L_{i+1}-L_i}{L_{i+1}}\right]e^{-x_i(1/L_i+1/L_{i+1})} + \tfrac{1}{2}B'_{i+1}\left[\frac{L_{i+1}+L_i}{L_{i+1}}\right]e^{x_i(1/L_{i+1}-1/L_i)} \quad \text{(A4)}$$

The coefficients B_1 and A_n can be found by imposing the boundary conditions

$$P_q(x) = P'_q(x)$$

and

$$\frac{dP'_q(x)}{dx} - \frac{dP_q(x)}{dx} = -g$$

at $x = x_o$. $P_q'(x)$ denotes the minority carrier density for $x \geq x_o$. Substituting the expressions for A_q, B_q, A_q' and B_q' into these equations gives

$$A'_n = -gL_q/h$$

and

$$B_1 = -gL_q/fh$$

where

$$f = \left(\frac{ce^{-x_o/L_q} + de^{x_o/L_q}}{ae^{-x_o/L_q} + be^{x_o/L_q}}\right)$$

and

$$h = de^{x_o/L_q} - ce^{-x_o/L_q} + f(ae^{-x_o/L_q} - be^{x_o/L_q})$$

All the coefficients A_i, B_i, A'_i abd B'_i can now be found sequentially using equations A1, A2, A3 and A4 allowing the minority carrier density $P_i(x)$ to be found for each region. If there are r competing recombination routes in each region such that in the i^{th} region the minority carrier recombination lifetime of the j^{th} recombination route is τ_i then $\tau_i^{-1} = \sum_{j=1}^{r} \tau_{ij}$ and the CL intensity $I_j(x_o)$ from the j^{th} recombination route is given by

$$I_j(x_o) = \int_{-\infty}^{x_1} \frac{P_1(x)dx}{\tau_1} + \sum_{i=2}^{n-1} \int_{x_{i-1}}^{x_i} \frac{P_i(x)dx}{\tau_i} + \int_{x_n}^{\infty} \frac{P_n(x)dx}{\tau_n}$$

Now considering the Jakubowicz dislocation model, the most general one-dimensional case with n surfaces representing the misfit dislocation was not derived. Instead a simpler case with only 3 surfaces was considered. For simplicity the two outer surfaces were considered to have equal reduced surface recombination velocity, s, with the inner surface having reduced surface recombination velocity s_z. The surfaces were positioned at x = - h, x = O and x = h. This situation is illustrated (two-dimensionally) in Figure A.1 with the electron beam at position x_o. If there are 3 surfaces then obviously P(x) must be evaluated for 4 regions. Again, denoting the minority carrier density in region i by $P_i(x)$ two cases must be considered, $x_o \geq h$ and $O \leq x_o \leq h$. Due to the symmetry about the origin then the two cases for $x_o \leq - h$ and $- h \leq x_o \leq O$ need not be considered further. The minority carrier density in any region can be found using the method of images. This method has been discussed by Morse and Feshbach (1953)

and will not be described here. For the current problem this method yields the following solutions for the minority carrier density in each region. When $x_o \geqslant h$ then

$$P_4(x) = \frac{gL}{2D}\left[e^{-|x-x_o|/L} + e^{-(x+x_o-2h)/L}(r_1 + t_1 R_{23}\alpha e^{-2h/L})\right]$$

$$P_3(x) = \frac{gL\alpha t_1}{2D} e^{-(x_o-x)/L}(1+R_{23}e^{-2x/L})$$

$$P_2(x) = \frac{gL\alpha T_{32}}{2D} e^{-(x_o-h-x)/L}(1+r_1 e^{-2(h+x)/L})$$

$$P_1(x) = \frac{gL\alpha T_{21}}{2D} e^{-(x_o-x-2h)/L}$$

where
$$r_1 = -(s_1-1)/(s_1+1)$$
$$r_2 = (s_2-1)/(s_2+1)$$
$$t_1 = 2/(s_1+1)$$
$$t_2 = 2/(s_2+1)$$

and
$$R_{23} = r_2 + t_2^2 r_1 e^{-2h/L}/(1-r_1 r_2 e^{-2h/L})$$

$$T_{32} = t_1 t_2 e^{-h/L}/(1-r_1 r_2 e^{-2h/L})$$

$$T_{21} = \alpha T_{32} t_1 e^{-h/L}$$

plus
$$\alpha = 1/(1-r_1 R_{23} e^{-2h/L})$$

When $0 \leqslant x \leqslant h$ the minority carrier density in each region is given by the equations

$$P_4(x) = \alpha\frac{gL}{2D} t_1 e^{-(x-x_o)/L}(1+R_{23}e^{-x_o/L})$$

$$P_3(x) = \alpha\frac{gL}{2D} e^{-|x-x_o|/L}(1+R_{23}e^{-2x_o/L}) \begin{cases} (1+r_1 e^{-2(h-x)/L}) & \text{for } x \geqslant x_o \\ (1+r_1 e^{-2(h-x_o)/L} & \text{for } x \leqslant x_o \end{cases}$$

$$P_2(x) = \frac{\alpha g L T'_{32}}{2D} e^{x/L}(1+r_1 e^{-2(h+x)/L})$$

$$P_1(x) = \frac{\alpha g L t_1 T'_{32}}{2D}$$

where $T'_{32} = t_2(e^{-x_o/L} + r_1 e^{-(2h-x_o)/L})/(1-r_1 r_2 e^{-2h/L})$

The CL intensity can be calculated from these equations in two ways,either by integration over all space or by calculating the number, N, of carriers recombining per second at each of the three surfaces. For example, at the innermost surface N is given by

$$N = \frac{DdP}{dx^3}\Big|_{x=0} - \frac{Ddp}{dx}\Big|_{x=0}$$

The resultant expression for the CL intensity is complex and is not included here.

References

Abrahams M.S., Blanc J. and Binocchi C.J., 1972, J. Appl. Phys., 45, 3315.

Adachi S., 1985, J. Appl. Phys., 58, R1.

Adachi S. and Oe K., 1983, J. Electrochem. Soc., 130, 2427.

Akimoto K., Dohsen M., Arai M., and Watanabe N., 1985, J. Cryst. Growth, 73, 117.

Aplin P., 1983, unpublished work.

Archard G.D., 1961, J. Appl. Phys., 32, 1505.

Argunova T.S., Ruvimov S.S., Sorokin L.M., and Shul'pina I.L., 1985, Sov. Phys. Sol. Stat., 27, 1778.

Attolini G., Frigeri C., Peloci C. and Salviati G., 1986, J. Appl. Phys., 49, 167.

Bachrach R.Z. and Krusor B.S., 1981, J. Vac. Sci. and Technol., 18, 756.

Bafleur M. and Munoz-Yague A., 1983, Thin Solid Films, 101, 299.

Bafleur M., Munoz-Yague A., Lauret W. and Brabant J.C., 1984, J. Cryst. Growth, 66, 472.

Bafleur M., Munoz-Yague A., and Rocher A., 1982, J. Cryst. Growth, 59, 531.

Bailey S.J., Preston A.R., Steeds, J.W. and Morkoc H., 1987, to be published.

Balk L.J., Kubalek and Menzel E., 1976, Scanning Electron Microscopy, Vol. I, 257.

Balkan A.N., Ridley B.K., Frost J., Andrews D.A., Goodridge I. and Roberts J., 1986, Superlatt. and Microstruct., 2, 357.

Balkan A.N., Ridley B.K. and Goodridge I., 1986, Semicond. Sci. Technol. 1, 338.

Bastard G., 1981, Phys. Rev. B 24, 4714.

Bastard G., 1982, Phys. Rev. B, 25, 7584.

Bastard G., Delande C., Meynadier, Frijlink P.M. and Voos M., 1984, Phys. Rev. B, 29, 7042.

Bimberg D. and Christen J., 1986, Acta Physica Polonica A, 69, 841.

Bimberg D., Mars D., Miller J.W., Baner R., Oertel D. and Christen J., 1987, Superlatt. and Microstruct., 3, 79.

Bloss W.L., Koteles E.S., Brody E.M., Sowell B.J., Salerno J.P. and Gormley J.V., 1985, Sol. Stat. Comm., 54, 103.

Blumtritt M., Gleichmann R., Heydenreich J. and Johansen H., 1979, Phys. Stat. Sol. (a), 55, 611.

Boas M.L., 1983, Mathematical Methods in the Physical Sciences, p.617, (J. Wiley and Sons, London).

Booker G.R., 1964, Discussions of the Faraday Soc., 38, 298.

Booker G.R., Titchmarsh J.M., Fletcher J., Darby D.B., Hockley M., and Al-Jassim M., 1978, J. Cryst. Growth, 45, 407.

Brown L.M., 1981, J. Phys. F, 11, 1.

Casey H.C. and Parrish M.B., 1978, Heterostructure Lasers, Chapter 4, (Academic Press, New York).

Castaldini A., Cavallini A. and Gondi P., 1985, Il Nuovo Cimento, 6P, 423.

Chai Y.G. and Chow R., 1981, Appl. Phys. Let., 38, 796.

Chai Y.G., Pao Y-C and Hier P., 1985, Appl. Phys. Let., 47, 1327.

Cherns D. and Stowell M.J., 1975, Thin Solid Films, 29, 107.

Cho A.Y. and Arthur J.R., 1975, Prog. in Sol. Stat. Chem., 10, 531.

Christen J., Bimberg D., Steckenborn A., and Weimann G., 1984, J. Appl. Phys., 44, 84.

Chu Y.M., Darby D.M. and Booker G.R., 1981, Inst. Phys. Conf. Ser., 36, 331.

Davidson S.M. and Dimitriadis C.A., 1980, J. Microscopy, 118, 295.

Dawson P., Duggan G., Ralph H.I. and Woodbridge K., Phys. Rev. B, 28, 7381.

Day J.C.C., 1987, unpublished work.

Dean P.J. and Herbert D.C., 1979, Excitons, (Springer-Verlag, Berlin), p55, ed. K. Cho.

Delalande C., 1987, Physica B, 146, 112.

Dingle R., 1974, Phys. Rev. Lett., 33, 827.

Dingle R., 1975, Festkorperprobleme, 15, 21.

Dohler G.H., 1983, J. Vac. Sci. and Technol. B, 1, 278.

Donolato C., 1978, Optik, 52, 19.

Donolato C., 1981, Inst. Phys. Conf. Ser., 60, 215.

Donolato C., 1986, J. de Physique, 47, 171.

Donolato C., and Klann H., 1980, J. Appl. Phys., 51, 1624.

Duggan G., Ralph H.I., and Moore K.J., 1985, Phys. Rev. B, 32, 8395.

Dupuy M., 1983, J. de Physique, 44, C4, 277.

Eades J.A., 1982, J. Phys. F., 15, 184.

Esaki L., and Tsu R., 1970, IBM J. Research, 14, 61.

Feynman R.P.,1964, The Feynman Lectures on Physics, (Addison-Wesley, Massachusetts), Vol. II, p.6.10.

Frank F.C., and van der Merwe J.H., 1949, Proc. Roy. Soc. A, 198, 216.

Franzosi P., Salviati G., Genova F., Stano A., and Taiariol F., 1986, J. Cryst. Growth, 75, 521.

Fouquet J.E. and Burnham R.D., 1986, IEEE J. Quantum Electronics, 22, 1799.

Fukiwara K., Nishikawa Y., Tokuda Y. and Makayama T., 1986, Appl. Phys. Lett., 48, 701.

Fujiwara K., Kanamoto K., Ohta Y.N., Tokuda Y. and Nakayama T., 1987, J. Cryst. Growth, 80, 104.

Gershenzon M., 1966, Semiconductors and Semimetals, (Academic Press, New York), Vol. 2, p.316, eds. Willardson R.K. and Beer A.C.

Gevers R., Art A. and Amelinckx S., 1963, Phys. Stat. Sol., 3, 1563.

Goldstein J.I., Costley J.L., Lorimer J.L. and Reed S.J.B., 1977, Scanning Electron Microscopy, Vol. I, 315.

Gomez A. and Hirsch P.B., 1978, Phil. Mag. A, 38, 733.

Gooch C.H., 1973, Injection Electroluminescent Devices, (J. Wiley and Sons), p.58.

Grande M. and Dunn K., 1983, unpublished work.

Greene R.L. and Bajaj K.K., 1985, Sol. Stat. Com., 53, 1103.

Greene R.L., Bajaj K.K., and Phelps D.E., 1984, Phys. Rev. B, 29, 1807.

Hackett W.H., 1972, J. Appl. Phys. 43, 1649.

Heinrich H. and Langer J.M., 1986, Festkorperprobleme, 26, 251.

Hirsch P.B., Howie A., Nicholson R.B., Pashley D.W. and Whelan M.J., 1965, Electron Microscopy of Thin Crystals, (Butterworths, London).

Hirth J.P. and Lothe J., 1968, Theory of Dislocations, (MacGraw-Hill, New York).

Holonyak N., Kolbas R.M., Landjg W.D., Alterelli M., Dupuis R.D. and Papkins P.D., 1980, J. Appl. Phys., 51, 1328.

Hopfield J.J., 1958, Phys. Rev., 112, 1555.

Hopfield J.J., Physics of Semiconductors, 1964, (Academic Press, New York), p.725.

Hornstrd J., 1958, J. Phys. Chem. Sol., 5, 129.

Iida S. and Ito K., 1971, J. Electrochem. Soc., 118, 768.

Ishikawa H., Kondon K., Sasa S., Tanaka H. and Hiyamiza S., 1986, J. Cryst. Growth, 76, 521.

Jakubowicz A., 1985, J. Appl. Phys., 57, 1194.

Jakubowicz A., 1986, J. Appl. Phys., 58, 2205.

Jarosik N.C., McCombe B.D., Shanabrook B.V., Comas J., Ralston J. and Wicks G., 1985, Phys. Rev. Lett., 54, 1283.

Joyce B.A., 1985, Reports on Progress in Physics, 48, 1637.

Kakibayashi H., Nagata F., Katayama Y. and Shiraki Y., 1984, Jap. J. Appl. Phys., 23, L846.

Kirchner P.D., Woodall J.M., Freeouf J.L. and Petit G.D., 1981, Appl. Phys. Lett., 38, 427.

Kittel C., 1976, Introduction to Solid State Physics, (J. Wiley and Sons, London).

Kolbas R.M. and Holonyak W., 1984, Amer. J. Phys., 52, 431.

Kotani T., Neda O., Akita K., Nishitani Y., Kusonoki T. and Ryuzan O., 19 7, J. Cryst. Growth, 38, 85.

Kunzel H. and Ploog K., 1981, Inst. Phys. Conf. Ser., 56, 519.

Kyser D.F. and Wittry D.B., (1964), The electron microprobe, (J. Wiley and Sons, New York), P691, eds. McKinley T.D., Heinrich K.F.J. and Wittry D.B.

Lambert B., Devand D., Regreny A. and Talalaeff G., 1982, Sol. Stat. Comm., 43, 443.

Lambert B., Devand D., Regreny A. and Talalaeff G., 1983, Physica B, 117, 714.

Leamy H.J., 1982, J. Appl. Phys., 53, R51.

Logan R.A. and Reinhart F.K., 1973, 44, 4172.

Lohnert K. and Kubalek E., 1984, Phys. Stat. Sol. a), 83, 307.

Loretto M.H. and Smallman R.E., 1975, Defect Analysis in Electron Microscopy, (Chapman and Hall, London).

Ludowise M.J., 1985, J. Appl. Phys., 58, R31.

Masselink W.T., Chang Y.-C. and Morkoc H., 1984, J. Vac. Sci. and Technol. B, 2, 376.

Masselink W.T., Chang Y.-C. and Morkoc H., 1985, Phys. Rev. B., 32, 5190.

Matteson S. and Shih H.P., 1986, Appl. Phys. Lett., 48, 47.

Matthews J.W., 1975, Epitaxial Growth, (Academic Press, New York).

Mendelson S., 1961, J. Appl. Phys., 35, 1570.

Matthews J.W., Blakeslee A.F. and Mader S., 1976, Thin Solid Films, 33, 253.

Miller R.C., Gossard A.C. and Tsang W.T., 1983, Physica B, 117, 714.

Miller R.C., Gossard A.C., Tsang W.T. and Manteanu O., 1982, Phys. Rev. B, 25, 3871.

Miller R.C., Tsang W.T. and Manteanu O., 1982, Appl. Phys. Lett., 44, 217.

Mimura T., Hiyanizu S., Fujii T. and Nanbu K., 1980, Jap. J. Appl. Phys., 19, L225.

Moore K.J., Dawson P. and Foxon C.T., 1986, Phys. Rev. B, 34, 6022.

Morse P.M. and Feshbach H., 1953, Methods of Theoretical Physics, (McGraw-Hill, New York), Chapters 7 and 9.

Nanbu K., Saito J., Ishikawa T., Kondo K. and Shibatoni A., 1986, J. Electrochem. Soc., 133, 601.

Neave J.H., Joyce B.A., Dobson P.J. and Norton H., 1983, Appl. Phys. A, 31, 1.

Ourmazd A., Wilshaw P.R. and Booker G.R., 1983, J. de Physique, 44, C4-289.

Pasemann L., 1981, Ultramicroscopy, 6, 237.

Pennycook S.J., 1981, Ultramicroscopy, 7, 99.

Petit G.D., Woodall J.M., Wright S.L., Kirchner P.D. and Freeouf J.F., 1984, J. Vac. Sci. and Technol. B, 2, 241.

Petroff P.M., Lang D.V., Strudel J.L. and Logan R.A., 1978, Scanning Electron Microscopy, Vol. I, 325.

Petroff P.M., Logan R.A., and Savage A., 1980, J. of Microscopy, 118, 255.

Petroff P.M., Miller R.C., Gossard A.C. and Wiegmann W., 1984, Appl. Phys. Lett. 44, 217.

Petroff P.M., Weisbach G., Dingle R., Gossard A.C. and Wiegmann W., 1981, Appl. Phys. Lett., 35, 965.

Ravi K.V., 1976, Thin Solid Films, 31, 171.

Ravi K.V. and Varker C.J., 1974, J. Appl. Phys., 45, 263.

Read W.T., 1953, Dislocations in Crystals, (McGraw-Hill, New York).

Roberts S., 1981, Inst. Phys. Conf. Ser., 60, 371.

Saito H., Borland J.O., Asaki H., Nagai H. and Nawata K., 1983, J. Cryst. Growth, 64, 521.

Sakaki H., Tanaka M. and Yoshimo J., 1955, Jap. J. Appl. Phys., 24, L417.

Schiller C. and Boulou M., 1975, Philips Tech. Rev., 35, 239.

Shinohara M., Ito T. and Inamura Y., 1985, J. Appl. Phys., 58, 3449.

Spivak G.V., Petrov V.I. and Antoshin M.K., 1986, Sov. Phys. Usp., 29, 364.

Shinohara M., Ito T., Wada K. and Inamura Y., 1983, Jap. J. Appl. Phys., 23, L371.

Shockley W., Electrons and Holes in Semiconductors, 1950, (Van Nostrand, Princeton), p.323.

Stowell M.J., 1975, Epitaxial Growth, (Academic Press, New York), Ed. Matthews J.W.

Stirland D.J., Grant I., Brozel and Ware R.M., 1983, Inst. Phys. Conf. Ser., 67, 285.

Susa N. and Okamoto H., 1984, Jap. J. Appl. Phys., 23, 317.

Suzuki H., 1962, J. Phys.Soc. Jap., 17, 322.

Suzuki Y., Seki, M., Horkoshi Y. and Okamoto H., 1984, Jap. J. Appl. Phys., 23, 164.

Tafto J. and Spence J.C.H., 1982, J. Appl. Cryst., 15, 60.

Tanaka M., Sakaki H. and Yoshino J., 1986, Jap. J. Appl. Phys., 24, L417.

Thomas G. and Goringe M.J., 1979, Transmission Electron Microscopy of Materials, (Wiley Interscience, USA).

Titsh marsh et al

Trommer R., 1981, Inst. Phys.Conf. Ser., 61, 51.

Tsang W.T., 1981, Appl. Phys. Lett., 39, 786.

Tsang W.T., 1985, Appl. Phys. Lett., 47, 391.

Varker C.J. and Ravi K.V., 1974, J. Appl. Phys., 45, 272.

Wang Y.H., Liu W.C., Chang C.Y. and Liao S.A., 1986, J. Vac. Sci. and Technol. B, 4, 30.

Warwick C.A. and Booker G.R., 1983, Inst. Phys. Conf. Ser., 61, 51.

Watanabe W., Fukunaya T., Kobayashi K. and Nakashina K., 1985, Jap. J. Appl. Phys., 24, L498.

Weisbuch C., Dingle R., Gossard A.C. and Wiegmann W., 1981a, Sol. Stat. Comm., 38, 709.

Weishbuch C., Miller R.C., Dingle R., Gossard A.C. and Wiegmann W., 1981, Sol. Stat. Comm., 37, 219.

Weng S., 1987, J. Vac. Sci. and Technol. B, 5, 725.

Weng S., Webb C., Chai Y.G. and Baudy S.G., 1985, Appl. Phys. Lett., 47, 391.

Werner K., Heinekce H., Weyers M., Luth H. and Balk, P., 1987, J. Cryst. Growth, 81, 281.

Wittry D.B., 1958, J. Appl. Phys., 29, 1543.

Wittry D.B., 1984, Electron Beam Interactions with Solids, (SEM Inc, AMF O'Hare, USA), p.99.

Wittry D.B. and Kyser D.F., 1967, J. Appl. Phys., 38, 375.

Wood G.E.C., Rathbun L., Ohno H. and De Simone D., 1981, J. Cryst. Growth, 64, 521.

Woodbridge K., Dawson P., Gowers J.P. and Foxon C.T., 1984, J. Vac. Sci. and Technol. B, 2, 163.

Yablonovitch E., Sandroff C.J., Bhat R. and Gmitter T., 1987, Appl. Phys. Lett., 51, 439.

Yacobi B.G. and Holt D.B., 1986, J. Appl. Phys., R1, 1986.

Zimmerman W., 1972, Phys. Stat. Sol. a), 12, 671.